



The
University
Of
Sheffield.

Solution Processed Electrolyte-Gated Thin Film Transistors and their Sensing applications

By

Talal M. Althagafi

A thesis submitted in partial fulfilment for the degree of Doctor of
Philosophy in Physics

Department of Physics and Astronomy
The University of Sheffield

January 2017

I dedicate this thesis to all my beloved family

*My Dad Mohammed Althagafi, my Mum Jumma Althagafi, my
Wife Hind Althagafi, and my kids: Albaraa, Rateel and Rasil.*

Acknowledgements

First of all, I would like to express a great praise and thank to **ALLAH**, who inspires me patience and guide me in completing my PhD thesis. I would like thank my brothers and sisters in Saudi Arabia for their love and support during my study for PhD degree.

I would like to express a deep and special thank to **Dr. Martin Grell**, who has supported and guided me to make my PhD study in right way. I would like to express my gratitude to him for his professional supervision, motivation, great patience, and massive knowledge.

I would like to present my deepest appreciation to my Co-supervisor **Dr. Patrick J Smith** in Mechanical Engineering Department for his encouragement and his help and advices in Inkjet printing and provide me all the facilities in his lab, Laboratory of Applied Inkjet Printing, University of Sheffield. Also, Special appreciation goes to **Dr. Christopher Tse**, form Sheffield University, and **Dr. Jonathan Stringer**, from Auckland University, for their help and support.

I would like to thank all my group members, **Dr. Krisna Adhitya**, **Mr. Abraham T Kirwa**, **Mr. Abbad Al Baroot**, who have made all moments during my PhD study memorable and delightful as well as for the spectacular discussions and their participate inside the lab.

Gigantic thank from my heart goes to my close friend **Dr. Saud Algarni**, for his incredible cooperation and generous contribution in my project. Also, Many thanks for my best friends **Dr. Hasan Albargi**, **Dr. Ateyyah Albaradi**, **Saif Althagafi**, **Fawaz Alzahrani**, **Yousef Al-Khammash**, **Dr. Hind Al-Khammash**.

Special appreciation goes to:

Prof. Iain McCulloch from Imperial College, London, for helpful discussions on catalyst residues in PBTTT.

Dr. Antonis Dragoneas from Max Plank institute for his effort and help in LabView programme and real time IV converter circuit.

Dr. Abdullah Al Naim from King Faisal University, Saudi Arabia, for his collaboration in XPS and SEM.

Dr. Debbie Hammond from Sheffield Surface Analysis Centre for her support on XPS and Auger spectroscopy.

Special thank goes to the **Saudi Cultural Attaché** in London and **Taif University** in Saudi Arabia for the scholarship.

Abstract

The thin film transistor (TFT) is one of the most important fundamental building blocks in modern electronic devices. Examples of TFT applications are in integrated circuits (ICs), amplifiers, addressing of flat panel displays, and also as chemical sensors, e.g. as ion-selective field effect transistors (ISFETs). Although the most common semiconductor materials used in thin film transistors (TFTs) is silicon (Si), the versatility of TFTs allows other semiconductors to be used instead of Si-based materials. Recent research effort has been directed towards alternative TFT semiconductors, for example solution-processable semiconductors that enable new manufacturing options. Since the 1990s, soluble semiconducting polymers have been intensely researched for TFT applications. The possibility to engineer their transport (HOMO/LUMO) levels via chemical synthesis, their low temperature processing from solution, and their mechanical flexibility offers the potential for economical device production, as well as large-area and flexible applications.

In the last few years, the interest as promising materials for the next generation of TFTs has shifted towards oxide based semiconductors such as ZnO due to their high performance and relative stability to ambient conditions. The potential of ZnO was boosted by the discovery that it can be derived by pyrolysis of an organic precursor that is soluble in polar organic solvents (e.g. alcohols, ketones) thus enabling solution processing of ZnO TFTs and other devices.

In addition, it has been demonstrated that both organic thin films and ZnO films can be gated by a field effect with very low threshold using deionized (DI) water as an electrolytic gate medium, leading to the 'water-gated thin film transistors' (WGTFTs). This discovery marks the beginning of a new method for the sensing of waterborne analytes, which differs from the classic ISFET in one significant point: Here, the aqueous sample under test is an active portion of the transducer. A number of works have since been undertaken using this discovery as a novel sensor concept for detecting waterborne analytes. Such sensors rely in the integration of analyte-specific sensitizers into the TFT architecture. For the selective sensing of ions, one of the most prominent families of water-insoluble ion sensitizers ('ionophores') are the calixarenes, a family of organic macrocycles. Calixarenes can be designed to selectively to complex specific cations, anions and neutral molecules.

The work in this thesis is concentrated on two major objectives from within the context introduced above:

- 1- The study and development of electrolyte- gated TFTs with solution- processed semiconductors with improved materials and device architectures.
- 2- Using WGTFTs as sensors for sensing of waterborne analytes via integrating the sensitizers into the WGTFT architecture.

The chapters presented in this thesis have been arranged beginning (Chapters 1 to 3) with basic theoretical concepts, device fabrication, and characterization. The second part of the thesis (Chapters 4 to 6) reports my results on electrolyte- gated TFTs, including high current TFTs, development of ZnO precursor route processing, and using WGTFTs as sensors. Chapters are summarized as in the following:

Chapter 1 gives an introduction to the terminology and the basic theory regarding thin film transistors, solution processed inorganic /organic semiconductors, charge carrier injection and transport in semiconductors, the electric double layer (EDL) in electrolyte, and the use of WGTFT for sensing applications.

Chapter 2 discusses the techniques employed for fabricating semiconductor devices. In this chapter two techniques to fabricate TFTs contacts substrates are described, thermal evaporating and inkjet printing. Thin films of semiconductors were coated on contact substrates via two methods, spin-casting and spray pyrolysis.

Chapter 3 describes in detail the techniques utilized for the morphological and electrical characterization of the fabricated TFTs. Optical microscopy, scanning electron microscopy (SEM), X-ray photoelectron spectroscopy (XPS), UV spectrophotometer, and profilometry were used to study the morphology, electronic, and optical properties of semiconducting films. Furthermore, the electrical characterizations of thin film transistor devices were studied by using Keithley 2400 source measure units controlled by bespoke LabView software in addition to a new method that was developed in our group previously, which called I-V Converter method.

Chapter 4 discusses in detail using Ionic liquid (IL) to gate an OTFT based on solution-processed organic semiconductor PBTTT. PBTTT is a high performance semiconducting polymer, but is only marginally soluble (requires hot chlorinated benzenes). This gives it resistance to dissolution even in ILs, which dissolve many other semiconducting polymers. Gating a PBTTT film with IL gives low threshold, very high carrier mobility OTFTs that deliver high currents at only 1V.

Chapter 5 discusses in detail an improvement of the established precursor route towards solution- processed inorganic semiconductor ZnO. In addition, a new precursor for solution processed inorganic semiconductor ZnO has been demonstrated.

The established (Zinc acetate, ZnAc) precursor route towards solution- processed ZnO films was improved by dissolving the ZnAc precursor in a mixed solvent. The characterisations of resulting ZnO film show improved morphology of ZnO films. Gating such ZnO-TFTs with a biologically realistic aqueous electrolyte show very high electron mobility and low sheet resistance at 1V.

A new precursor-route semiconducting zinc oxide (ZnO) films was obtained by spraying aqueous solutions of the Zinc salt Zinc Chloride (ZnCl_2) onto source-drain substrates heated to at least 250 °C. Resulting films are insoluble in water (while Zinc Chloride is highly soluble in water), and a number of further studies confirm that they consist of Zinc oxide, ZnO. When these films are gated with DI water, they give similar TFT characteristics to the ZnO films that derived from Zinc Acetate (ZnAc) precursor route. This establishes a new precursor route to ZnO avoiding organic solvents altogether.

Chapter 6 is dedicated to WGTFT as sensor for waterborne ions and divided into two sections:

Section 1 shows that WGTFTs using the semiconducting polymer PBTTT display sensitivity to divalent waterborne cations, without deliberately introducing ion sensitizers (ionophores). Sensitivity and selectivity are innate to PBTTT itself, we assign it to residues of the catalyst used for PBTTT polymerisation which act as ionophores.

Section 2 builds on the discovery that ionophores mixed into an organic semiconductor film lead to ion- sensitive WGTFTs without the use of a separate ion- selective membrane, as it was required in previous designs. We deliberately added a calcium- selective calixarene ionophore to casting solution of the semiconducting polymer, rrP3HT, which shows no innate cation response. Resulting WGTFTs displayed near- Nernstian response selectively for Ca^{2+} ions added to the gating water.

Chapter 7 summarizes the presented thesis, and provides viewpoint for potential future work.

Table of Contents

1. THIN FILM TRANSISTOR (TFT) HISTORY	1
1.1 STRUCTURE OF THIN FILM TRANSISTOR (TFT).....	1
1.2 OPERATION PRINCIPLE OF TFT	4
1.3 QUANTITATIVE DESCRIPTION OF TFT OPERATION.....	5
1.4 TFT SEMICONDUCTORS.....	9
1.4.1 <i>Solution-Processed Inorganic Semiconductors</i>	10
1.5 ORGANIC SEMICONDUCTORS	14
1.5.1 <i>Conjugation and Band Gap</i>	15
1.5.2 <i>Benzene and Thiophene Ring</i>	17
1.5.3 <i>Charge Carrier Injection and Transport in Organic Semiconductors</i>	20
1.5.4 <i>Organic Semiconductor Materials</i>	30
1.6 ELECTROLYTES AS GATE MEDIA IN TFTS.....	33
1.6.1 <i>Electric Double Layers (EDLs)</i>	35
1.6.2 <i>Examples of Electrolytes used as TFT Gate Media</i>	39
1.7 WATER-GATED TFTS (WGTFTS).....	42
1.7.1 <i>Operation Principle of WGTFTs</i>	42
1.7.2 <i>Water-gated Transistors as Sensors</i>	45
1.7.3 <i>Ion-selective WGTFTs</i>	46
1.7.4 <i>Calixarenes</i>	52
2 THIN FILM TRANSISTOR (TFT) FABRICATION	54
2.1 SUPPORTING SUBSTRATES	54
2.1.1 <i>Substrate Cutting</i>	54
2.1.2 <i>Substrate Cleaning</i>	55
2.1.3 <i>Ultraviolet Light Ozone Cleaning</i>	56
2.2 DEPOSITION TECHNIQUES FOR TFT CONTACTS	56
2.2.1 <i>Thermal Evaporation Technique</i>	56
2.2.2 <i>TFT Contacts Substrate Fabrication by Thermal Evaporation</i>	58
2.3 INKJET PRINTING TECHNIQUE	62
2.3.1 <i>TFT Contacts Substrate Fabricated by Inkjet Printing</i>	65
2.4 DEPOSITION TECHNIQUES FOR THIN FILM SEMICONDUCTORS.....	68
2.4.1 <i>Spin Coating Method</i>	68
2.4.2 <i>Spray Pyrolysis Method</i>	72
3. EXPERIMENTAL METHODOLOGY AND ELECTRICAL CHARACTERIZATION	77
3.1 CHARACTERIZING THIN FILM MORPHOLOGY AND ELECTRONIC PROPERTIES	77
3.1.1 <i>Optical Microscopy</i>	77
3.1.2 <i>Surface Profilometry</i>	78

3.1.3	<i>Scanning Electron Microscopy</i>	79
3.1.4	<i>UV-Vis Spectrophotometry</i>	82
3.1.5	<i>X-ray Photoelectron Spectroscopy</i>	85
3.2	ELECTRICAL CHARACTERIZATION OF THIN FILM TRANSISTORS.....	87
3.2.1	<i>TFT Characterization with Source Measure Units</i>	88
3.2.2	<i>I-V Converter Method</i>	97
3.2.3	<i>Real Time TFT Measurements</i>	104
4	ORGANIC THIN FILM TRANSISTOR GATED WITH IONIC LIQUID	106
4.1	INTRODUCTION.....	106
4.2	OTFT FABRICATION.....	107
4.3	IONIC LIQUID-GATED ORGANIC TRANSISTOR ELECTRICAL CHARACTERISTICS.....	108
4.4	IONIC LIQUID-GATED PBTTT OTFT PERFORMANCE.....	108
4.5	SUMMARY AND CONCLUSIONS.....	115
5	PRECURSOR-ROUTE TO ZINC OXIDE SEMICONDUCTOR (ZNO) WGTFT	118
5.1	MIXED ORGANIC SOLVENT FOR ZNO PRECURSOR ZINC ACETATE (ZnAc).....	119
5.1.1	<i>Preparation of ZnO Films from Zinc Acetate (ZnAc) Precursor Solutions</i>	120
5.1.2	<i>Results and Discussion</i>	122
5.1.3	<i>Conclusion</i>	134
5.2	ZINC CHLORIDE (ZnCl ₂) AS A PRECURSOR FOR SOLUTION-PROCESSED ZNO.....	135
5.2.1	<i>Preparation and Processing of ZnCl₂ Solution</i>	135
5.2.2	<i>Result and Discussion</i>	136
5.2.3	<i>Conclusion</i>	146
6	WATER-GATED THIN FILM TRANSISTORS AS SENSORS FOR WATER-BORNE ANALYTE	148
6.1	INNATE SENSITIVITY OF PBTTT TO DIVALENT WATER-BORNE CATIONS.....	149
6.1.1	<i>Experimental Section</i>	149
6.1.2	<i>Electrical Characteristics</i>	150
6.1.3	<i>Control Experiments</i>	157
6.1.4	<i>Conclusions</i>	166
6.2	DETECTING WATER-BORNE CATIONS WITH SENSITIZED POLYTHIOPHENE.....	170
6.2.1	<i>Experimental Section</i>	170
6.2.2	<i>Results and Discussion</i>	172
6.2.3	<i>Control Experiments</i>	176
6.2.4	<i>Effect of Voltage Sweep Rate</i>	179
6.2.5	<i>Conclusions</i>	183
7.	OVERALL CONCLUSION AND PROPOSED FUTURE WORK	184

List of Figures

Figure 1-1: Comparison of typical architecture of <i>p</i> -type metal oxide semiconductor field effect transistor (MOS-FET) and Thin Film Transistor (TFT), with channel length L , channel width W . The dashed line indicates the flow of charges in the channel. ...	2
Figure 1-2: Different configurations of TFTs: staggered (a) bottom-gate-top-contact and (b) top-gate-bottom-contact; coplanar (c) bottom-gate-bottom contact and (d) top-gate-top-contact. The dashed line indicates the flow of charges in the channel and showing the injection area of carriers charge from source contact.....	3
Figure 1-3: Simplified sketch of the operation of a TFT with <i>p</i> -type semiconductor, (G), (D), (S), and (SC) refer to gate, drain, source, and semiconductor, respectively.	5
Figure 1-4: TFT's operating regimes is presented by an output characteristics: (a) is the linear regime, in which V_G applied ($V_G > V_{th}$), $V_D = 0V$. The accumulation layer of carriers (blue) is fully developed. (b) denotes the start of drain current saturation when V_G applied, $V_D = V_G$. The accumulation layer of carriers (green) is triangular and TFT reaches pinch-off in which I_D becomes independent of the applied drain voltage and begins to saturate. (c) is the saturation regime, in which V_G applied, $V_D \gg V_G$ and the accumulation layer (red) pitches off within channel, leaving a carrier-depleted region within the channel.....	9
Figure 1-5: shows unit cell of the wurtzite structure of ZnO [26].	12
Figure 1-6: The structure of benzene ring.	18
Figure 1-7: Chemical structure of pentacene.	19
Figure 1-8: The structure of Thiophene ring. Right shows the delocalized π electron system.....	20
Figure 1-9: Example of polythiophene segment before removing an electron (Top) and after removing an electron (Bottom). It is clear that removing an electron leads to redistribution of the π -bonds and then conformational change in the nucleus positions and molecular orbitals, <i>i.e.</i> the bond lengths and angles.....	21
Figure 1-10: A diagram illustrating an electron injection into organic semiconductor P3HT, and the energy levels drawing of electron and hole injection barriers from different metal contacts into P3HT without applying voltage.	22
Figure 1-11: The energy level of P3HT organic semiconductor during applying voltage with Au and Ag contacts.....	23

Figure 1-12: (left) represents the thermionic emission mechanism for the charge injection from a metal into an organic/inorganic semiconductor, while (right) represents Fowler-Nordheim tunnelling mechanism for the charge injection from a metal into an organic/inorganic semiconductor..... 25

Figure 1-13: Energy illustrations displaying band tilting (left) and band bending (right). 26

Figure 1-14: the electronic levels of organic semiconductors (P3HT and PBTTT); HOMO (Red line) and LUMO (Purple line). Valence band (Blue line) and conduction band (Green line) for inorganic semiconductor (ZnO). Yellow line shows the Fermi level for gold metal. 27

Figure 1-15: A chemical structure of rr-P3HT (regioregular poly(3-hexylthiophene)). 31

Figure 1-16: A chemical structure of semiconducting polymer poly(2,5-bis(3-hexadecylthiophen-2-yl)thieno[3,2-b]thiophene) (PBTTT)..... 33

Figure 1-17: Charge and discharge of EDL capacitor. By applying bias with opposite polarity on the electrodes (capacitor plates), cations and anions start to move towards the electrodes (Left) until they balance the charges on the electrode's surface, leading to EDLs. When removing the applied voltages and connecting the electrodes (e.g. via a resistor), the capacitor plates will discharge and ions will diffuse until an even distribution is regained. Figure adapted from ^[71]. 36

Figure 1-18: The electrical double layer's models: (a) the Helmholtz model, (b) the Gouy–Chapman model, and (c) the Stern model. The distance of the Helmholtz double layer from the electrode is in Stern model, IHP and OHP refer to the inner Helmholtz plane and outer Helmholtz plane. IHP denotes to the space of closest contact of adsorbed ions while OHP denotes to that of the non- adsorbed ions. OHP represents the starting point of diffuse layer. ψ_0 is the potential at the metal contact surface and ψ is the potential at the metal surface/electrolyte interface. Figure adapted from ^[71] 38

Figure 1-19: The chemical structure of EMITSFI ionic liquid. 42

Figure 1-20: Schematic cross section of a thin film transistor with voltage (V) and electric field (E) in a dielectric (top) and electrolytic gate (bottom) when a positive gate voltage is applied. Note the similarity of the bottom right image to Fig. 1.17..... 43

Figure 1-21: A illustration showing the electrolyte- gated impermeable/ permeable organic semiconductor: left) in Field Effect mode, and right) in Electrochemical mode. ^[10] 44

Figure 1-22: The experimental determination of an ion selectivity for an analyte. The activity of analyte (a_i) \approx concentration (c) corresponding to the meeting of the two lines of the curve, produces a potential identical to that of the interferent. 49

Figure 1-23: Electrochemical transducer for making a potentiometric measurement with an ISE. 50

Figure 1-24: The native tBu-calix[4]arene indicating the hydrophobic upper rim and hydrophilic lower rim with cavity shape (Top). (Bottom) shows tBu-calix[6]arene and tBu-calix[8]arene.^[110] 52

Figure 2-1: Picture of a Teflon holder used within cleaning processing..... 56

Figure 2-2: The picture of Edwards E306 Bell-jar Evaporator (top) and the configuration inside evaporator (bottom). 60

Figure 2-3: A shadow evaporation stack containing a dozen of cleaning substrates. 61

Figure 2-4: Transistor substrate geometry for S/D contacts (left) and contact substrate after deposition of Chromium and gold on amorphous SiO₂ ('Quartz') substrates, (right). 61

Figure 2-5: (left) Schematic diagram of a piezoelectric inkjet print head. (Right) Schematic representation of wave propagation and reflection in a piezoelectric tubular actuator. 63

Figure 2-6: Diagram showing the parameters that are used in modelling the relationship between final track width and contact angle. w is the width of the track and $p = \Delta x$ is the spacing between each deposited droplet.^[129] 65

Figure 2-7: shows the JetLab 4xl inkjet printing system (right) and the fluid reservoir and printhead used in the experimental activity presented in this thesis. These pictures have been taken from microfab Technologies website..... 67

Figure 2-8: Transistor substrate geometry for S/D contacts (left) printed contact substrates (middle) and Optical micrograph of printed / fused Ag contacts; channel length $L = 40 \mu m$ and line width of $100 \mu m$ (right). 67

Figure 2-9: (a) shows the type of spin-coater used in my experiments . (b) the different steps of spin coating. 1) Deposition solution. 2) Start spinning. 3) Flow of fluid dominates and 4) Evaporation of solvent (drying). 69

Figure 2-10: Schematic diagram of a compressed air atomizers and temperature controller. 73

Figure 2-11: Description of the deposition mechanisms initiated for film growth with increasing substrate temperature in spray pyrolysis processing.	74
Figure 3-1: Picture of Nikon optical microscope.	78
Figure 3-2: Picture of Veeco Dektak XT Surface contact profilometer.	79
Figure 3-3: Scanning electron microscope (SEM) block diagram ^[140]	81
Figure 3-4: Simplified diagram of a double beam UV- visible spectrophotometer. ...	83
Figure 3-5: Picture of Thermo Unicam UV-500 double-beam spectrophotometer....	85
Figure 3-6: Photoelectric process to for XPS principle.	86
Figure 3-7: A photo of the Keithley units (top) and probe-heads (bottom). Two tungsten (W) needles are connected to drain and source contact and gold (Au) needles (gate needle) in form of L-shape overlapping the droplet that covered the active area.	89
Figure 3-8: A screenshot of Labview-code of the output characteristic (Top) and transfer characteristic (Bottom).	90
Figure 3-9: Output characteristics of an electron- transporting OTFT. Dotted and continuous line shows the point where the condition $ V_D = V_G - V_{th} $ is met, TFT reaches pinch-off. Beyond pinch-off, I_D becomes independent of the applied drain voltage and begins to saturate.....	92
Figure 3-10: The transfer characteristics (Top) represents the linear regime, at low V_D . While, the transfer characteristics (bottom) denotes saturated regime on a logarithmic scale (green), and on a square root scale (red).	93
Figure 3-11: Shows an example of anticlockwise TFT hysteresis.	96
Figure 3-12: Current to voltage converter circuit diagram.	97
Figure 3-13: Shows saturated transfer characteristics (dashed red) parametric in time and V_s (V_{in}) applied to the source (blue) of water-gated PBTTT TFT.....	99
Figure 3-14: Displays saturated drain current (dashed red) parametric in time and V_{in} applied to the source (blue) of ILs-gated OTFT.....	101
Figure 3-15: Shows saturated transfer characteristics of IL-gated PBTTT TFT on a logarithmic scale (blue), and on a square root scale (dashed red) after eliminating the time parameter.	102
Figure 3-16: Shows IL gated PBTTT TFT and extracting threshold voltage V_{th} from Saturated transfer characteristics (dashed red) parametric in time and V_S (V_{out}) applied to the source (blue).	103
Figure 3-17: A screenshot for real- time characterisation taken from I-V converter assistant LabView program.	105

Figure 4-1: The chemical structure of EMITSFI ionic liquid.....	108
Figure 4-2: Output characteristics for IL- gated PBTTT OTFT with Au source/drain contacts.....	109
Figure 4-3: Saturated transfer characteristics parameteric in time for IL- gated PBTTT OTFT with Au source/drain contacts (red short dash). Green long dashes show the saturated transfer characteristic for same device gated with water. Solid blue line shows the drive voltage (V_{in}) that applied to the source, (as described in Chapter 3 section 3.2.2).....	110
Figure 4-4: Saturated transfer characteristics for IL- gated PBTTT OTFT with eliminating the time, with Au source/drain contacts.....	111
Figure4-5: Output characteristics for IL- gated PBTTT OTFT with printed silver source and drain contacts.....	113
Figure 4-6: Saturated transfer characteristics for IL- gated PBTTT OTFT with printed printed silver source and drain contacts (red short dash), parametric in time. Drive voltage in solid blue. Inset: Optical micrograph of printed / fused Ag contacts; channel length $L = 40 \mu m$	113
Figure 4-7: Saturated transfer characteristics for IL- gated PBTTT OTFT with eliminating the time, with Ag source/drain contacts.....	115
Figure 5-1: XPS spectra of Zn 2p orbitals in ZnO films resulting from the thermal conversion of precursor ZnAc cast from EtOH.....	123
Figure 5-2: XPS spectra of Zn 2p orbitals in ZnO films resulting from the thermal conversion of precursor ZnAc cast from mixed solvent, EtOH: Acetone 1:1.	123
Figure 5-3: XPS spectra of O1 s for ZnO films resulting from the thermal conversion of precursor ZnAc cast from EtOH.	124
Figure 5-4: XPS spectra of O1 s for ZnO films resulting from the thermal conversion of precursor ZnAc cast from cast from mixed solvent, EtOH: Acetone 1:1.....	124
Figure 5-5: SEM images of ZnO films resulting from the thermal conversion of precursor ZnAc cast from EtOH.	126
Figure 5-6: SEM images of ZnO films resulting from the thermal conversion of precursor ZnAc cast from mixed solvent, EtOH: Acetone 1:1.	126
Figure 5-7: Scheme of water- gated ZnO TFT architecture.....	128
Figure 5-8: Output characteristics for ZnO TFTs gated by PBS. ZnO film resulting from precursor cast from pure EtOH. Insets to output characteristics display magnified output characteristics at low V_G	129

Figure 5-9: Output characteristics for ZnO TFTs gated by PBS. ZnO film resulting from precursor cast from mixed EtOH/acetone (1:1). Insets to output characteristics display magnified output characteristics at low V_G 129

Figure 5-10: Saturated transfer characteristics for ZnAc precursor route ZnO TFTs gated by PBS electrolyte. Precursor cast from pure EtOH. Blue scale: represents transfer characteristics on $I_D^{1/2}$. Orange scale represents transfer characteristics on $\log I_D$ 130

Figure 5-11: Saturated transfer characteristics for ZnAc precursor route ZnO TFTs gated by PBS electrolyte. Precursor cast from mixed EtOH: acetone (1:1). Transfer characteristics are shown in two different representations (on $I_D^{1/2}$ (Blue) and $\log I_D$ (Orange) scale). 130

Figure 5-12: Picture of sprayed aqueous $ZnCl_2$ solutions onto heated (450 °C) TFT contact substrates. 136

Figure 5-13: Optical transmission spectra for 3 sprayed films: Aqueous $ZnCl_2$ solution onto hot (450°C) substrate (blue, dashed), ZnAc in ethanol/acetone 1:1 onto hot substrate (green, dotted), aqueous $ZnCl_2$ solution onto ambient temperature substrate, dried under vacuum, heated afterwards (red, dot dash). 137

Figure 5-14: Quantified survey scan of of a spray pyrolyzed $ZnCl_2$ film. 138

Figure 5-15: Highly resolved XPS spectra of spray pyrolyzed films in the O 1s peaks, A: represents ZnO, B: denotes oxygen deficient region in ZnO matrix, and C assigns hydroxide (-OH surface groups), or to oxygen defects. 140

Figure 5-16: Highly resolved XPS spectra of spray pyrolyzed films in the Zn 2p peaks at 1021 eV / 1045 eV. Note the splitting of Zn 2p into Zn 2p_{3/2} and Zn 2p_{1/2}. Inset: Zn LMM Auger peak at ~ 988 eV. 141

Figure 5-17: Scheme of water- gated TFTs using films of spray pyrolysed aqueous $ZnCl_2$ solutions. 142

Figure 5-18: Output characteristics of water- gated TFTs using films of spray pyrolysed aqueous $ZnCl_2$ solutions in the transistor channel. 143

Figure 5-19: Linear transfer characteristics ($V_D = 0.1$ V) of water- gated TFTs using films of spray pyrolysed aqueous $ZnCl_2$ solutions in the transistor channel. 144

Figure 5-20: Saturated transfer characteristics of water- gated TFTs using films of spray pyrolysed aqueous $ZnCl_2$ solutions in the transistor channel. Root (red dashed) and log (blue) drain current scales. 144

Figure 6-1: Output characteristics of water-gated PBTTT OTFTs. 151

Figure 6-2: Linear transfer characteristics of water- gated PBTTT OTFTs with different CaCl_2 concentrations (red), each referenced to same characteristic taken under DI water (blue) immediately before and (green) DI water immediately after. Substrates were discarded after single use. Hysteresis arrows are the same for DI and CaCl_2 . 152

Figure 6-3: The alternative values of threshold shift ΔV_{th} that can be extracted from the same linear transfer characteristics plotted on a linear I_D scale by linear extrapolation to $I_D = 0$ 153

Figure 6-4: Threshold shift ΔV_{th} vs. $\log(c)$ scale and vs. $\log(c - c_{\text{st}})$ scale (inset, $c_{\text{st}} = 4.5 \mu\text{M}$). Slope s in the inset is $55 \pm 2.7 \text{ mV/decade}$ 155

Figure 6-5: Product of carrier mobility and specific capacitance for all water- gated PBTTT OTFTs gated with CaCl_2 solutions of different concentrations. 156

Figure 6-6: PBTTT OTFTs gated with solutions of various cations. **6-6a**: Monovalent cations (Na^+ , K^+). **6-6b**: Divalent cations (Ba^{2+} , Mg^{2+} , Zn^{2+}). All PBTTT–OTFT were electrically addressed with a gold (Au) gate needle. 158

Figure 6-7: A summary plot showing threshold voltage shift for PBTTT OTFTs gated with solutions of various cations. Extracted from Fig. 6-6..... 159

Figure 6-8: Linear transfer characteristics of water- gated ZnO OTFTs with different CaCl_2 concentrations (red), each referenced to same characteristic taken under DI water (blue) immediately before. 160

Figure 6-9: Threshold shift for water- gated ZnO OTFTs gated with CaCl_2 solutions of different concentrations against logarithmic concentration scales. All ZnO–TFTs were electrically addressed with a Tungsten (W) gate needle. Fig. 6-8 is similar to Fig. 6-4 but with a different semiconductor, ZnO vs. PBTTT. 161

Figure 6-10: The product of carrier mobility and specific capacitance (μC_i) for water-gated ZnO OTFTs gated with CaCl_2 solutions of different concentrations against logarithmic concentration scales. Fig. 6-9 is analogous to Fig. 6-5 but with a different semiconductor, ZnO vs. PBTTT. 162

Figure 6-11: Linear transfer characteristics of water- gated ZnO-TFTs of various cations. Monovalent cations (Na^+ , K^+) and divalent cations (Ba^{2+} , Mg^{2+}). All ZnO–TFTs were electrically addressed with a Tungsten (W) gate needle. 163

Figure 6-12: A summary plot showing threshold voltage shift for ZnO TFTs gated with solutions of various cations. According to Fig. 6-11. 164

Figure 6-13: Linear transfer characteristics of rrP3HT OTFTs gated with various cations of (Ca^{2+} , Ba^{2+} , Zn^{2+} , K^+ , and Na^+) (red), referenced to same characteristic

taken under DI water (blue) immediately before. OTFTs were electrically addressed with an Au gate needle.....	165
Figure 6-14: A summary plot showing threshold voltage shift for P3HT OTFTs gated with solutions of various cations. According to Fig. 6-13.....	166
Figure 6-15: (left) Linear transfer characteristics of rrP3HT OTFTs gated with DI water (blue, solid line), and 100 mM CaCl ₂ solution (red dashes). rrP3HT casting solution was deliberately doped with Pd(0) catalyst, Pd ₂ (dba) ₃ . rrP3HT : Pd(0) catalyst OTFTs were electrically addressed with a gold gate needle. Right the chemical structure of Pd ₂ (dba) ₃	168
Figure 6-16: Design of our Ca ²⁺ sensitive water- gated OTFT. The semiconducting rrP3HT film is doped with 1% wt./wt of 'calcium ionophore VI', the ionophore's molecular structure is shown in the inset.....	172
Figure 6-17: Output characteristics of DI water gated rrP3HT: 1% Calcium ionophore OTFTs.....	173
Figure 6-18: (Top)Transfer characteristics of water and different concentrations of CaCl ₂ solutions gated rrP3HT: 1% Calcium ionophore VI OTFTs. Dark blue: DI water, coloured graphs for increasing concentration from 1 μM → 100 mM. (Bottom) The same transfer characteristics of gated Ca concentrations shifted along the V _G axis for best overlap with DI water gated transfer characteristic. ΔV _{th} was taken as the V _G shift required for best overlap.	174
Figure 6-19: Threshold shift ΔV _{th} plotted against log (Ca), and the insert against log (c Ca + 3.7 μM) according to eq. 6-1b.....	175
Figure 6-20: Response of P3HT transistors (a) without and (b) with 1% 'Calcium ionophore VI' sensitizer to 0.1M NaCl, 0.1M KCl, 0.1M BaCl ₂ and 0.1M CaCl ₂ . The selective sensitizer imparts sensitivity to Ca ²⁺ (b1) but not to Ba ²⁺ (b2). Response of P3HT TFT with and without 1% 'Calcium Ionophore VI' to 0.1M NaCl (a3, b3), KCl (a4, b4), and ZnCl ₂ (a5, b5). P3HT: 1% 'Calcium ionophore TFT displays little threshold response to 0.1M Na ⁺ , K ⁺ , and Zn ²⁺ solutions.....	177
Figure 6-21: Shows threshold voltage shift of P3HT transistors with 1% 'Calcium ionophore VI' sensitizer to 0.1M CaCl ₂ , 0.1M BaCl ₂ , 0.1M NaCl, 0.1M KCl, and 0.1M ZnCl ₂ compared to threshold voltage of P3HT transistors without sensitizers for the same solutions, as shown in Fig. 6-20.	178

Figure 6-22: Transfer characteristics of water (black color) and different concentrations of CaCl_2 solutions gated rrP3HT: 1% Calcium ionophore VI OTFTs. Delay time was set at 1s for equilibration before recording drain current $I_D(V_G)$ 180

Figure 6-23: Transfer characteristics of water (black color) and different concentrations of CaCl_2 solutions (coloured graphs for increasing concentration from 1 μM \rightarrow 100 mM) gated rrP3HT: 1% Calcium ionophore VI OTFTs. Delay time was set at 3s for equilibration before recording drain current $I_D(V_G)$ 180

Figure 6-24: Threshold shift ΔV_{th} plotted against $\log(\text{Ca})$, and the insert against $\log(c \text{ Ca} + 80 \mu\text{M})$ according to eq. 6-1b. Delay time was set at 1s for equilibration before recording drain current $I_D(V_G)$ 181

Figure 6-25: Threshold shift ΔV_{th} plotted against $\log(\text{Ca})$, and the insert against $\log(c \text{ Ca} + 2.6 \mu\text{M})$ according to eq. 6-1b. Delay time was set at 3s for equilibration before recording drain current $I_D(V_G)$ 182

List of Tables

Table 1-1: The shapes of hybrid orbitals: sp ³ , sp ² , and sp hybrid orbitals ^[42]	16
Table 4-1: The comparison of Figures- of- merit I _{on} and R _{on} between the data from this work and data from recent publications. The table contains a collection of semiconductors produced by either evaporated processed or solution processed, and gated with different gate medium (liquid electrolytes, solid electrolytes, dielectrics). The R _{on} and I _{on} were extracted from transistor characteristics presented in the particular publications.	116
Table 5-1: Summary of the observed XPS peak positions, and their FWHM, for ZnO films via ZnAc precursor route from different solvents: EtOH route and Mixed route.	125
Table 5-2: Performance characteristics of electrolyte- gated TFTs with solution- processed ZnO.....	132
Table 5-3: Elemental composition for ZnO film resulting from precursor ZnCl ₂	139
Table 6-1: shows all three readings, their mean, and standard deviation, when the set of characteristics shown in Fig. 6-2.....	154

Fundamental concepts

1 Thin Film Transistor (TFT) History

The transistor is a semiconductor device used to control the current or voltage or used for amplification or switching of an electronic signal and electrical power. Also, it can be used as transducer to convert the signal resulting from the interaction of sensitizers with an analyte into electrical signal. Transistors are the heart of many electronic devices in our lives such as computers, televisions, mobile phones, and many other gadgets that we use today. The concept of the field-effect transistor was thought up in the 1920s by Julius Edgar Lilienfeld,^[1] by using a vacuum tube as a signal processing device. Vacuum tubes, practically, were very useful and successful, but had drawbacks (size, power consumption, and warm up time), that made an alternative that serves the same purpose with a smaller footprint desirable. Dawon Kahng and Martin Atalla in the 1960s demonstrated the first working example of field effect-transistor (FET), known as a metal oxide semiconductor field effect transistor (MOSFET)^[2]. The semiconductor in these transistors is usually highly doped crystalline silicon (Si). Si-based transistor was an exceptional alternative to vacuum tube in terms of its small size and lower consumption of power. Moreover, due to a remarkable development in integrated circuits (ICs) by Kilby and Noyce,^[3] millions of transistors can be built in one piece, or chip. The discovery of MOSFET was followed by another remarkable discovery by Paul Weimer^[4] who investigated the first thin film transistor (TFT) based on undoped inorganic materials. Based on this investigation, devices can be designed with different materials in different shapes, which in turn have different electronic applications. For example, TFT liquid-crystal display (TFT-LCD) and Organic Thin Film Transistors (OTFTs).

1.1 Structure of Thin Film Transistor (TFT)

The TFT is a field-effect transistor, in which a semiconductor layer, a dielectric layer and metallic contacts are deposited on a non-conducting substrate, usually glass. It differs from the traditional transistor (MOSFET), in which the semiconductor is

normally the substrate, e.g., silicon wafer, as seen in Fig.1-1. Another difference is that TFT uses an undoped semiconductor in the channel.

The basic structure of TFTs mainly consists of three terminals: source (S), drain (D), and gate (G) in addition to semiconductor and insulator layers. Source and drain contacts are deposited on the substrate, separated from each other by a channel, which has a length (L) and width (W). A thin layer of semiconductor is deposited directly on source and drain contacts. The third terminal, gate metal, is placed on a thin layer of electrically insulating material, called the dielectric layer, which commonly is referred to as the gate insulator. The dielectric layer separates the gate metal from the semiconductor layer.

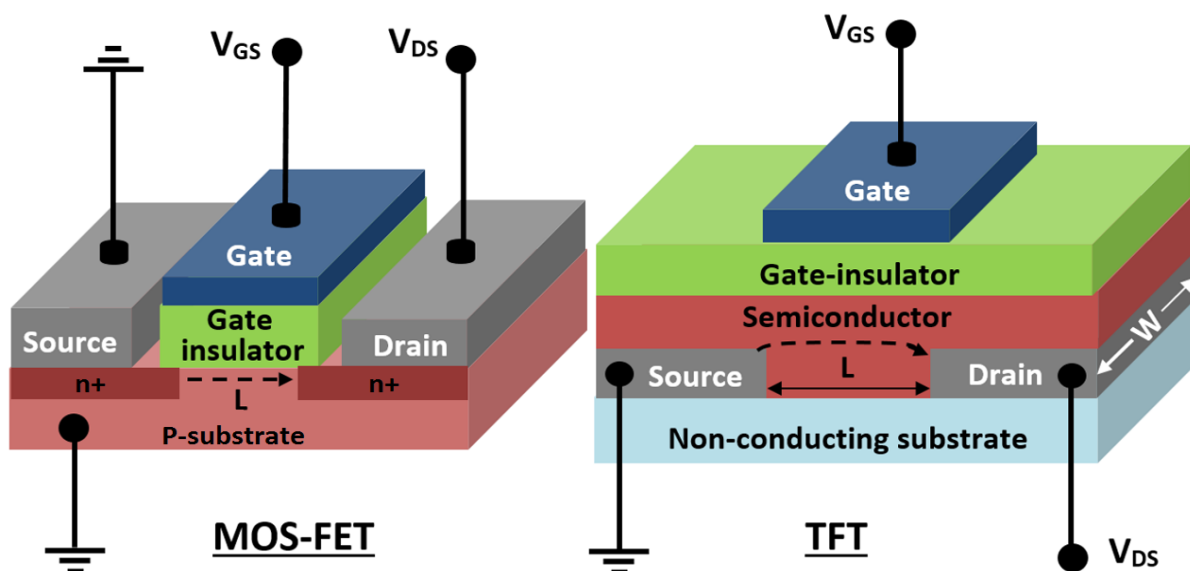


Figure 1-1: Comparison of typical architecture of *p-type* metal oxide semiconductor field effect transistor (MOS-FET) and Thin Film Transistor (TFT), with channel length L , channel width W . The dashed line indicates the flow of charges in the channel.

Depending on the positioning of layers for contacts and semiconductors, four possible architectures can be employed for TFT, as seen in Fig.1-2. These architectures are divided into two categories depending on the location of source and drain contacts in respect of the semiconductor; they can either be staggered or coplanar. The gate electrode can be deposited on the a gate insulator either at the bottom or at the top. Thus, these structures are usually referred to as bottom-gate/top-contacts or top-gate/bottom-contacts.

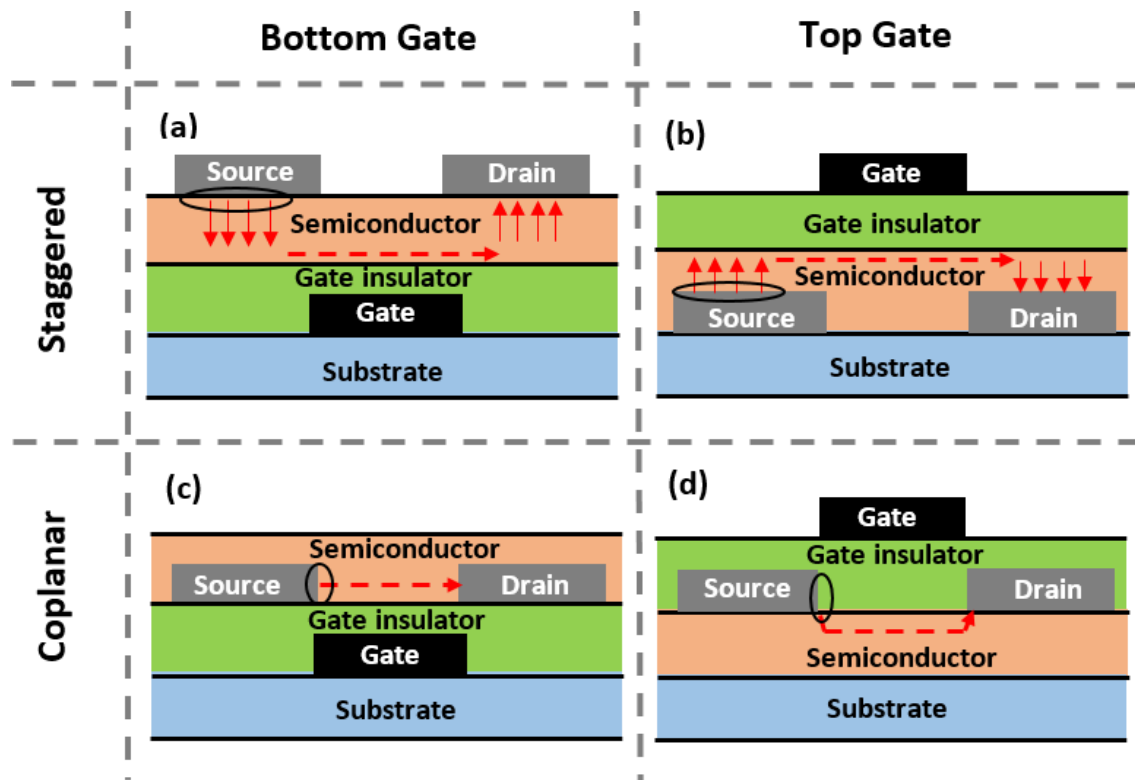


Figure 1-2: Different configurations of TFTs: staggered (a) bottom-gate-top-contact and (b) top-gate-bottom-contact; coplanar (c) bottom-gate-bottom contact and (d) top-gate-top-contact. The dashed line indicates the flow of charges in the channel and showing the injection area of carriers charge from source contact.

Each of these architectures has advantages and disadvantages, mainly dependent on the materials used to produce the field effect transistors. For example, the configuration of the staggered bottom/gate has big advantages for applications that need to protect the semiconductor material from the influence of the taillight, as in LCDs.^[5] Therefore, this architecture is widely used for the construction of hydrogenated amorphous silicon (a-Si:H) TFTs where a-Si:H is sensitive to light, which can be shielded by the metal gate electrode. On other hand, if the semiconductors require a very high temperature for the crystallization process, such as in a TFT-based polycrystalline silicon (poly-Si), a coplanar top/gate structure is usually required.^[5] Such high temperature in other configurations might damage the properties of other materials placed before the semiconductor layer.^[5] In fact, top gate (both coplanar or staggered) is usually preferred due to the fact that the semiconductor surface is always protected by the gate insulator, which is in contrast to bottom gate (both coplanar or staggered) configurations in which the surface of the semiconductor is exposed to air which can lead to unfavourable effects such as instability. However, bottom gate configurations can be useful for facilitating impurity adsorption during annealing.^[5]

1.2 Operation Principle of TFT

Unlike metal oxide semiconductor field effect transistor (MOSFET), which operates on inversion mode, the operation mode in thin film transistor (TFT) relies only on accumulation mode due to the fact that most semiconductor materials used in TFTs are usually undoped (intrinsic) semiconductors. Therefore, the accumulation of a majority charge carriers at the interface of the gate insulator and semiconductor creates the conduction channel in a thin film transistor (TFT).

Thin film transistor (TFT) is a voltage-operated device (or voltage-controlled), in which the current is derived through a semiconductor channel from source to drain by applying a voltage on the gate and drain electrodes of opposite polarity with respect to the charge carriers in a semiconductor. Ideally, no current flows into the gate electrode, since the gate electrode is insulated from the semiconductor channel by the gate insulator. Typically, the source terminal is connected to the ground and it could be utilized as a reference for the bias applied to the drain and gate electrodes.

By applying a sufficiently large voltage at the gate contact (V_G), the resulting electric field accumulates charge carriers at the interface of the gate insulator and semiconductor, as seen in Fig. 1-3. The thickness of the accumulation layer is typically restricted to just a few unit cells (1-2nm) or molecular layers in organic transistors; it is thinner than the thickness of the semiconductor.^[6] The charge carrier concentration in this accumulation layer can be very high ($10^{18} - 10^{20} \text{ cm}^{-3}$).^[6, 7]

As the accumulation layer is so thin it is often quantified as an electric displacement D , which dimensionally is a surface charge density (charge / area). The nature of the accumulated charge carriers at the interface depends on the applied gate voltage with respect to the charge carriers in the semiconductor. Negative charges (electrons) in an n-type semiconductor layer are induced by applying a positive gate voltage, while a negative gate voltage induces positive charges (holes) in p-type semiconductors. The accumulation layer turns the channel conductive. Applying a voltage at the drain electrode (V_D), allows the charge carriers to move through the conducting channel from the source to the drain and produce a drain current (I_D).

Usually the voltage applied to the gate needs to exceed a certain minimum level before an accumulation layer forms; this is called the threshold voltage (V_{th}). Hence, to switch the TFT 'on', the applied gate voltage should be beyond threshold voltage. Generally, a low threshold is desirable. Threshold voltage is controlled by properties of the semiconductor related to charge carrier transport. A quantitative discussion, therefore, follows at the end of Section 1.5.3.2, 'Charge Carrier Transport', which gives an equation (Equation 1-15) for V_{th} .

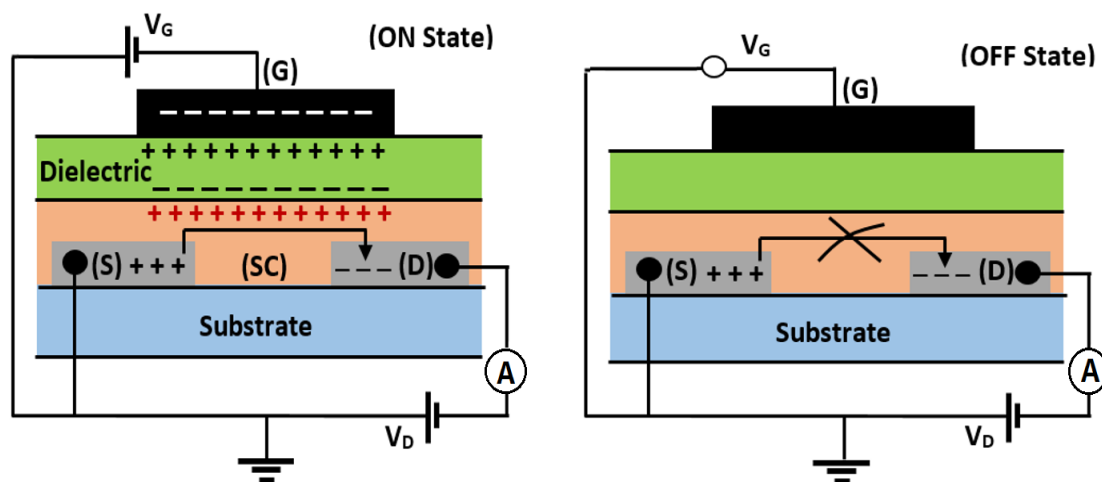


Figure 1-3: Simplified sketch of the operation of a TFT with p-type semiconductor, (G), (D), (S), and (SC) refer to gate, drain, source, and semiconductor, respectively.

1.3 Quantitative Description of TFT Operation

TFT operation can be described by three regimes, defined by the relative magnitudes of the gate voltage (V_G), the drain voltage (V_D), and threshold voltage (V_{th}).

The first regime is called the subthreshold regime, in which the applied bias on the gate contact is smaller than the threshold voltage ($|V_G| < |V_{th}|$). In the subthreshold regime, no accumulation layer is formed and, therefore, the drain current (I_D) is very small. The lowest gate voltage (below V_{th}) that allows the drain current (I_D) to rise is called the onset voltage or switch-on voltage (V_{SO}). Above V_{SO} , the increase of the gate voltage leads to an exponential rise in the drain current. Thus, the logarithm for drain current becomes proportional to the gate voltage. The drain current (I_D) in this regime can be given by the following equation:^[8]

$$I_D = K\mu C_i \frac{W}{L} \left(1 - e^{-\frac{qV_D}{kT}}\right) e^{\frac{qV_G}{nkT}} \quad 1-1$$

where K is a constant for a specific TFT architecture and the materials used; k refers to the Boltzmann constant, T denotes the absolute temperature, q is elementary charge, C_i is the gate insulator capacitance, L and W denote length and width of the channel, respectively, μ is the mobility – a quantitative discussion of mobility, therefore, follows at the end of Section 1.5.3.2 ‘Charge Carrier Transport’, which gives a particular equation. $n \geq 1$ is known as the ideality factor, and it is discussed below.

The increase of $\log I_D$ with applied V_G can be characterized by a quantity called subthreshold slope (S), or inverse subthreshold slope, which is called subthreshold swing (S^{-1}). This quantity is used to show the transition between the TFT’s ‘Off’ and ‘On’ states; a low subthreshold swing value means that the TFT switches between two states at small gate voltage changes, whereas, a high value indicates transition between the two states above a large range of V_G . The subthreshold swing (S^{-1}) can be calculated from the following equation: [8]

$$S^{-1} = \frac{\partial \log_{10}(I_D)}{\partial V_G} \quad 1-2$$

The subthreshold swing unit is (mV decade⁻¹).

Also, the subthreshold swing is related to the ideality factor (n) and can be expressed as: [8]

$$S^{-1} = \ln(10) \frac{nkT}{q} \quad 1-3$$

Since the ideality factor can be expressed as:

$$n = 1 + \frac{C_s}{C_i} \quad 1-4$$

Where C_s is the the specific capacitance of carrier traps in the semiconductor and C_i is the gate insulator capacitance.

A quantitative discussion of traps, therefore, follows at the end of Section 1.5.3.2.

At 300 K, Equation 1-3 can be written as: [8]

$$S^{-1} = 60 \frac{mV}{dec} \left(1 + \frac{C_s}{C_i} \right) \quad 1-5$$

From the equation (1-5), C_s and C_i should be taken into account in order to minimize the value of the subthreshold swing S^{-1} . Low voltage switching between the TFT's 'Off' and 'On' states requires the subthreshold swing S^{-1} to be as small as possible. It has been shown that the values of subthreshold swing for OTFTs usually are in the range of 500 mV to 5 V/decade.[8] However, lower subthreshold swings of 130 mV decade⁻¹ has been reported using high capacitance dielectric gate media. [9] In addition, using electrolytes as gate media in OTFTs shows a lower value for subthreshold swings (70 mV decade⁻¹)[10] due to the high capacitance of the gate medium. Since electrolytes had been used as the gate medium in the experimental activities presented in this thesis, a quantitative discussion regarding the high capacitance of the electrolytes, the types of electrolytes used and the electrolyte-gating TFT is in Section 1.6.

Once the gate voltage exceeds the threshold voltage (V_{th}), an accumulation of a thin layer of charge carriers is created in the semiconductor's channel; therefore, a conducting channel is formed at the gate dielectric/semiconductor interface, as seen in Fig. 1-4a. At low V_D , the drain current (I_D) follows Ohm's law; I_D is proportional to the V_G and V_D . This describes the second regime of the TFT's operation and known as the linear regime. The linear drain current (I_D) is always constant along the channel and can be given by the following equation:[8]

$$I_D = \mu C_i \frac{W}{L} \left((V_G - V_{th}) V_D - \frac{V_D^2}{2} \right) \quad 1-6$$

wherein μ denotes the mobility of charge carriers, W is the channel width and L refers to the channel length.

For $|V_D| \ll |V_G - V_{th}|$, the term quadratic in V_D can be ignored and Equation 1-6 can be simplified to:

$$I_{D,lin} = \mu C_i \frac{W}{L} (V_G - V_{th}) V_D \quad 1-7$$

The third regime occurs when the value of drain voltage increases and approaches the value of the gate voltage. In this situation, the density of the charge carrier in the accumulation layer will reduce nearby the drain contact and the drain-gate voltage declines and pinch-off of the channel arises Fig. 1-4b. Once the condition $|V_D| \geq |V_G - V_{th}|$ is met, TFT reaches pinch-off. Beyond pinch-off, I_D becomes independent of the applied drain voltage and begins to saturate, as seen in Fig. 1-4c. This regime is known as the saturation regime. The following equation expresses the saturation drain current ($I_{D,sat}$):^[8]

$$I_{D,sat} = \frac{W}{2L} \mu_{FE} C_i (V_G - V_{th})^2 \quad 1-8$$

The above equations can be used to describe the operation of TFTs made of either inorganic or organic semiconductors even though the charge transport mechanism is different.

Practically, two different types of measurements can show the electrical characteristics of the shift from the linear regime to the saturation regime in TFTs. The first one is called *output characteristics*, in which the I_D is plotted against the V_D at different V_G . The second measurement is *transfer characteristics*, in which the I_D versus gate V_G is plotted at a fixed V_D . At $V_{G,max} \gg V_D$, the linear transfer characteristics are displayed, while saturated transfer characteristics are shown when $V_{G,max} < V_D$. In addition, the I_D from a transfer characteristic measurement may be plotted either on a square-root scale or on a logarithmic scale, in response to either Equations 1-7, 1-8, or 1-1. Output characteristics provide qualitative information about the effectiveness of channel pinch-off, and therefore saturation, current leakage to the gate, and contact resistance, whereas, the transfer measurement provides a more quantitative analysis tool where important electrical parameters can be extracted such as mobility, on/off drain current

ratio, threshold voltage, and subthreshold slope. More details about these characteristics will be elaborated in Chapter 3, Section 3-2.

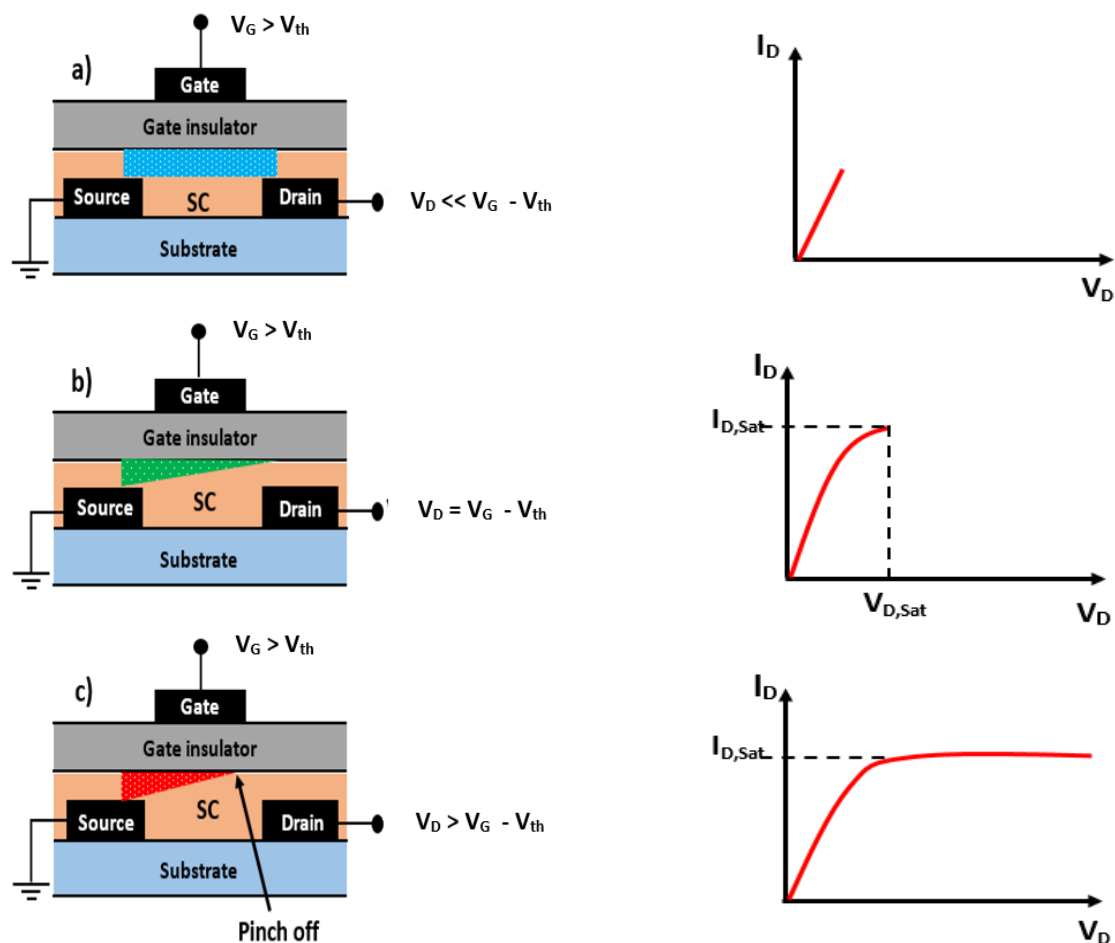


Figure 1-4: TFT's operating regimes is presented by an output characteristics: (a) is the linear regime, in which V_G applied ($V_G > V_{th}$), $V_D = 0V$. The accumulation layer of carriers (blue) is fully developed. (b) denotes the start of drain current saturation when V_G applied, $V_D = V_G$. The accumulation layer of carriers (green) is triangular and TFT reaches pinch-off in which I_D becomes independent of the applied drain voltage and begins to saturate. (c) is the saturation regime, in which V_G applied, $V_D \gg V_G$ and the accumulation layer (red) pinches off within channel, leaving a carrier-depleted region within the channel.

1.4 TFT Semiconductors

The most common semiconductor materials used in TFT is silicon (Si), for example, in computer CPUs the basic logic sets are realized by Si-based TFTs. Due to the fact that TFT design is very versatile, other compound semiconductor materials and many oxide semiconductors have been employed in TFTs. In addition, organic materials have also been utilized as semiconductors in TFTs, referred to as organic thin-film transistors (OTFT). Semiconductor thin film-based-Si is usually produced by high

vacuum processes such as Chemical vapour deposition (CVD), reactive-ion etching (RIE), Plasma Enhanced Chemical Vapour Deposition (PECVD), and physical vapour deposition (usually sputtering). Accordingly, these techniques are not amenable to high-yield, or to low-temperature flexible plastic and paper substrates. Consequently, these requirements (vacuum, high thermal, and complicated processes) have driven a search for alternative highly processable semiconductors. In fact, there are several inorganic semiconductors and polymer organic semiconductors that could be processed from solution, which also work in TFTs. Therefore, compared to deposition methods used for Si-based TFTs, easier and cheaper solution-based processes, such as drop cast, spin-coater, spray pyrolysis, and inkjet printing, can be employed to create a uniform thin film-based TFT. Furthermore, in Chapter 6, solution-processed semiconductors offer advantages for the integration of sensitizers into sensor transistor architectures.

Within this thesis, two different types of solution-processed semiconductors were used, namely solution-processed precursor route inorganic semiconductors (Section 1.4.1), and solution-processed semiconducting polymers (Section 1.5.4).

1.4.1 Solution-Processed Inorganic Semiconductors

Solution processing of inorganic semiconductors can be performed in a number of ways: For example, chemical and electrochemical bath deposition, processing of true solutions of precursor molecules, or processing of colloidal dispersions of inorganic semiconductors. In (electro) chemical bath deposition, solutions of ions are (electro) chemically reduced and precipitate onto a substrate as the intended semiconductor. Precursor solutions typically are metal-organic compounds dissolved in organic solvents and cast onto the intended substrate. Formation of the inorganic semiconductor is then by pyrolysis, *i.e.* the thermally driven decomposition of the metal-organic precursor into an inorganic semiconductor; pyrolysis may occur after or even during deposition ('spray pyrolysis' onto a hot substrate). Alternatively, inorganic nanoparticles (NP) can be stabilized as colloidal dispersions in solvent with the assistance of surface capping agents to support their dispersion. After deposition, films are heated to burn off capping agents and fuse particles into a coherent film.

A large number of solution-processed inorganic semiconductors, especially II-VI semiconductors, have been reported. For instance, chemical bath deposition (CBD) of cadmium selenide (CdSe) and zinc sulfide (ZnS) thin films,^[11, 12] electrodeposition (ED) of cadmium telluride (CdTe) and cadmium sulfide (CdS) thin films,^[13, 14] sprayed CdS thin films for solar cells,^[15] spin-cast deposition of CdSe-CdS,^[16] and inkjet printing of zinc oxide (ZnO)^[17] from NP dispersion. In addition, 'conductive ink' formulations on the basis of colloidal metal nanoparticles are now commercially available.^[18]

Among II-VI semiconductors, ZnO has attracted great interest since the first reports of ZnO-based transparent TFTs in 2003 by Hoffman *et al.*,^[19] Carcia *et al.* ^[20] and Masuda *et al.*^[21] A high mobility of $80 \text{ cm}^2 \text{ V}^{-1} \text{ s}^{-1}$ from an IGZO single-crystalline semiconductor layer in a TFT has been reported by Nomura *et al.*^[22] Therefore, ZnO is considered to be one promising material for the next generation of TFT and flat-panel display drivers due to several features such as: (1) processing from solution; (2) low temperature processing – growth temperature for high quality ZnO film is less than $700 \text{ }^\circ\text{C}$ ^[23] which is lower than for poly-Si and GaN film and the temperature processing can be lowered to $300 \text{ }^\circ\text{C}$ when ZnO gets doped, e.g. by lithium;^[24] (3) uniform films can be formed on various and large area substrates; (4) ZnO has wide and direct band-gap of $\sim 3.37 \text{ eV}$ at room temperature, (5) large exciton binding energy of $\sim 60 \text{ meV}$; (6) high optical transparency; (7) high electron densities of $\sim 10^{21} \text{ cm}^{-3}$ for undoped ZnO;^[25] (8) environmental friendly (non-toxic); (9) insensitive to visible light, which make ZnO a suitable semiconducting materials in the fabrication of transparent thin-film transistors; (10) 'Zinc ores (e.g. sphalerite (zinc sulphide), smithsonite (zinc carbonate), hemimorphite (zinc silicate), wurtzite (another zinc sulphide) are plentiful and cheap.

At ambient temperature and pressure, the most common crystal structure of ZnO is wurtzite structure, which is the thermodynamically more stable phase of ZnO,^[23] as seen in Fig 1-5. The wurtzite structure is a hexagonal lattice with two interrelating sublattices of Zn^{2+} and O^{2-} . Each Zinc ion is coordinated by a tetrahedra of oxygen ions, and vice-versa. Since the structure phase of ZnO is stable at ambient pressure and temperature, therefore, it is not necessary to store ZnO in a vacuum in the same manner as organic semiconductors.

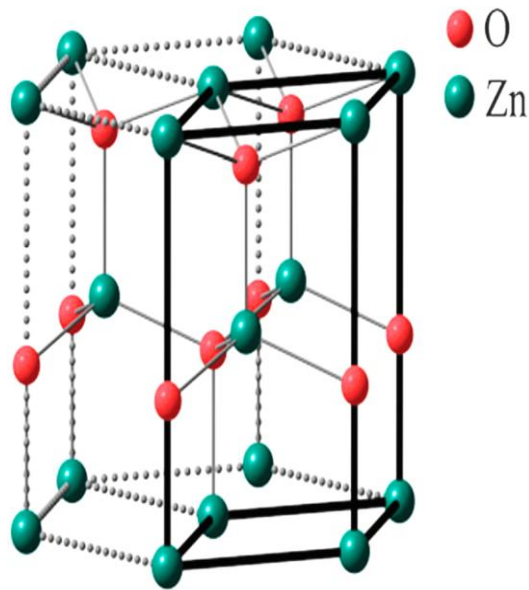


Figure 1-5: shows unit cell of the wurtzite structure of ZnO [26].

ZnO crystals more often are *n-type* semiconductors unless deliberately doped to display p-type behaviour. This can be achieved by using different growth methods to introduce a precise dopant concentration such as by using an ion implantation method.[27] Although p-type conductivity in ZnO films has been reported, a reproducible and reliable ZnO with high quality p-type conductivity has not yet been accomplished.[23] In addition, electron mobility TFT is far larger, $110 \text{ cm}^2\text{V}^{-1} \text{ s}^{-1}$ [28] has been reported vs a hole mobility of only $7.8 \text{ cm}^2\text{V}^{-1} \text{ s}^{-1}$ [29]. The reason for this is due to the fact that the carrier mobility in the valence band is much lower than the carrier mobility in the conduction band, since the valence band in p-type ZnO is mainly formed from the oxygen *p* orbitals, which limits the carrier mobility.[5]

Practically, ZnO is usually unintentionally lightly n-doped, for reasons that are still controversial; n-doping was attributed to the presence of oxygen vacancies; however, studies have demonstrated that oxygen vacancies are actually deep donors and the n-type conductivity in ZnO cannot arise from these donors.[23] Alternatively, zinc interstitials and Zn antisites have been proposed as n-dopants. Nevertheless, some studies have shown that Zn interstitials and Zn antisites do not cause *n-type* conductivity in ZnO.[23] On the other hand, hydrogen would more often be the reason that causes the n-type doping. In nearly all growth and processing environments, the

hydrogen is present which acts as a shallow donor.^[23] Solution-processed ZnO thus complements solution-processed organic semiconductors, which are more often *p*-type.

The ZnO valence band (VB ~ -7.7 eV) is located unfavourably for hole injection even from metals have high work function, e.g. gold (Au) (work function for Au is ~ 5.1 eV), while the conduction band (CB ~ -4.4 eV) is realistically well matched for electron injection^[30] even from Aluminium (Al), see Section 1.5.3, Fig. 1-14. The band gap of ZnO is direct with value of ~ 3.37 eV at room temperature and the exciton binding energy is ~ 60 meV.^[23] Such of a wide and direct band gap gives rise to a variety of applications in the blue/UV region, including light-emitting diodes, laser diodes, photodetectors and optical applications that are dependent on excitonic effects.

ZnO is nearly insoluble in organic solvents and most of the reported displays employing ZnO-based TFTs are produced by sputtering and pulsed laser deposition methods.^[28, 31-33] However, in 2007, Loutfy *et al.*^[34] reported that ZnO can be prepared using pyrolysis under air of the metal-organic precursor zinc acetate (ZnAc, H₃C-CO-O-Zn-O-CO-CH₃). ZnAc can be dissolved in and processed from organic solvents (e.g. methoxyethanol, or ethanol).^[24, 34-36] Several articles have studied the effect of pyrolysis at the temperature at which ZnO resulted from precursor zinc acetate.^[34, 36, 37] All results show that the thermal decomposition of the coated film from the precursor into ZnO occurred at ~ 310 °C. The formation of a stable ZnO crystal takes place between 300 and 400 °C, whereas the formation of a larger crystal of ZnO takes place between 400 and 500 °C.^[34] In addition, the effect of temperature on coated substrates by precursor has been studied and the results have displayed that the resulting ZnO has random crystal orientations from the step-heating process while, when coated substrates are placed on a pre-heated hot stage (> 450 °C) a crystalline ZnO thin film with a wurtzite structure is created.^[34] Thus, ZnO which resulted from the precursor at the pre-heated hot stage could produce a high carrier mobility than the step-heating process. On the other hand, a high and more stable performance TFT of ZnO from a solution processed with a low processing temperature (~300 °C) can be produced from Li-doped ZnO.^[24] It has been found that by replacing the dielectric gate medium with

high capacitance solution-processed (ionic-liquid), the mobility increases dramatically at low voltages with excellent operational stability.^[24]

On casting from a precursor solution, aggregates may transfer to the substrate, creating the formation of ZnO grains with defined boundaries or non-uniform spatial distribution of grain structure on thermal conversion, since the charge carrier mobility is often limited by the presence of grain boundaries.^[22] In this case the electron transport is more likely to follow a hopping mode rather than band-like conduction (more details will be found in Section 1.3.2.). In addition, small grain size may explain why the mobility of ZnO from a precursor route is always lower than that resulting from ZnO by sputtering and pulsed laser deposition methods, e.g. mobility of $5.25 \text{ cm}^2 \text{ V}^{-1} \text{ s}^{-1}$ from precursor route as reported by Ong *et al.*^[34] compared to $110 \text{ cm}^2 \text{ V}^{-1} \text{ s}^{-1}$ ^[28] from a pulsed laser deposition method. However, the mobility of Li-doped ZnO from a precursor route can reach up to $85 \text{ cm}^2 \text{ V}^{-1} \text{ s}^{-1}$ as reported by Adamopoulos *et al.*^[38] Nevertheless, the electron mobility found in precursor-route ZnO is still higher than the mobility in amorphous silicon ($< 1 \text{ cm}^2 \text{ V}^{-1} \text{ s}^{-1}$) and most organic semiconductors.

Within this thesis, I will present work on ZnO prepared from solution-processed precursors. Details of the processing are in Chapter 2, Sections 2.3.1.2 and 2.3.2.2. Results, including the discovery of a new precursor for ZnO TFTs, are presented in Chapter 5.

1.5 Organic Semiconductors

The interest in semiconducting organic materials as an alternative to the ubiquitous inorganic semiconductors is based on the possibility of engineering their bandgaps via chemical synthesis and their low temperature processing, often from solutions, which offers the potential for economic device production, as well as large-area and flexible applications. Moreover, the possibility of processing them into devices from a solution will open up alternative semiconductor device manufacturing options, e.g. via printing.^[39] The first organic TFTs were reported in the 1980s by Tsumura *et al.*^[40] and Clarisse *et al.*^[41] The following sections will discuss conjugation as the origin of

semiconducting properties in organic materials, as well as the charge injection and charge transport.

1.5.1 Conjugation and Band Gap

Before describing the terms conjugation and band gap, it is very important to mention how the conduction of charge in organic semiconductors is first created, meaning how the energy between ground and excited states of organic molecules is reduced down to a few eV- i.e., into the range of semiconductor band gaps. It is well known that organic molecules are composed of carbon atoms in rings or long chains. Therefore, to understand how the conduction of charge is formed in these rings or long chains, the concept of *hybridization* in carbon atoms should be explained first.

In a ground state, a carbon atom consists of 6 electrons. These electrons are arranged into orbitals as $1s^2 2s^2 2p_x^1 2p_y^1 2p_z^0$. However, a carbon atom is excited when one electron from $2s^2$ orbital is promoted into $2p_z^0$, and the electronic configuration of the carbon atom in the excitation state becomes $1s^2 2s^1 2p_x^1 2p_y^1 2p_z^1$. This provides four unpaired valence electrons. When two carbon atoms in an excitation state come closer to the internuclear axis, $2s^1 2p_x^1 2p_y^1 2p_z^1$ orbitals of these atoms are intermixed. The process of this intermixing of atomic orbitals is called *hybridization*. This type of hybridization is called sp^3 , in which the overlap between two sp^3 hybrid orbitals creates a strong bond (sigma (σ) bond) between s orbitals of the two carbon atoms. The remaining sp^3 hybrid orbitals ($2p_x^1 2p_y^1 2p_z^1$) are directed along the four corners of a regular tetrahedron with an angle of 109.5° between the corners. These orbitals forms σ bonds with, i.e. hydrogen atoms such as in Alkanes hydrocarbons.

The atomic orbitals in a carbon atom can be hybridized also into sp and sp^2 hybrid orbitals. In sp^2 hybrids, only $2s^1 2p_x^1 2p_y^1$ are hybridized, while $2p_z^1$ remains not hybridized. When two sp^2 hybrid carbon atoms approach together and orbital take places along the internuclear axis, a σ bond is formed between s orbitals. The unhybridized ($2p_z^1$) orbitals of both atoms are overlapped and form pi (π) bonds, while the remaining sp^3 hybrid orbitals ($2p_x^1 2p_y^1$) are equi-spaced in a plane with an angle

of 120° with respect to each other and they can form σ bonds with, *i.e.* hydrogen atoms such as in Alkenes hydrocarbons.

In the sp hybrid, only $2s^1 2p_x^1$ are hybridized, while $2p_y^1 2p_z^1$ remain not hybridized. When two sp hybrid carbon atoms come closer along the internuclear axis and overlap, a sigma (σ) bond is formed between s orbitals, while the two remaining unhybridized orbitals of both carbon atoms are overlapped and form pi (π) bonds. The remaining sp hybrid orbitals of both carbon atoms form σ bonds with, *i.e.* hydrogen atoms such as in Alkynes hydrocarbons. The formation of two sp hybrid orbitals has an angle of 180° .

Table 1-1 illustrates the three- dimensional shape of hybrid orbitals.

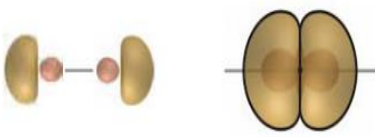


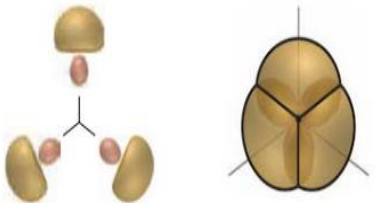

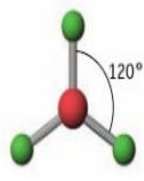
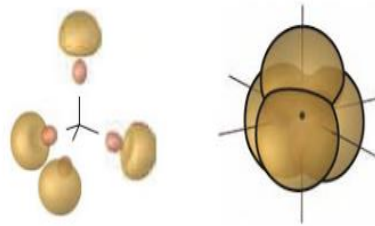

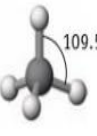
Hybrid Orbitals	Arrangement of Hybrid Orbitals	Geometry	Example
Two electron pairs sp		 Linear	 180° <chem>BeCl2</chem>
Three electron pairs sp^2		 Trigonal-planar	 120° <chem>BF3</chem>
Four electron pairs sp^3		 Tetrahedral	 109.5° <chem>CH4</chem>

Table 1-1: The shapes of hybrid orbitals: sp^3 , sp^2 , and sp hybrid orbitals [\[42\]](#).

Organic molecules formed by fully (sp^3) hybridized carbon only are referred to as 'saturated'; saturation leads to localized molecular orbitals without semiconducting properties. Conjugation requires the presence of (several) unsaturated carbons in the molecule, *i.e.* carbon atoms that are sp^2 or sp hybridized (or both). The conjugation leads to delocalization of electrons over large distances (large compared to the length of a chemical bond). Delocalizing electron clouds over larger distances reduces the spacing in energy between their ground and excited states down to a few eV- *i.e.*, into the range of semiconductor band gaps. Therefore, organic semiconductors are conjugated molecules, *i.e.* they contain alternating single/double or single/triple bonds along a carbon-based chain. The simplest example of a conjugated polymer is poly(acetylene), which is composed only of carbon and hydrogen atoms in a linear chain.

1.5.2 Benzene and Thiophene Ring

A key structural motif found in many functional organic semiconductor molecules is the benzene ring, which will be discussed here in more detail as the prototype of conjugated molecules. Since the orbitals of an sp^2 hybrid have an angle of 120° as regards each other, they can be arranged as a regular hexagon, a geometric figure with six sides and six corners, each with an internal angle of 120° . The resulting molecule is the benzene ring, which contains six sp^2 hybridized carbon atoms. In the Benzene ring, the three sp^2 hybrid orbitals of each carbon atom form three σ bonds, two bonds with its neighbours and one with a hydrogen (H) atom, as seen in Fig 1-6. The 6 remaining atomic $2p_z$ orbitals overlap with a neighbouring $2p_z$ orbital to form (π) bonds. These are less strong as sigma bonds, and extend further away from their 'parent' atoms.

Fig 1-6 shows the two possible structures resulting from pairwise overlap of neighbouring $2p_z$ orbitals, called the 'mesomers' of benzene. However, it is impossible to determine with which of its two possible neighbours any given $2p_z$ orbital will overlap. Therefore, the π -bond electrons resulting from the double bonds are completely delocalized around the whole ring, shown as a circle in the ring in 6 (right), which is a more realistic representation of benzene than either mesomer. The fully (delocalized

π -system) leads to lower overall energy. Delocalized π orbitals are responsible for the low energy excitation in the system and the conductive nature of organic semiconductor materials, albeit a single benzene ring is not yet big enough to force the 'band gap' (energy difference between the ground state and first excited state) down to semiconductor values (see below).

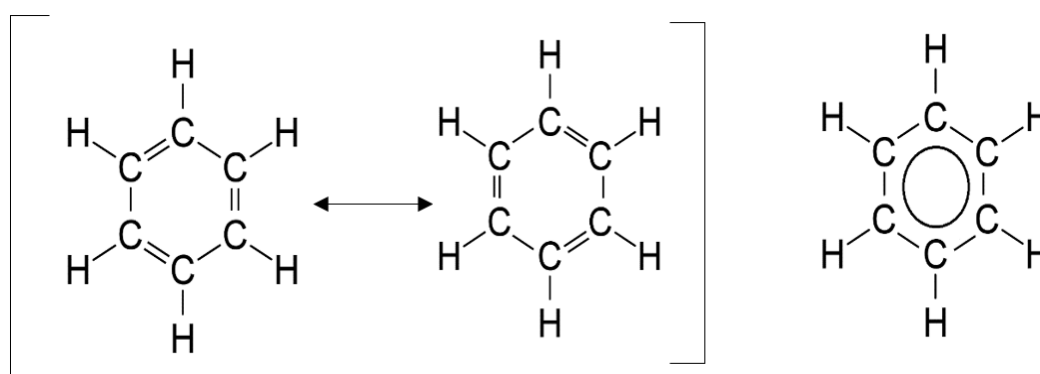


Figure 1-6: The structure of benzene ring.

Alternatively, the π electrons' behaviour within an organic molecule can be understood by the *molecular orbital (MO) theory*, in which electrons between the interactive atomic orbitals in a molecule are not mentally derived from hybridized atomic orbitals, as in the above description, but are treated as moving under the effect of the nuclei in the whole molecule. The interaction between atoms creates two molecular orbitals called *bonding molecular orbital (π)* and an *antibonding molecular orbital (π^*)*. The energy of a bonding molecular orbital is lower than the energy of the original atomic orbitals which in turn stabilizes the molecule, whereas an antibonding molecular orbital has a higher energy and destabilizes the molecule. Note, however, that conjugated molecules are still held together by the strong sigma bonds, which are localized even when described within the *MO* picture.

In conjugated molecules, the anti-bonding only indicates an excited state of π -orbitals. The bonding and anti-bonding orbitals are also known as the *highest occupied molecular orbital (HOMO)* and the *lowest unoccupied molecular orbital (LUMO)*. When a π electron system is large enough to reduce the *HOMO/LUMO* energy gap to less than 4 eV, the corresponding molecule is called an 'organic semiconductor'.^[43] The concept of *HOMO* is similar to the valence band, whereas *LUMO* is symmetric to the

conduction band in an inorganic semiconductor. The correspondence is so close that the HOMO/LUMO energy gap is commonly called the organic semiconductor's bandgap (E_g).

A single benzene ring acts as an insulator and it is transparent to visible light, meaning that the band gap between *HOMO* and *LUMO* levels is larger than 4 eV. Larger molecules are required, where the overlap of π orbitals is extended further. These often also include linear (rather than ring-shaped) conjugated sequences, rings fused at their edges ('acenes'), and 'heteroatoms' (atoms other than carbon); the most common are sulphur (S), oxygen (O), and nitrogen (N). Fig 1-7 shows the important organic semiconductor 'pentacene' as an example for the acenes. HOMO/LUMO band gap for solid pentacene has been assessed in the range from 1.9 to 2.2 eV.^[44]

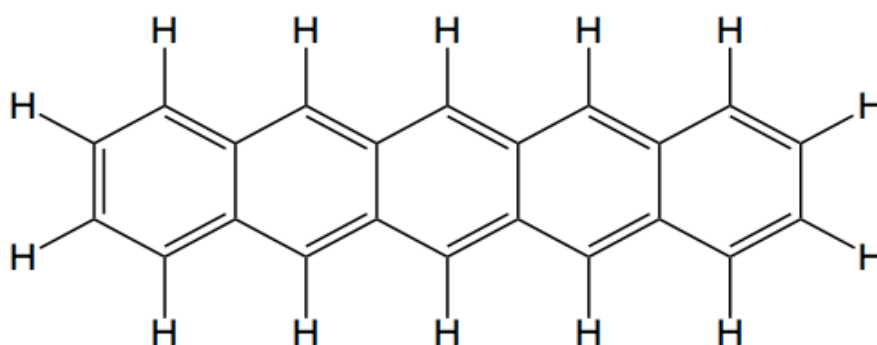


Figure 1-7: Chemical structure of pentacene.

As an important example for a 'heterocycle' (cyclic molecule containing atoms other than carbon), Fig. 1-8 shows the 'thiophene' ring. Thiophene rings are conjugated molecules containing four carbon atoms and one sulphur atom to form a pentagon-like structure, as seen in Fig. 1-8. In such structures, the electron pairs of sulphur atoms are extremely delocalized in the π electron system, since there are two electrons from sulphur together with four electrons from carbon to produce six π electrons in the ring.

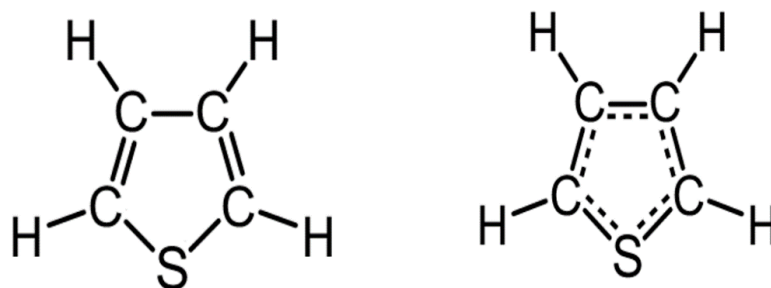


Figure 1-8: The structure of Thiophene ring. Right shows the delocalized π electron system.

Again, a single thiophene ring is not large enough to give band gaps $< 4\text{eV}$, however thiophene-based structures are often used as building blocks for semiconducting polymers. For example, the polymers known as P3HT and PBTTT are synthetic 'beads' of Thiophene rings with additional flexible, non-conjugated sidechains attached to the rings to make such polymers soluble in organic solvents. P3HT and PBTTT are discussed in detail in Section 1.5.4.

1.5.3 Charge Carrier Injection and Transport in Organic Semiconductors

The use of organic semiconductors in devices relies on the efficient injection of charge carriers, and their ability to move across a film. For injection, a charge must be inserted into the molecular unit either by adding an electron to an antibonding (π^*) orbital (*LUMO*) or by removing an electron from a bonding (π) orbital (*HOMO*). The addition or removal of an electron will be at the interface between a metal contact and an organic semiconductor. However, controlled doping of organic semiconductors with spatial resolution is problematic. This favours devices that work with undoped (intrinsic) semiconductors, like the organic TFTs introduced in Section 1.1. The lack of free carriers at room temperature requires a careful combination of metals and semiconductors to facilitate injection, to be discussed in Section 1.5.3.1.

Another essential factor for highly effective organic semiconductor device performance is achieving efficient charge transport in organic semiconductors. While π electrons are delocalized over distances far longer than one chemical bond, or one polymer repeat unit, delocalization is still limited by the size of the molecule, or by a few polymer repeat units. This is quite unlike in classic, inorganic crystalline

semiconductors, where carriers in bands are (ideally) localized over the entire crystal with a wave-like motion. Carrier transport in organic semiconductors is, therefore, characterized by 'hopping' (properly called 'thermally assisted tunnelling') between molecular units, rather than a wave-like motion in bands. This will be discussed in Section 1.5.3.2.

1.5.3.1 Charge Carrier Injection

To inject a hole / an electron into an organic semiconductor, an electron must be removed from the *HOMO* level of a molecule/an electron must be added into the *LUMO* level of a molecule. Addition or removal of a localized charge also leads to a conformational change in the nucleus positions and molecular orbitals, *i.e.* the bond lengths and angles, of the molecule supporting the injected charge carrier, Fig. 1-9. This relaxation to a new position corresponds to a new minimum energy, called geometric reorganization energy. The combination of the charge carrier with the geometric distortion of the molecule is called '*polarons*' (either *electron polaron* and *hole polaron*). Other names, which could be used by chemists, are *radical anions* and *radical cations*, instead of *electron polarons* and *hole polarons*, respectively. Therein *radical* stands for the net spin due to the unpaired remaining (or added) electron. Often, colloquially, however, *radical ions* and *polarons* are simply referred to as *hole* or *electron*.

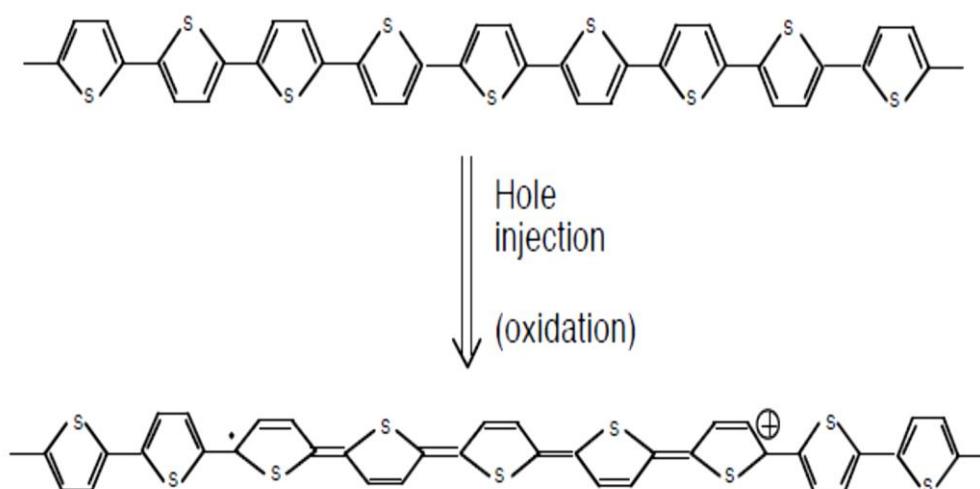


Figure 1-9: Example of polythiophene segment before removing an electron (Top) and after removing an electron (Bottom). It is clear that removing an electron leads to redistribution of the π -bonds and then conformational change in the nucleus positions and molecular orbitals, *i.e.* the bond lengths and angles.

The energy required to remove an electron from the *HOMO* (*i.e.*, inject a hole into the *HOMO*) is, therefore, somewhat less than the *HOMO* level, and is called the semiconductors' 'ionisation potential' (I_p). Similarly, the energy gained when adding an electron to the *LUMO* is somewhat higher than the *LUMO* level, and is called the semiconductors' 'electron affinity' (E_a).

Practically, in a device based in undoped organic semiconductors, carriers are injected from metal contact. In order to obtain an efficient injection of hole/electron, I_p and E_a therefore have to be associated and matched to the metal's work function, Φ . Fig. 1-10 illustrates an organic semiconductor (P3HT) sandwiched between 2 metal electrodes. The horizontal lines in Fig. 1-10 indicate the energy a carrier will have at a particular location. The offset between the work function of silver and the electron affinity of P3HT at the P3HT/silver interface shows an 'injection barrier' of 1.73 eV, which will make the injection of electrons into P3HT difficult. It is evident that, for better electron injection, either a metal with a smaller work function, or a semiconductor with deeper electron affinity would be favourable to minimize or eliminate the barrier. For example, Ahles *et al.*^[45] used a calcium electrode ($\Phi = 2.8$ eV) to inject electrons into pentacene, despite its shallow electron affinity (*LUMO* = 2.5 eV).

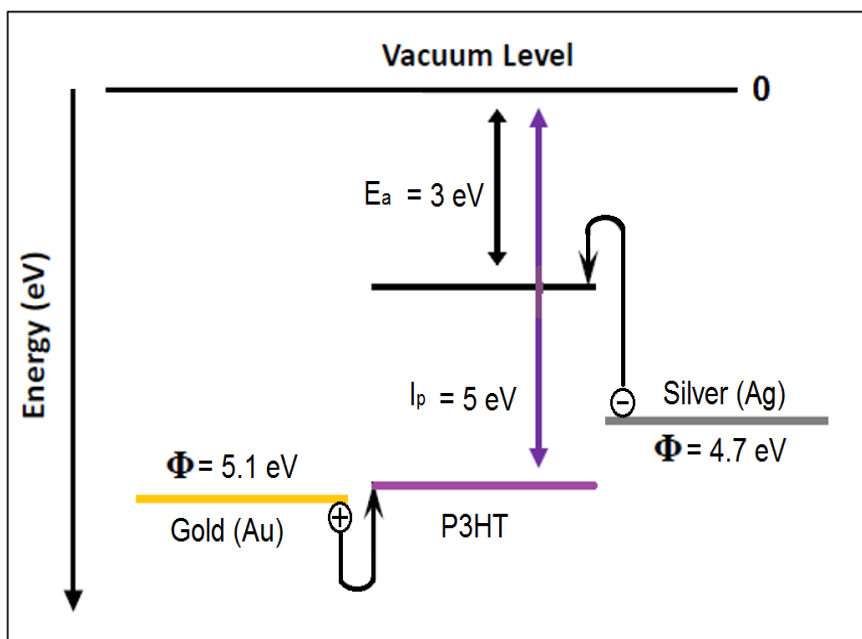


Figure 1-10: A diagram illustrating an electron injection into organic semiconductor P3HT, and the energy levels drawing of electron and hole injection barriers from different metal contacts into P3HT without applying voltage.

At the gold/P3HT interface, the injection barrier for an electron injection would be even higher (2.1 eV) due to the higher work function of gold. However, the injection of holes into the *HOMO* of P3HT is barrier-free, because the work function of gold is lower than the ionization potential of P3HT. The energy in Fig. 1-10 rises down the graph as this is the energy needed to eliminate an electron from a certain level to the vacuum level.

When a voltage (potential) is applied between the electrodes, an electric field will be generated within the semiconductor. Therefore, HOMO and LUMO levels become tilted toward vacuum levels, as seen in Fig. 1-11. The gradient of tilted energy level equals the electric field which is determined by the magnitude of the applied potential. However, as long as no carriers are injected, bands remain flat, i.e. free of curvature. The situation is rather different in a Schottky contact (Metal/doped semiconductor contact), where free carriers are present due to the doping of the semiconductor. In the Schottky junction, bands are curved near the contact, even when no external voltage is applied (but also, when a voltage is applied).

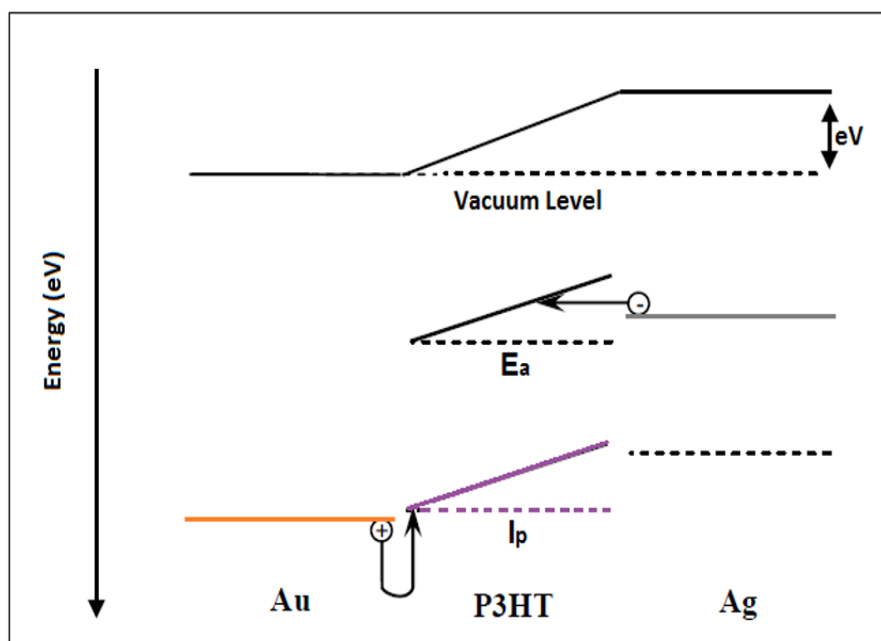


Figure 1-11: The energy level of P3HT organic semiconductor during applying voltage with Au and Ag contacts.

What Fig 1.11 describes is a diode in the absence of dopants, or already injected carriers. Here, 'flat bands' means bands in a semiconductor that contains no free charge carriers, neither from dopants, nor from injection. Then bands are horizontal or

tilted, but not curved. Bands are flat at zero and for many non- zero applied voltages (tilted bands still are flat) - as long as no carriers are injected. For contrast, compare e.g to the Schottky junction (metal – doped semiconductor contact), where bands curve near the interface ('Band bending' is the opposite of flat bands). In a Schottky diode, bands bend even at zero applied volts, and without any injection.

In the flat band situation, thermionic (or Schottky) emission and field emission (or Fowler-Nordheim tunnelling) mechanisms can be used to explain the injection from a contact metal into an organic semiconductor. Thermionic emission deals with the possibility of an electron gaining enough thermal energy to overcome the barrier of injection, while field emission deals with travel through the barrier by quantum mechanical tunnelling, Fig. 1-12. The first mechanism can be quantified by the Richardson-Schottky equation, which describes the relationship between the injected current density J_{RS} with temperature (T) and electric field (E).

$$J_{RS} \propto T^2 \exp\left(-\frac{\Phi_B}{kT}\right) \cdot \exp\left(\frac{\beta_{RS}\sqrt{E}}{kT}\right) \quad 1-9$$

wherein Φ_B indicates to the barrier height and β_{RS} is a constant. J_{RS} dominates the injection at high temperatures and low fields. k is the Boltzmann constant.

In contrast, the second mechanism, field emission, depends highly on the E-field but not on the temperature. Equation 1-10 describes Fowler-Nordheim tunnelling:

$$J_{FN} \propto \frac{E^2}{\Phi_B} \exp\left(-\frac{\gamma \Phi_B^{\frac{3}{2}}}{E}\right) \quad 1-10$$

where γ is a constant.

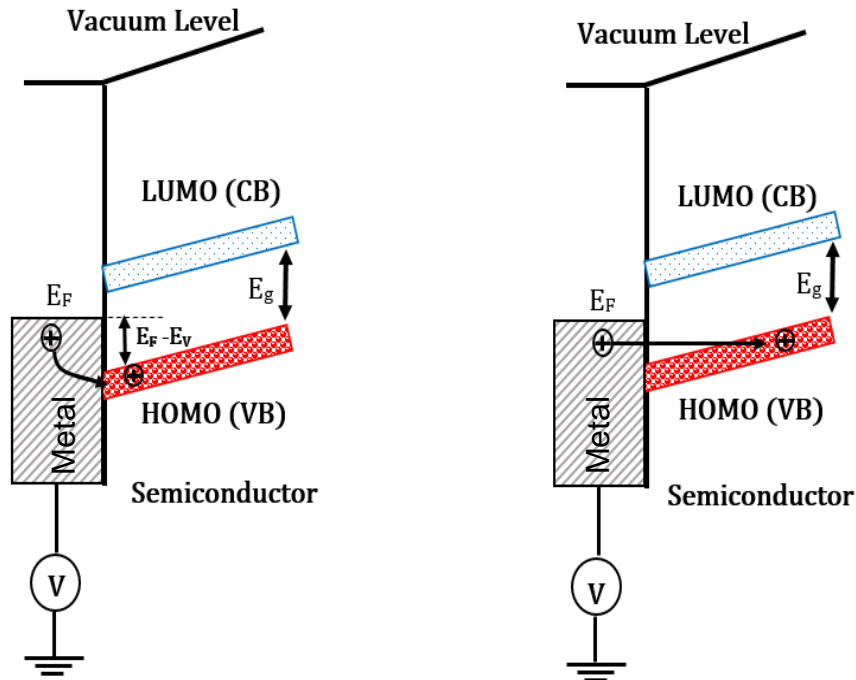


Figure 1-12: (left) represents the thermionic emission mechanism for the charge injection from a metal into an organic/inorganic semiconductor, while (right) represents Fowler-Nordheim tunnelling mechanism for the charge injection from a metal into an organic/inorganic semiconductor.

In real devices, observed injection current densities do not strictly follow the above equations due to the complex physical and chemical interactions that occur at the interface between metal and semiconductor. As such this interaction leads to development of dipoles at the interface, which in turn means the vacuum levels for the metal with the semiconductor are misaligned. An increase or a decrease in the injection barrier can result from such dipoles, which can be used deliberately to improve injection by modifying the contact surface with a self-assembling monolayer (SAM) [46] or thin metal oxide. [47]

Also, the situation is very different when there are some free carriers in the semiconducting film; doping can be used as a deliberate strategy to overcome injection barriers. Free carriers will move towards (or away from) the contacts of opposite (equal) polarity as the carrier sign and thus re-distribute the electric field in the device. This is known as ‘band bending’, as illustrated in Fig. 1-13. Now the band’s slope is significantly higher at the contact/semiconductor interface (smaller tunnelling barrier), i.e. the field is effectively concentrated at the interface, leading to enhanced injection.

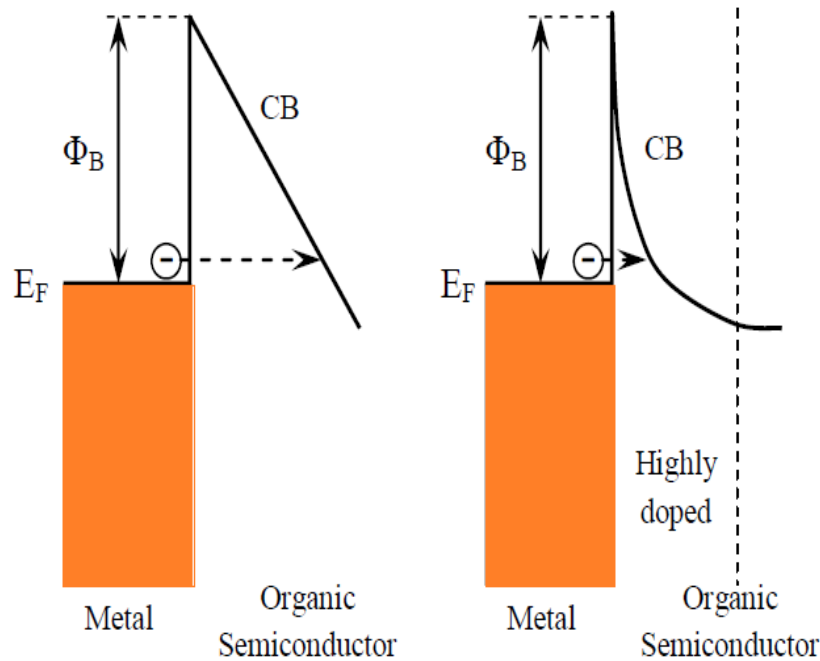


Figure 1-13: Energy illustrations displaying band tilting (left) and band bending (right).

For instance, a Schottky junction has been recognized in a pentacene OTFT by Schroeder *et al.* via the utilization of iron (III) chloride doping.^[48] In addition, the doping of the organic semiconductor in transistor applications is not desirable, and therefore has to be limited to the contact area.^[47]

It should be mentioned that Equations 1-9 and 1-10 formally predict 'infinite' current density in the limit of zero barriers. This is physically unrealistic since, instead, the resulting current density will then be limited by the transport of carriers across the semiconductor, rather than by crossing the metal/semiconductor contact. Practically, the problem of carrier injection into an organic semiconductor device can be considered solved when the contacts can deliver more current than the device can carry, e.g. the drain current of a TFT. According to Equations 1-6 to 1-8, TFT current is, in part, controlled by the mobility of charge carriers, which will be discussed in the next section.

Figure 1-14 shows the electronic levels of organic/inorganic semiconductors used in the experimental activities presented in this thesis (P3HT, PBTTT and ZnO) compared with a typical contact metal, gold (Au).

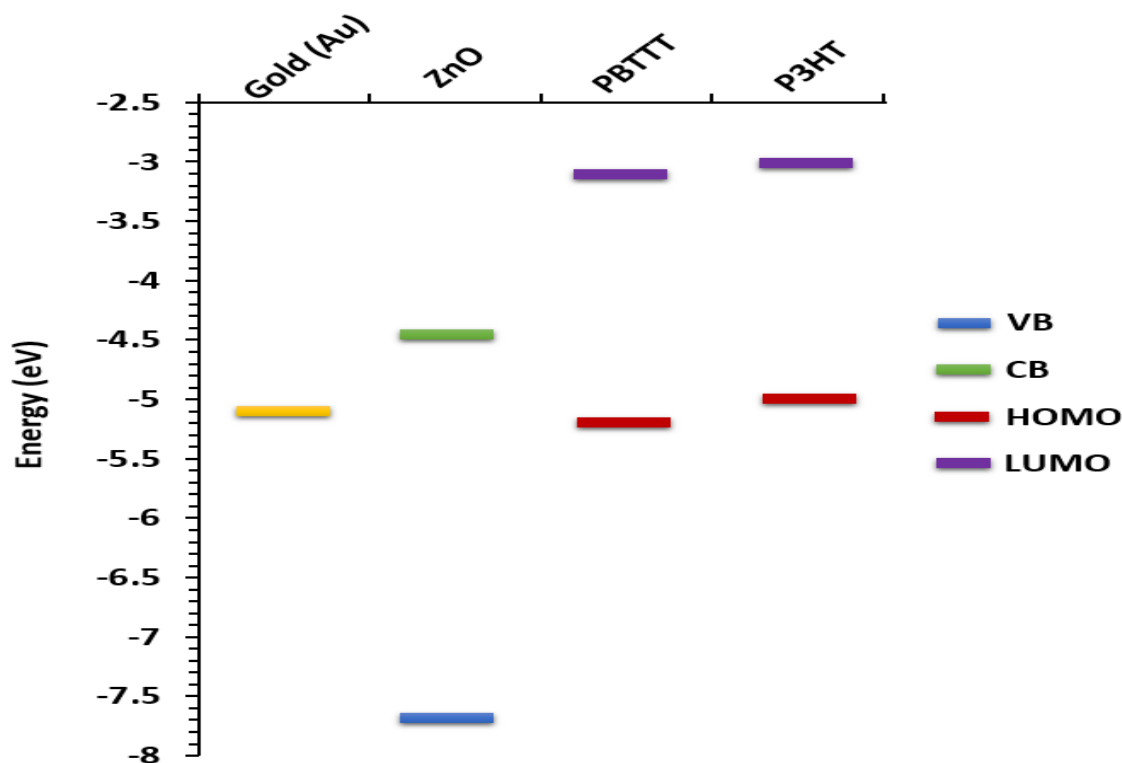


Figure 1-14: the electronic levels of organic semiconductors (P3HT and PBTTT); HOMO (Red line) and LUMO (Purple line). Valence band (Blue line) and conduction band (Green line) for inorganic semiconductor (ZnO). Yellow line shows the Fermi level for gold metal.

1.5.3.2 Charge Carrier Transport

After injection from an electrode into an organic semiconductor, carriers should be travelling from source to drain electrode as fast as possible to give high drain current. The transport of charge carriers in a semiconductor can be limited by three factors within a semiconductor bulk, which are *mobility*, *space charge*, and *traps*. Limitations due to space charge (space charge limited transport, SCLC) is often observed for diode architectures (electrode/semiconductor/electrode sandwich) but are not relevant in transistor architectures. Here I will, therefore, only discuss mobility and traps.

In ordered (*i.e.*, crystalline) inorganic semiconductors such as silicon or germanium, the atoms are connected by strong covalent bonds to create the crystal, defined by a unit cell that is repeated in all directions. Strong bonds lead to strong electronic

interactions between the atomic orbitals which, therefore, overlap to form so-called 'bands', wherein charge carriers are fully delocalized and can be described as delocalized waves with a wave vector, k . The mobility of charge carriers in bands is high and limited only by scattering at lattice defects or vibrations (phonons). By increasing the temperature, which in turn increases the phonons, the mobility decreases.

In organic semiconductors, interactions between neighbouring molecules are far weaker than the bonds within the molecule (van der Waals interactions vs. covalent bonds), even when the material is crystalline ('molecular crystals'). The weak electronic interactions lead to narrow energy bands (bandwidths below 500 meV),^[49] which can be easily disrupted by disorder, including thermal vibration. This in turn leads to scattering of the charge carriers with a mean free path that approaches the distance between neighbouring molecules.^[49] Usually, carriers are instead localized as polarons on a particular molecule and cannot move in the way described above. Instead, carrier transport will be by so-called 'hopping', in which the carriers move via thermally assisted tunnelling from one location (i.e., molecule or chain) to another as revealed by time of flight measurements. The mobility in the hopping mode is low but rises with increasing temperature. However, band-like motion can only be noticed in highly pure organic molecular crystals at low temperatures up to room temperature.^[49]

Conceptually, because of structural disorder and structural defects in undoped amorphous or polycrystalline semiconductors (a-Si, precursor route ZnO) carrier transport is also by localized carriers rather than by 'infinitely' delocalized waves, and the issues discussed here for organic semiconductors also apply in part.

After applying a bias, charge carriers in semiconductors will move ('drift') in the direction of the applied field. The mobility (μ) of carriers is given by the average drift velocity (v) of carriers per unit of electric field (E), as given by the following equation:

$$v = \mu E \qquad 1-11$$

μ is typically quoted by units $\text{cm}^2\text{V}^{-1}\text{s}^{-1}$.

This definition applies to both coherent (band-like) incoherent (hopping-type) motion. However, mobility for coherent motion typically is higher by several orders of magnitude. The mobility in organic semiconductors strongly varies between different species due to the packing of the chain and degree of order in addition to the density of impurities and structural traps.^[8] However, mobilities can reach up to $10 \text{ cm}^2\text{V}^{-1}\text{s}^{-1}$ or even higher,^[50] more than in amorphous silicon ($< 1 \text{ cm}^2\text{V}^{-1}\text{s}^{-1}$), but lower than in single crystal inorganic semiconductors that have mobilities of up to $1000 \text{ cm}^2\text{V}^{-1}\text{s}^{-1}$.^[51]

Real organic, undoped amorphous or polycrystalline semiconductors are characterized by the presence of so-called charge carrier ‘traps’, which have a profound impact on carrier transport and device characteristics in general. In organic semiconductors, they can be defined as sites that have ionisation potential significantly above the average *HOMO* (*hole traps*) or electron affinity significantly lower than the *LUMO* (*electron traps*). ‘Significantly’ above/below means a large difference in comparison to Bässler’s Gaussian standard deviation. Physically, traps can be impurities or chemically degraded molecules (e.g. by oxidation).^[52]

In partly crystalline materials (undoped amorphous or polycrystalline semiconductors), the boundaries of crystalline grains often act as traps. As traps are localized sites, they have a far stronger impact on the ‘hopping’ transport of localized carriers, rather than for the band-like transport of delocalized carriers. Depending on trap depth, trapped carriers can be immobilized more or less permanently. Trapping therefore explains the unipolar character of most organic semiconductors: a hole transporting material simply is material with many deep traps for electrons, thus more or less completely disabling electron transport (and vice versa). Still, even in a hole transporter, there are still some hole traps, which strongly affect transport and device properties.

A trapped carrier represents a space charge which effectively weakens (i.e, screens) applied ‘transport’ fields. In the TFT, the most relevant example here, this leads to both an effectively reduced mobility and an effectively weakened gate voltage. This leads to a higher threshold and a shallower subthreshold swing. Threshold is given by the following equation for the TFT threshold voltage:^[8]

$$V_{th} = V_{FB} + \frac{qp_0d_s}{C_i} \quad 1-12$$

Therein, V_{FB} is the flat band voltage, q is the charge of one charge carrier (+/- e), p_0 denotes the trap density in the semiconductor (including the semiconductor/insulator interface), d_s is the thickness of the semiconducting film, and C_i the specific capacitance of the gate medium.

V_{FB} is given by the *HOMO/LUMO* levels of the semiconductor, and the work functions of the contact metals. With reasonable choices, V_{FB} can be significantly smaller than 1 Volt, even 0 Volt is possible ('normally on' TFT). However, V_{th} can be largely increased by carrier traps, which may occur in the semiconductor bulk, or at the interface of the semiconductor and insulator. Equation 1-14 simultaneously illustrates the need for semiconductors and interfaces with low trap density, and the benefit of high capacitance gate insulators (e.g. from electrolyte gate media (Section 1-6 below)), as C_i moderates the impact of traps and helps to keep V_{th} low.

Similarly, trap density controls the 'ideality factor' n and subthreshold swing S^{-1} (Equations 1-3, 1-5), as the trap capacitance C_s in Equation 1-5 is related to trap density via:

$$C_s \propto p_0 \quad 1-13$$

Taken together, Equations 1-5 and 1-12 show that S^{-1} approaches the best possible (*i.e.*, smallest) value in terms of the limit of low trap density and high C_i .

1.5.4 Organic Semiconductor Materials

Organic semiconductors can be classified into two categories: low molecular weight and high molecular weight polymers. Low molecular weight organic semiconductors are relatively small molecules and often insoluble in solvents. Thin films have to be formed by vacuum deposition or organic vapour phase deposition. High molecular weight polymers consist of (usually) linear chains that repeat the same chemical unit many times (100s or 1000s of times). This unit is hence called the 'repeat unit'. A

conjugated repeat unit leads to a conjugated, i.e. semiconducting, polymer. Typically, the repeat unit also shows laterally attached, shorter chains of saturated carbon (around 6 to 12 Carbon/chain). In solution, these sidechains can adopt many conformations, hence they provide an entropy of solution. This makes semiconducting polymers soluble in (some) organic solvents and allows their convenient processing into thin films. For a given weigh-in of polymer per unit volume of solvent, polymer solutions display far higher viscosity than for the same weigh-in of a low molecular weight material, the more so the higher the polymer molecular weight, *i.e* the number of repeat units per chain. This allows the formation of high quality films from rather dilute solutions.

Two types of high molecular weight polymers have been used in our work: PBTTT and P3HT. Both of them are mainly hole-transporting semiconductors.

1.5.4.1 Poly(3-hexylthiophene-2,5-diyl), (P3HT)

P3HT is a conjugated polymer made of a backbone of thiophenes with laterally attached hexyl chains as a side group, as seen in Fig 1-15. As we described in Section 1.5.2, Thiophene is a conjugated cyclic compound of five atoms comprising one sulphur atom. P3HT has been widely used as an organic semiconductor in thin film transistors.^[53-59]

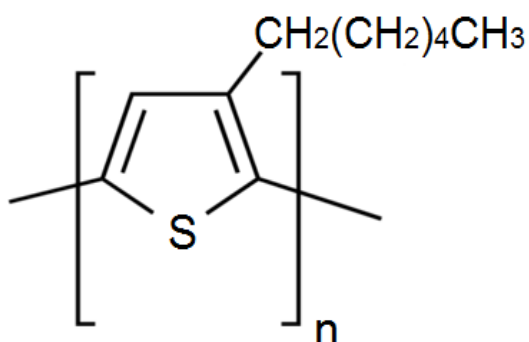


Figure 1-15: A chemical structure of rr-P3HT (regioregular poly(3-hexylthiophene)).

Alkyl side-chains assist the P3HT to dissolve easily in organic solvents, which allow P3HT to be easily processed from a solution. There are three ordering formats for the

position of alkyl chains on thiophene rings; they can be head to tail (HT), head to head (HH), or tail to tail (TT). The HH and TT couplings cause twisting in the thiophene rings and lead to an increase in the torsional angle. Subsequently, this leads to disruption of the π -conjugation and produces larger band gap and loses conductivity. Polymers with HH and TT couplings are referred to as regioirregular due to the fact that they do not have regiochemical control. On the other hand, increasing the long chain ordering leads to determining the energy level and then increasing the charge transport. To arrive at such a goal the ordering format HT is the best. This format is known as regioregular P3HT ('rrP3HT'). Regioregular P3HT was initially synthesized by McCullough *et al.*^[60] Moreover, fully head-to-tail coupled rr-P3HT can be synthesized by a reaction of 2,5-dibromothiophene monomers with high reactive metal "Rieke" zinc (Zn^*) at a low temperature.^[61]

Regioregular P3HT is more rigid and coplanar than regioirregular P3HT and crystallizes to a larger degree. X-ray scattering showed that the polymer chains form a well-defined lamellar structure. Within these ordered lamellae, the overlap between the frontier π -orbitals of adjacent molecules is significant, which can lead to high mobility of up to $0.4 \text{ cm}^2 \text{ V}^{-1} \text{ s}^{-1}$.^[55] Nevertheless, like all crystalline polymers, crystallinity is not complete; the ordered lamellar structure has spaces between ordered units which are filled with amorphous polymer sections. The ionization potential of rrP3HT is typically 4.9 – 5.0 eV.^[62]

The drawback of P3HT is its sensitivity to oxidation.^[63] For that reason, in 2005, a new improved material, called PBTTT, has been reported by McCulloch *et al.* ^[64]. This material is also dependant on a thiophene ring, as will be described below.

1.5.4.2 (Poly(2,5-bis(3-hexadecylthiophen-2-yl)thieno[3,2-b]thiophene), (PBTTT)

PBTTT comprises pairs of thiophene rings fused at two corners, as seen in Fig 1-16. PBTTT has shown better π electron delocalization due to the fusion of thiophenes which decreases the *HOMO* level by 0.1 eV compared to rrP3HT.

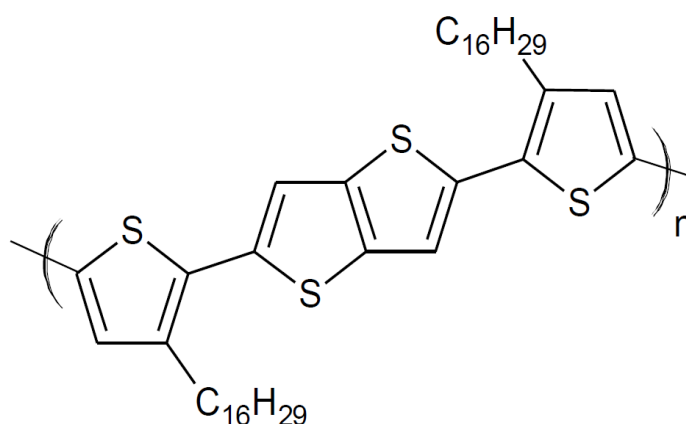


Figure 1-16: A chemical structure of semiconducting polymer poly(2,5-bis(3-hexadecylthiophen-2-yl)thieno[3,2-b]thiophene) (PBTtT).

This a chemical structure leads to more stability against degradation, and decreases the probability of charge carriers getting trapped. PBTtT is known for its extremely high carrier mobility of $\sim 3.5 \text{ cm}^2 \text{ V}^{-1} \text{ s}^{-1}$.^[65, 66] However, PBTtT is only marginally soluble due to its predominantly inflexible nature; note its more rigid backbone structural design compared to the chemically associated, but more flexible P3HT. For that reason hot chlorinated benzenes have been used to dissolve PBTtT.

It should be mentioned that the symmetry of the PBTtT repeat unit does not allow for regioirregular formats. Regioregularity, therefore, does not have to be controlled during synthesis, and polymerization chemistry and its catalysis is significantly different from rrP3HT. PBTtT polymerization is catalyzed by an organometallic Pd(0) compound, Tris(dibenzylideneacetone)dipalladium(0), $\text{Pd}_2(\text{dba})_3$.^[64]

1.6 Electrolytes as Gate Media in TFTs

As mentioned in Section 1.1 the accumulation of charge carriers in a TFT is located at the semiconductor/gate dielectric interface. Therefore, gate dielectrics play a crucial role in TFT technology: gate dielectrics with high specific capacitance improve the transistor's performance^[10] as they lead to lower threshold and higher charge carrier concentration for a given gate voltage. For instance, as seen in Equations 1-7 and 1-8, the drain current is directly proportional to the specific capacitance (C_i); Equation 1-14 shows that increasing the specific capacitance leads to decrease the threshold voltage, and Equation 1-5 shows an improved subthreshold slope for higher C_i . High

specific capacitance can be obtained by increasing the dielectric constant or decreasing the thickness, as seen in following equation:

$$C_i = \frac{\epsilon_0 k}{d} \quad 1-14$$

where ϵ_0 represents the vacuum permittivity, k refers to the relative permittivity of the gate insulator, and d denotes the thickness of the gate insulator.

The typical gate insulator material used in TFTs is silicon dioxide (SiO_2). However, SiO_2 materials show a low dielectric constant ($k=3.9$).^[67] Another issue for the use of SiO_2 in OTFTs is the presence of hydroxyl (-OH) groups in its surface, which act as trap sites. In order to reduce (-OH) groups, the surface of SiO_2 must be treated with, e.g., polyethylene^[68] or by chemically 'capping' -OH groups with a self-assembling monolayer. SiO_2 has been used as gate insulator with organic semiconductors for proof-of-principle, but practically sacrifices key advantages (low cost, flexibility) of organic semiconductors.

Alternatively, polymeric insulators such as polyvinyl alcohol (PVA), poly(vinyl phenol) (PVP) or poly(methyl methacrylate) (PMMA) have been used.^[67] However, flexible and solution-processable polymer dielectrics display relatively low dielectric constants and they need to be rather thick to prevent pinholes that lead to gate leakage current,^[67] since increasing thickness leads to decreased C_i , and raises threshold voltage. The capacitances of SiO_2 or polymer dielectrics range between 5-30 nF/cm².^[67] However, significant development has been made with PVP and similar polymers that were crosslinked after solution processing with a bifunctional trichlorosilane^[69] or dianhydride^[70] and can give much thinner, pinhole-free insulators with high gate capacitance ($C_i > 100$ nF/cm²), and a threshold voltage of less than 1V.

As an alternative to dielectric insulators (such as SiO_2 and polymeric insulators), electrolytes have been used as the gate medium in TFTs. The term 'electrolyte' refers to materials that contain free mobile ions. Most electrolytes are found in liquid form but there are also a number of solid electrolytes. The simplest and most common examples are salts dissolved in solvent, for example NaCl in water. Dissolving salt in

a polar solvent will release both positive ions (cations) and negative ions (anions). This process is called salt dissociation. Water in particular can also undergo a process called 'autoprotolysis', *i.e.* a small fraction of water molecules (H_2O) spontaneously dissociate into cations (H_3O^+) and anions (OH^-) – *i.e.* a self-ionisation reaction. Depending on the degree of dissociation, electrolytes are classified as either strong or weak. Materials that are completely or for the most part ionized (dissociated) are called strong electrolytes, while weak electrolytes only are slightly ionized, such as water due to autoprotolysis.

The use of electrolytes as the gate medium in TFTs is due to their high capacitance, typically in the range of 1-10 $\mu\text{F}/\text{cm}^2$,^[10] which far exceeds the capacitances of conventional dielectrics. The extremely high capacitance means that, for a given gate voltage, orders of magnitude higher carrier densities are accumulated at the surface of the semiconductors. High capacitance also reduces the threshold, *cf.* Equation 1-14. Therefore, robust field effect transistors operating at low voltages can be obtained.

The concept of an electric double layer (EDL) that is responsible for such huge capacitance, a few types of electrolytes that have been used as a gate medium for our TFTs, and an overview of water-gated thin film transistors (WGTFs) will be discussed in the following sections.

1.6.1 Electric Double Layers (EDLs)

When two electrodes are in an electrolyte solution, and a voltage is applied between them, ions of opposite polarity move towards the electrodes to form a thin sheet or 'cloud' of ions close to the interface of the wires. This is somewhat similar to the Schottky junction at the electrode/doped semiconductor interface, Fig. 1-17. Taken together, the electronic charge that resides on the outermost electrode surface and the excess of oppositely charged ions in the electrolyte close to the electrode surface is known as the Electric Double Layer (EDL).

Note, as two electrodes are required to apply a voltage (potential difference) to an electrolyte, EDLs always come in pairs of opposite electric polarity, one close to each

electrode, as seen in Fig. 1-17. This combination is known as an electric double layer capacitor. The EDL that formed close to the positively charged electrode (anode) is called an anionic EDL while the other EDL formed close to the negatively charged electrode (cathode) is referred to as a cationic EDL. The EDL is extremely thin (in the order of 1 nm) and, therefore, produces very high capacitance in the range of 1-10 $\mu\text{F}/\text{cm}^2$.^[10]

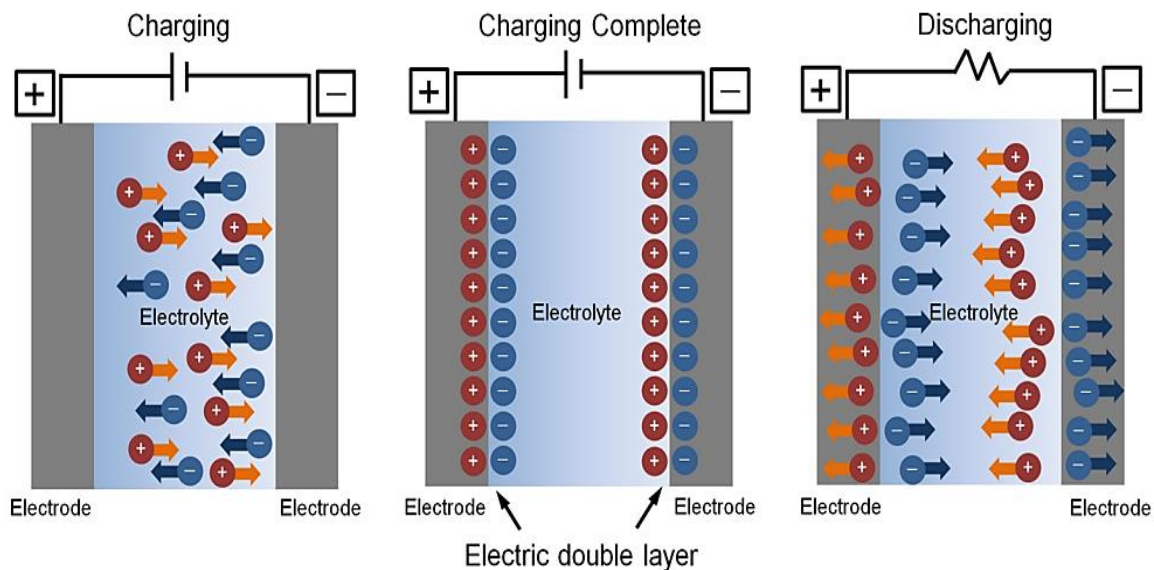


Figure 1-17: Charge and discharge of EDL capacitor. By applying bias with opposite polarity on the electrodes (capacitor plates), cations and anions start to move towards the electrodes (Left) until they balance the charges on the electrode's surface, leading to EDLs. When removing the applied voltages and connecting the electrodes (e.g. via a resistor), the capacitor plates will discharge and ions will diffuse until an even distribution is regained. Figure adapted from ^[71].

The concept of the double layer at the surface of a metal being in contact with an electrolyte was first described by *Helmholtz*. In the *Helmholtz model*, a uniform thin layer of counter-ions forms close to the metal surface which is surrounded by solvent molecules. Solvent molecules in turn prevent ions from reaching the metal surface. Therefore, a very small distance, which is in the order of nm, separates the ions from the metal surface. This is known as the '*Helmholtz plane*' or '*compact layer*'. Once the charge per area of the electrodes becomes balanced by counter-ions, the electrical potential drops across this layer only, while remaining constant in the bulk electrolyte (zero potential). Hence, the electric field is concentrated in the EDLs, Fig1-18a. This simplistic model fails though to explain EDL capacitance quantitatively; in particular, it does not describe the dependency of capacitance on electrolyte strength/ion concentration. In addition, it ignores the diffusion due to the huge concentration

gradient between the compact layer and bulk electrolyte, and the adsorption of ions on the metal surface. Consequently, Gouy and Chapman developed a new model that depends on the thermal motion's effect of ion distribution and electrostatic attraction. Gouy and Chapman proposed that there is an interplay between electrostatic and diffusion processes keeping a layer of counter-ions on the metal charged surface. Therefore, the electrical potential falls exponentially, rather than abruptly, away from the electrode towards the electrolyte bulk, Fig1-18b. In fact, the Gouy-Chapman model represents considerable improvement and provides a better approximation of reality than the Helmholtz theory. Nevertheless, this model still has limited quantitative application. For example, they assume that ions behave as point charges and there are no physical limits, such as the Helmholtz (compact) layer, for ions in their approach to the electronic surface, which is not true. Furthermore, this theory does not correctly predict experimental capacitances. Subsequently, the Gouy-Chapman diffuse double layer model was modified by a new model called Stern's model. This model actually results from the combination of the Helmholtz and Gouy-Chapman models. Stern's model states that ions do have a finite size, so cannot approach the metal surface closer than a few nm and consequently have a closest approach to the metal surface in the order of the ionic radius. Therefore, the charges at the interface are not balanced completely by the Helmholtz layer alone but also by a contribution of a diffuse layer. Hence, the electric potential first drops abruptly at the outer Helmholtz plane and then exponentially in the diffuse layer toward the electrolyte bulk, as seen in Fig1-18c. The width of the diffusion layer decreases with increasing ion concentration.

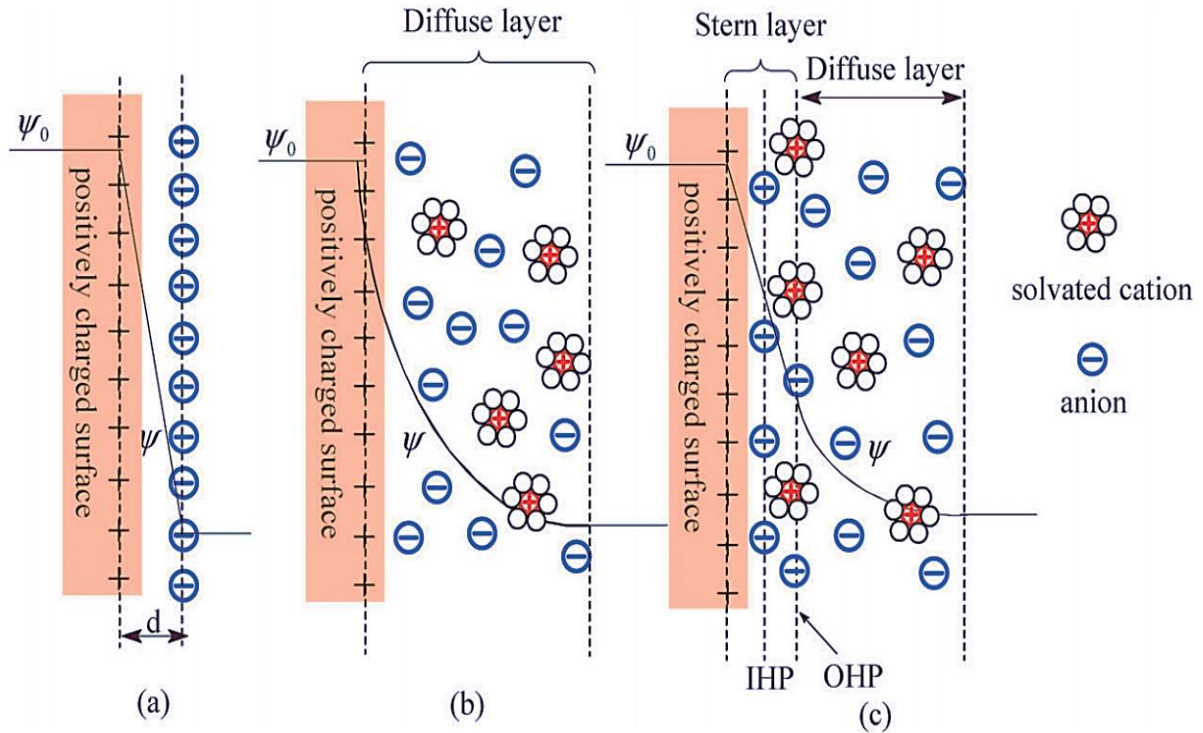


Figure 1-18: The electrical double layer's models: (a) the Helmholtz model, (b) the Gouy–Chapman model, and (c) the Stern model. The distance of the Helmholtz double layer from the electrode is in Stern model, IHP and OHP refer to the inner Helmholtz plane and outer Helmholtz plane. IHP denotes to the space of closest contact of adsorbed ions while OHP denotes to that of the non- adsorbed ions. OHP represents the starting point of diffuse layer. ψ_0 is the potential at the metal contact surface and ψ is the potential at the metal surface/electrolyte interface. Figure adapted from [71]

Based on Stern's model, mathematically there are two capacitors in series in each EDL with a total capacity as in following equation [72]:

$$\frac{1}{C_S} = \frac{1}{C_{HZ}} + \frac{1}{C_{GC}} \quad 1-15$$

where C_S is the total capacitance of one EDL, C_{HZ} is the Helmholtz layer's capacitance and can be expressed by Equation 1-16 with the distance d representing the distance of the double layer between the metal surface and the centre of counter-ions. C_{GC} represents the capacitance of the Gouy-Chapman diffused double layer, and it can be given by:

$$C_{GC} = \frac{4zeN_A C_\infty \lambda_D}{\psi_D} \sinh\left(\frac{ze\psi_D}{2k_B T}\right) \quad 1-16$$

Where ψ_D is the electrical potential in the diffuse layer, e is the primary charge, C_∞ is the molar concentration of the electrolyte in the bulk, λ_D is the Debye length, z is the

electrolyte's valency, N_A denotes Avogadro's number, k_B is the Boltzmann constants, and T is temperature. Note that the capacitance of an EDL capacitor then results from the serial combination of both (anionic and cationic) EDL.

Note that the mobile ions impart electrical conductivity to electrolytes. However, the current flow in an electrolyte stops when EDLs are fully developed, as the EDLs screen the electrolyte bulk from the applied voltage. Conductivity has to be measured under an AC voltage to avoid the build-up of EDLs at the electrodes used for measurement. Electrolytes are DC insulators, but AC conductors, which differentiates them from dielectrics that insulate at all frequencies. The required AC frequency is given by the time the EDL needs to build up; in weak electrolytes that may be as long as ~ 1 s. Water is known to be conductive at 50 Hz ('hairdryer in the bathtub'). Furthermore, each electrolyte will be electrochemically destroyed by electrolysis when a sufficiently high DC voltage is applied to it. This critical voltage is a materials' property known as the electrolytes' 'electrochemical window'. The electrochemical window sets an upper limit for the practical use of electrolytes as gate media.

1.6.2 Examples of Electrolytes used as TFT Gate Media

1.6.2.1 Deionised Water (DI water)

Pure water, or deionized Water (DI water), is a weak electrolyte through its 'autoprotolysis', sometimes called auto-ionization or auto-dissociation, in which a water molecule, H_2O is deprotonated by losing the nucleus of one of its hydrogen atoms and becomes a hydroxide ion (OH^-). Immediately, another water molecule will be protonated by the free hydrogen atoms to form hydronium ions (H_3O^+).



The equilibrium of the above equation is strongly weighted on the non-ionized ($2H_2O$) side; at 25 °C the concentration of H_3O^+ is only 10^{-7} mol/L (10^{-7} M), while the concentration of H_2O is 55.6 M. The concentration of H_3O^+ in an aqueous medium is

commonly expressed as the negative decadic logarithm of the concentration of H_3O^+ measured in mol/L; this is known as pH. The pH of DI water at 25 °C is therefore 7.

Both hydroxide ions (OH^-) and hydrogen ions (H^+) lead to a residual electric conductivity even in otherwise completely deionized water; the conductivity of DI water (measured under AC conditions for the reasons described above) is less than for normal tap water due to the larger amounts of acids and dissolved salts in tap water. The conductivity of tap water is around 1000 S cm^{-1} ^[73] whereas, DI water shows a resistivity of $10^{-18} \text{ M}\Omega\cdot\text{cm}$, i.e. has a low conductivity of $0.05 - 0.1 \mu\text{S cm}^{-1}$.^[74] However, the conductivity of DI water increases to 1 S cm^{-1} once it is exposed to the atmosphere allowing the carbon dioxide to dissolve and create carbonic acid.^[75] Kergoat *et al.* reported that the EDL capacitance of DI water is about $3 \mu\text{F}\cdot\text{cm}^{-2}$ ^[57] at a frequency $\sim 1\text{Hz}$. Water has limited stability at applied voltages of 1.23 V .^[10] This is known as an electrochemical window, which is similar to the dielectric breakdown in gate dielectrics.

The capacitance of DI water can be increased by adding some salts. For example, the capacitance of EDL when adding NaCl to DI water is about $10.6 \mu\text{F}\cdot\text{cm}^{-2}$ at 0.5V while it increases to $34.6 \mu\text{F}\cdot\text{cm}^{-2}$ at 1V .^[76] Some salts such NaCl, CaCl_2 , KCl, and BaCl_2 have been used in our experiments as analyte solutions (water-borne cations) or as control solutions.

1.6.2.2 Phosphate Buffered Saline (PBS)

A buffer solution is used in order to keep the pH of the solution constant even when a small quantity of acid or base is added by chemical reactions or by other means. This is because a buffer solution encloses both an acidic and a basic component, the choice (and to some degree, concentration) of components defines the buffer's pH. One of the most used buffer solutions in biological research is phosphate-buffered saline (PBS) solution. PBS is a water-based salt solution comprising sodium chloride (NaCl), sodium phosphate (Na_3PO_4), and (in some preparations) potassium chloride (KCl) and potassium phosphate (KH_2PO_4). PBS buffers at $\text{pH} = 7.4$. Also, ion concentrations of PBS are close to those in living organisms, and it is non-toxic to cells.^[58, 59, 77] It is therefore frequently used in the life sciences and in the development of biosensors to

simulate bodily fluids. Because PBS is a more concentrated electrolyte than DI water, PBS displays higher capacitance up to somewhat higher frequencies than DI water. Therefore, low threshold voltage, and consequently high drain current and low sheet resistance, can be obtained in PBS-gated TFTs, as we will see in Chapter 5.

1.6.2.3 Ionic Liquids (ILs)

Ionic liquids (ILs) belong to the family of molten salts but differ from conventional molten salts due to having low melting points, lower than 100 °C or even lower than room temperature. They are entirely composed of cations and anions. Compared with other electrolytes, ILs provide many distinct benefits such as high ionic conductivity, high thermal stability (stable below 300 °C) which can offer a wide liquid series for organic catalysis and inorganic synthesis, negligible vapour pressures which can minimize the exposure to toxic volatile vapours, broad electrochemical windows ranging from 2 to 6 V (typically 4.5V), non-flammability and conductivity of 10^{-1} Sm^{-1} . ILs are solvent-free due to the absence of a solvation shell, which offers a well identified ion size.^[78, 79] ILs can be printed using an inkjet printing method and consequently gel into a quasi-solid film.^[80] The formation of EDLs using ILs produces very high capacitance in the range of 5-17 μFcm^{-2} at 1 and 10 Hz.^[10]

1-ethyl-3-methylimidazolium-bis (tri fluoro methyl-sulfonyl) imide (EMITFSI), shown in Fig. 1-19, is one example of ILs that has been used to gate our organic field-effect transistors. EMITFSI shows a very high electrochemical window, about 4.3V, and high capacitance up to about 11 μFcm^{-2} at 0.1 Hz and $\sim 5 \mu\text{Fcm}^{-2}$ at 10 Hz.^[81, 82] Indeed, the electric double layer capacitance of ILs remains considerably higher than for aqueous electrolytes up to kHz frequencies. Such a high electrochemical window and capacitance means maximum electric displacement is 10 times bigger compared to DI water or any water-based salt such as PBS. Therefore, low voltage and high current can be achieved with an IL-gating semiconductor.

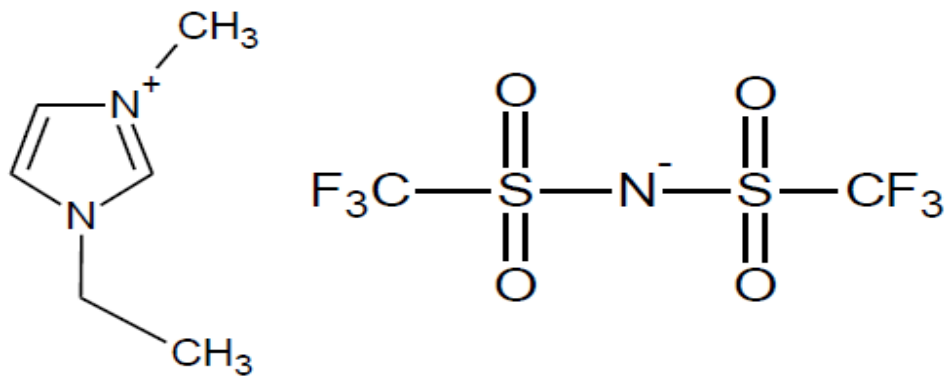


Figure 1-19: The chemical structure of EMITSFI ionic liquid.

1.7 Water-gated TFTs (WGTFs)

Following on from the above discussion of electrolytes, it is evident that they may be useful as an alternative to dielectrics as TFT gate media. As the capacitance of EDL capacitors is in the range of $10 \mu\text{F}/\text{cm}^2$, EDL gate media lead to a large concentration of charge carriers (about 10^{14} - 10^{15} charges cm^{-2}) [71, 83] in the transistor channel at relatively low applied gate voltages. Electrolytes have therefore been used for TFT gating, including solid (polymer) electrolytes [65, 84] and ionic liquids (ILs). [81, 82, 85-88] In 2010, Kergoat *et al.* [57] demonstrated that OTFTs can be gated by DI water. Since then a number of works have been reported using gating of organic and inorganic semiconductors TFFs with DI water. [35, 36, 89]

1.7.1 Operation Principle of WGTFs

Fig. 1-20 illustrates the operation of a water-gated TFT (bottom), in comparison to a dielectric-gated TFT (top). Note the similarity to the EDL capacitor in Fig. 1-17, only now, one of the capacitor's plates is the TFT channel. The charge on this 'capacitor plate' is the channel accumulation layer.

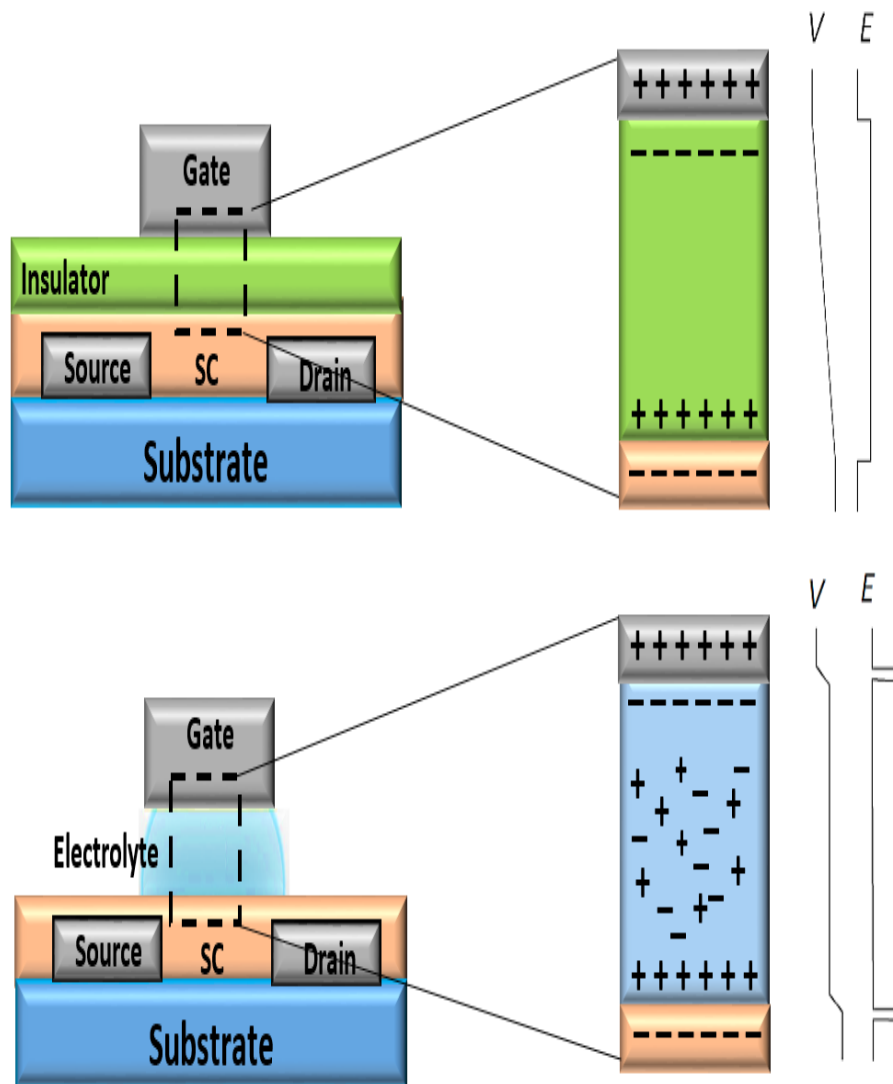


Figure 1-20: Schematic cross section of a thin film transistor with voltage (V) and electric field (E) in a dielectric (top) and electrolytic gate (bottom) when a positive gate voltage is applied. Note the similarity of the bottom right image to [Fig. 1.17](#).

Fig. 1-21 illustrates the operation of a WGTFT in the field-effect mode (called the electric double layer EDL transistor); an alternative mode of operation is possible, known as the 'electrochemical transistor' (ECT). The ECT mode is only observed for semiconductors that are permeable to water-borne ions. Impermeable semiconductors prevent ions passing from the electrolyte into the semiconductor bulk. In this case, only the field effect operation is observed. Due to the high EDL capacitance, the threshold is low, typically 300 mV^[57] or less, well below the electrochemical window of water (1.23 V).

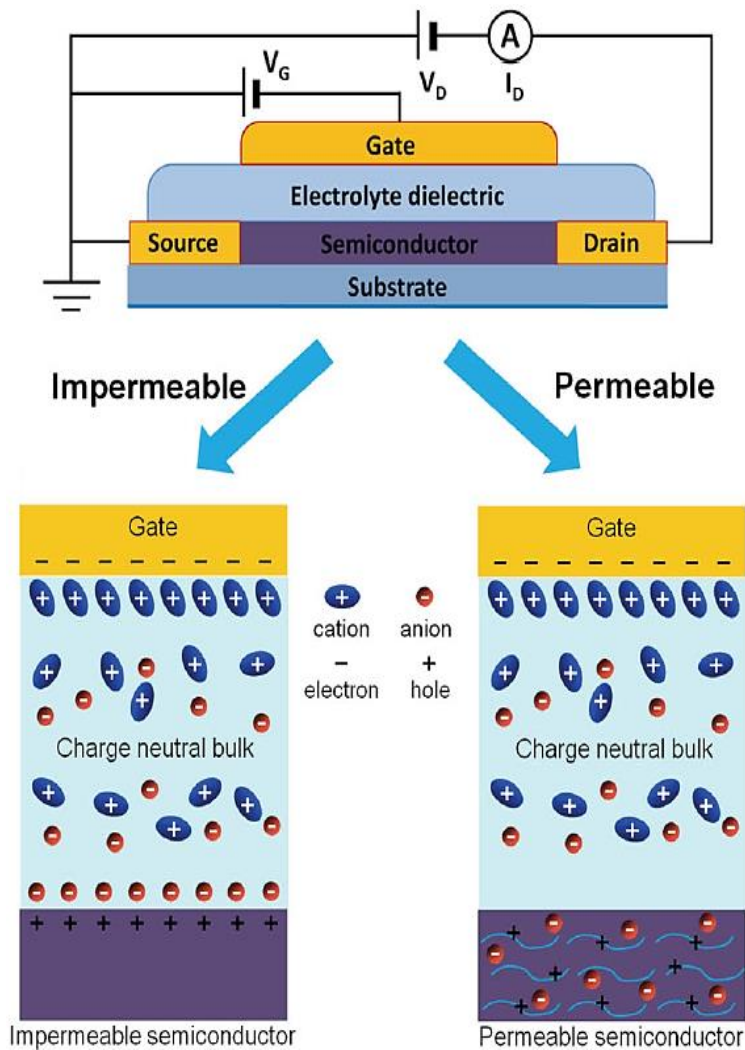


Figure 1-21: A illustration showing the electrolyte- gated impermeable/ permeable organic semiconductor: left) in Field Effect mode, and right) in Electrochemical mode. ^[10]

If a permeable semiconductor is used in combination with salt solutions or buffers instead of pure water used as gate media, the gate voltage may drive ions and pass through the water/semiconductor interfaces and dope the semiconductor bulk, as illustrated in Fig. 1-21. Electrochemical doping is well recognized for some polymer semiconductors once they come into contact with electrolyte.^[10] However, Kergoat *et al.* claimed that P3HT transistors operate only at field-effect mode^[57] due to P3HT's high hydrophobicity and density. In some cases, transistors may operate as organic electrochemical transistors (OECTs) and show field effect gating via the EDLs at the same time, for example in fibre-based transistors.^[90] It has been shown that at low potentials the charge carriers are only accumulated at the interface whereas electrochemical doping occurs at a high potential and with a prolonged operation

time.^[91] However, it is practically recommended not to exceed gate voltages of 0.7 V to avoid degradation, and to limit the possibility of parallel ECT action,^[56, 57] as described above. Within the current thesis, ECT behaviour is considered undesirable and is avoided by choosing impermeable semiconductors.

1.7.2 Water-gated Transistors as Sensors

The discovery of WGTFTs by Kergoat *et al.* ^[57] is particularly remarkable, as it paved the way for new sensor technologies where the aqueous sample is an active part of the transducer. Furthermore, TFTs can be operated in both standing (drops) ^[57] and flowing water.^[92] Therefore, WGTFTs, in principle, are a new sensor family, in which the chemical information at material-electrolyte interfaces can be transduced into a change of the TFTs' electrical characteristics, such as threshold voltage^[93] or mobility.^[92]

To turn a water-gated transistor into a sensor for analytes dissolved in water, a further element has to be introduced into the TFT structure – namely, a 'sensitizer' (also known as a 'receptor') that selectively binds to water-borne analyte, and consequently influences the WGTFTs' electrical characteristics. Therefore, that measurement of TFT characteristics can be exploited to transduce presence and concentration of the analyte. The incorporation of specific sensitizers or receptors can be achieved using two methods: (1) sensitizer molecules can be integrated directly into the semiconducting film or (2) they can be immobilized on the surface of the gate electrode.

As was mentioned in Section 1.6.1, WGTFT is considered a capacitor where electrolyte/channel interface is one of the plates and the gate electrode above the channel is the second plate. Therefore, if the sensitizers' layer is coated on the channel and interacts with the analyte from the water or test solution, the surface potential (electric potential) will change depending on these interactions (e.g. via interfacial dipole moments, or binding of ions). This changes the TFT's flat band voltage, hence its threshold (according to Equation 1-14). Also, analyte binding may affect carrier mobility in the semiconductor. On the other hand, when the gate electrode is sensitized, the electrode's surface potential will be affected, hence effectively its work

function, again leading to a shift of the flat band voltage and threshold – but in this case, not mobility. Consequently, analyte binding is expressed through the transistor characteristics. In this way, a WGTFT can transduce water-borne analytes into an electrical signal; a number of examples are in the literature.^[58, 59, 77, 94, 95]

Most of the research works has been focused on the semiconductor-analyte interface.^[58, 77, 94, 95] Examples include immobilization of DNA, antibodies, protein, and phospholipid (PL) on the semiconducting layer. These detections were addressed by using a carboxylic acid derivative of e.g., P3HT, to directly attach biomolecule sensitizers or through modifying the organic semiconductor surface with a specific detection layer. Alternatively, as an example of a WGTFT with a sensitized gate electrode, Casalini *et al.*^[59] functionalized a gold gate electrode with a thiol-based self-assembled monolayer to sensitize for dopamine.

1.7.3 Ion-selective WGTFTs

An important specific family of water-borne analytes are water-borne ions, as these are ubiquitous in natural water. Various sensitive methods, e.g. atomic absorption spectroscopy,^[96] atomic emission spectroscopy^[97, 98] and mass spectroscopy^[99] have been established to detect water-borne cations at low concentrations. However, such techniques lack the feature of portability to the point of need due to the requirement of expensive instrumentation and infrastructure.^[100] As a lower cost and more portable alternative, organic chemistry has developed organic metal complexing agents as sensitizers that bind to water-borne cations; these are known as ‘ionophores’. Most important cations now have ‘their’ selective ionophores. Many ionophores are almost insoluble in water.^[101, 102] One example of ionophores (calixarenes, which have been used in this project) will be discussed in Section 1.7.4.

Successful attempts to detect ions with transistor-based transducers go back to Bergveld^[103] in 1970, who reported the first ‘ion-sensitive field effect transistor’ (ISFET). ISFET was created by removing the metal gate from MOSFET and exposing the silicon oxide gate insulator directly to a solution in addition to using a reference electrode.

Recently, organic WGTFTs have been sensitized to detect and measure the concentration of specific ions in water. This was by integrating an 'ion-selective membrane' (ISM) into the WGTFT architecture. An ISM typically is a plasticized PVC membrane that contains an 'ionophore' as the cation-selective sensitizer. Such ISMs are cast from solutions containing poly(vinyl chloride) (PVC), plasticizer, and an ion exchanger as well as the ionophore itself.^[104-106] ISMs mediate the contact between water-borne ions and the ionophore, which itself is insoluble in water.

When an ISM is inserted between two solutions of its ionophores', a 'target' ion at different concentrations, the ISM develops a potential difference between its surfaces. The two solutions are called the 'inner' and 'outer' solution; in a traditional ion sensor the inner solution has a known ion concentration to act as a standard or reference to compare to the unknown concentration of the 'outer (test or analyte solution). The potential difference (voltage) across the membrane is related to the ionic activities of the inner and outer solutions, and approximately given by the Nernst equation:^[56]

$$E_m = \Delta V = 2.3 \frac{RT}{zF} \log \left(\frac{a_{analyte}}{a_{inner}} \right) \quad 1-18$$

where E_m (ΔV) is the membrane potential, R the universal gas constant ($8.314 \text{ J K}^{-1} \text{ mol}^{-1}$), T is the temperature in kelvins, z is the valency of the detected ions (e.g. 1 for Na^+ , 2 for Ca^{2+}), F is the Faraday's constant ($9.643 \times 10^4 \text{ C mol}^{-1}$) and a is the corresponding activity of the target ion in the analyte and the inner (standard) filling solution, respectively. $2.3 \frac{RT}{zF}$ is the Nernst slope (s) or slope of calibration curve.

Activity (a) is a measure of the "effective concentration" of a type in a mixture, in the sense that the chemical potential of species relies on the activity of a real solution in the same way that it could relies on concentration for an ideal solution. The concentration (c) can be related to activity (a) through using the activity coefficient (γ) where $[a] = \gamma(c)$. With dilute aqueous solutions the activity coefficient: $\gamma = 1$.

Therefore, in the limit of low concentration often: $\frac{a_{analyte}}{a_{inner}} \approx \frac{c_{analyte}}{c_{inner}}$.

At the standard condition of 298 K (25° C), and where a_{inner} is fixed by the internal structure of the electrode, Equation 1-20 can be expressed by:

$$\Delta V = \frac{0.05916}{z} \log(a_{analyte}) \quad 1-19$$

The slope (s) of the curve is related to the ΔV to $\log a_{analyte}$ and is equal to 59.16 mV for $z = 1$ and 29.58 mV for $z = 2$.

The potential difference across the membrane results from a chemical interaction between the analyte and ionophore on the membrane's surface. However, in reality, no ionophore is completely selective towards a single analyte. As a result, the signal of the membrane potential relies on a chemical interaction process for each ion that interacts with the membrane's ionophore. Selectivity is quantified by selectivity coefficients $K_{I,J}$, (a measure of the preference of the electrode for the interfering ions against the major ions) where I : target or 'primary' ion, and J : interfering or discriminated ion. Interference leads to a modification of Equation 1-21 into a new equation called the Nikolsky-Eisenman (NE) equation:^[107]

$$\Delta V = \frac{0.05916}{z} \log \left[a_I + K_{I,J} (a_J)^{\frac{z_I}{z_J}} \right], \quad 1-20$$

where a_I and a_J are the sample solution activity of the preferred (target) and interfering ion, respectively; z_I and z_J are the charges of the primary and interfering ions, respectively.

The selectivity coefficients $K_{i,j}$ can be defined as:

$$K_{I,J} = \frac{a_I^{\frac{z_I}{z_J}}}{(a_J)^{z_J}} \quad 1-21$$

If the value of $K_{I,J} = 1$, this means that the membrane responds to both the ions (I and J ions). The smaller the value of $K_{I,J}$ (less than 1), the more responsive to the analyte

ions over interfacing ions. Commercially, the value of selectivity coefficients are provided by the manufacturer; however, the value experimentally can be determined easily by adding constant concentration of interfering ions to a different concentration of analyte. From the calibration curve, Fig. 1-22, one can identify the value of $K_{I,J}$.

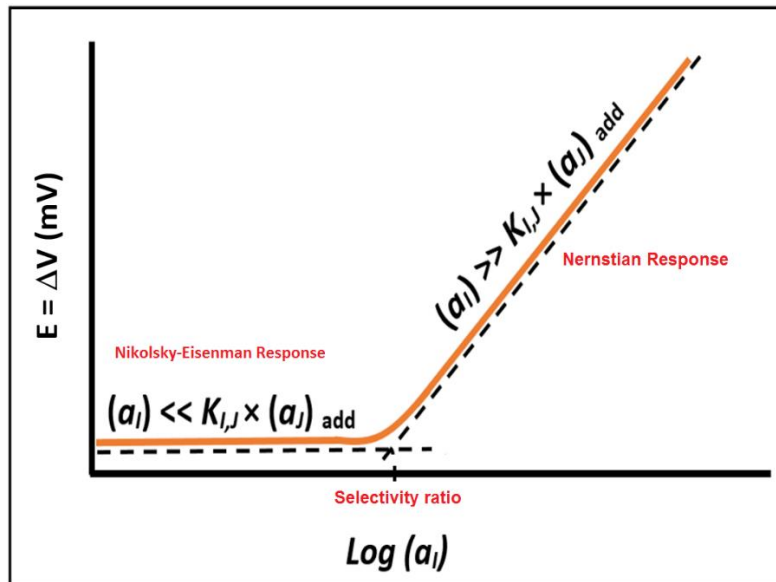


Figure 1-22: The experimental determination of an ion selectivity for an analyte. The activity of analyte (a_i) \approx concentration (c) corresponding to the meeting of the two lines of the curve, produces a potential identical to that of the interferent.

If the analyte's activity is larger than $K_{I,J} \times (a_J)_{add}$, the membrane potential is a linear function of $\log(a_I)$, as given by Equation 1-21. However, If the analyte's activity is significantly smaller than the $K_{I,J} \times (a_J)_{add}$, the membrane potential remains constant. The value of $K_{I,J}$ can be calculated from the intersection of the two linear regions of the analyte's activity and interferent.

Practically, Nikolsky-Eisenman behaviour is more realistic than Nernst behaviour, as the Nernst equation predicts infinite membrane potential with a limit of zero analyte ion concentration, which is not practically observed. Nikolsky-Eisenman instead levels off at a low analyte ion concentration, giving a limit-of-detection (LoD) which approximately equals the value of the selectivity ratio that can be easily extracted from the calibration curve, as seen in Fig. 1-22. Therefore, the selectivity ratio in Fig. 1-22 equals to the lower detection limit:

$$a_{st} = K_{I,J} a_J^{z_I/z_J} \quad 1-22$$

Equation 1-22 can be rewritten as:

$$\Delta V = \frac{0.05916}{z} \log(a_I + a_{st}) \quad 1-23$$

where a_{st} is a constant characteristic of the respective ion-sensitive system and approximately equal to the concentration of the LoD , since observed LoD is frequently governed by the existence of other interfering ions.

In a traditional ion sensor, ion-selective electrodes (ISEs) or electrochemical cell, the membrane potential can be measured as the potential difference between the two identical reference electrodes (Silver chloride electrodes); One reference electrode has a constant potential, while, the other reference electrode is selective electrode (ISE), as seen in Fig. 1-23.

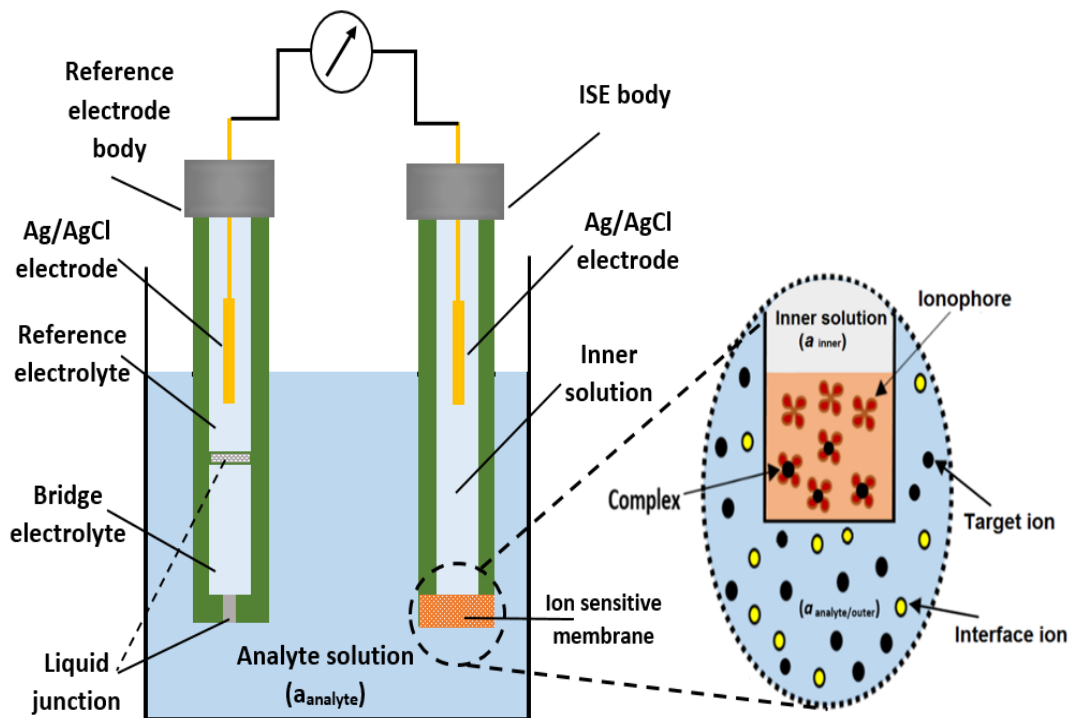


Figure 1-23: Electrochemical transducer for making a potentiometric measurement with an ISE.

Ag | AgCl | reference electrolyte | bridge electrolyte | Analyte solution | membrane | inner solution | AgCl | Ag.

When the two electrodes immersed into analyte solution, the potential difference measured at these two electrodes is seen in the potentiometer (i.e. a voltmeter). The potential of reference electrode creates from the different mobilities of ionic species between analyte solution and bridge solution of the reference electrode. The value of this potential can be small and constant through using a bridge electrolyte has high concentration (e.g. 0.1M KCl). The electrical potential across the membrane in ISE electrode originates from a charge separation, due to a non-uniform distribution of ionic species between the membrane and the analyte solution phase boundary. The potential difference measured in the potentiometer is therefore equal to the membrane potential, according to the Nernst equation (1-21).

In order to measure the potential difference between a sensing electrode (ISE) and a reference electrode, a voltmeter must have much higher input impedance than the impedance of an ion selective electrode. However, practically, no voltmeter has infinite impedance, hence there will be a small current flowing through the photometer. This means that there must also be the same current flowing through the membrane in order to close the electric circuit. However, this is an advantage of the TFT measurement. If anything, our membrane would be compromised by a gate current but not by the drain current.

Sensitized PVC membranes have since been integrated with water-gated TFTs that consequently acted as cation-selective sensors. For example, Schmoltnner *et al.* [56] introduced an ion-selective PVC membrane to a water-gated transistor for the selective detection of Na⁺. Nevertheless, the design of Schmoltnner *et al.* is rather complicated – a two compartment water cell (a test solution and a reference compartment), are separated by the ion-selective PVC membrane.

The reference compartment is only the part that is in direct contact with the semiconductor, while the analyte compartment is addressed with an electrochemical reference electrode as a gate contact. They reported selectivity towards Na⁺ down to μM with near-Nernstian characteristics. On another occasion and in order to avoid using a reference electrode, Melzer *et al.* [108, 109] modified the gate electrode of an electrolyte-gated OFET with an ion-selective PVC membrane. They used several

membranes with different ionophores towards K^+ , Ca^{2+} and Cl^- to detect these at biologically relevant concentrations.

1.7.4 Calixarenes

It is evident from the above discussion that the ionophore is the key to selective detection of ions with a low LoD. One of the most prominent families of water-insoluble ionophores are the calixarenes. Calixarenes are phenolic macrocycles derived from the base-catalyzed condensation of *p*-substituted phenols and formaldehyde. The term calixarene was suggested based on their shape as they are similar to ancient Greek vases of the *calyx krateri* design, hence 'calix', whereas 'arene' stands for the aromatic nature of the macrocycles. Figure 1-24 shows a calix[4]arene which considers the smallest calixarene containing four benzene rings, while a calix[6]arene and calix[8]arene have 6 and 8 units in the ring, respectively.

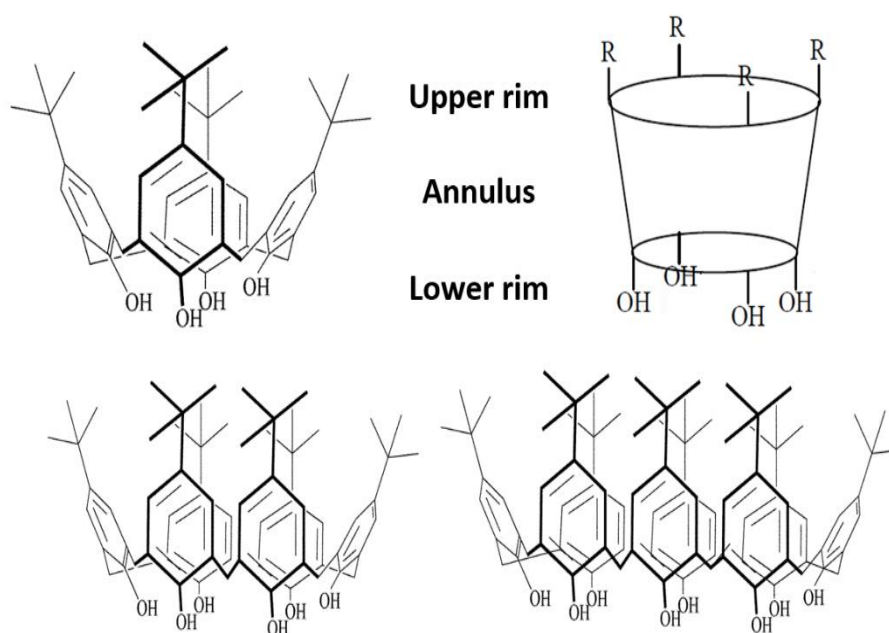


Figure 1-24: The native tBu-calix[4]arene indicating the hydrophobic upper rim and hydrophilic lower rim with cavity shape (Top). (Bottom) shows tBu-calix[6]arene and tBu-calix[8]arene.^[110]

Calixarenes have been utilized widely in research due to several features such as ease of synthesis, low toxicity, different cavity sizes, high melting points, large numbers of donor groups, low solubility, high chemical and thermal stability.^[111] The most commonly used calixarene is *p*-*t*-butylcalix[4]arene which is composed of 4 *p*-*t*-

butylphenol moieties joined in the 2 and 6 sites by methylene.^[112] Both rims, the phenolic and aromatic ring, can be functionalized or modified with varying degrees to obtain a specific receptor, which in turn allows to complex certain cations or molecular species selectively.^[111, 112] Calixarenes have therefore been extensively used to transduce water-borne species. The response to analyte binding can be expressed by changes in colour ('chromoionophores'), fluorescence, or electrical potential.^[112]

One example of calixarene, which has been used in our project, is *p*-*tert*-butylcalix[4]arene phosphine oxide that selectively complexes calcium ions (Ca^{2+}) in its central cavity, as described by McKittrick *et al.*^[113] They used it with a PVC membrane-based electrochemical transducer (ion selective electrodes (ISE)) to sense water-borne Ca^{2+} . They found the equilibrium constants ($K_{I,J}$) (namely, the equilibrium constants for target cation vs. co-cation binding to the ionophore) and co-cation concentrations, which can be extracted from the logarithm for selectivity coefficients ($\log K_{I,J}$), is 1 for Ca^{2+} whereas for Na^+ is 0.0063. In other words, the ionophore binds to Ca^{2+} 158 times stronger than to Na^+ . Although they did not explicitly quote a limit of detection, Fig. 1 in their report suggests it is down to μM with near-Nernstian characteristics.

The work on ion-selective WGTFTs presented above also used calixarenes as ionophores, embedded in plasticized PVC membranes. However, the preparation of the PVC membrane is cumbersome and slow, and its incorporation into the TFT architecture is not always straightforward. In Chapter 6 of this thesis, I demonstrate a simpler way to incorporate a calcium-selective calix[4]arene into an OTFT architecture to give a novel ion-sensitive WGTFT. More details of this are in Chapter 6.

2 Thin Film Transistor (TFT) Fabrication

This chapter describes the fabrication of organic and inorganic thin film transistors (TFT). It is important to mention here that the TFT configuration used in this thesis is Top-Gate Bottom-Contacts Transistor. This chapter is divided into three sections. The first section (2.1) focuses on the process of cutting and cleaning glass substrates. The second section (2.2) consists of a description of deposition techniques used to create TFT contacts, which include thermal evaporation and inkjet printing methods. The third section (2.3) will explain the deposition techniques used to produce the thin film of organic and inorganic semiconductors, which are spin coating and spray pyrolysis.

2.1 Supporting Substrates

All supporting substrates in this work were sourced from Ossila Ltd, Sheffield, UK. Three types of supporting substrates have been used. The first type is ultra-flat glass substrates with a roughness of around 1nm and a size of 20 mm x 15 mm and thickness of 1.1 mm. They are already covered by 20 nm SiO₂ of synthetic quartz (silica). These substrates come with small squares of the transparent conductor indium tin oxide (ITO) in the corners of the substrates to assist identifying the SiO₂ coated side. The second type is crystalline highly doped p-type Si wafers with 300 nm thickness of thermal deposited oxide. This wafer is already cut into rectangles with a size of 2 cm x 1.5 cm. For the third type, sometimes I used microscope slides as substrates instead, which are made of soda lime glass.

2.1.1 Substrate Cutting

Microscope slides have a thickness of 1.1 mm and a size of 75mm x25mm. These substrates were cut into size of 20 mm x 15 mm using a diamond-tipped glass cutter. The cutter carefully scratched the substrates deeply from the end of one side towards the end of the other side. Then, the substrates were broken over an edge along the ruled scratch. Finally, the samples were puffed with dry nitrogen in order to remove any remaining cracks from the scratching.

2.1.2 Substrate Cleaning

In order to avoid any side effects resulting from uncleaned substrates within the deposition process or after the deposition process such as hindering the adhesion of subsequent layers, preventing the formation of crystalline film, obtaining devices with high off current, or even non-working devices, substrates must be cleaned before any further processing. Organic residuals and fingerprint on glass substrates have been removed by using a number of organic solvents with sonication in several steps. As a first step, all substrates were cleaned with acetone and a woven fibre wipe and dried using dry nitrogen. Acetone is a de-greasing agent, which is usually used to remove fatty residues. Secondly, substrates were held in a Teflon holder, which is designed to hold substrates with a size of 20 mm x 15 mm, ensuring that both sides of the substrate will be cleaned without touching each other, Fig. 2-1. The substrates then were immersed into a cleaned Petri dish filled with 1:100 diluted Hellmanex alkaline cleaning solution. Then they were placed in a sonic bath for 5 minutes at 60 °C. After that, the substrates were removed from the diluted Hellmanex solution and rinsed thoroughly with deionized water and dried with dry nitrogen. As a third step, dried substrates were held again in the Teflon holder and immersed into a cleaned Petri dish with Acetone solvent and placed in a sonic bath for 5 min at 60 °C. Then, the substrates were rinsed with clean Acetone and dried with the aid of dry nitrogen. The third step was repeated but with alcohol propan-2-ol (iso-propanol, IPA) instead of Acetone. All the steps in the process were carried out in a cleanroom at room temperature with clean tweezers and gloves and each substrate was kept in a clean small box.

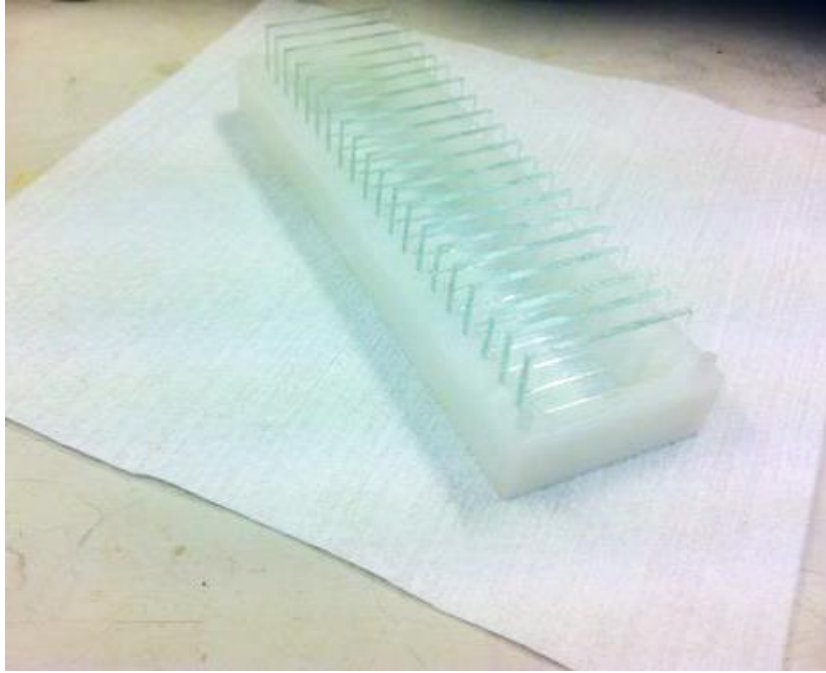


Figure 2-1: Picture of a Teflon holder used within cleaning processing.

2.1.3 Ultraviolet Light Ozone Cleaning

Ultraviolet (UV) light ozone treatment (Bioforce Nanosciences Inc., model: UV.TC.220) was also used to clean all substrates of the residual organic matter that may still have been on the surface of the substrates even after cleaning as in Section 2.1.2. In this step, the substrates were inserted into a box illuminated with 'hard' UV that generates ozone from atmospheric oxygen. The treatment time was around 4 to 5 minutes for all substrates. Ozone is a strong oxidizing agent that breaks down any remaining organic residue on the substrate surface.

2.2 Deposition Techniques for TFT Contacts

This section describes in detail the deposition techniques employed to fabricate TFT sources and drain contacts. The techniques utilized to create TFT source and drain contacts are thermal evaporation (Section 2.2.1) and inkjet printing (Section 2.2.2).

2.2.1 Thermal Evaporation Technique

Thermal evaporation is a physical vapour deposition (PVD) method that is one of the traditional micro-fabrication techniques used to deposit very thin layers of low molecular weight organic materials, inorganic materials, and metals. The basic idea of

thermal evaporation is the transfer of the solid state of materials to the vapour state under a high vacuum. The high vacuum plays an essential role in preventing any oxidation, colliding, or reaction between the evaporated molecules/atoms with ambient atmosphere or remaining gas molecules in the vacuum chamber, which in turn leads to the creation of a long mean free path of evaporated atoms/molecules toward the substrates. The relation between the mean free path and the vapor pressure is given by:^[114]

$$\lambda = \frac{k_B T}{P \pi d^2 \sqrt{2}} \quad 2 - 1$$

wherein λ is the mean free path of molecules/atoms, P denotes the vapor pressure, d is the diameter of the atoms/molecules, k_B refers to the Boltzmann constant and T denotes the absolute temperature.

The vacuum pressure usually ranges between 10^{-4} - 10^{-8} Torr using a rotary and high vacuum pump. At a pressure of 10^{-6} Torr, the mean free path, without collision, for a travelling particle with a diameter of 0.4 nm is 60 m. In our evaporation device, the distance between substrates and hot source is only around ≈ 15 cm.

Different forms of holder materials can be used to hold the evaporant, for example tungsten boats or quartz crucibles for Gold (Au) and low molecular weight materials, or tungsten coils for Chromium (Cr) and Aluminum (Al). After loading the evaporant on a suitable mount, e.g. a small wire of pure gold on a tungsten boat, the tungsten boat is connected to the heating source. By increasing the DC current that passes through the tungsten boat, the temperature of the boat will increase through Joule (i.e., resistive) heating. Increasing the temperature of the heater leads to the evaporation of atoms/molecules of gold once the vapor pressure of the evaporant is sufficiently high^[115] and then the evaporant atoms/molecules will deposit on cooler surfaces inside the evaporation chamber via a condensation process.

A quartz crystal microbalance is mounted close to the substrate at the same distance from the heating source in order to measure the deposition rate and the final thickness of the film on the substrates. A quartz crystal microbalance (QCM) consists of a thin

slice cut from a complete quartz crystal with metallic electrodes connected to a device that is programmed to determine the thickness of the deposited film on substrate. The thickness of a film can be calculated by detecting the changes of resonant frequency of the QCM once the quartz slice is exposed to the evaporant, which allows calculation of deposited mass and thickness (via the evaporant's density). The change of resonant frequency as a function of mass deposited is given by the Sauerbrey equation:^[116]

$$\Delta f = -\frac{2f_0^2}{A\sqrt{\rho_q\mu_q}}\Delta m \quad 2 - 2$$

where, Δf is the frequency changes, f_0 is the resonant frequency, ρ_q is the density of quartz (= 2.648 g/cm³), μ_q is the shear modulus of the quartz (=2.947x10¹¹ g·cm⁻¹·s⁻²), A is the exposed area of the quartz crystal, and Δm is the mass changes. The quality of the finally deposited film on substrate is affected by several factors such as the evaporation rate, the temperature of the substrate, the position of substrates towards the evaporation source, in addition to unclean substrates and the presence of the ambient gas in the evaporator device before the vacuum is established.

2.2.1.1 TFT Contacts Substrate Fabrication by Thermal Evaporation

The metal contacts of TFT substrates were deposited using an Edwards E306 Bell jar Thermal Evaporator, as seen in Fig. 2-2 (top). The preparation of the TFT source and drain contacts substrates was carried out as follows: cleaned substrates (as described in Section 2.1) were placed on steel frames (sourced from Ossila Ltd), where the SiO₂ coated side of the glass substrates must be the side exposed to the metal evaporant. Then a thin shadow mask (sourced from Ossila Code E291) with 5 contact pairs per substrate was located in front of the SiO₂ coated side of the glass substrates, Fig. 2-3. The substrates covered by shadow masks were then placed on two parallel steel pieces inside the thermal evaporator at a distance of 15 cm from the evaporation source. A magnetic piece was placed on the rear side to keep the shadow masks stable during evaporation. A pure gold (Au) wire was positioned in the middle of a small tungsten boat, which was already connected to one terminal of a heating source of the evaporator, Fig. 2-2 (bottom). Because the adhesion of gold to a glass surface is very weak, the other heating terminal of the evaporator was used to connect to the

chromium (Cr) or aluminium (Al) metal. Chromium or aluminium are used as an adhesion layer and assist the gold layer to stick strongly to the glass surfaces. After closing the jar, the vacuum system was then evacuated by pumping that allows the pressure in the jar to reach down to 10^{-7} Torr. By adjusting the current flow through the heating source, the atom/molecules start to evaporate. Inside the evaporator there is a shutter which was used as a barrier blocker to prevent evaporants from reaching the substrate until a steady evaporation rate was met, *i.e.* 0.03 Angstrom/second for Au. Then the shutter was removed and allows the Au vapours with a steady evaporation rate to deposit on substrates covered by shadow masks. A quartz crystal microbalance (QCM) continuously monitored the thickness of the deposited film. Once the required film thickness was obtained, the shutter was moved back to prevent evaporants from reaching the substrates. Finally, an adhesion layer a few nm- thick (5-7nm) of Cr was deposited first on the substrate and followed by a thin layer, 120 nm of Au, through a shadow mask, it is shown to scale in Fig. 2-4.

Gold metal has attractive properties as it is chemically inert and does not form oxide layers on its surface, which can provide a reliable smooth surface that can make good conductivity. In addition, gold is the favourite metal for hole injection when using a p-type semiconductor, as described in Chapter 1, Section 1.5.3.1.

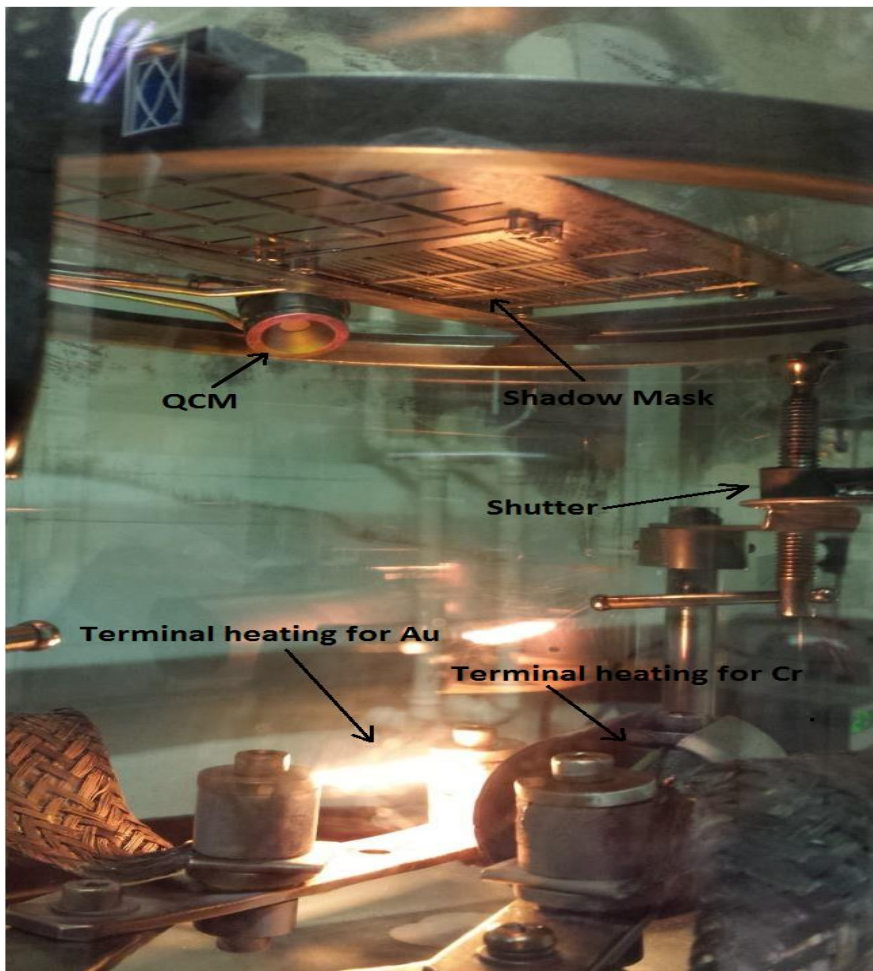


Figure 2-2: The picture of Edwards E306 Bell-jar Evaporator (top) and the configuration inside evaporator (bottom).

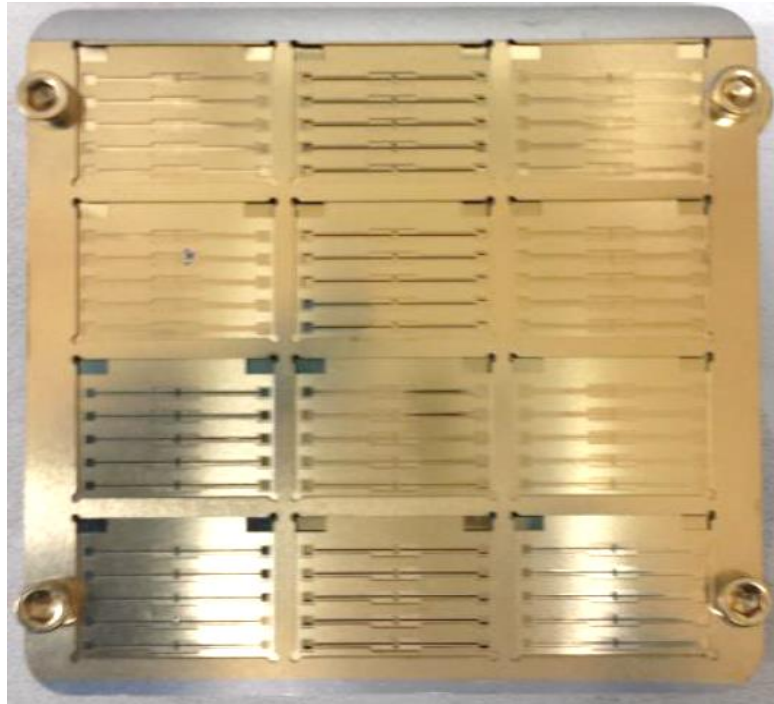


Figure 2-3: A shadow evaporation stack containing a dozen of cleaning substrates.

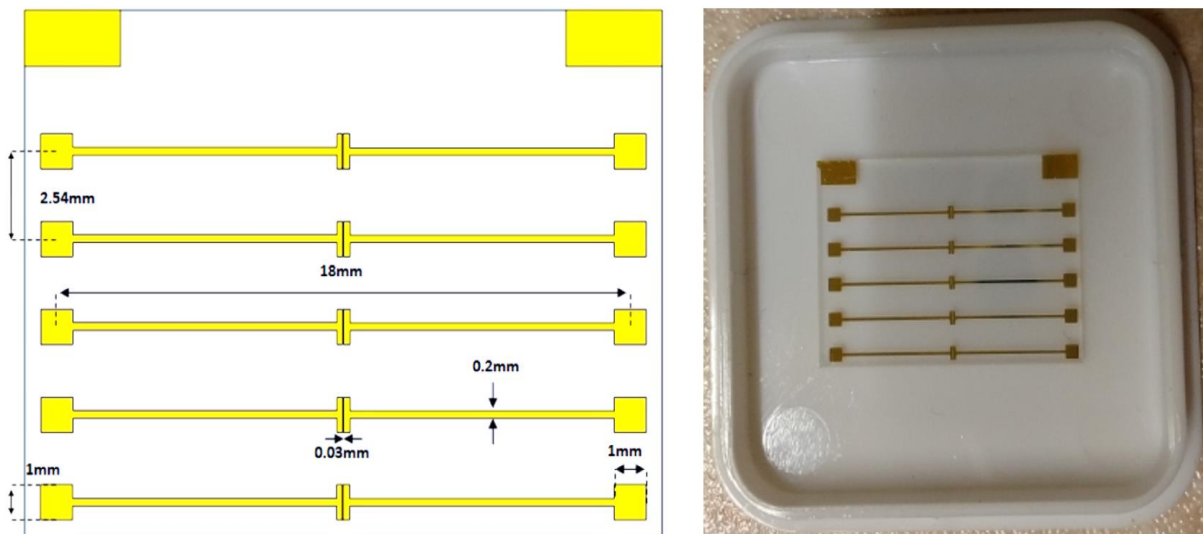


Figure 2-4: Transistor substrate geometry for S/D contacts (left) and contact substrate after deposition of Chromium and gold on amorphous SiO₂ ('Quartz') substrates, (right).

After deposition, the shadow masked 5 source and drain contacts per substrate. The contact pair geometry had a width/length (W/L) = 1 mm/30 μm = 33.3. The active area between the source and drain was linked to pads by a thin metal line ('wire') of 16.57 mm in length. We found this geometry to be excellent for electrolyte-gating.

2.2.2 Inkjet Printing Technique

Inkjet printing is an additive and non-contact method in which a very small volume of a liquid phase material, called material-laden ink, is ejected from a chamber through a nozzle and positioned precisely in well-defined structures. The deposition of droplets on a substrate can be performed using a computer control, which can be termed a 'direct-write' technique. Various functional materials and thin films with applications in electronic devices are printed using inkjet printing; examples include biosensor fabrication,^[117] printed electronics,^[118] and photovoltaics.^[119]

The generation of a droplet in inkjet printing results from a pressure pulse within an ink-containing vessel. There are two main printheads to produce the necessary pressure pulse, which are thermal inkjet printheads and piezoelectric inkjet printheads. The majority of work that seeks to print functional inks and devices has employed piezoelectric inkjet printheads, which was used to print source and drain contacts for my TFT substrates.

The operation principle of piezoelectric inkjet printheads^[120], Fig. 2-5 left, can be explained in detail as follows: the application of a short voltage pulse leads the piezoelectric actuator (PZT) to shift radially outward; therefore, a negative pressure wave is produced in the ink inside the vessel (Fig. 2-5 (right a)). This wave splits into two waves, one towards the nozzle aperture and the other towards the supply source, with half amplitude, as shown in Fig. 2-5 (right b). Upon reaching the orifice and supply source, the two pressure waves are reflected and, according to acoustic wave theory, the pressure wave that reflected from the nozzle aperture retains its phase because the orifice of the nozzle is much smaller than the cross-sectional area of the vessel which is considered as being closed side. The pressure wave that is reflected from the supply returns with a reversed phase because the inside diameter of the supply tube is significantly larger than that of the vessel, which is considered as being open side (Fig. 2-5 (right c)). The two reflected pressure waves meet in the middle of the vessel. At the same time, the voltage across the PZT declines causing the actuator to travel radially inward and produce a positive wave in the ink (Fig. 2-5 (right d)). This is a positive-pressure wave that interferes with the meeting of the reflected waves, which

leads to double the positive wave and annihilates the negative pressure wave. The double-amplitude pressure wave then approaches the nozzle end (Fig. 2-5 (right e)).

The resulting positive pressure has a sufficient magnitude to instigate deformation of the meniscus at the nozzle and produce a fluid ligament, comprising adequate kinetic energy to break away from the nozzle as a near-spherical droplet, as this minimizes surface energy.

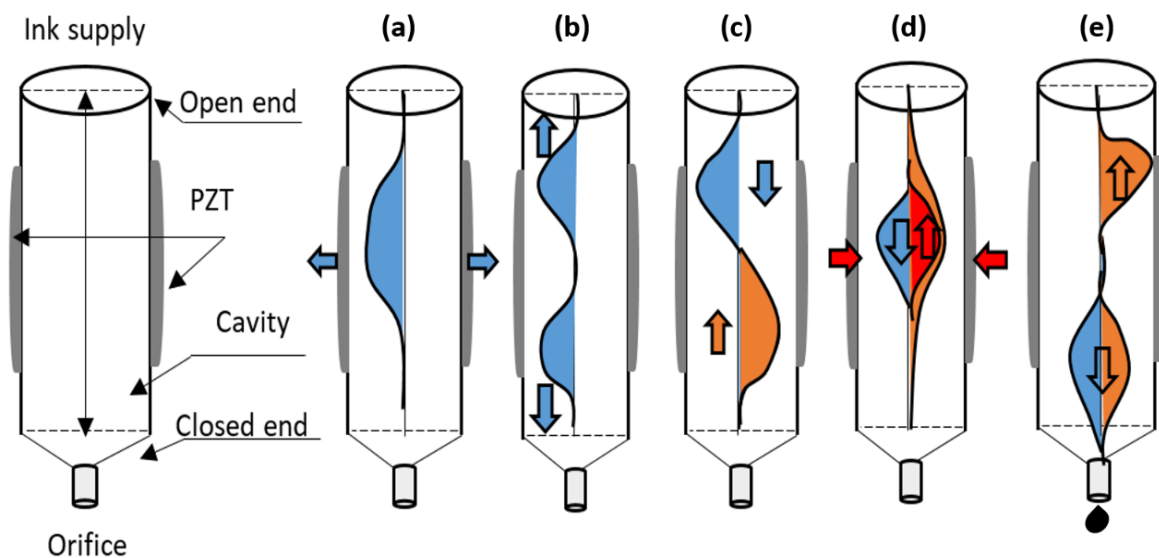


Figure 2-5: (left) Schematic diagram of a piezoelectric inkjet print head. (Right) Schematic representation of wave propagation and reflection in a piezoelectric tubular actuator.

The physical fluid properties such as viscosity and surface tension play an important role in the formation and generation of a droplet. It has been shown that inks with a viscosity value between 0.5-40 mPa.s and a surface tension between 20-70 mN.m⁻¹ are suitable for allowing droplets to be ejected.^[121] The size of the orifice through which the ink is extruded plays an important role in creating very high-resolution patterns. The orifice diameter in inkjet printing lies within the range of 10–100 μm, which yields a droplet in the range of only ~ 1–1000 pL and therefore high-resolution patterns can be formed.

There are two main types of metal-containing inks: a nanoparticle (NP) ink, in which a metal nanoparticle is suspended in solvent by ligands, and a metal-organic decomposition (MOD) ink that consists of a metal salt dissolved in a suitable solvent.

Although MOD inks have several advantages, such as the reducing of nozzle clogging, and do not require colloidal stabilizers, NP inks are usually used extensively because of higher particle loading, lower contact resistances, and commercial availability.^[120] The conductive ink most used by research groups is silver NP ink due to its lower final bulk resistivity compared to gold and copper inks. In term of price, silver ink is much cheaper than gold. Although the copper is commercially available with high conductivity and is cheaper than silver, copper' nanoparticles are oxidized spontaneously in air, which make it difficult for handling.^[120] Silver ink has been widely used in inkjet printing to produce silver conductive tracks in different type of substrates.^[122-127]

Film uniformity of printed electrodes in addition to the line width and channel length are one of the most essential elements for TFT contacts. Therefore, numerous attempts for achieving uniform and, as much as possible, narrower lines with high conductivity by employing different metal-containing inks has been effectuated by many research groups. In the inkjet printing, the production of a minimized feature, e.g. a narrower line width with a high resolution, is related to the diameter of the ejected droplet, which can be obtained by reducing the nozzle diameter,^[128] by reducing the voltage,^[129] by increasing the substrate's temperature or by heating the cartridge of the printer.^[130]

It has been shown also that the space distance (so-called space steps or droplet spacing Δx) between droplets is of importance to create a uniform track.^[122] The final track width (w) can be calculated by the given equation:^[122]

$$w^2 = \frac{\frac{\pi d^3}{6\Delta x}}{\frac{\theta}{4\sin^2\theta} - \frac{\cos\theta}{4\sin\theta}} \quad 2-3$$

where d is the droplet diameter, Δx is the droplet spacing, θ is the equilibrium contact angle formed by an ink droplet on the substrate.

When droplet is ejected from the printhead at substrate moving with speed U at frequency f , the ejected droplet will deposit with a center-to-center spacing; $\Delta x = \frac{U}{f}$. In

order to produce a uniform track, the droplet spacing must be less than a droplet's diameter in case the contact angle of the substrate is less than 90° , but for contact angles greater than 90° , the droplet spacing must be greater than twice the radius of curvature.^[122] However, if the droplet spacing is too large, the line will not form because the droplets will not overlap.^[122] Also, high frequency leads to produce bulges in the track, while low frequency separates drops from fixed U .^[122]

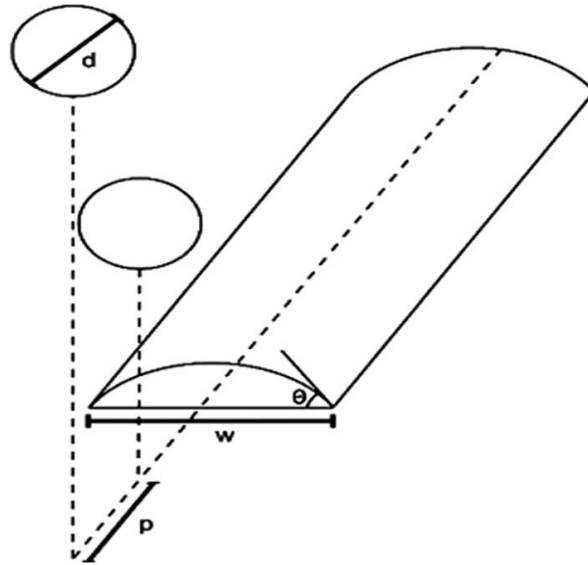


Figure 2-6: Diagram showing the parameters that are used in modelling the relationship between final track width and contact angle. w is the width of the track and $p = \Delta x$ is the spacing between each deposited droplet.^[129]

The final desired pattern can be solidified by a number of mechanisms including: solvent evaporation or chemical reaction. Often some additional processes are required, such as sintering or annealing, in furtherance of melting the metallic nanoparticles to create conducting tracks.

2.2.2.1 TFT Contacts Substrate Fabricated by Inkjet Printing

All printing of contact substrates was carried out at room temperature with clean tweezers and gloves. The conductive ink used in the experimental activity presented for printing TFT contact substrates was silver nanoparticle ink sourced from SunChemical, Slough, GB. This ink is designed for piezoelectric inkjet printing to produce conductive features on different types of substrate. It consists of a 20 wt% suspension of silver nanoparticles (with a size range of 20–50 nm) in ethanol and ethylene glycol, similar to a procedure reported by Smith *et al.*^[122, 127] Ethylene glycol

is an organic component with the formula $(\text{CH}_2\text{OH})_2$ and it is used to as a ligands to stabilize and disperse the silver nanoparticles. Also, some organic binders are usually added to the ink in order to mechanical integrity, assist the ink to adhere well the substrate and to promote the printability of the ink. The viscosity and surface tension of this ink are 12 mPa.s and 27–31 mN/m at room temperature, respectively.

Inkjet printing was performed using a JetLab 4xl printing system (Microfab, Inc., Plano, TX), as seen in Fig. 2-7, equipped with a 60 μm diameter drop-on-demand piezoelectric printhead (MJ-AT-01-60, Microfab, Inc.). A cleaned glass substrate (described in Section 2.1) with a size of 75 mm \times 25 mm was placed in a platform that can be moved along the X and Y axes while the Z axis can be modified by moving the printhead up and down (the printhead is placed above the substrate). The distance between the printhead (nozzle) and glass substrate was set at 2 mm. The patterns used in the printing source and drain electrodes are similar to the patterns produced by a shadow mask in thermal evaporation (Fig. 2-4). The data information of our pattern was inserted into the inkjet programme and determined the positions in the X and Y axes for each track and square shapes. Different shapes can be printed easily by inserting the data information into the inkjet programme. The printing frequency was set at 100 Hz, piezo actuator voltage to 60 V, and the pulse width to 10 μs . The droplet spacing for the source and drain tracks was set at 0.035 mm, which allows the droplet to be overlapped and produce uniform tracks. Finally, the printed substrates were allowed to dry at room temperature for 10 minutes and then were positioned on a hotplate at 200 $^\circ\text{C}$ for 60 minutes to eliminate the remaining carrier solvent and organic components as well as to sinter the silver nanoparticles to make good conductivity. The channel length (L) between the source and drain contacts was 40 μm and the channel width was 2mm, as seen in Fig. 2-8.

The resistance among the small pad (used for external contacting), and the ‘source’ contact to the TFT channel, was measured as $\sim 40 \Omega$. The dimensions of the printed tracks, channel length, and channel width were measured using a Nikon optical microscope (described in Chapter 3). The microscope was calibrated using a grating that had a line spacing of 10 μm . All printed substrates were kept in clean a small box to be ready for the deposition of the semiconductor.

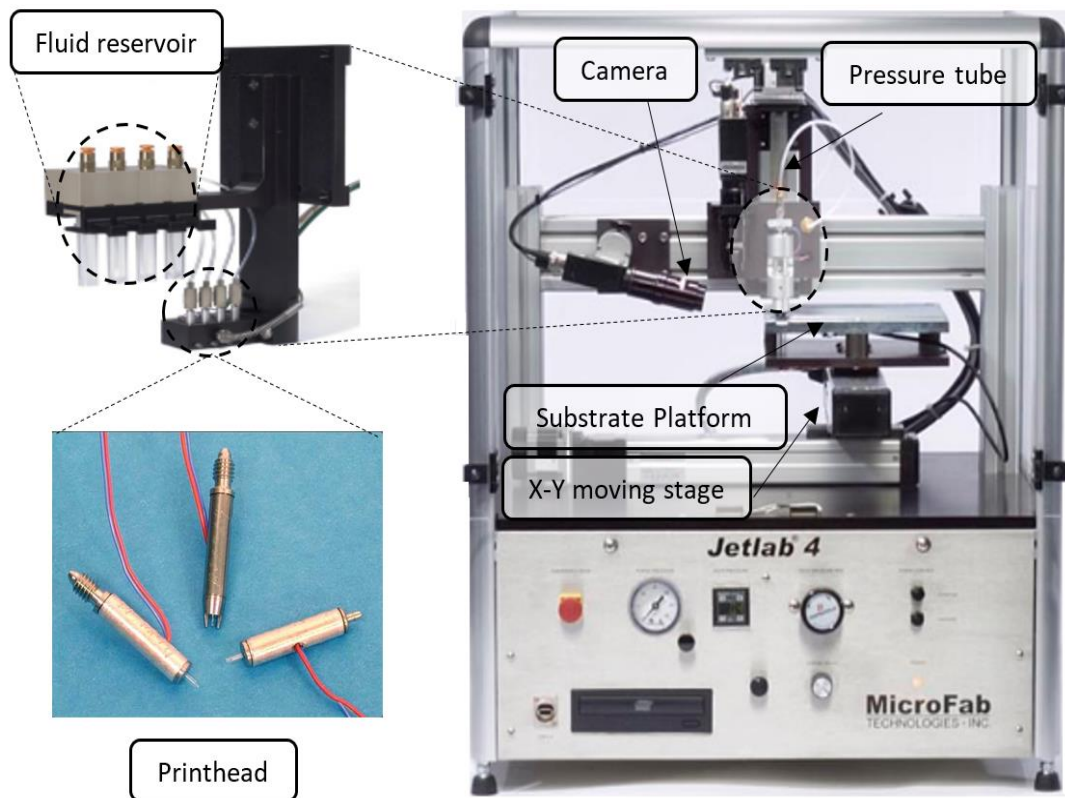


Figure 2-7: shows the JetLab 4xl inkjet printing system (right) and the fluid reservoir and printhead used in the experimental activity presented in this thesis. These pictures have been taken from microfab Technologies website.

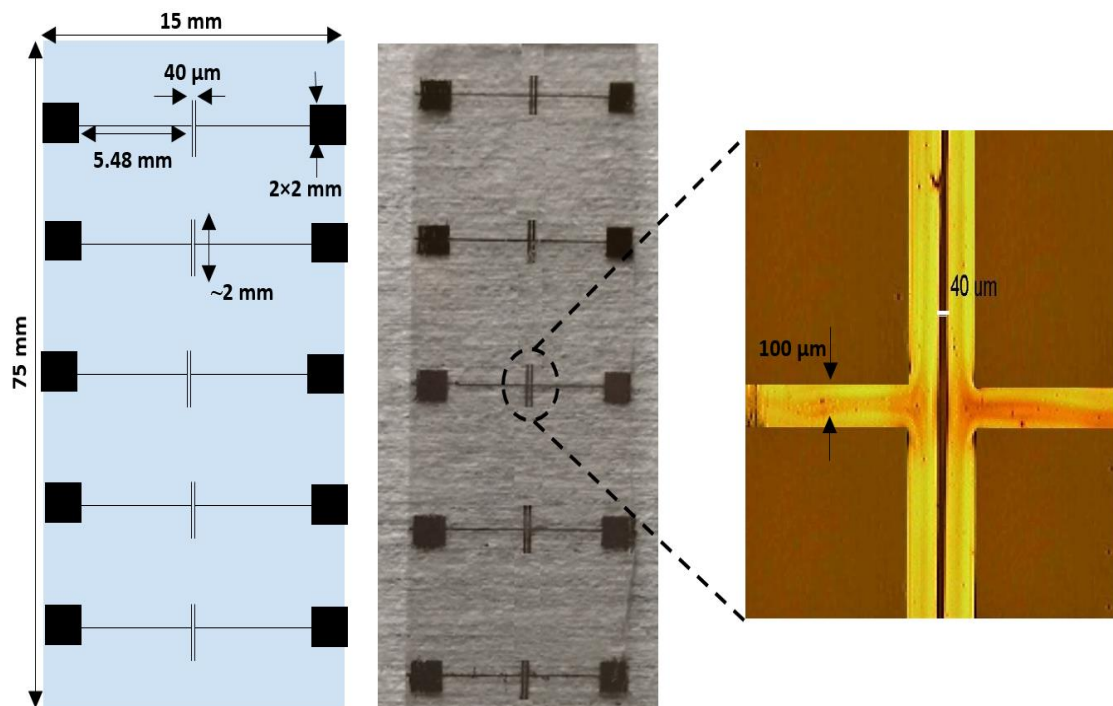


Figure 2-8: Transistor substrate geometry for S/D contacts (left) printed contact substrates (middle) and Optical micrograph of printed / fused Ag contacts; channel length $L = 40 \mu\text{m}$ and line width of $100 \mu\text{m}$ (right).

2.3 Deposition Techniques for Thin Film Semiconductors

2.3.1 Spin Coating Method

Spin coating (sometimes called spin casting) is one of the common deposition methods used for soluble materials; best results are achieved when the solute is a polymer, for example the organic semiconductor poly(3-hexyl thiophene), P3HT. Films of uniform thickness on large areas without the need for evaporators can be obtained with spin coating. Spin coating is characterized by the speed, simplicity and reproducibility of the process for batch production.

Spin coating machines, Fig. 2-9a, are usually made from *Polytetrafluoroethylene* (PTFE), called Teflon, or natural Polypropylene (NPP) which has a high resistance to all chemical attack and is easy for cleaning. Spin coaters are usually covered by a transparent lid with a small hole in the middle to allow one to lay a small droplet from a solution on the substrate that is held down on a turntable by a vacuum inside the spin-coater. In addition, dry nitrogen is always used within the spinning chamber in order to eliminate and purge the moisture and ambient oxygen while the spin coating is in process.

There are two different deposition operations: dynamic deposition, in which a small amount of solution through a small hole is applied onto the substrate while spinning is in the operating mode and static deposition, in which a small amount of solution via a hole in the lid is placed on the substrate before the onset of spinning.

The basic principle of this technique can be easily described in the following steps, as seen in Fig. 2-9b: a small drop of solution (generally a few mg of material dissolved in mL of solvent), is placed on the surface of the TFT contacts substrate that is held down on the turntable by a vacuum inside the spin-coater. Then the substrate is accelerated to the desired speed for the selected time, leading to the solution spreading out across the substrate producing a wet and uniform thin film. This method works under a centrifugal force term, in which the solution is spread across the substrate by the balance of forces that leads to impulse the solution off the surface and causes it to

adhere to the surface. During the fast spinning process, the wet thin film begins to dry because of the evaporation of the solvent, thus a uniform thin film is created.

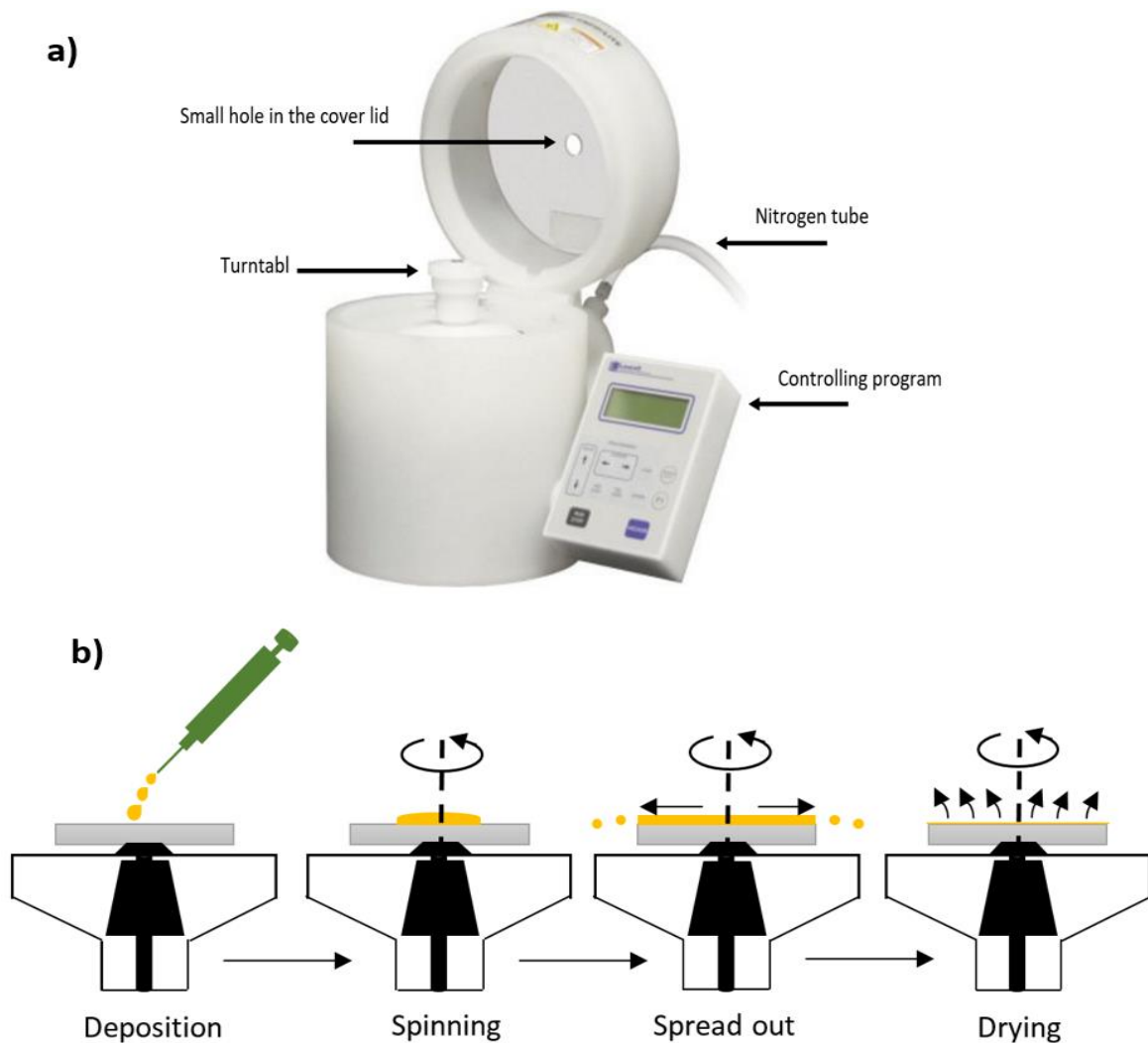


Figure 2-9: (a) shows the type of spin-coater used in my experiments . (b) the different steps of spin coating. 1) Deposition solution. 2) Start spinning. 3) Flow of fluid dominates and 4) Evaporation of solvent (drying).

The thickness of the resulting film can be calculated roughly according to following equation:^[131]

$$d \approx \left(\frac{\eta}{4\pi\rho\omega^2} \right)^{1/2} t^{-1/2} \quad 2 - 4$$

where d : is the resulting film, η is the viscosity of the solution, ρ is the solution density, and ω is the angular velocity of spinning, t is the spinning time.

It is well established that the morphology and quality (charge carrier mobility, for example) of the deposited films are strongly linked to the solvent used, since highly volatile solvents will evaporate too fast, creating a poor film, and prevent the polymer chains from ordering and crystallizing. Also, poor films can be obtained from solvents that do not wet the substrate well. Therefore, low volatility solvents (high boiling solvent) will slowly evaporate and wet the surface well creating a film with good adhesion. Also, low volatility solvents give the molecules more time to orient themselves, leading to more crystalline films, which is favourable for high carrier mobility in semiconducting polymers.

A spin-coater was used in the the present thesis to produce a thin film of organic and inorganic semiconductors. Three different semiconducting materials were employed in the experimental activities presented in this thesis. Organic semiconducting polymers include regioregular poly (3-hexyl thiophene-2,5-diyl) (rrP3HT) (sourced from Sigma Aldrich (Cat. No. 698989)) and poly(2,5-bis(3-hexadecylthiophen-2-yl)thieno[3,2-b]thiophene) (PBTTC-16) (sourced from Ossila Ltd (Order Code: M141)). Zinc acetate dihydrate [$\text{Zn}(\text{CH}_2\text{COOH})_2 \cdot 2\text{H}_2\text{O}$] (sourced from Sigma Aldrich (Cat. No. 379786)) was used as a precursor to produce an inorganic ZnO semiconductor. The concentration of the semiconducting solution for spin coating typically ranges between 5 and 20 mg of semiconducting polymer or precursor per mL solvent.

2.3.1.1 Spin Casting Organic Polymer Semiconducting

Organic polymer semiconducting rrP3HT was prepared for spin coating by dissolving 10 mg/ml in 1,2 dichlorobenzene (DCB). The vial containing the solution was placed on a hot plate at 65 °C being continuous stirred with a magnetic stirrer for 30 minutes. For organic polymer semiconducting PBTTC-16, 7 mg/ml was dissolved by stirring with a magnetic stirrer into hot DCB at 110 °C for 45 minutes. Because the rigid backbone structure of PBTTC makes it difficult to dissolve, PBTTC requires hot DCB and vigorous stirring with a magnetic stirrer. The solutions were cooled down at room temperature. Then, a polytetrafluoroethylene (PTFE) syringe filter with a size of 0.45 μm was used to filter the rrP3HT and PBTTC solutions before the spin-coating process. Because of the use of chlorinated solvents and in order to avoid any chemical

reactions between the solvent and solute, the preparation of the organic semiconducting polymers used was done under dimmed light conditions and using dark or brown glass solution vials. In fact, the *DCB* solvent was used due to the fact that it has a low vapour pressure that hugely assists to make extra ordered and close packed film in TFTs and increase the lifetime of the resulting film.^[132]

Thin films of semiconducting rrP3HT or PBTTT were obtained, as described in Section 2.3.1, by spinning a small volume of the semiconducting polymer solutions onto contact substrates that were already prepared by thermal evaporation (Section 2.2.1.1), inkjet printing (Section 2.2.2.1) or prefabricated substrates.^[89] For rrP3HT, the speed of spin coating was set at 2000 rpm for 60s, whereas for PBTTT it was set at 5000 rpm for 40s. After casting, films were dried under a dynamic vacuum at 110 or 180 °C for 40 min or 1h. The thin film transistors were now ready for electrical studies and more details are in Chapter 6.

2.3.1.2 Spin Casting Precursor Solution for ZnO

Zinc acetate dihydrate (ZnAc) was used to prepare a precursor solution for the ZnO spin-coating process. Note, the low weight of PBTTT leads to more viscous solutions due to the polymeric nature of PBTTT, and therefore to higher film thickness according to Equation 2-4, whereas, for ZnAc compensation is required by using a higher weight of ZnAc. For that reason, 21.9 mg of ZnAc (0.1 M) was used and dissolved in ethanol (EtOH) and 1:1 EtOH/acetone solvent by continuous stirring with a magnetic stirrer at 80°C for prolonged periods, until a transparent, homogenous solution was obtained. The precursor solutions were filtered with a 0.45µM filter. The ZnAc precursor solution was cast onto contact substrates (Section 2.2.1.1) using a spin coater (described in Section 2.3.1) at 2000 rpm for 50s and thermally converted into ZnO in the atmosphere on a hotplate at 450 °C for 12 minutes. ZnAc coating and conversion were repeated three times to obtain the desired thickness. The comparison between ethanol (EtOH) and 1:1 EtOH/acetone solvents and their effect on resulting films will be discussed in detail in Chapter 5, Section 5.1.

2.3.2 Spray Pyrolysis Method

Pyrolysis is a chemical treatment that decomposes organic materials by heat. Spray pyrolysis relies on a soluble precursor that, under heat, will decompose in the desired final product. Spray pyrolysis is therefore related to chemical vapour deposition (CVD), but uses a carrier solvent rather than a vacuum as the deposition medium. An important example is Zinc acetate (ZnAc) that decomposes into the II-VI semiconductor, Zinc oxide (ZnO). But note, while ZnAc is a simple and well known chemical, this route to ZnO was only discovered in 2007.^[34] The potential of a given substance to act as a precursor to a desirable pyrolysis product is not always obvious.

Spray pyrolysis is a processing method being used in research to produce thin and thick films, including dense and porous films, ceramic, and powders.^[133] Also, multi-layered films can be easily prepared using this method. Among all deposition methods, spray pyrolysis techniques have several advantages such as cost-effective processing, because it uses simple and inexpensive equipment, the potential for mass production, the potential for deposition over a large area, different substrate types with complex geometries can be coated, high-quality substrates or chemicals are not required, and the final film is characterized by homogeneity, uniformity and high quality with a thickness ranging from 0.1 to 10 micrometers.^[133, 134] This technique has been employed in solar cell production,^[135] optoelectronic devices,^[136] and field effect transistors.^[87]

The principle operation of spray pyrolysis can be performed simply by spraying a precursor solution towards a heated substrate by an atomizer, then the film will be formed. Therefore, the equipment required in the spray-pyrolysis essentially involves an atomizer, precursor solution, and a temperature controller. There are different types of the atomizer used in the spray pyrolysis technique including a compressed air atomizer, electric field atomizer, and ultrasound atomizer. The compressed air atomizer, in which the spray of precursor solution is produced via a jet of air, was used in this work as seen in Fig. 2-10.

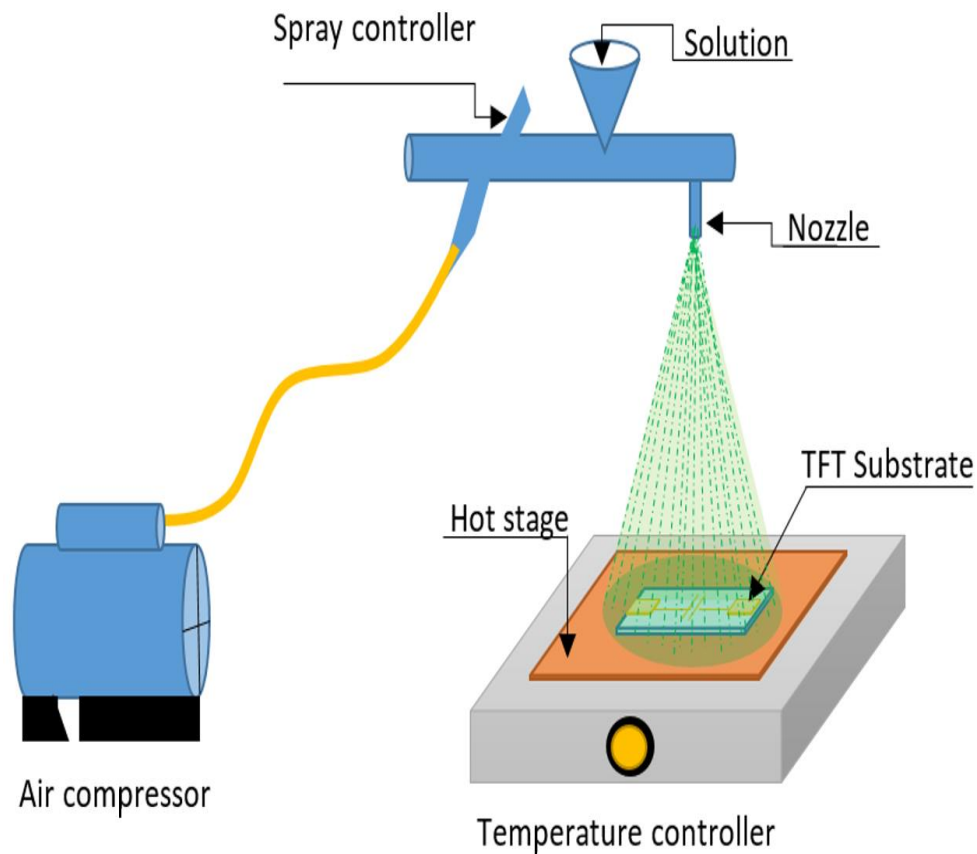


Figure 2-10: Schematic diagram of a compressed air atomizers and temperature controller.

2.3.2.1 Decomposition of Precursor and the Effect of Temperature

The droplets are transported through the ambient air with an initial velocity that is determined by the pressure air atomizer and eventually evaporated because of the solvent used. The formation of film by spray pyrolysis on a substrate results from the molecules that lose kinetic energy once they collide on a surface. These molecules spread and interact with other adsorbed molecules which leads to the formation of an island that can grow in size and consolidate, forming a continuous film with a uniform structure and undergo thermal decomposition. Different parameters control the shape and size of the structure such as substrate temperature and volume of the droplet.

There are four processes that can occur and are related to the growth of the film with increasing substrate temperature, as proposed by Viguie and Spitz.^[137] These processes are shown in Fig. 2-11.

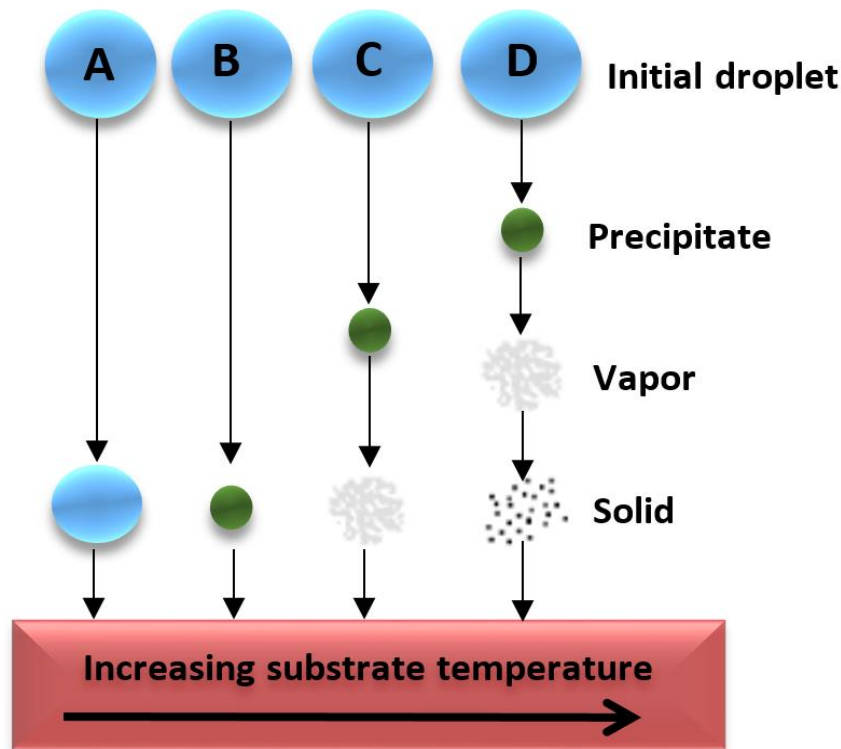


Figure 2-11: Description of the deposition mechanisms initiated for film growth with increasing substrate temperature in spray pyrolysis processing.

In the process (A) in which the temperature of substrate is low, the sprayed droplet splashes on the surface of the substrate. Then followed by vaporization causing a dry precipitate in which decomposition occurs.

In the process (B) in which the temperature of substrate is higher, the solvent completely vaporizes before the droplet reaches the surface of the substrate. Then, the precipitate imposes upon the surface where decomposition occurs.

In the process (C) in which the temperature of substrate is higher than in the process (B), the solvent completely evaporates as the droplet approaches the surface, followed by melting and vaporizing the precipitate. The vapour then diffuses to the surface, followed by decomposition. This process is known as chemical vapour deposition (CVD).

In the process (D), at the highest temperatures, the compound evaporates before it reaches the surface and the chemical reaction takes place in the vapour phase forming a homogeneous nucleation (solid particles) that deposit on the substrate

Viguie and Spitz reported that films deposited by the processes (A) and (B) possess a rougher microstructure with high adhesive to the substrate. Also, the deposited films produced from the fourth mechanism (D) would have a powdery appearance. Most spray pyrolysis depositions follow the process (A) and (B). The mechanism (C) does not occur in most spray pyrolysis depositions because of the low temperature that does not allow for the vaporization of a precursor or may result in the precipitate decomposing without melting and vaporization.^[133] However, it is believed that the deposited films showing homogeneous and smooth as well as a mirror-like appearance are probably proceeds by the third mechanism (C).^[133]

It has been demonstrated that the substrate surface temperature determines the morphology, electrical and optical properties of deposition film. For example, the film morphology can be changed from a dense to a porous microstructure by increasing the substrate temperature.^[138] Moreover, ZnO film, e.g., showed a low resistivity of 10 Ω cm when an aqueous solution of zinc acetate was deposited on a hot substrate at 490 °C whilst improving in crystallinity.^[139] Also, high transmission (90–95%) in the visible range has been showed for ZnO films deposited on a hot substrate at 420 and 490 °C.^[139] This was attributed to a high substrate temperature that leads to decrease thickness of the film as well as increase the structural homogeneity of ZnO film.^[139]

Furthermore, it has been shown that the structure and properties of a deposited film are influenced by solvent, type of solute, concentration of solute, and additives. For example, Stelzer et al.^[138] reported that the solubility of the precursors, spreading behaviour of the droplets on the substrate, and electrical conductivity of yttria-stabilized zirconia (YSZ) will change when changing the boiling point of the mixture solvent (from 50:50 vol% to 80:20 vol% of butyl carbitol and ethanol).

In a compressed air atomizer, the generation of a spray from a precursor solution requires high air pressure. The diameter of a generated droplet is decreased by increasing the air pressure. Moreover, the size of the droplet and then the density of droplets is influenced by the distance between the nozzle and the substrate surface. Also, it has been found that thermophoretic forces push the droplets away from a substrate, since the vapour molecules from the hotter area possesses higher kinetic energy than those from the cooler side which in turn causes them to rebound.^[133]

Thermophoretic forces are observed when dispersions of particles in a solvent, or aerosols, are exposed to a temperature gradient. Even if there is only one type of particle, this may experience a thermophoretic force. However, the magnitude and direction of the force may be different for different particles. Typically, this will be positive (pointing from high to low temperature) for large particles, and negative for smaller particles, and proportional to the temperature gradient. If there are several particles in a mixture, the differences in forces may lead to ‘thermophoresis’, i.e. the separation of particles in a temperature gradient. In order to cover the substrate and obtain such a film, as many droplets as possible are required to be transported into the heated substrate.^[133]

2.3.2.2 Deposition of Inorganic Semiconducting Solution by Spray Pyrolysis

As a trial-and-error attempt at an alternative precursor route to ZnO, I also sprayed 0.1 M aqueous solutions of the zinc salts: zinc chloride (ZnCl_2) and zinc sulphate (ZnSO_4) onto a TFT contact substrate (described in Section 2.2.1.1) held at various temperatures from 200 to 450 °C on a hot plate by using a pressure air atomizer at 1.5 bar pressure. I used a commercial GaGa Milano 134K airbrush with a 0.2 mm nozzle. The spraying was by 3 ‘puffs’ from a distance of 15 cm above the substrate lasting 1 ... 2 seconds in 20 s intervals. Contact substrates were then kept on the hot plate for 30 more minutes. In Chapter 5, Section 5.2, I will report that, somewhat surprisingly, some of these attempts did lead to semiconducting ZnO films.

All procedures in this thesis were performed in a cleanroom at room temperature with clean tweezers, lab glassware and gloves. Also, all chemicals and solvents employed in this thesis were used without any further treatment.

3 Experimental Methodology and Electrical Characterization

This chapter is divided into two sections: Section 3.1 describes the methods employed to characterize the morphology and electronic properties of semiconducting films that were fabricated in Chapter 2, and Section 3.2 introduces the electrical characterization (output and transfer characterizations) of thin film transistor devices.

3.1 Characterizing Thin Film Morphology and Electronic Properties

One of the most important actions before characterizing TFTs electrically is to assess the morphology of the device. This includes source and drain contacts and the semiconductor film. Results of morphological characterization assist in interpreting electrical characteristics and optimizing preparation routines. Optical microscopy, surface profilometry, scanning electron microscopy (SEM), UV spectrophotometer, and X-ray photoelectron spectroscopy (XPS) were used. However, not all the above methods were used with each sample.

3.1.1 Optical Microscopy

Optical microscopy is used routinely to ensure high quality contact substrates that fabricated by thermal evaporation (Section 2.2.1.1) and inkjet printing (Section 2.2.2.1), and to detect any problem with TFT contact substrates. A conventional Nikon optical microscope, Fig. 3-1, which has the ability to zoom up to 100x magnification was used to identify the best TFT contact substrates. This microscope is characterized by working in either reflection or transmission mode (lighting from above or below, respectively); reflection mode e.g. allows one to recognize a layer of Cr underneath the Au layer; (mis)alignment and shorts between source and drain can be spotted in either mode. Shorts may arise when evaporants are not placed correctly toward the supporting glass substrates during shadow mask evaporation. Moreover, the microscope was calibrated using a grating that had a line spacing of 10 μm in order to measure the channel length and width of the transistor's contacts.

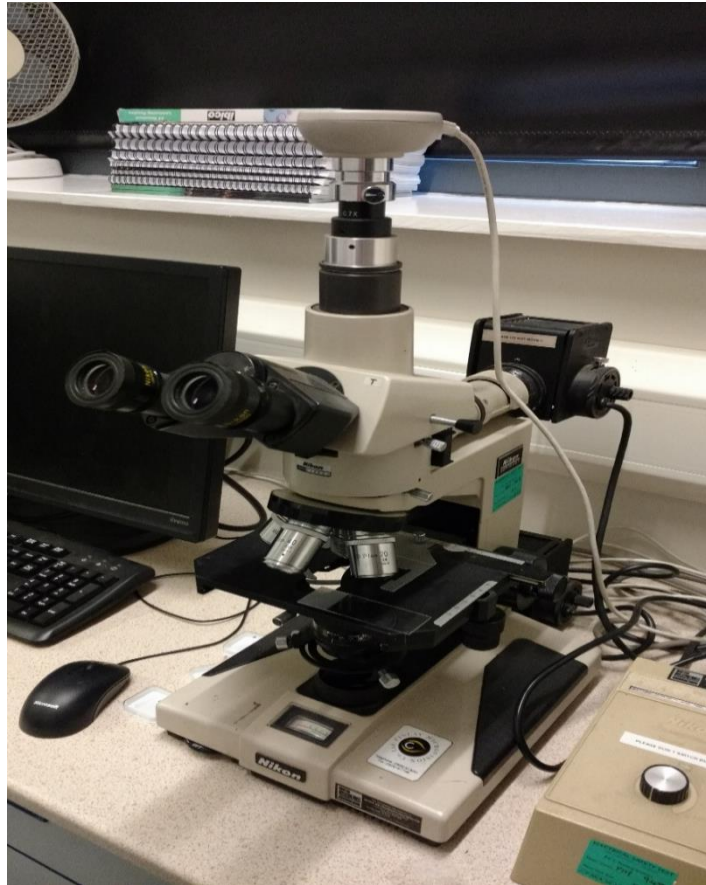


Figure 3-1: Picture of Nikon optical microscope.

3.1.2 Surface Profilometry

A surface profilometer is a common measuring instrument employed to quantify a surface's roughness by measuring a surface's profile. In addition, profilometry can be used to measure the thickness of deposited films. There are two types of surface profilometers: contact profilometers and non-contact profilometers, called optical profilometers (this type will not mentioned). Veeco Dektak XT Surface contact profilometer, Fig. 3-2, was used in order to quantify the thickness of deposited semiconductors.

The fundamental principle behind this technique involves lowering a tiny tip (diamond stylus with radius ranging from 20 nm to 50 μm) vertically until it comes into contact with a sample and then scanning laterally in one direction across the sample surface for a specified distance, specified stylus force, and speed that can be programmed by PC software. According to the surface's roughness, the diamond stylus during the

scan process rebounds. Therefore, the mechanical signals of the stylus's motion on the sample surface is transferred to electrical signals by a Linear Variable Differential Transformer (LVDT) linked directly to the stylus. Surface profile is recorded and stored in a digital format. Then the results are analysed and displayed as a one-dimensional height profile with a height resolution of 1 nm.

In order to measure the thickness of a soft film deposited on a hard substrate, a sharp scalpel should be used to scratch some area on the tested film. After placing the substrate sample inside the profilometer, the stylus scans across the scratches. The depth of the scratch is equal to the thickness of the tested film.

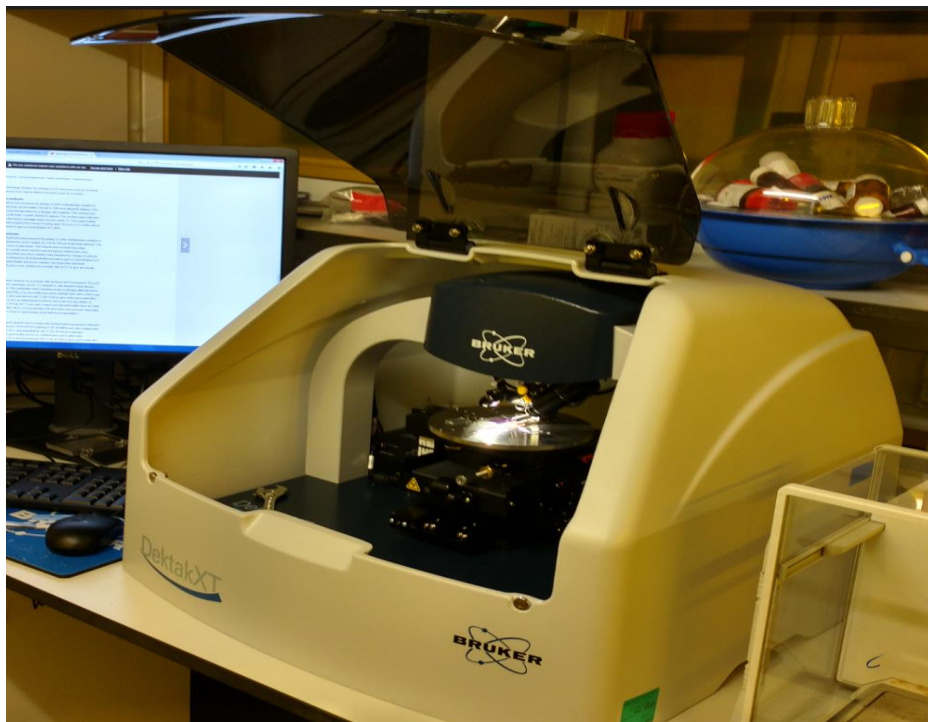


Figure 3-2: Picture of Veeco Dektak XT Surface contact profilometer.

3.1.3 Scanning Electron Microscopy (SEM)

Scanning Electron Microscopy (SEM) belongs to the extensive family of scanning microscopes. The images created by SEM result from electrons instead of light. SEM is used widely in the medical and physical science communities due to several advantages compared to light microscopy such as much higher magnification (>100,000X), which produces much higher resolution levels for closely spaced

specimens and greater depth of field up to 100 times, which allows more of a sample to be in focus at one time. The degree of magnification can be significantly controlled due to the fact that SEM uses electromagnetic lenses rather than optical lenses.

The basic principle behind this method includes generating a beam of incident electrons from a gun (e.g. thermal emission source) through an electron column, which is held within a vacuum and located above the sample chamber, Fig. 3-3. A series of electromagnetic lenses in the SEM column focus the electrons into a small beam. This focused beam is directed and positioned by scanning coils positioned near the end of the column. The incident electron beam is scanned in a raster pattern over the surface for imaging. The beam's minimum focal diameter is about 1nm. Depending on the evaluation objectives, the energy of the incident beam can be as low as 100 eV or as high as 30 keV.

Once the beam hits the sample, electrons and X-rays are ejected from the surface. These X-rays, backscattered electrons, and secondary electrons are detected by an electron detector and exhibited as brightness on a display monitor or converted into a digital image file. The electrons from the sample are emitted due to elastic and inelastic scattering events within the surface and near-surface of a sample. Backscattered electrons are high-energy electrons from an elastic collision of an incident electron typically with a sample atom's nucleus. Secondary electrons result from inelastic scattering, *i.e.* by collisions with the nucleus where substantial energy loss occurs, and have a lower energy of 50 eV or less. In standard detection mode (the most common mode), the secondary electrons provide very high-resolution images of a surface, exhibiting details of less than 1 nm in size, while, the resolution image from backscattered electrons is generally poorer than secondary electron images due to the fact that they arise from deeper positions within the sample. However, the information from backscattered electrons can be used along with the spectra from the characteristic X-rays and can furnish data about the distribution of different elements in the test specimen.

A certain level of conductivity of tested samples is required in order to use SEM since the incident electron builds up surface charges during imaging. For non-conductive

samples, a thin cover layer of conductive material should be used. Usually a sputter coater is used for producing a thin layer of gold over non-conductive material.

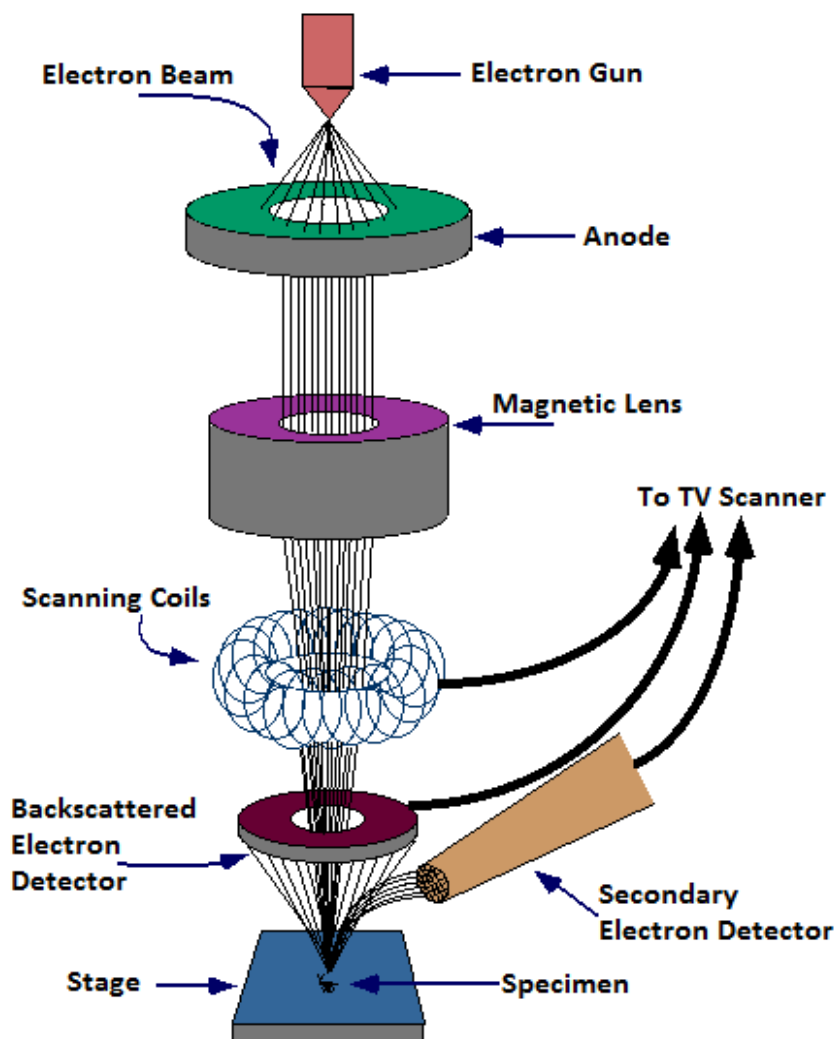


Figure 3-3: Scanning electron microscope (SEM) block diagram [\[140\]](#).

In this thesis, an SEM has been used to evaluate the surface morphology of the precursor-route ZnO prepared using different solvents in order to identify the difference between them. The energy of the incident electrons was set at 15 keV, providing magnifications from (50,000 to 85,000) and a resolution of less than 10 nm. The measurement of SEM was executed by our research partners in King Faisal University, Al-Ahsa, Saudi Arabia. The results are in Chapter 5, Section 5.1.2.2.

3.1.4 UV-Vis Spectrophotometry

In the ultraviolet-visible spectral region, many atoms and molecules undergo electronic transitions, meaning that the photons of UV and visible light have sufficient energy to induce electronic transitions between the different electronic energy levels. For instance, the energy of UV and visible can be absorbed by molecules that have π -electrons or non-bonding electrons, which in turn these electrons will transit to higher anti-bonding molecular orbitals. Also, semiconductors absorb light with photon energy larger than their band gap. Spectrophotometry is therefore an important method used to measure how much a substance absorbs light by measuring the intensity of a monochromatic light beam after it passes through a sample, while scanning the wavelength of the monochromatic beam across the optical spectrum.

Spectrophotometers are extensively used in many industries including semiconductors, laser and optical manufacturing. The most common spectrophotometers are employed in the UV (185 - 400 nm) and visible (400 - 700 nm) regions of the spectrum, and some of these spectrophotometers also operate into the near-infrared area (700 up to 1200 nm) as well. The most common samples used in a UV-Vis spectrophotometer are liquids. However, the absorbance of gases and even of solids can also be measured by UV-Vis spectrophotometer. Samples are usually located in a transparent chamber, known as a cuvette. The cuvette must be transparent for the wavelengths of interest.

A UV-Vis spectrophotometer comprises of a radiation (light) source, holders for the samples, a diffraction grating in a monochromator to distinct the different wavelengths of light, and a detector. The radiation source is often a Tungsten filament (300-2500 nm), or more recently, light emitting diodes. The detector is usually a photomultiplier tube, or a photodiode. Photodiode detectors and photomultiplier tubes are utilized with scanning monochromators, which act as a filter for the radiation and allow a single wavelength to reach the detector at one time.

There are two types of the spectrophotometer; single beam or double beam. In a single beam spectrophotometer, the intensity of the incident radiation (I_0) must be measured before measuring the sample. In this type, all of the light passes through the sample,

while in a double-beam instrument, as seen in Fig. 3-4, the radiation is split into two beams: one beam serves as a reference and the other beam passes through the sample. The intensity (I_0) of the reference beam is set as 100% Transmission (or zero absorbance).

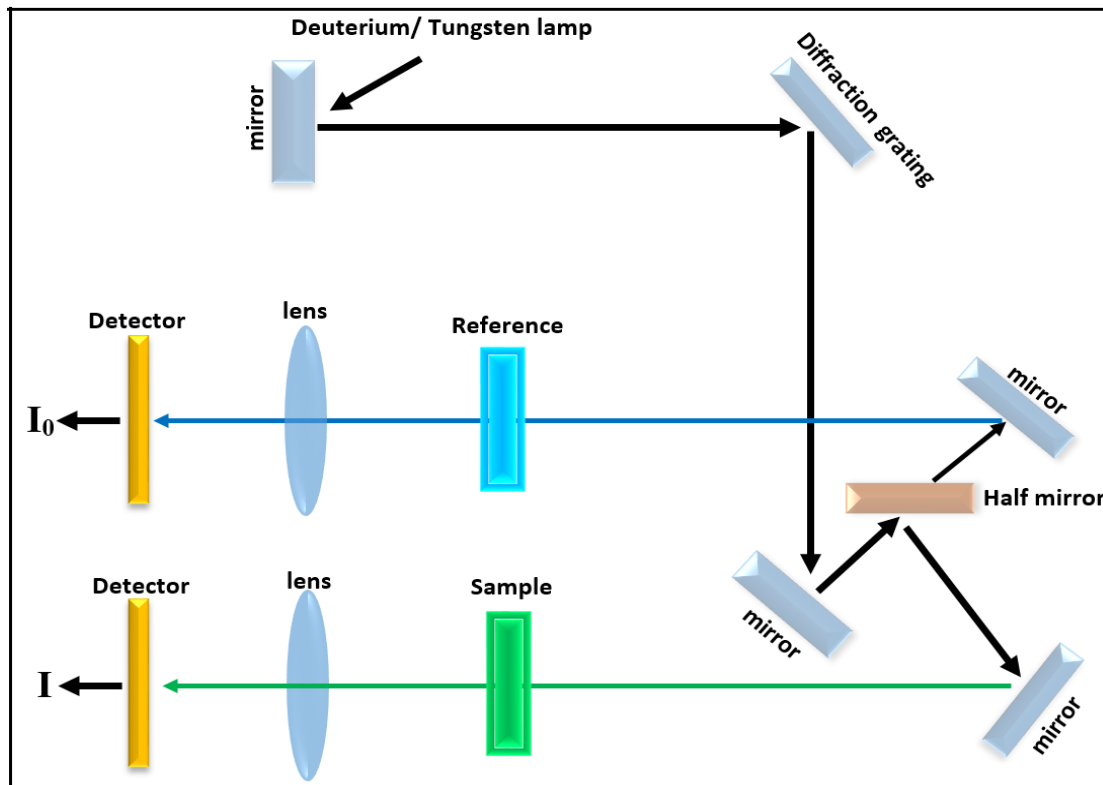


Figure 3-4: Simplified diagram of a double beam UV- visible spectrophotometer.

When the beam of light passes through or is reflected from a sample, the difference between the intensity of the incident radiation (I_0) and intensity of the transmitted radiation (I) represents the amount of light absorbed or reflected. To account for reflection, in double beam spectrometers I_0 is taken as the intensity measured in the reference path. The amount of light transmitted or absorbed is shown as either transmittance (T) or absorbance (A), as in the following equations:

$$T = \frac{I}{I_0} \text{ or } \%T = \left(\frac{I}{I_0}\right) \times 100 \quad 3 - 1$$

While the logarithm of the inverse ratio I_0 / I is known as the absorbance A :

$$A = -\log T$$

3 – 2

T and A depend on wavelength (λ), a spectrophotometer scans λ and displays and records T or A against wavelength.

The electronic and optical properties of different materials including films, optical filters, and pigments can be studied by UV-Visible transmission spectroscopy. In an optoelectronics application, the most important feature of semiconductors is the optical band gap. For instance, a large direct optical band gap corresponds to good transmission in the visible region and good absorption in the UV region.^[141] It is easy to find the optical band gap values from the absorption edge (λ_{edge}) spectra using the following equation:

$$E = \left(\frac{h \cdot c}{\lambda_{edge}} \right) \quad 3 - 3$$

where h : Planck's constant = 4.1356×10^{-15} eV. sec, c is the speed of light.

Within this thesis, a Thermo Unicam UV-500 wavelength scanning double-beam spectrophotometer, as seen in Fig. 3-5, has been used to extract the absorption edge λ_{edge} and optical band gap of ZnO that was prepared via the precursor route. This instrument has a wavelength range of 190-900nm with a resolution 1.5 nm. Spectroscopic substrates, known as 'quartz' or 'fused silica' substrates were used. These types of substrate are transparent in the UV region, which allows radiation to pass over the spectral region of interest. The results are in Chapter 5, Section 5.2.2.1.



Figure 3-5: Picture of Thermo Unicam UV-500 double-beam spectrophotometer.

3.1.5 X-ray Photoelectron Spectroscopy (XPS)

X-ray Photoelectron Spectroscopy (XPS), also known as Electron Spectroscopy for Chemical Analysis (ESCA) was developed by Kai Siegbahn in 1960. In XPS, the elements constituting the surface of the thin film and chemical state of an element can be identified,^[142] and often also at least partly the chemical bonds they have formed.

The basic principle behind this method depends on the photoelectric effect, since XPS measures the energy spectrum of electrons ejected from a surface when irradiated with X-rays, i.e. photons that far exceed the threshold frequency for electron ejection. X-rays have sufficient energy to excite and eject core electrons from atoms on the surface, as shown in Fig. 3-6. The kinetic energy of emitted core electrons then can be measured and used to determine the identity of their 'parent' atoms – electrons that are emitted from the top 1-10 nm of the sample being analysed.

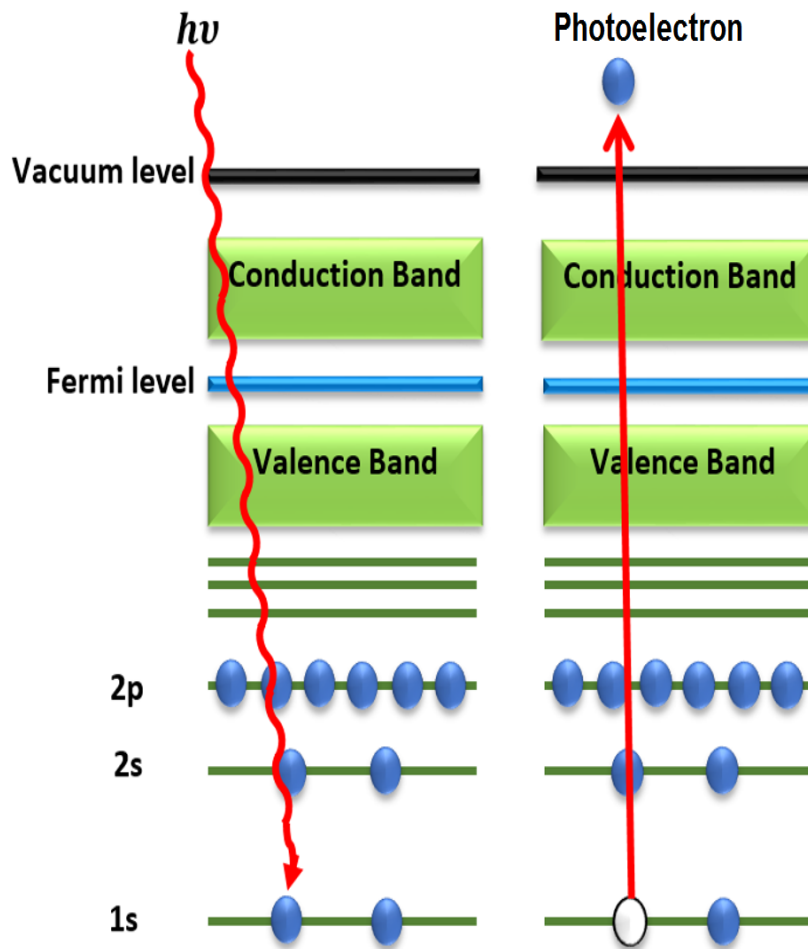


Figure 3-6: Photoelectric process to for XPS principle.

The kinetic energy (E_k) of emitted (escaped) core electrons can be calculated by the following equation:

$$E_k = h\nu - E_b - \varphi \quad 3 - 4$$

where h : Planck's constant, ν stands for an exciting radiation frequency, E_b is the binding energy of the core electronic level, and φ is the work function of the spectrometer (not the sample). By comparing measured E_b to known values taken on standard compounds, the chemical identity and relative abundance of surface atoms can be determined.^[143] For example, electrons ejected at binding energies $E_b \sim 530$ eV from the oxygen 1s (O 1s) shell, and 1020 and 1045 eV from Zinc $2p_{1/2}$ and $2p_{3/2}$ shells are the main point; a surface which displays XPS which peaks at these energies is thus likely to contain ZnO.^[144-148] More detailed conclusions can be drawn when

these peaks are recorded with high resolution, as the energy levels of inner shells undergo chemical shifts (typically less than 2 eV) depending on the chemical bonds their atom engages in. For example, the O 1s peak for oxygen shows a different chemical shift for oxygen bonded to a metal or to hydrogen. Finding these peaks concurrently in parallel with Zn 2p peaks strongly suggests a film of ZnO with –OH surface groups.

In this thesis, XPS analyses were carried out at Sheffield Surface Analysis Centre by Dr Debbie Hammond. Survey scans were collected between 1200 to 0 eV binding energy, at 160 eV pass energy and 1 eV intervals. Zn 2p, C 1s, O 1s and Zn LMM peaks with high-resolution were collected over a suitable energy range at 20 eV pass energy and 0.1 eV intervals. The binding energy scales were calibrated assuming the main C 1s peak fell at 285 ± 0.1 eV.^[149] due to the fact that the surface of ZnO always encloses graphitic carbon that is adsorbed on the surface during the exposure of the sample to ambient atmosphere.^[150] For that reason, graphitic carbon is used as a reference for ZnO XPS calibration of the binding energy scale. Also, XPS analyses for other samples were performed by our research partner, Dr Abdullah Al Naim in King Faisal University, Al-Ahsa, Saudi Arabia. The results are in the Chapter 5, Section 5.1.2.1 and Section 5.2.2.2.

3.2 Electrical Characterization of Thin Film Transistors

Within this thesis, TFTs were characterized by measuring both output and transfer characteristics, as introduced in Chapter 1, Section 1-3. More detail for the conventional TFT characterization methods that are used to determine output and transfer characteristics will be presented in Section 3.2.1. A new measurement method for monitoring and identifying the drain current in real time has been developed by our previous group. This method is characterized by repeating the measurement continuously in real time, which is useful for monitoring and identifying the presence of an analyte in real-time; more detail is in Section 3.2.2.

3.2.1 TFT Characterization with Source Measure Units

For the present studies, two Keithley 2400 source measure units, Fig.3-7(top), controlled by bespoke LabView software were employed. These units can be used to source voltage and to measure resulting current or as a current source while measuring the required voltage to drive the set current. These two programming options are called voltage source-current meter and current source-voltage meter. The former mode was used where the current is measured by applying voltages on the gate and drain electrode. The electrical connection between our TFT device and these units was through coaxial cables linking the units to two Suss microtec PH100 probe-heads fitted with contact needles. One unit was linked to the TFT drain, the other to the TFT gate, while the TFT source was grounded via a third probehead, Fig 3-7 (bottom). These two probe-head connections (drain and gate contacts) with units represent the electrical source of the TFT (drain and gate contacts), while the source contact was electrical connected to the ground.

The application of drain and gate voltages and the measurement of resulting drain and gate currents were performed using bespoke LabView software on a PC connected to the Keithley units via GPIB-PCI cables. (Note, ideally gate current should be zero in DC operation, but it is, nevertheless, measured). LabView software was programmed with two separate modes to differentiate between output and transfer characteristics, Fig. 3-8. In addition, a number of further options can be selected to obtain the required final results. For instance, the number of voltage sweeps, the value of the voltages, the step size of the voltage and delay time between the steps etc. After selecting the required options, the software drives measurement automatically, displays results and exports these results as an excel data file for detailed analysis, as will be described in the following sections.

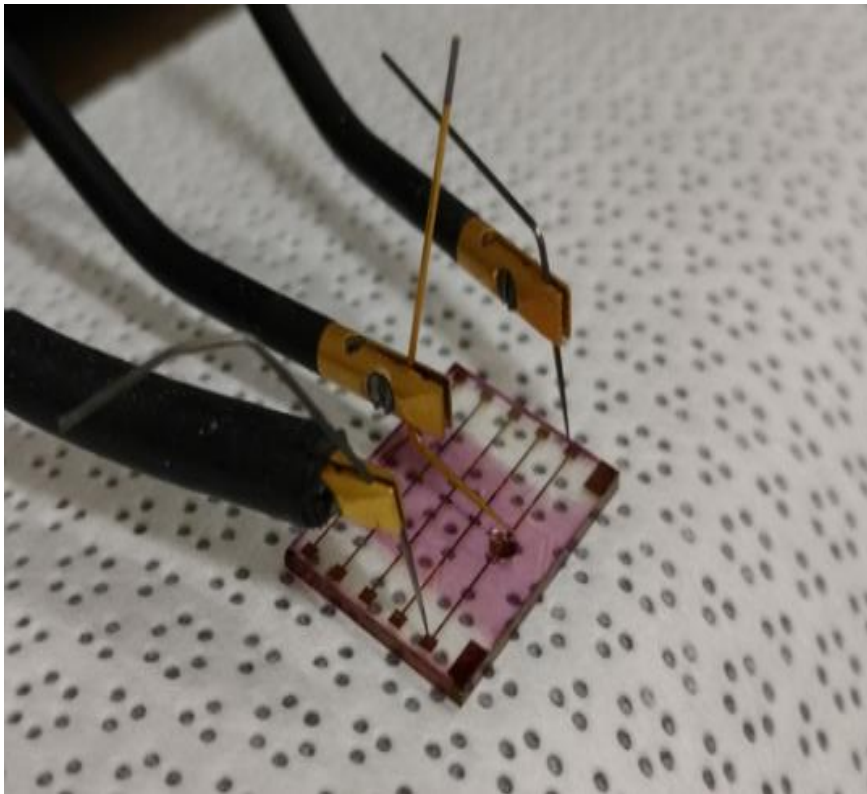
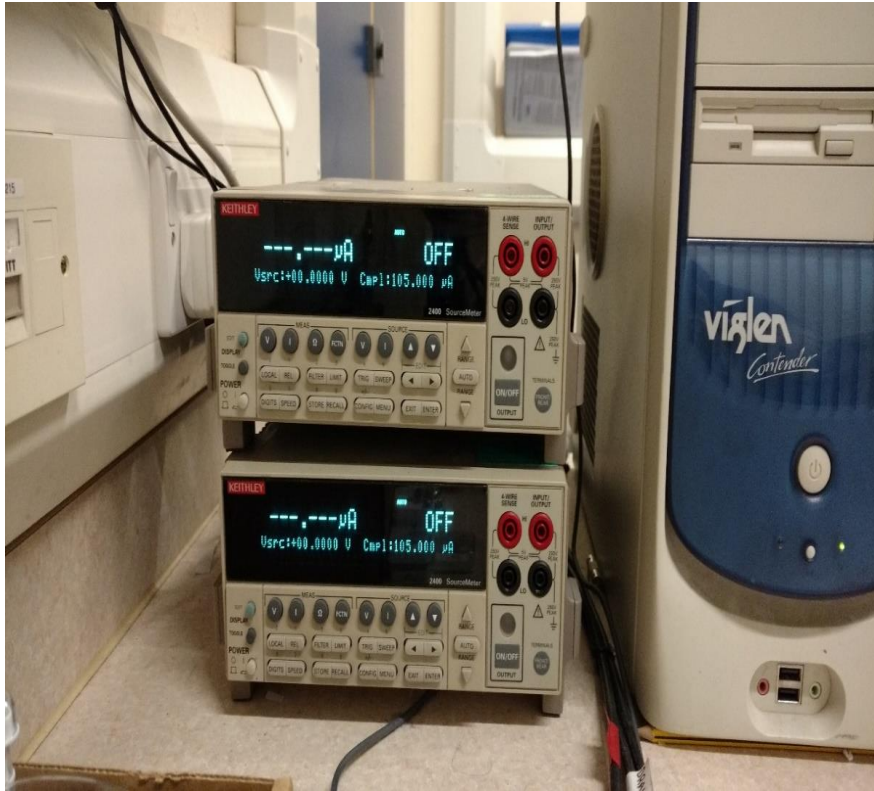


Figure 3-7: A photo of the Keithley units (top) and probe-heads (bottom). Two tungsten (W) needles are connected to drain and source contact and gold (Au) needles (gate needle) in form of L-shape overlapping the droplet that covered the active area.

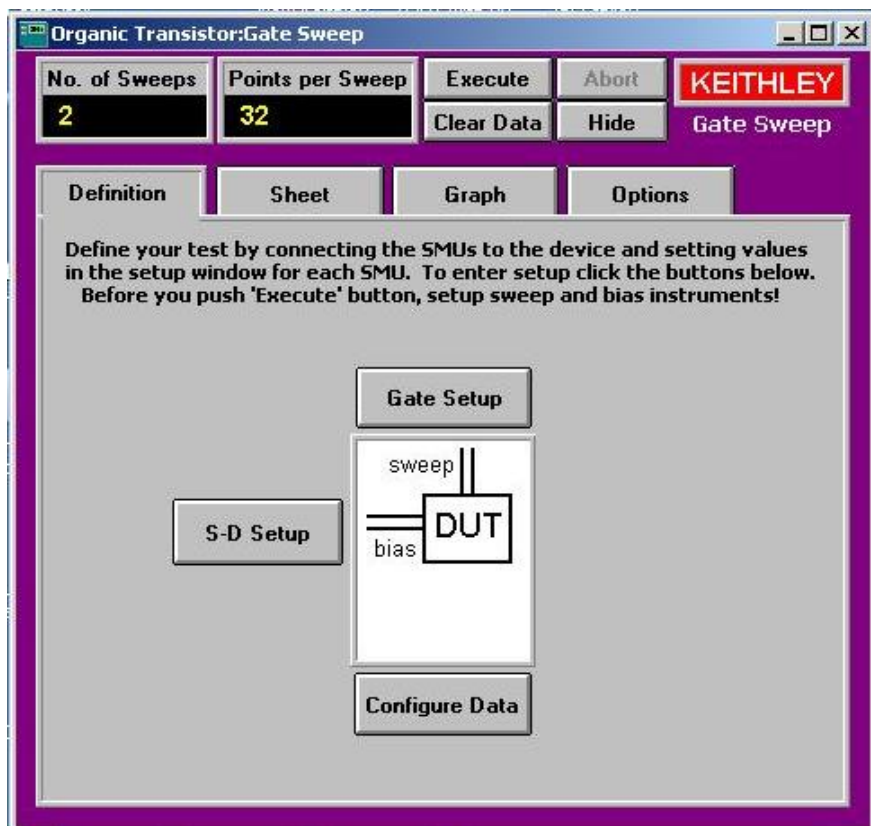
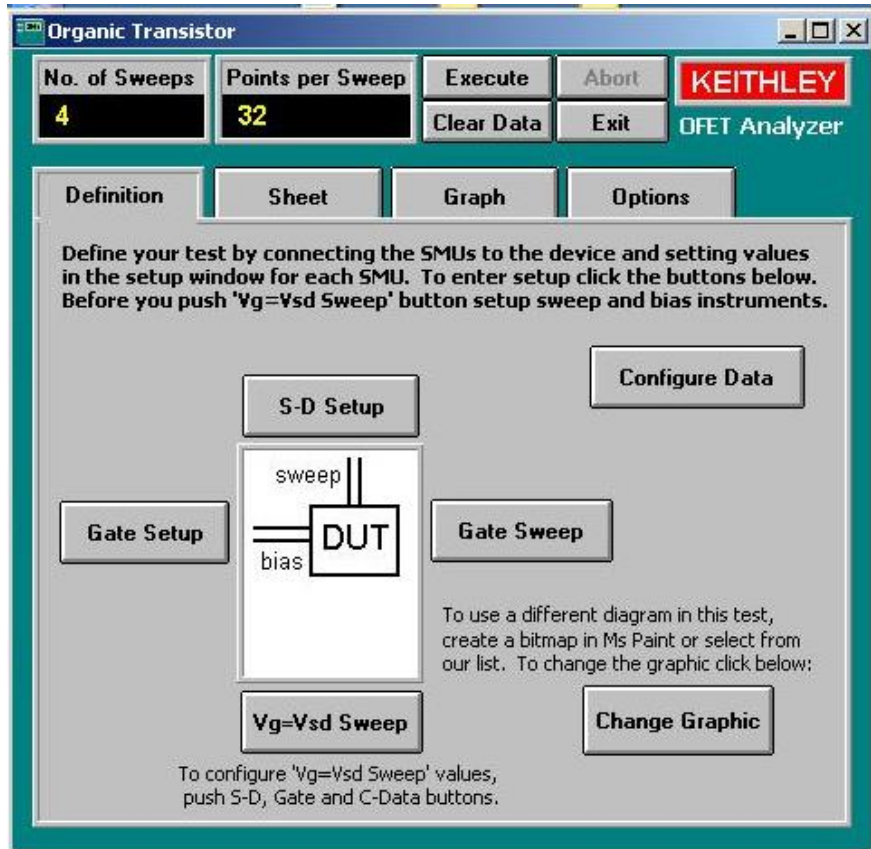


Figure 3-8: A screenshot of Labview-code of the output characteristic (Top) and transfer characteristic (Bottom).

3.2.1.1 Output Characteristics

Output characteristics are a family of drain current (I_D) versus drain voltage (V_D) plots at a fixed gate voltage (V_G). This can be done by sweeping V_D in a number of small steps starting from zero up to a maximum modulus of V_D and returning to zero in reversed steps, while gate voltage (V_G) remains fixed. Both drain and gate voltages should have opposite polarity to semiconductor carrier polarity. This procedure is repeated for a number of different V_G , which results in a family of $I_D(V_D)$ characteristics parametric in V_G , known as the TFT's output characteristics. When gating via an electrolyte, the most important consideration in the choice of experimental parameters (maximum drain and gate voltage) is the electrochemical window of an electrolyte. The electrochemical window of an electrolyte used should be taken into account when applying the voltage. For example, for water, the applied voltage should not exceed 1V.

Output characteristics are particularly useful to diagnose compliance with, or deviation from, theoretical behaviour, as presented in Chapter 1, Section 1.3. A graphic example of an output characteristic is presented in Fig. 3-9, which displays ideal behaviour, meaning it follows Equations 1-7 and 1-8 in Section 1.3, Chapter 1. At low V_D , linear behaviour ($I_D \sim V_D$) is displayed, while at high V_D , I_D saturates (no longer increases with increasing V_D).

Output characteristics are particularly useful to identify deviations of real from ideal TFT behaviour. When the value of the I_D still increases steadily in the saturated regime at high V_D , this indicates doping in the TFT's semiconductor. Doped semiconductors carry an ohmic current even at $V_G = 0V$; in an effective circuit model this can be represented by an ohmic resistor in parallel to the TFT. In addition, hysteresis (a difference between I_D measured at the same V_D while ramping V_D up vs ramping V_D down) may appear in output curves as a result of impurities in the semiconductor bulk or at the interface of the insulator and the semiconductor. Also, when the output curve particularly does not intersect the origin ($0 V_D, 0 I_D$) but the apparent I_D near $V_D = 0$ changes sign (the sooner the higher V_G) this indicates a gate current leakage, in which the current leaks across the gate medium.

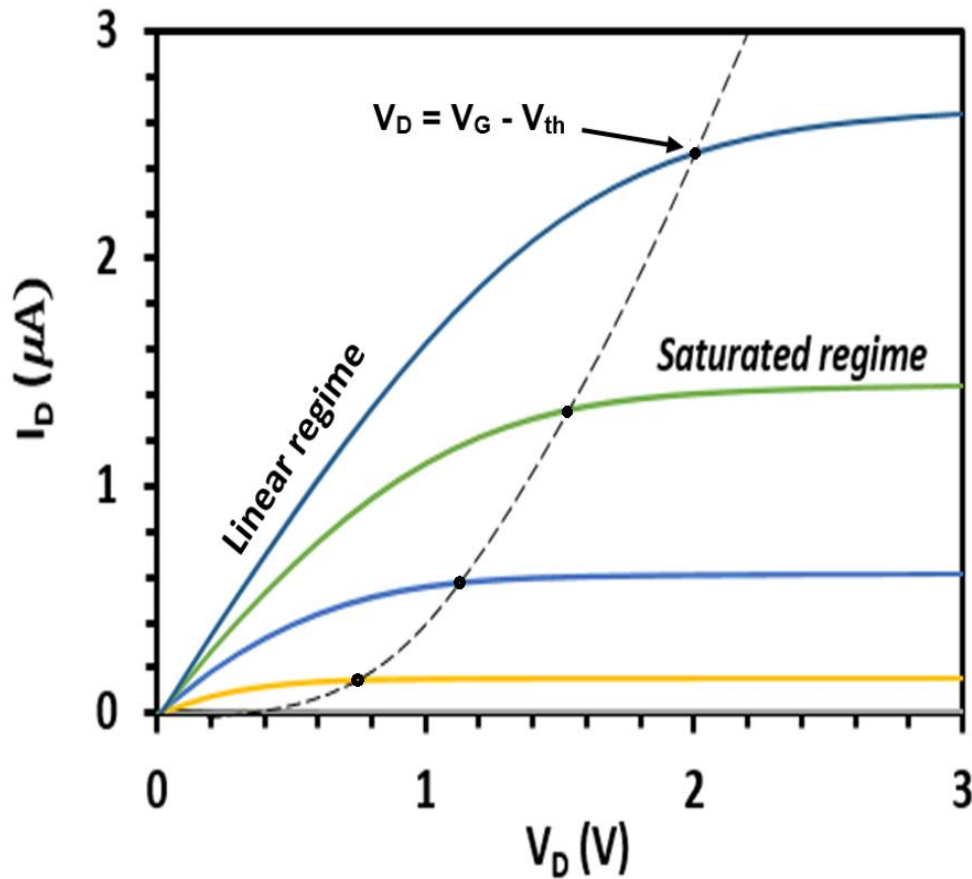


Figure 3-9: Output characteristics of an electron-transporting OTFT. Dotted and continuous line shows the point where the condition $|V_D| = |V_G - V_{th}|$ is met, TFT reaches pinch-off. Beyond pinch-off, I_D becomes independent of the applied drain voltage and begins to saturate

3.2.1.2 Transfer Characteristics

Transfer characteristics are a family of drain current (I_D) versus gate voltage (V_G) plots with a fixed drain voltage (V_D) as parameter. At a small value of drain voltage ($V_{G,max} \gg V_D$) the linear transfer characteristics are displayed, as seen in Fig. 3-10 (top) while the saturated transfer characteristic is shown when a large value of drain voltage ($V_{G,max} < V_D$) is applied. The drain current (I_D) on a saturated transfer characteristic can be plotted either on the square root scale or on a logarithmic scale, as seen in Fig. 3-10 (bottom). This is corresponding to the equations of subthreshold behaviour and saturated drain current, described in Chapter 1, Section 1.3.

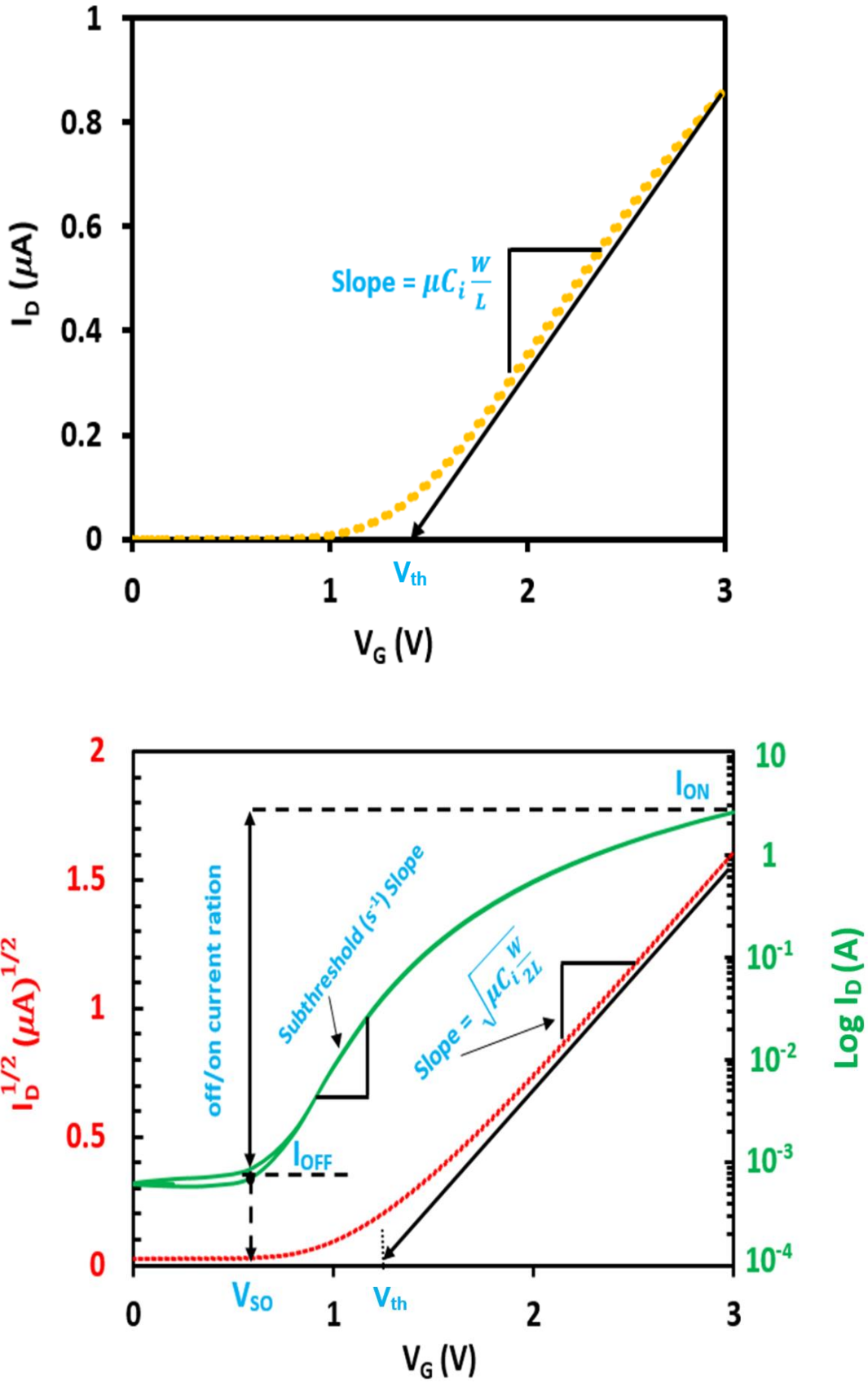


Figure 3-10: The transfer characteristics (Top) represents the linear regime, at low V_D . While, the transfer characteristics (bottom) denotes saturated regime on a logarithmic scale (green), and on a square root scale (red).

3.2.1.3 TFT Parameter Extraction

The transfer characteristics provide a more quantitative analysis where important electrical parameters can be extracted such as mobility (μ), threshold voltage (V_{th}), on/off current ratio (I_{ON}/I_{OFF}), and subthreshold voltage (S^{-1}).

1- Mobility

The efficiency of charge transport (or the rapid movement of the charge carriers through a semiconductor) is described by the mobility (μ). From Equations 1-7 and 1-8 in Chapter 1, Section 1.3, the mobility (μ) of TFTs can be expressed by:

In linear regime:

$$\mu_{lin} = \frac{L}{WC_i} \left(\frac{\partial I_D}{\partial V_G} \right) \quad 3 - 5$$

Wherein C_i denotes the specific capacitance, W is the channel width and L refers to the channel length, I_D is the drain current and V_G is the gate voltage.

In saturated regime:

$$\mu_{sat} = \frac{2L}{WC_i} \left(\frac{\partial \sqrt{I_{D,sat}}}{\partial V_G} \right)^2 \quad 3 - 6$$

If TFT geometry $\frac{W}{L}$ and the specific capacitance C_i are known, the mobility can be easily calculated from the slope of the linear transfer characteristic above the threshold (Fig. 3-10(top)) or from the slope of the $I_{Sat}^{1/2}$ vs V_G plot of the saturated transfer characteristic (Fig. 3-10 (bottom)), Equations 3-5 and 3-6 can be written as:

$$\mu_{lin} = \frac{L}{C_i W} \text{ Slope} \quad 3 - 7$$

$$\mu_{sat} = \frac{2L}{C_i W} \text{ Slope}^2 \quad 3 - 8$$

Mobility is measured in $\text{cm}^2 \text{V}^{-1} \text{s}^{-1}$. In particular, μ is often used as a figure of merit to compare the performance of several semiconductor materials. However, when electrolyte gate media are used, C_i is often not precisely known,^[35, 57] hence the evaluation of mobilities from electrolyte-gated transistors should be treated with caution when it is measured against data published in the literature. We instead prefer to use μC_i as a figure-of-merit for a semiconductor/gate medium combination, rather than quantifying mobility (property of the semiconductor) and specific capacitance (property of the gate medium) separately.

2- Threshold Voltage

There are two possible ways to extract the value of the threshold voltage (V_{th}):^[71] from linear transfer characteristics plotted on a linear I_D scale (Fig. 3-10 (top)), by linear extrapolation of drain current $I_D(V_G)$ curves to $I_D = 0$. or from saturated transfer characteristics plotted on a root I_D scale (Fig. 3-10 (bottom)) regime from a square root scale at high V_D . In either case, we fit a straight line to the characteristics at high V_D and read the threshold as the intercept of that line with the V_G axis.

3- Subthreshold Voltage and Onset Voltage

The subthreshold behaviour can be read from the transfer characteristic plotted on a $\log I_D$ vs V_G scale for V_G below the threshold. Subthreshold behaviour is usually quantified by the inverse subthreshold slope (subthreshold swing S^{-1}) that describes how many volts (or millivolts) increase is required for a tenfold increase in subthreshold drain current. Also, the onset voltage (V_{SO}) can be read from the $\log I_D$ plot, since V_{SO} is defined as the voltage where the I_D first rises with V_G .

4- On/Off Current Ratio

The ratio between highest and lowest drain current I_D represents the on/off drain current ratio, according to following equation:

$$\frac{I_{on}}{I_{off}} = \frac{I_D, (V_G = \text{max Volt})}{I_D, (V_G = 0 \text{ Volt})} \quad 3 - 9$$

From Fig. 3-10 (bottom), the $\log I_D$ plot provides a direct reading of the transistor's 'on/off ratio'.

3.2.1.4 Hysteresis

One of the most common phenomena that appeared with OTFT is hysteresis. This phenomenon can be shown in both characteristics of TFTs, and it can be shown with an open loop between upwards and downwards sweeps of I_D curves.^[151] When the values of a downwards I_D sweep's direction (the return sweep from the maximum voltage to zero) are significantly higher than the values of an upwards I_D sweep's direction, as seen in Fig 3-11, this is known as 'anticlockwise' hysteresis, otherwise as 'clockwise' hysteresis. The hysteresis effects in devices are produced as a result of the delay in the release of charge carriers from traps that are located in the interfaces between semiconductor and dielectrics as well as in the bulk of the semiconductors.^[152] Therefore, the applied voltage, either gate voltage or drain voltage, is altered in a different direction. In accordance with the IEEE standard on organic transistors^[153] we have always chosen to take the data from the upwards sweeping of voltage (*i.e.* away from zero towards the maximum magnitude).

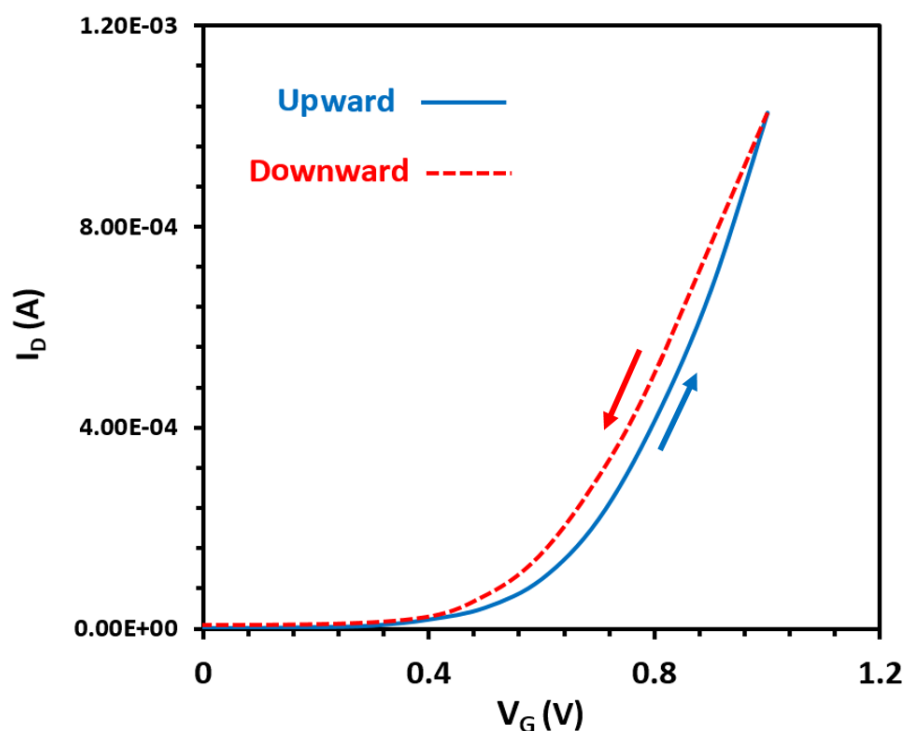


Figure 3-11: Shows an example of anticlockwise TFT hysteresis.

3.2.2 I-V Converter Method

Source measure units such as Keithley instruments, described in the previous section, depend on recording the measurement of electrical characterizations of OFTFs and later the recorded data can be analyzed. However, in order to use TFTs as sensor devices one needs to observe and read the change of analyte concentrations immediately, hence TFT saturated characteristics should be measured in real time. Such a method is called a continuous TFT characterization method that displays TFT parameters in real time. For that reason, a new circuit, called a I-V converter circuit, has been developed by prior graduates of the Sheffield TFT group (Hague *et al.*^[154]). The I-V converter concept was advanced and integrated with a LabView control and data analysis program by Dr. Dragoneas.^[155] The following sections will discuss the I-V converter circuit, the operation and the calculation of TFT parameters from the I-V converter.

3.2.2.1 Electrical Circuit and Operation

Other than in conventional characterization, the I-V converter circuit has been built up by contacting the source of the TFT with a suitable alternating drive voltage (sinusoidal voltage, $V_s(t)$) from a programmable signal generator, as seen in Fig. 3-12.

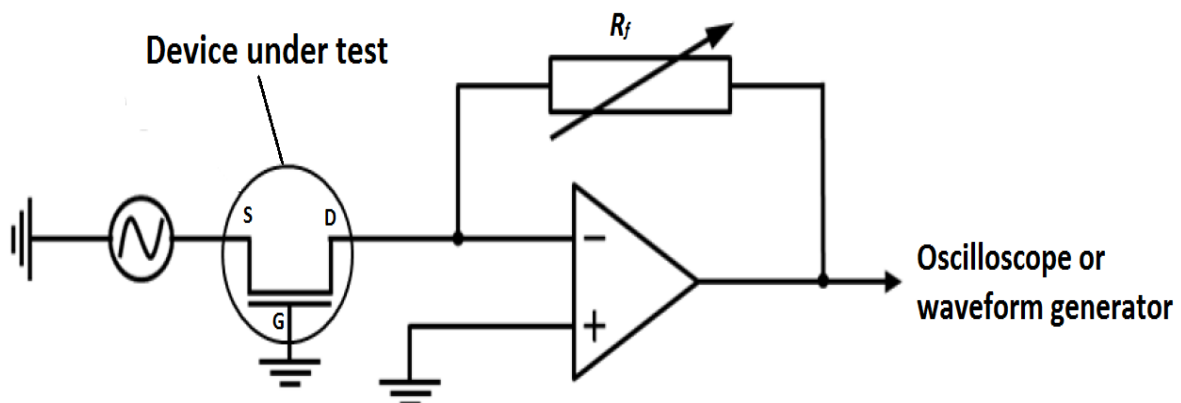


Figure 3-12: Current to voltage converter circuit diagram.

The gate of the TFT is connected to the ground and the drain is linked to the inverting input of a high input impedance operational amplifier (op-amp). The op-amp has its

non-inverting input linked to the real ground and its output is connected to its inverting input via a feedback resistor (R_f). The value of R_f can be altered by using an external resistance box. In this circuit, the current through the feedback resistor is equal in magnitude and opposite in sign to the TFT drain current. It thus cancels the TFT drain current which leads to generation of virtual ground at the inverting input. Therefore, both TFT gate and drain terminals are effectively grounded. The output voltage $V_{Out}(t)$ of the op-amp adjusts itself to precisely cancel the TFT drain current according to following equation:

$$V_{out} = -R_f \cdot I_D \quad 3 - 10$$

where I_D is the drain current of the TFT. The minus sign is due to the opposite sign of the feedback current to the drain current. Consequently, V_{out} is proportional to I_D , hence the term ‘current-to-voltage converter’ is sometimes also called ‘transimpedance amplifier’.

A positive (negative) source voltage V_S with both gate and drain (effectively) grounded is equivalent to a grounded source with both gate and drain equal and negative (positive). A hole (electron) transporting TFT will therefore turn ‘on’ and deliver saturated drain current when the source voltage is positive (negative) and its magnitude is larger than the magnitude of the threshold voltage, V_{th} . Therefore, the drain current in this equation vs. time under sinusoidal V_S drive displays a saturated transfer characteristic parametric in time. Also, Dragoneas *et al.* ^[155] later implemented a modified version of the circuit, which amplified V_{out} 10- fold; therefore, Equation 3-10 can be written as:

$$V_{out} = -10R_f \cdot I_{D,sat} \quad 3 - 11$$

The I-V converter circuit is connected to a digital oscilloscope/signal generator that connects to a PC computer through a USB connector. The signal generator is used to drive V_S , (called ‘ V_{in} ’) while the digital oscilloscope records $V_{out} \sim I_{D,sat}$. Both voltages are displayed on the PC screen, as seen in Fig. 3-13. One possible mode of

measurement is to adjust R_f so that the peak output voltage matches the input signal in magnitude. For that reason we used a dial-in 'resistance box' for R_f .

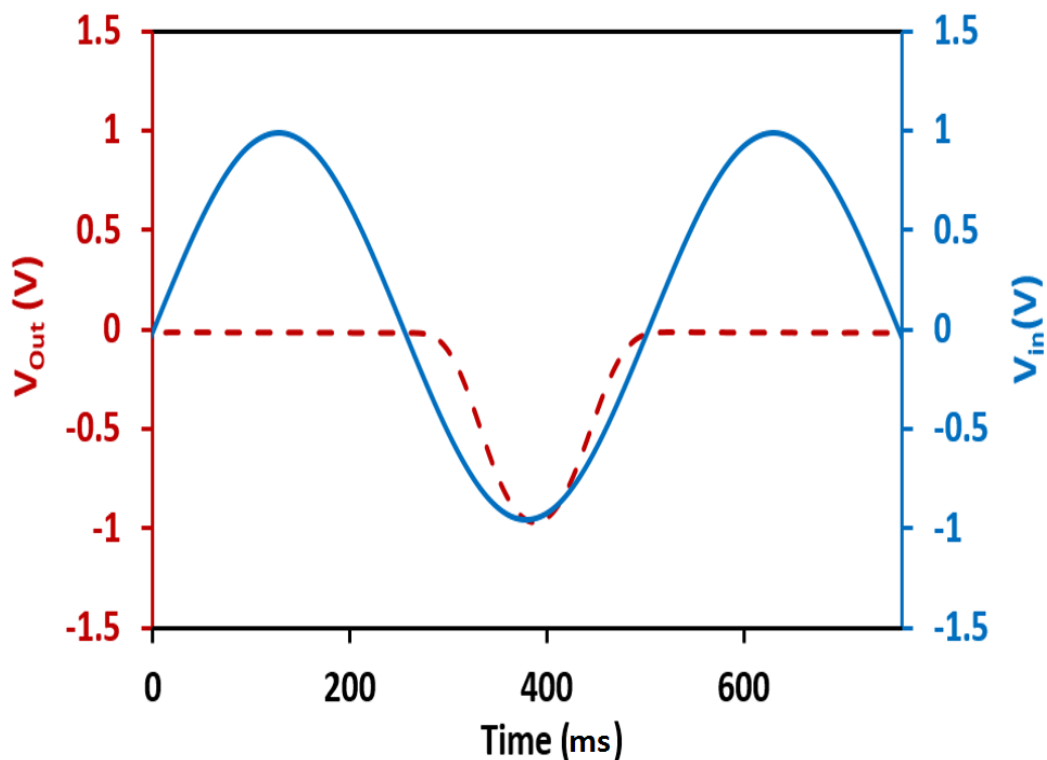


Figure 3-13: Shows saturated transfer characteristics (dashed red) parametric in time and V_s (V_{in}) applied to the source (blue) of water-gated PBTTT TFT.

Using a sinusoidal source signal reduces the bias-stress over the gate dielectric by exposing the gate medium equally to positive and negative voltage bias, with a zero average. Previous studies have shown that the threshold voltage can be affected by the gate-bias^[154] albeit this is unlikely to be an issue in liquid electrolyte gate media. Note the described measurement scheme is 'blind' to gate leakage currents, as source-gate leakage does not reach drain, and drain-gate leakage will not occur as both gate and drain are at the same potential.

This circuit offers an effective tool to characterize rapidly the changes of threshold and mobility of TFT in real time. The I-V converter shows the similar results of TFT parameters obtained by Keithley instruments, meaning that the I-V converter is a reliable alternative to source-measure unit based TFT characterization. The I-V converter is portable which means it could be employed outside labs since it could be

electrically supplied by economical batteries; more detail about this system is reported in Hague *et al.*^[154]

3.2.2.2 Consideration for Electrolyte-gated TFTs using I-V Converter

In fact, the I-V converter has been developed for dry gated TFT where no phase shift between V_{in} and V_{out} will occur at V_{in} frequency up to 100 Hz.^[154] On the other hand, for electrolyte-gated TFTs, shifting in phase appears well below 100 Hz. Shifting in phase means that the peak of V_{out} ($I_{D,sat}$) lags behind the peak of V_{in} . Such a phenomenon will affect the output taken from the I-V converter. This phenomenon results from the slow build-up of electric double layers in the electrolyte.^[57] In order to overcome such a phenomenon, the frequency should not exceed 1Hz. As we mentioned before, the input voltage ($V_s = V_{in}$) for electrolyte should not exceed the electrochemical window for the electrolytes used. In our case and the electrolyte most used was DI water so we set the drive voltage (V_{in}) between 0.5-1V, below the 1.23 V electrochemical window of water.

3.2.2.3 Calculation of Saturated Drain Current

From Fig. 3-13, TFT saturated drain current can be calculated according to following equation:

$$I_{D,Sat.} = -\frac{V_{out}}{10 \times R_f} \quad 3 - 12$$

By using this equation, Fig. 3-13 can be plotted with $I_{D,Sat}$ rather than V_{Out} , as seen in Fig. 3-14 and the saturated drain current can be read directly from the graph.

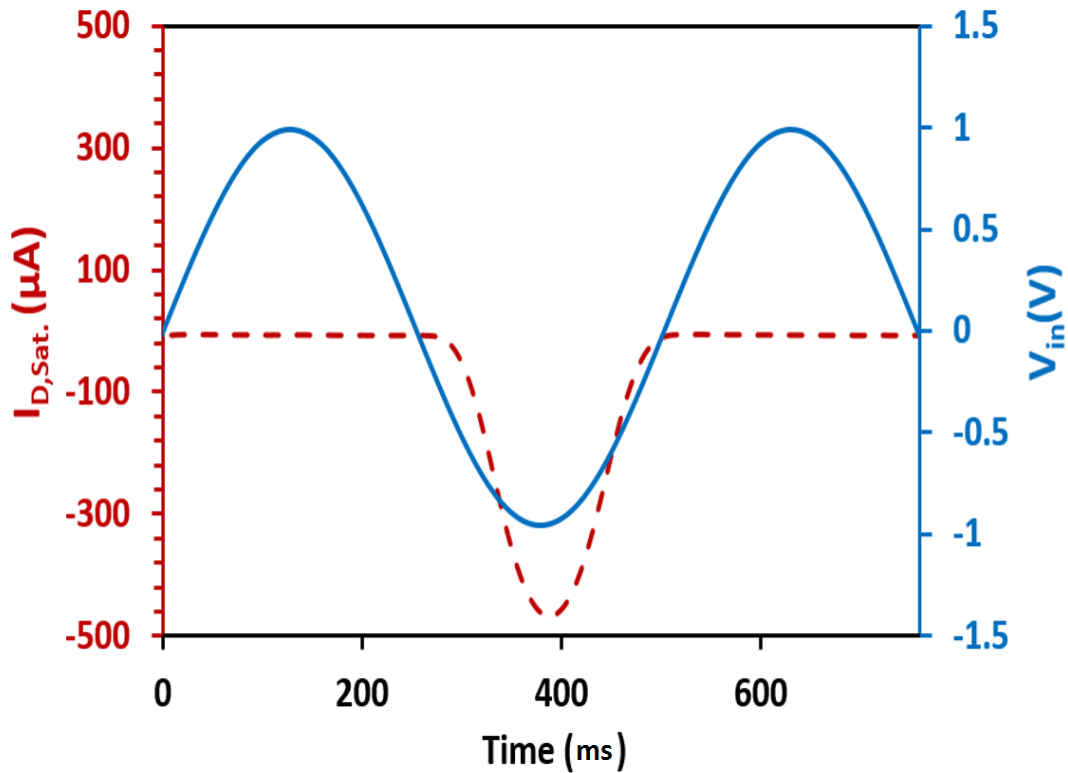


Figure 3-14: Displays saturated drain current (dashed red) parametric in time and V_{in} applied to the source (blue) of ILS-gated OTFT.

The difference between the converted saturated transfer (data from I-V converter) and the standard transfer characteristic (data from Keithley method) is related to the applied drain-voltage V_{DS} since, in a converted saturated transfer, V_{DS} has continuous value while the V_{GS} is swept with the same value as V_{DS} , meaning that $V_{DS} = V_{GS}$. In general, the transistor will always be in the saturation regime, $V_{DS} > |V_{GS} - V_T| > 0$. Therefore, as long as a 'normally off' field-effect transistor is under consideration in the study, there is no difference between the I/V converter and conventionally measured characteristics.

3.2.2.4 Calculation of Threshold Voltage and Mobility

I-V converter measurements provide two possible ways to extract mobility and the threshold voltage, which will be described in the following section.

1- Eliminating the Time from I-V Converter Measurements

By reference to Fig.3-14 that shows the saturated transfer characteristic parametric in time and so by eliminating the time parameter, the same data points in term of square root and logarithm can be plotted as seen in Fig 3-15.

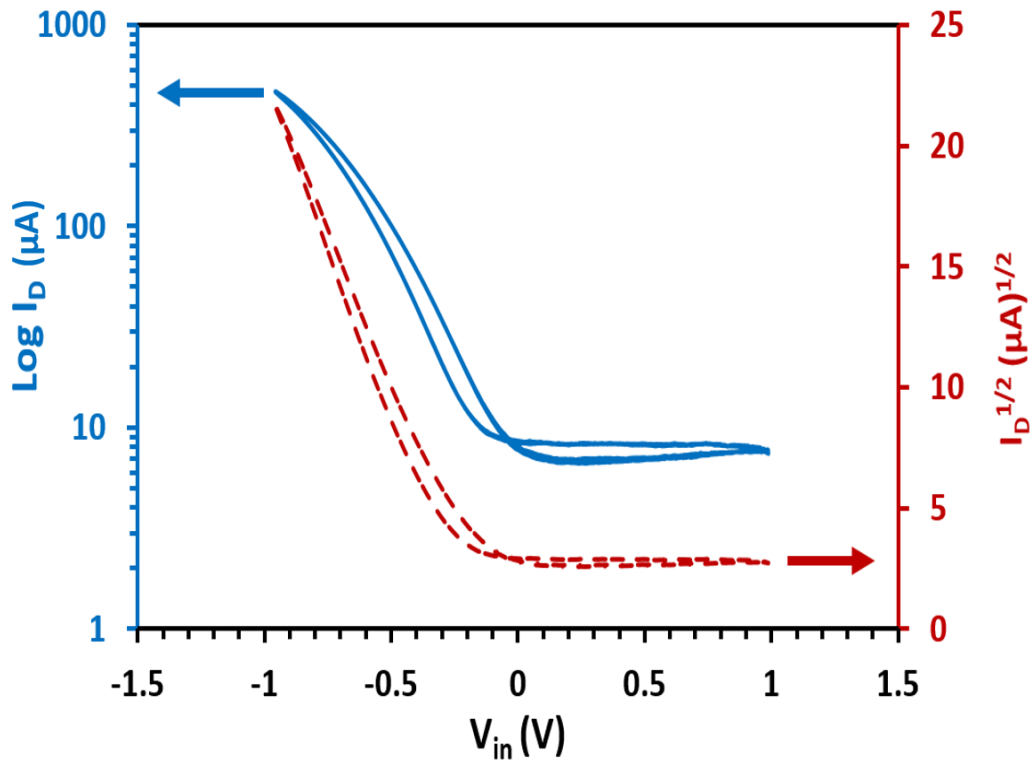


Figure 3-15: Shows saturated transfer characteristics of IL-gated PBTTT TFT on a logarithmic scale (blue), and on a square root scale (dashed red) after eliminating the time parameter.

From this figure one can easily extract the mobility and threshold voltage; as clarified earlier in Section 3.2.1.3.

2- Direct Evaluation of Parametric Characteristics

The threshold and mobility can easily be measured directly from the I-V converter data without eliminating time. In order to calculate mobility we need first to extract the threshold voltage from the I-V converter data as seen in Fig 3-16. From this figure, a straight line should be fitted to V_{out} in the rising flank and the intercept of this line at a point on the x-axis. This point faces a point in the V_{in} signal, which equals a value on

the V_{in} -axis. This value denotes the threshold voltage. After extracting the value of the threshold voltage, this value can be used to calculate the mobility:

$$\mu = \frac{1}{10R_f C_i} \times \frac{2L}{W} \times \frac{|V_{out}|}{(|V_{in}| - |V_{th}|)^2} \quad 3 - 13$$

In this equation V_{out} may have the same value as V_{in} once they are matched by adjusting feedback resistance, but Equation 3-13 is valid with or without matching.

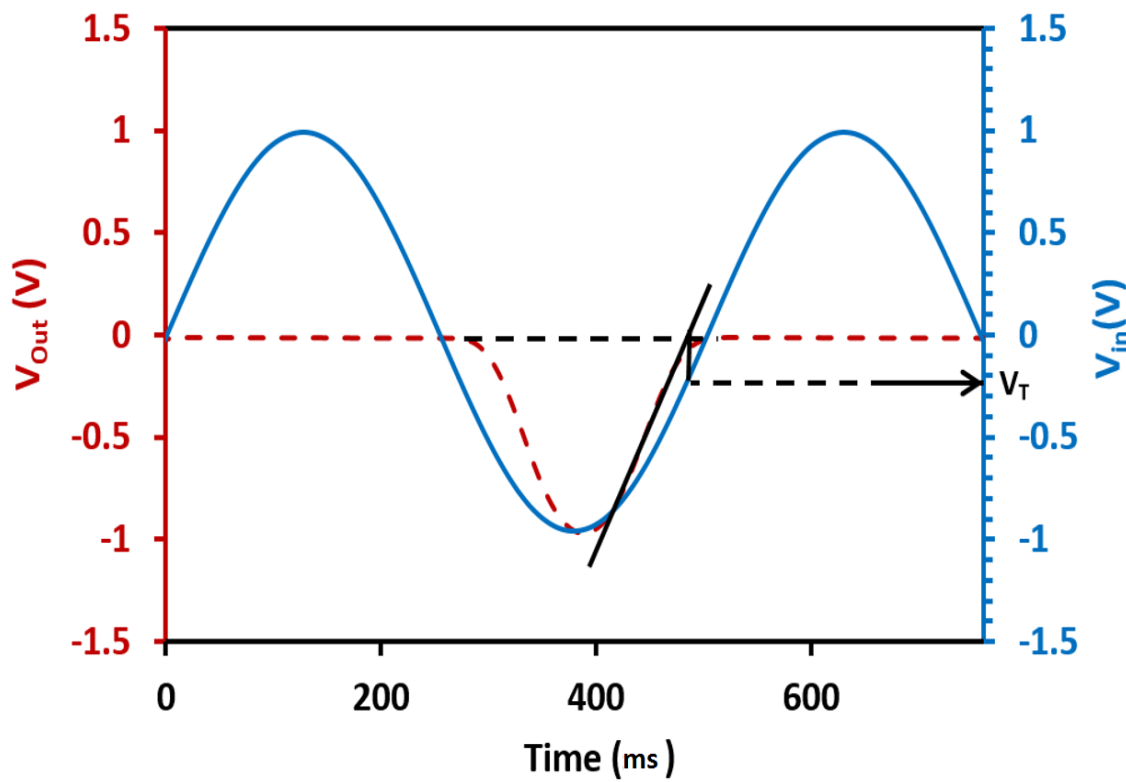


Figure 3-16: Shows IL gated PBTFT TFT and extracting threshold voltage V_{th} from Saturated transfer characteristics (dashed red) parametric in time and VS (V_{out}) applied to the source (blue).

3.2.2.5 On/off Ratio Calculation

By dividing the positive (maximum) peak of output voltage over the negative (minimum) peak of output voltage, the on/off ratio of an n -type semiconductor device can be easily calculated. Whereas, dividing the minimum peak of output voltage over

the maximum peak of output voltage gives the on/off ratio of an *p-type* semiconductor device:

$$\text{For } n\text{-type device: } \frac{I_{on}}{I_{off}} = \left| \frac{V_{out,max}}{V_{out,min}} \right| \quad 3 - 14$$

$$\text{For } p\text{-type device: } \frac{I_{on}}{I_{off}} = \left| \frac{V_{out,min}}{V_{out,max}} \right| \quad 3 - 15$$

3.2.3 Real Time TFT Measurements

The extraction of parameters automatically in real time, without evaluation from parametric saturated transfer characteristics graphs as in the previous sections, was developed by a former member of the Sheffield transistor group, Dr. Dragoneas.^[155] Dragoneas wrote a LabView program containing a number of selectable options such as the capacitance of the gate dielectric C_i , the channel's width and length, the semiconductor's type (n-type or p-type), the frequency of signal, the feedback resistance R_f , the amplitude of applied voltage V_{in} , and a shape of signal. This LabView program on a PC is connected to an I-V converter by using a Pico-scope digital oscilloscope/signal generator. The Pico-scope signal generator is connected to a TFT source; the Pico-scope's signal input channel is connected to the I/V converter's V_{out} . Furthermore, the Pico-scope is linked to a LabView program on a PC by a USB connection. The collected data are displayed in digitized form with the help of Microsoft Windows dynamic-link library. Before starting measuring, the required settings must be selected from the aforementioned options. Then, one can use the software and apply a source voltage (input voltage V_{in}) drive to the TFT. Several TFT parameters can be measured automatically and one can read them immediately from the PC display. These parameters include threshold, mobility, ratio between on and off currents. Fig. 3-17 shows an example of the user interface during TFT characterization.

This program is known as the 'I-V converter assistant' and it has been reported by Dragoneas.^[155] The I-V converter assistant is designed for a dry-gated transistor and provides a dependable independent determination of threshold voltage and mobility in

real time. For the characterization of electrolyte-gated transistors, the related settings, such as low frequency and low peak source voltage, should be determined in order to avoid phase lag and exceeding the electrochemical window.

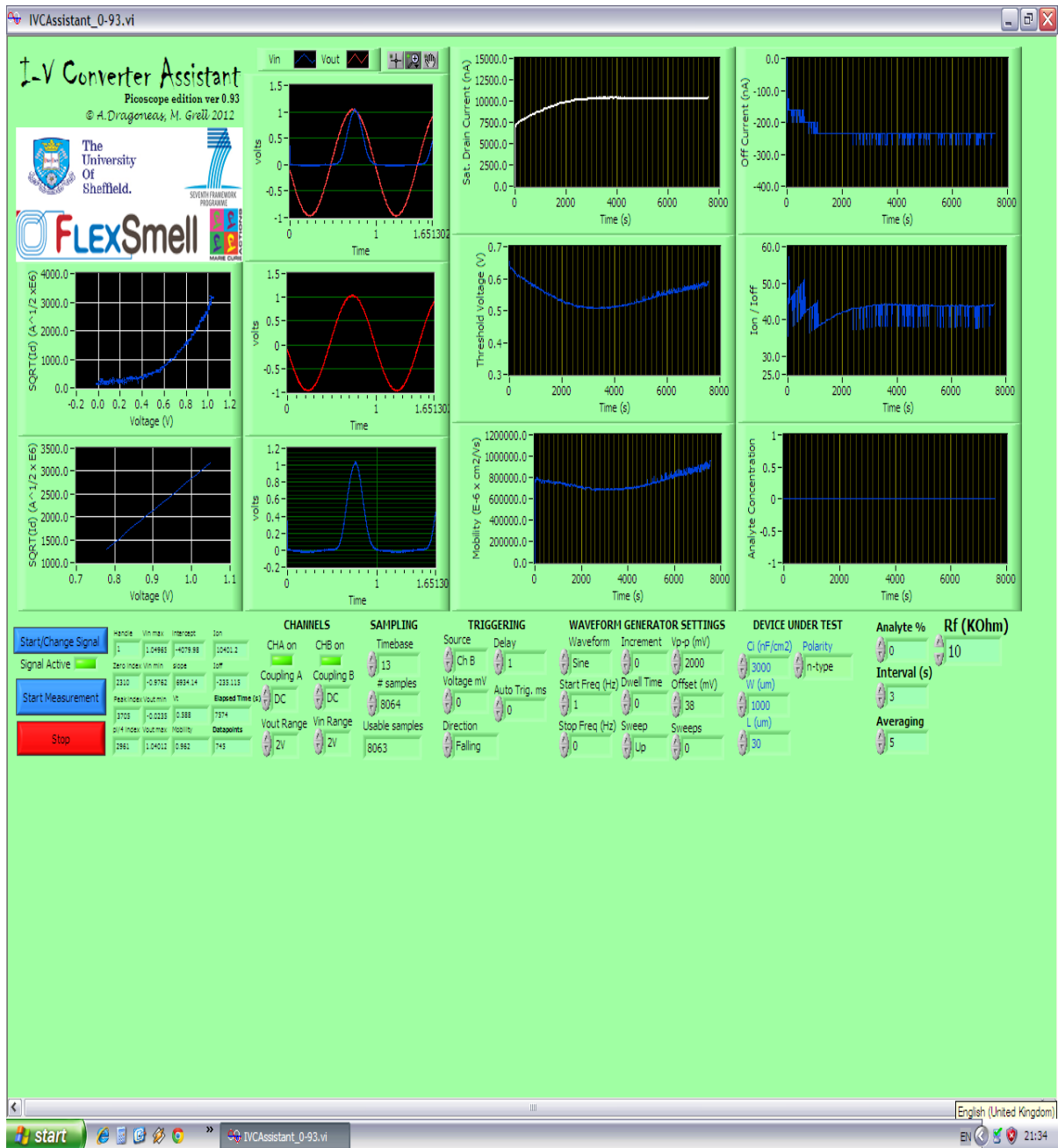


Figure 3-17: A screenshot for real- time characterisation taken from I-V converter assistant LabView program.

4 Organic Thin Film Transistor Gated with Ionic Liquid

4.1 Introduction

Organic semiconducting polymers have received huge interest because they can be processed from solutions. Also one of the driving forces nowadays is to process all device components from solutions, not just the semiconductor. However, charge carrier mobility in organic semiconductors is lower than conventional semiconductors. Such low mobility may not be enough in applications where TFTs have to supply current, e.g. to drive LEDs. This chapter reports one approach to maximize OTFT current.

As was described in Chapter 1, Equations 1-8 and 1-14, gate dielectrics play a crucial role in the TFT's performance, since gate dielectrics with high specific capacitance, combined with high mobility semiconductors and low threshold voltage leads to maximum drain current for a certain gate voltage. However, the mobility (μ) at the interface between insulator and semiconductor can be substantially reduced by the polarity of some gate media.^[156] In addition, it is noted that every insulating gate medium has limited stability at applied voltage levels (for gate dielectrics this is called dielectric breakdown while for electrolytes it is called electrochemical window). Thus, the saturated drain current will be limited according to Equation 1-8 as V_G is limited to a practical maximum $V_{G(max)}$, by the failure of the gate medium. Furthermore, the geometry factor W/L in Equation 1-8 is somewhat arbitrary. Therefore, two figures-of-merit independent of W/L , namely the lowest sheet resistance R_{\square} and the maximum sheet current I_{\square} , are defined to quantify the ability of an OTFT to deliver current, as in following equations:

$$I_{\square} = \frac{L}{W} I_{D,sat}(V_G = V_{G(max)}) \quad 4-1$$

$$R_{\square} = \frac{V_{G(max)}}{I_{\square}} \quad 4-2$$

In recent years, electrolytes encompassing solid (polymer) electrolytes,^[65, 84] DI water,^[57, 89] and ionic liquids (ILs)^[81, 86, 88] have been used as gate dielectric layers due to their extraordinarily high capacitance produced by the formation of electric double layers (EDLs) at the interfaces of gate-electrolyte and semiconductor-electrolyte when a gate voltage is applied. The capacitance value of EDL is in the range of 1-10 $\mu\text{F}/\text{cm}^2$ which exceeds the capacitances of conventional dielectrics (see Chapter 1, Section 1.6). Such an extremely high capacitance means that a very high density of carriers is accumulated at the surface of the semiconductors. Therefore, low V_T , and high I_{\square} / low R_{\square} can be obtained. Among these electrolytes, ionic liquids (ILs) display unique characteristics as described in Chapter 1, Section 1.6.2.3. Nevertheless, ILs are strong solvents^[79] and therefore not normally suitable for use with soluble organic semiconductors, since IL-gated OTFTs in previous reports have been used vacuum evaporated organic semiconductors only.^[81, 86, 88]

In this chapter, an OTFT that employs a solution-processed organic polymer, namely poly(2,5-bis(3-hexadecylthiophen-2-yl)thieno[3,2-b]thiophene) (PBTTT), was gated with an IL. PBTTT is recognized for its extremely high carrier mobility of $3.5 \text{ cm}^2 \text{ V}^{-1} \text{ s}^{-1}$.^[65, 66] As was described in Chapter 1, Section 1.5.4.2, PBTTT has a more rigid backbone architecture compared to P3HT; therefore, only hot chlorinated benzenes are required to dissolve PBTTT.^[66] PBTTT's poor solubility extended to EMITSFI-ionic liquid, which had previously been utilized as a gate medium for vacuum evaporated organic semiconductors.^[81, 86] The results of IL-gated PBTTT TFTs show good figures-of-merit I_{\square} and R_{\square} .

4.2 OTFT Fabrication

Two types of TFT contacts substrates have been used in this chapter. First, prefabricated substrates with gold (Au) source/drain (S/D) that have a width (W) = 2 mm / (length) $L = 10 \mu\text{m}$ ($W/L = 200$), as described in ^[89]. Alternatively, printed contact substrates are described in Chapter 2, Section 2.2.2.1. Briefly, inkjet printing has been used to print silver source/drain contacts of $W = 3 \text{ mm}$ / $L = 40 \mu\text{m}$ ($W/L = 75$). The deposition of PBTTT on these substrates was described in Chapter 2, Section 2.3.1.1. Briefly, 7 mg/ml PBTTT-C16 was dissolved by stirring with a magnetic stirrer into hot

DCB at 110 °C for 45 minutes, spun onto contact substrates from hot DCB at 5000 rpm for 40s. Then, the films were dried under a dynamic vacuum at 110 °C for 1hr.

4.3 Ionic Liquid-gated Organic Transistor Electrical Characteristics

For electrolyte gating, 5 to 8 μL of EMITSFI IL (sourced from Aldrich, catalogue No. 711691), or DI water (for comparison), was applied via a microliter syringe over the channel area of TFT and electrically addressed by an L-shaped Gold (Au) gate needle (American Probe and Technologies). EMITSF IL, Fig 4-1, is 1-ethyl-3-methylimidazolium-bis (tri fluoro methyl-sulfonyl) imide ionic liquid and it is one example of ILs that shows a very high electrochemical window, about 4.3V, and high capacitance up to about $11 \mu\text{Fcm}^{-2}$ at 0.1 Hz and $\sim 5 \mu\text{Fcm}^{-2}$ at 10 Hz.^[81, 82] For electrical characterization, two Keithley 2400 source/measure units (described in Chapter 3, Section 3.2.1) was used to record output characteristics and a bespoke current/voltage (I/V) converter setup (explained in Chapter 3, Section 3.2.2) was used to record saturated transfer characteristics. All electrical measurements were carried out under an ambient atmosphere.

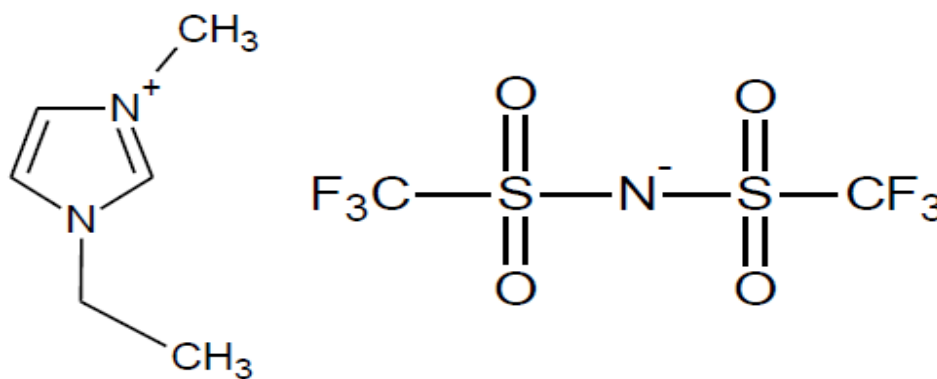


Figure 4-1: The chemical structure of EMITSFI ionic liquid.

4.4 Ionic Liquid-gated PBTTT OTFT Performance

Output characteristics, and saturated transfer characteristics for OTFT Au contacts gated with (EMITSFI IL) are in Fig. 4-2 and Fig. 4-3. The transfer characteristic here is presented in two forms; parametric with time (Fig. 4-3), and after eliminating time (Fig. 4-4), as described in Chapter 3, Section 3.2.2.4. More details about the

acquisition and evaluation of parametric transfer characteristics as well as the reasons for doing so were discussed by prior graduates of the Sheffield TFT group.^[35, 89, 154, 155, 157]

Output characteristics for PBTTT OTFT gated with IL show near-ideal form, with slight hysteresis. The linear $I_D(V_D)$ behaviour for low V_D , indicates ohmic contacts as a result of good hole injection at the Au/PBTTT source contacts. Drain current is saturated at large negative V_D and V_G , as expected from Equation 1-8. At $V_D = V_G = -1V$, a drain current $|I_D|$ of 1.52 mA is recorded. By using Equations 4-1 and 4-2, this leads to $I_{\square} = 7.6\ \mu\text{A}/\square$ and $R_{\square} = 131.6\ \text{k}\Omega/\square$. Compared to other recent reports of high performance OTFTs, the sheet resistance reported here is exceptionally low, see Table 4-1. PBTTT was also gated with DI water, as seen in Fig. 4-2. Drain currents for DI water gating are lower than for IL gating due to the high capacitance of ILs, but owing to the molecular engineering of PBTTT for high carrier mobility, water-gated PBTTT drain current is considerably larger than for reported water-gated P3HT.^[57]

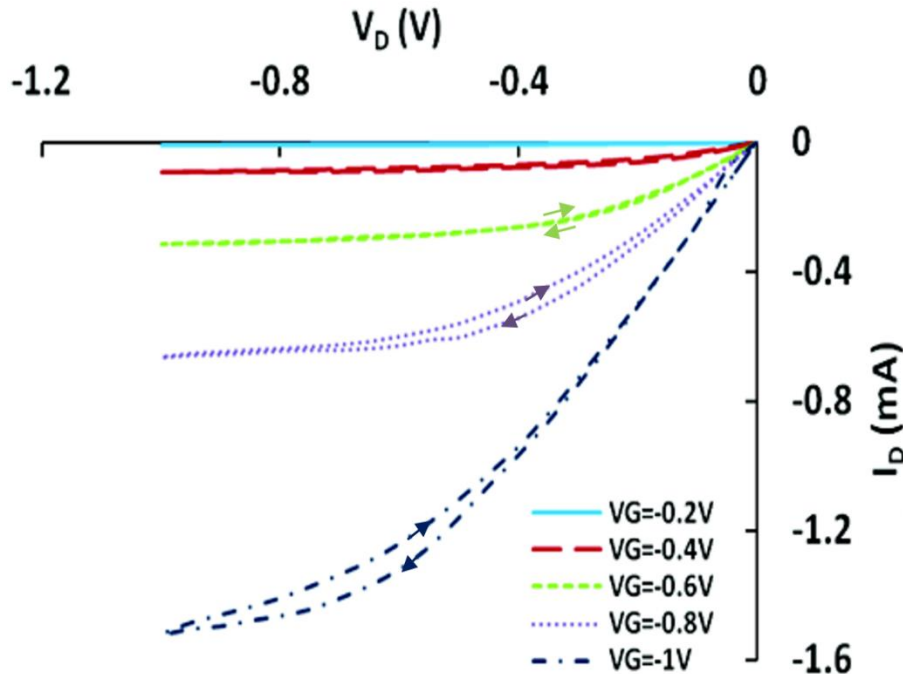


Figure 4-2: Output characteristics for IL- gated PBTTT OTFT with Au source/drain contacts.

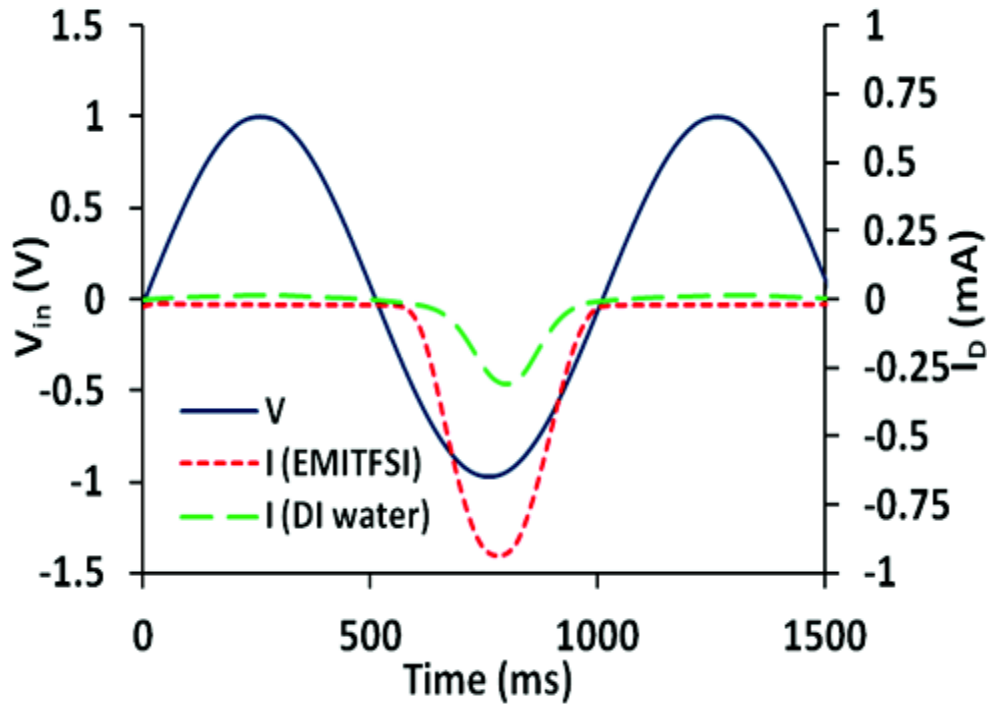


Figure 4-3: Saturated transfer characteristics parametric in time for IL- gated PBTFT OTFT with Au source/drain contacts (red short dash). Green long dashes show the saturated transfer characteristic for same device gated with water. Solid blue line shows the drive voltage (V_{in}) that applied to the source, (as described in Chapter 3 section 3.2.2).

In order to prove such high currents are not parasitic currents in the IL, a control experiment, in which IL was applied on a blank contact substrate without organic semiconductor, displays maximum currents of only $0.45 \mu\text{A}$, which indicates that the observed characteristics exclude parasitic currents in the IL.

By eliminating the time in Fig. 4-3, the saturated transfer characteristics can be plotted in the form $I_D^{1/2}$ vs V_G , as shown in Fig. 4-4. The charge carrier mobility in the saturated regime μ_{sat} , and threshold voltage V_{th} , can be easily estimated (as described in Chapter 3, Section 3.2.2.4). For IL gating PBTFT OTFT, the value of V_{th} is -0.36 V .

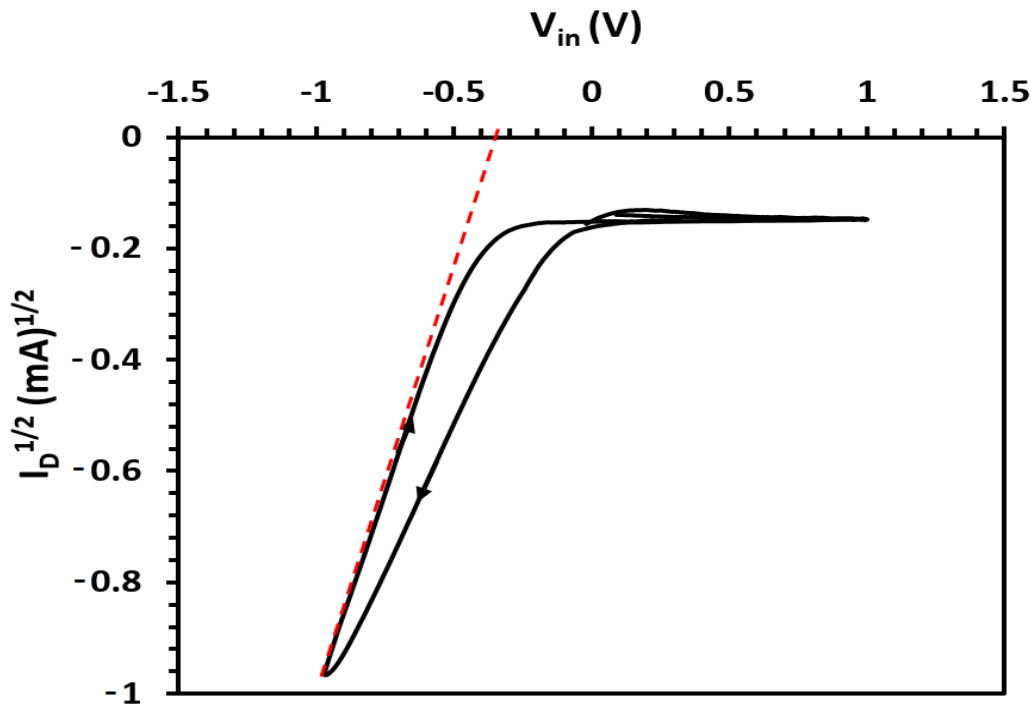


Figure 4-4: Saturated transfer characteristics for IL-gated PBTTT OTFT with eliminating the time, with Au source/drain contacts.

In the case of electrolyte-gated TFTs, the calculation of carrier mobility from standard transistor equations is problematic because of uncertainty about the accuracy of the figure for specific capacitance C_i .^[35, 57] Therefore, the figure-of-merit μC_i was used, which can be easily and directly extracted from measured characteristics without assumptions about C_i .^[9] Once evaluating saturated transfer characteristics at high gate voltage, the slope of $\sqrt{I_D}$ vs. V_G plot, $\sim 0.0476 \pm 0.0001 \text{ A}^{1/2}/\text{V}$ and where $2L/W = 0.01$ by using Equation 3-8 in Chapter 3, this gives $\mu C_i = 2.27 \pm 0.01 \times 10^{-5} \text{ A}/\text{V}^2$. If the specific capacitance (C_i) is considered as $\sim 7 \pm 0.07 \text{ } \mu\text{F}/\text{cm}^2$, as reported by Ono *et al.*^[81] for the EMITFSI-IL at low frequency (1 Hz), the saturated mobility (μ_{sat}) is $\sim 3.24 \pm 0.3 \text{ cm}^2/\text{Vs}$, which is an extraordinary carrier mobility for a polymer organic semiconductor. However, high and extraordinary mobility is expected with PBTTT where Hamadani and coworkers report a mobility of $\sim 1 \text{ cm}^2/\text{Vs}$ for dielectric-gated PBTTT OTFTs. Moreover, very high density of carriers at the surface of the semiconductors can be accumulated when TFT is gated with a high capacitance IL, which in turn leads to increases in the mobility.^[158]

As mentioned before, ILs have broad electrochemical voltage windows; however, when the drive voltage exceeded 1.2 V, we found that the on/off ratio drops (on/off ~ 2200 under 1 V drive), and the overall device performance rapidly degrades. We consider this degeneration is associated to the electrolysis of water: ILs are hygroscopic and will rapidly absorb water from atmospheric humidity. Although the EMITSFI IL employed in this report has an 'electrochemical window' of 4.3 V,^[79] the practical window is therefore reduced to only 1.23 V, the 'electrochemical window' for water. For that reason the maximum voltage we used in subsequent experiments was limited to 1V. Xie *et al.*^[88] also limited gate voltage to 1V in IL-gated TFTs. They found that mobility decreases again in IL-gated TFTs at gate voltages > 1V,^[88] perhaps due to a binding between holes in the organic semiconductor and anions in the IL.

It is desirable to process all OTFT components from solution, not just the organic semiconductor but also the TFT contacts. Consequently, we used inkjet printing to create source and drain contact (as described in Chapter 2, Section 2.2.2.1). Then thin film of semiconducting PBTTT was formed on printed Ag substrates by spin coating. Characteristics for IL-gated PBTTT OTFTs with printed Ag contacts are shown in Fig. 4-5 and Fig. 4-6.

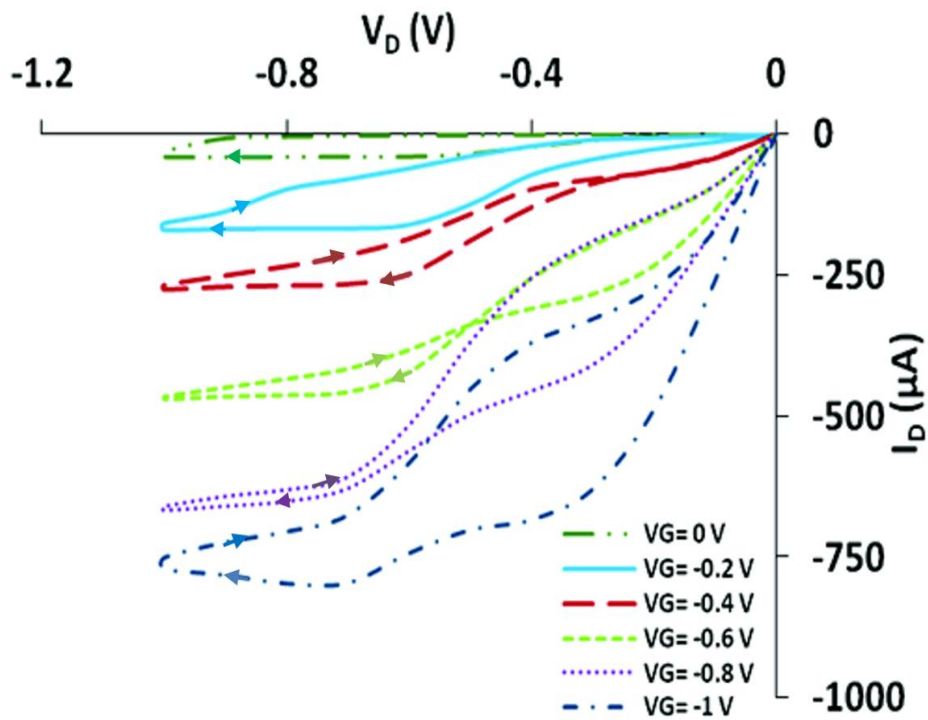


Figure 4-5: Output characteristics for IL-gated PBTTT OTFT with printed silver source and drain contacts.

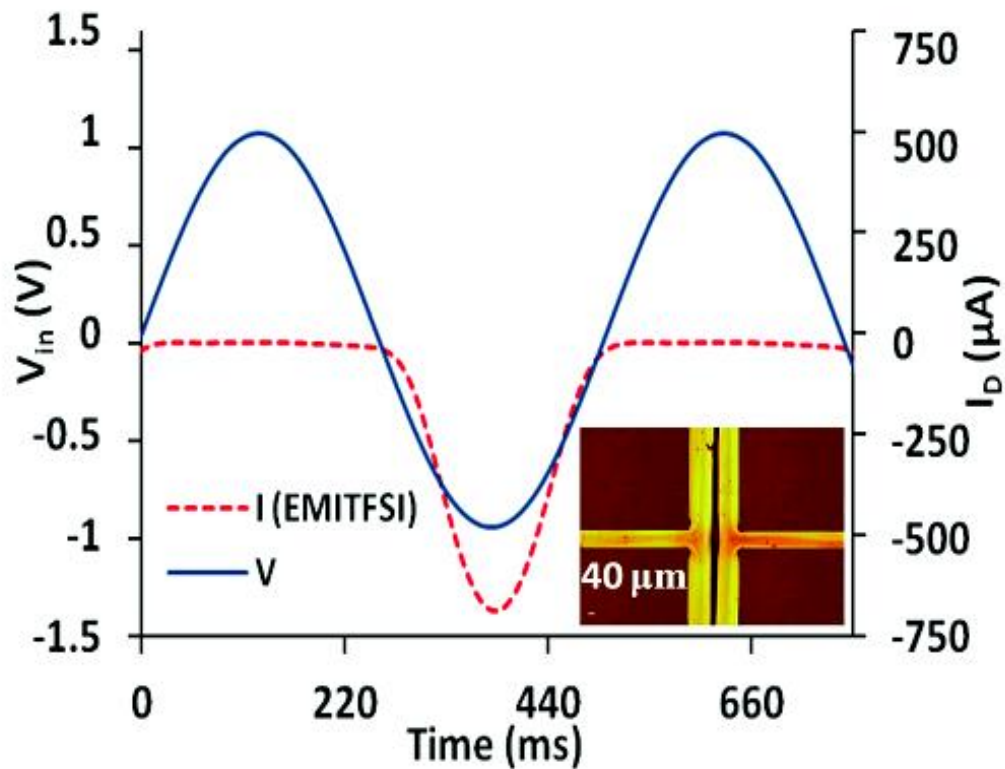


Figure 4-6: Saturated transfer characteristics for IL-gated PBTTT OTFT with printed printed silver source and drain contacts (red short dash), parametric in time. Drive voltage in solid blue. Inset: Optical micrograph of printed / fused Ag contacts; channel length $L = 40 \mu\text{m}$.

From the output characteristics, Fig. 4-5, significant hysteresis can be seen. Also at a low gate voltage, drain current at a low drain voltage is not linear, but drain current remains sublinear initially and curves upwards only at a higher drain voltage. Such sub-linear shape is the evidence of a considerable hole injection barrier at the printed Ag / PBTTT contact due to the lower work function of Ag compared to Au which does not match the *HOMO* of PBTTT. The resulting contact resistance is exacerbated by the exceptionally high conductivity of the IL-gated channel. However, the tunnelling injection at the contact is assisted by gate voltage, which resolves the injection problem at the contact at high gate voltage. Therefore, high drain current is delivered at $V_G = V_D = -1V$ even with printed Ag contacts. PBTTT with printed Ag contacts gated with IL shows even higher sheet current ($I_{\square} = 9.7 \mu A$) and low sheet resistance ($R_{\square} = 102 \text{ k}\Omega/\square$) compared to OTFTs with Au S/D contacts ($I_{\square} = 7.6 \mu A/\square$ and $R_{\square} = 131.6 \text{ k}\Omega/\square$). This is probably due to the longer channel length (L) in the printed channels which increase the apparent carrier mobility (and hence, sheet current), since the longer channels dilute the relative contribution of contact resistance, even when contacts are ohmic.^[159] However, the sheet current/sheet resistance metric in general is doubted by the dependence of apparent mobility on channel length (L), but it is nevertheless widely used for characterizing conductive surfaces, e.g. synthetic metal films, since mobility as a metric is doubted because of its apparent dependency on L , and can be used by one as a figure of merit to compare the performance of several semiconductor materials. The threshold voltage for IL-gated PBTTT OTFT, with Ag printed source/drain contacts is $\sim -0.15 \text{ V}$, as seen in Fig. 4-7.

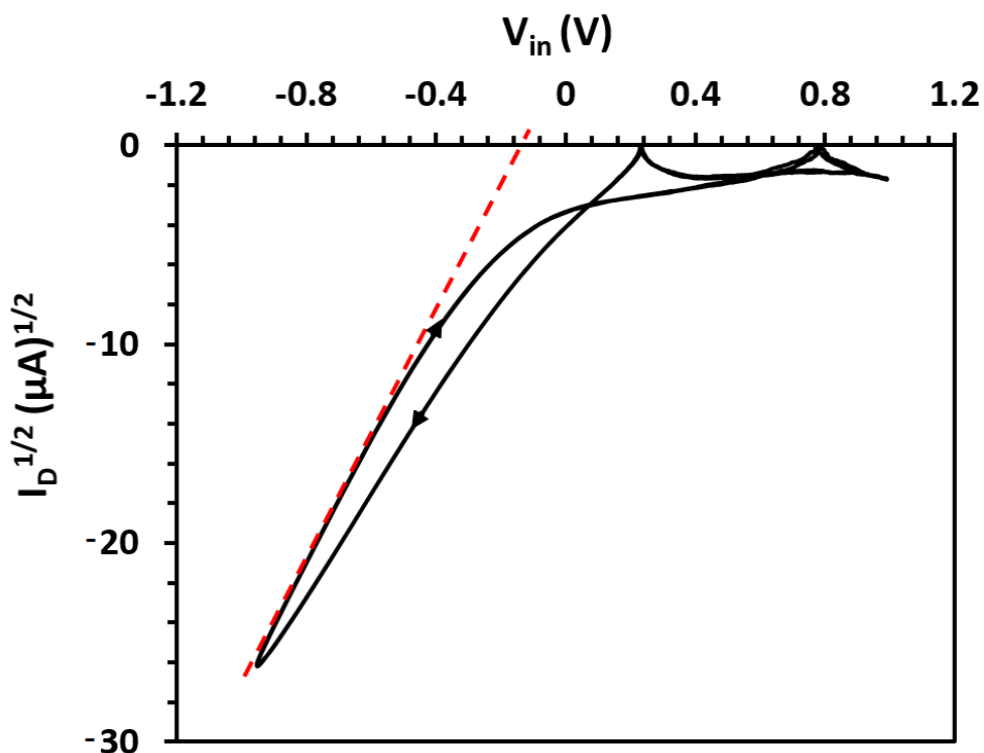


Figure 4-7: Saturated transfer characteristics for IL-gated PBTTT OTFT with eliminating the time, with Ag source/drain contacts.

4.5 Summary and Conclusions

In summary, this is the first report showing an organic solution-processed semiconducting polymer, namely, PBTTT, gated with very high capacitance IL. The performance of resulting IL-gated PBTTT OTFTs in the sense of high sheet current and low sheet resistance, displays very good results compared to a few high-performance OTFTs from recent literature. The comparison with other reports is summarized in Table 4-1. This table includes a range of semiconductors processed from solution as well as evaporated, gated with different gate media including dielectrics, solid electrolytes and liquid electrolytes. I_{\square} and R_{\square} have been calculated from characteristics in the respective reports.

Table 4-1

Reference	Semiconductor	Deposition	h^+ / e^-	Gate medium	I_{\square} [$\mu A/\square$]	R_{\square} [$M\Omega/\square$]
Hasegawa <i>et al</i> [160]	C ₈ -BTBT	Ink jet (2 shot)	h^+	Dielectric	69	0.87
Klauk <i>et al</i> [161]	DNTT	Evaporation	h^+	Dielectric	0.54	5.56
Bao <i>et al</i> [70]	Pentacene	Evaporation	h^+	Dielectric	0.3	6.7
Horowitz <i>et al</i> [57]	P3HT	Spin casting	h^+	Water	0.0054	111
Grell <i>et al</i> [89]	ACN-conditioned BBL nanobelts	Drop casting	e^-	Water	0.35	2.28
Berggren <i>et al</i> [84]	P3HT	Spin casting	h^+	Solid electrolyte	0.0175	57
Frisbie <i>et al</i> [88] Takeya <i>et al</i> [81]	Rubrene	Evaporation	h^+	Ionic Liquid	0.66	0.3
Takeya <i>et al</i> [86]	C ₆₀	Evaporation	e^-	Ionic Liquid	0.027	37
Heeney <i>et al</i> [66]	PBTTT	Spin casting	h^+	Dielectric	25	2.4
Torsi <i>et al</i> [65]	PBTTT	Spin casting	h^+	Solid electrolyte	0.459	2.18
This work	PBTTT (Au contacts)	Spin casting	h^+	Ionic Liquid	7.6	0.132
This work	PBTTT (inkjet Ag contacts)	Spin casting	h^+	Ionic Liquid	9.7	0.102
This work	PBTTT (Au contacts)	Spin casting	h^+	Water	1.6	0.64

Table 2: The comparison of Figures- of- merit I_{\square} and R_{\square} between the data from this work and data from recent publications. The table contains a collection of semiconductors produced by either evaporated processed or solution processed, and gated with different gate medium (liquid electrolytes, solid electrolytes, dielectrics). The R_{\square} and I_{\square} were extracted from transistor characteristics presented in the particular publications.

Our figures-of-merit for entirely solution-processed OTFTs compare favourably within Table 4-1, which is the result of the concurrent high capacitance, high carrier mobility, and low threshold, of the PBTTT/EMITSFI EDL transistor. In addition, IL-gated OTFTs that use semiconducting polymer PBTTT, open up avenues to explore the physics of polymer organic semiconductors at extremely high charge carrier concentrations, which has already led to intriguing insights in evaporated low-molecular weight organic semiconductors.^[88] However, as a concluding remark, the lifetime of a PBTTT device's operation is still limited to not much longer than 1 hr. The reason may be due to an ultimate slow dissolution of PBTTT in IL. See future work section for some points that could overcome the limited durability of PBTTT OTFTs gated with ILs.

5 Precursor-route to Zinc Oxide Semiconductor (ZnO) WGTFTs

Semiconducting organic polymers that can be processed from solution into devices have been developed as an alternative to conventional semiconductors that require vacuum conditions for deposition. Solution-processable semiconductors pave the way for alternative semiconductor device manufacturing options, e.g. via printing.^[39] However, solution-processable organic semiconductors often display low mobility and suffer poor stability under ambient conditions and the best performing semiconducting polymers are often well soluble only in environmentally unacceptable halogenated solvents.^[64] For that reason, solution-processable inorganic semiconductors have recently attracted a significant consideration as an alternative for their better stability under ambient air.

Since ~ 2000, the II-VI semiconductor Zinc oxide (ZnO) has been the focus of intense research interest. ZnO is a large direct band gap semiconductor that can be processed e.g. by magnetron sputtering or pulsed laser deposition.^[28, 31-33] It is attractive due to the ease of control over its chemical composition/stoichiometry, non-toxicity, good film forming properties, and high electron mobility. ZnO is used for a wide range of applications, including sunscreen,^[162, 163] food supplements,^[163] IR reflecting windows^[163], but also exceeding semiconductors devices.

In an important paper in 2007,^[34] Loutfy *et al.* have shown that ZnO can be processed via a soluble organic precursor, Zinc acetate (ZnAc), with subsequent pyrolysis (chemical conversion driven by high temperature) of ZnAc → ZnO. Since then, many workers have used e.g. ZnAc → ZnO spray pyrolysis (spraying of precursor solution onto a heated substrate) to deposit ZnO films.^[87, 164]

In this chapter, I present studies on the improvement of precursor-route ZnO films. Firstly, I show that the choice of solvent used for the processing of the precursor, ZnAc, leads to different properties of the resulting ZnO films. An appropriate choice of solvent (i.e., choosing a good solvent for the precursor) leads to higher mobility in the resulting films. Secondly, I present the discovery of an alternative precursor-route to ZnO,

where the precursor is an aqueous solution of the Zinc salt, ZnCl₂. In both cases, resulting ZnO films were again used in electrolyte-gated TFTs as an application example, and for characterization of their electrical properties. However, given the wide spectrum of uses for ZnO, this will only be seen as one of the many applications that improved or entirely novel precursor-routes to ZnO may have.

5.1 Mixed Organic Solvent for ZnO Precursor Zinc Acetate (ZnAc)

The discovery of water-gated organic semiconductors by Horowitz et al.^[57] has prompted an interest in establishing such thin film transistors (TFTs) into a novel type of biosensor. In a biosensing application, organic TFTs have been gated with a biologically realistic aqueous electrolyte (phosphate-buffered saline (PBS), a mixture of salts that buffers pH at ~ 7.4^[58, 59, 77] while bio sensitizer molecules (e.g. enzymes) were attached either at the semiconductor/water interface,^[58, 77] or at the gate electrode^[59] (as described in Chapter 1, Section 1.7.2). However, organic semiconductors can be doped by penetrating ions from such highly concentrated electrolyte, PBS, and then electrochemical transistor behaviour competes with field effect gating,^[10] which makes the transducer's output difficult to interpret. Beside the high mobility of ZnO compared to organic semiconductors, ZnO does not suffer from electrochemical doping even when gated with PBS.^[36] In 2007, Loutfy *et al.*^[34] reported the first precursor route to ZnO via casting a soluble precursor, zinc acetate, following thermal conversion into ZnO under ambient air. Loutfy et al. obtained mobility of 5.25 cm² V⁻¹ s⁻¹ with good off/on ratio in the precursor-route ZnO TFTs gated with an inorganic dielectric. In 2012, Al Naim *et al.*^[35] reported a precursor route ZnO gated with DI water-showing similar mobility as reported by Loutfy *et al.* for dry-gated devices but with low threshold voltage due to high EDL capacitance even with DI water. However, up to now, precursor-route ZnO mobility still falls short of the performance of ZnO once deposited by methods such as pulsed laser or magnetron sputtering deposition.^[28, 31-33]

In this chapter, I report a new processing solvent mix for ZnAc leading to precursor-route ZnO films that work considerably better in electrolyte-gated TFTs than any previously reported precursor-route ZnO films.

5.1.1 Preparation of ZnO Films from Zinc Acetate (ZnAc) Precursor Solutions

As described in Chapter 2, Section 2.3.1.2, the ZnO precursor solution was prepared by dissolving 0.1M (21.9mg/mL) of zinc acetate dihydrate $Zn(CH_2COOH)_2 \cdot 2H_2O$ either in ethanol (EtOH), 2-propanol, acetone, or 1:1 EtOH/Acetone. All these solutions were stirred at 80 °C for prolonged periods. Then, the precursor solutions were filtered with a 0.45 μ M filter to prepare for spin coating. Water-gated TFTs with ZnO film resulting from a ZnAc precursor using EtOH as the casting solvent for the precursor have been reported previously.^[35, 36] However, we found that pure EtOH is not a good solvent for ZnAc. The time required to completely dissolve 0.1M ZnAc in EtOH is around 5 to 7h in the presence of heating and stirring. Also, after dissolving and storage at ambient temperature, ZnAc precipitates again from the EtOH solution within an hour. Therefore, we had to re-heat and stir again for 30 minutes. When pure acetone and 2-propanol were used, we observed similarly poor solubility of the ZnAc. Loutfy *et al.*^[34] used methoxyethanol solvent to dissolve zinc acetate (ZnAc) but they do not evidently report the quality of the solvent. However, we found that a 1:1 mix of EtOH and acetone is a better solvent for ZnAc than either EtOH, acetone, or 2-propanol, alone. The time required to completely dissolve 0.1 M of ZnAc was reduced to around 2 to 3h with heating and stirring. Also, the amount of ZnAc precipitate was reduced even after several days of storage, and only a gentle heating is required to dissolve such ZnAc precipitates. Simple Hildebrand solubility theory explains solubility as the result of matching Hildebrand parameters, δ , between solvent and solute. When a high and a low δ solvent are mixed, the resulting mixed solvent may be a better match to solute the Hildebrand parameter than either solvent alone. The Hildebrand solubility parameter δ for a pure liquid substance is defined as the square root of the cohesive energy density, where the cohesive energy density is the amount of energy required to completely separate the molecules of the liquid from their neighbours into a gas (an ideal gas). This is closely related to the (molar) latent heat of vaporisation (ΔH) of the liquid^[165]:

$$\delta = \sqrt{c} = \sqrt{\frac{\Delta H - RT}{V_m}} \quad 5 - 1$$

Wherein c is the cohesive energy density, ΔH is the molar heat of vaporization, and V_m the molar volume. RT is the molar enthalpy (*i.e.*, internal energy) of the resulting ideal gas, and is therefore, subtracted from the heat of vaporization to obtain an energy of vaporization. The solubility parameter concept can be generalised to solids and polymers, even if these may not be able to evaporate without decomposition. In order for a material to dissolve, the same interactions need to be overcome as for evaporation, since the molecules are separated from each other and surrounded by the solvent. On the other hand, enthalpy is re-gained from the new interactions between solute and solvent. As a general rule, two solvents will be miscible, or a polymer will be soluble in a solvent, when their Hildebrand parameters are similar to each other. Exceptions from this rule may occur when solute and solvent can engage in specific interactions (rather than van- der- Waals interactions only), e.g. when mixing a hydrogen bond donor with a hydrogen bond acceptor. The Hildebrand parameters δ of EtOH and acetone are 12 and 9.77 (cal cm⁻³)^{1/2}, respectively,^[166] suggesting $\delta \sim 11$ (cal cm⁻³)^{1/2} for a 1:1 mix. That is close to the Hildebrand parameter for methoxyethanol used by Loutfy *et al.*,^[34] $\delta = 10.8$ (cal cm⁻³)^{1/2}.

Finally, ZnO films were prepared on TFT source and drain contacts substrates as described in Chapter 2, Section 2.3.1.2. Briefly, 5 source/drain gold contact pairs per substrate with geometry width/length (W/L) = 1 mm/30 μm = 33 were fabricated through a shadow mask using a high vacuum evaporator to deposit first a 7 nm Cr adhesion layer, and then 120 nm Au. Around 40 μL from ZnAc precursor solutions were dispensed onto source/drain contacts substrates and spin cast at 2000 rpm for 50 s. The film was thermally converted into ZnO on a hotplate at 450 °C for at least 12 minutes. ZnAc coating and conversion were repeated three times. The thermal conversions were performed under ambient air. The final film thickness was estimated, using Veeco Dektak³ ST Surface, as 44.2 \pm 3 nm.

5.1.2 Results and Discussion

5.1.2.1 X-Ray Photoelectron Spectroscopy Surface (XPS)

XPS is used to identify the elements constituting the surface of thin films. Also XPS often allows, at least partly, the chemical bonds they have formed to be identified. As described in Chapter 3, Section 3.1.5, XPS analyses were collected between 1200 to 0 eV binding energy, at 160 eV pass energy and 1 eV intervals. High-resolution Zn 2p, C 1s, O 1s and Zn LMM peaks were collected over an appropriate energy range at 20 eV pass energy and 0.1 eV intervals. As any surface always comprises graphitic carbon that is adsorbed during exposure of the sample to the air atmosphere,^[150] the binding energy scales were calibrated assuming the main C 1s peak fell at 285 ± 0.1 eV, as a reference for ZnO XPS calibration of the binding energy scale.^[149]

Fig. 5-1 shows the XPS peaks for Zn 2p orbitals from ZnO films via the ZnAc precursor route cast from EtOH and Fig.5-2 displays Zn 2p orbitals' precursor-route ZnO films cast from a mixed solvent. Fig. 5-3 and Fig. 5-4 display O 1s XPS peaks spectra for precursor-route ZnO films cast from EtOH and mixed solvent, respectively. Zn 2p orbitals in Fig. 5-1 and Fig. 5-2, are split into Zn 2p_{1/2} and Zn 2p_{3/2} orbitals and the positions of these orbitals are in the range of what was found in the literature,^[144-148] which indicates that these orbitals are related to the Zinc element in the resulting ZnO films. The (non-Gaussian) O 1s peaks in Fig. 5-3 and Fig. 5-4 have been fitted as a superposition of two overlapping Gaussians: The lower energy Gaussian corresponds to O²⁻ ions bound into the regular wurtzite structure of ZnO (Zn-O-Zn) and the higher energy Gaussian is attributed to oxygen in metal-OH (M-OH) surface groups.^[144] The positions of both oxygen peaks are also in the range of what was found in the literature.^[144-148]

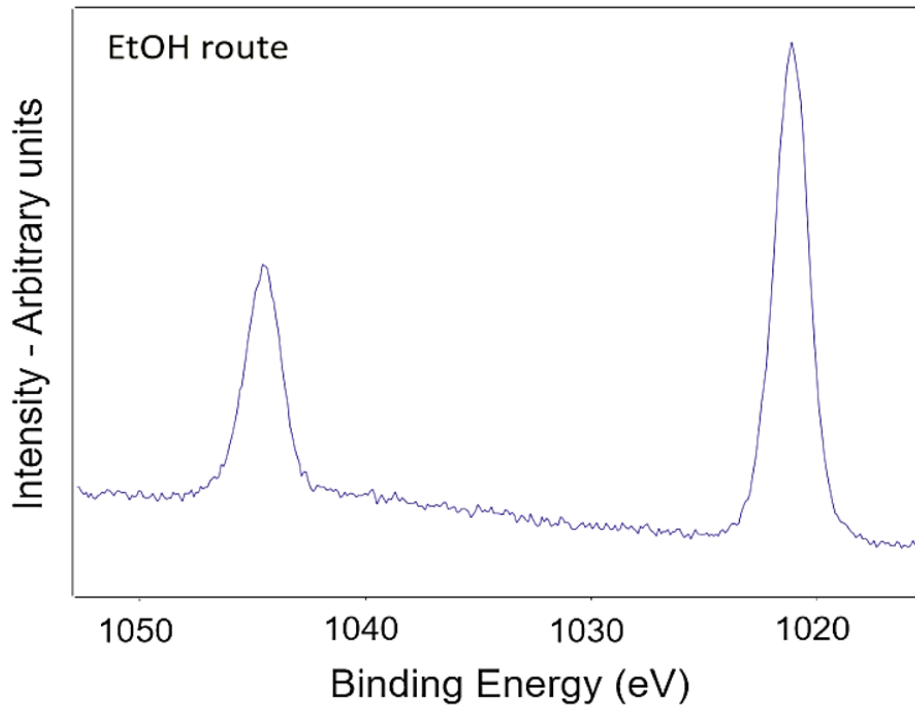


Figure 5-1: XPS spectra of Zn 2p orbitals in ZnO films resulting from the thermal conversion of precursor ZnAc cast from EtOH.

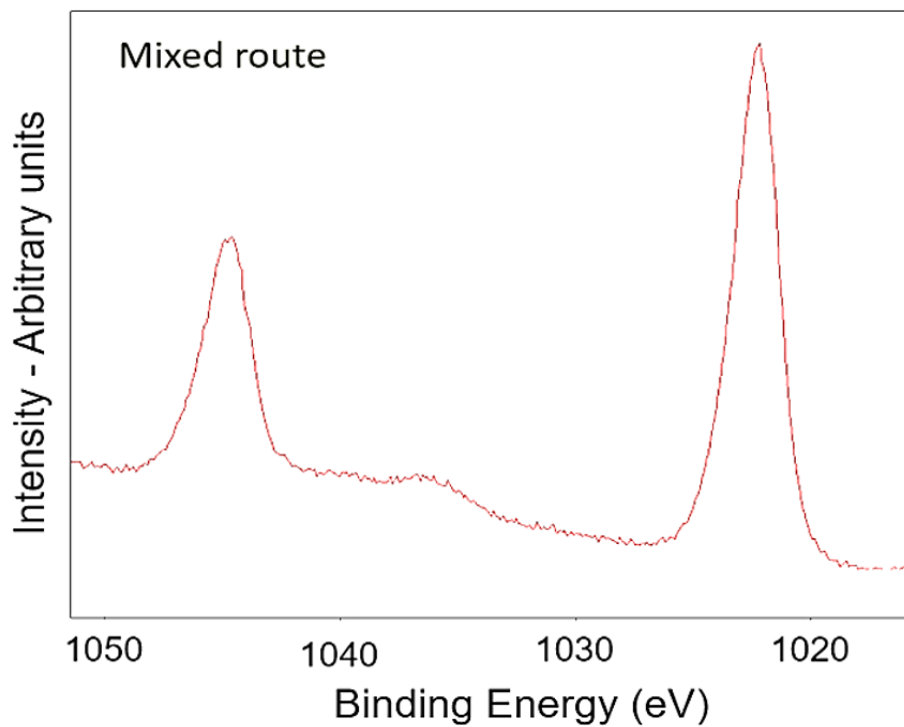


Figure 5-2: XPS spectra of Zn 2p orbitals in ZnO films resulting from the thermal conversion of precursor ZnAc cast from mixed solvent, EtOH: Acetone 1:1.

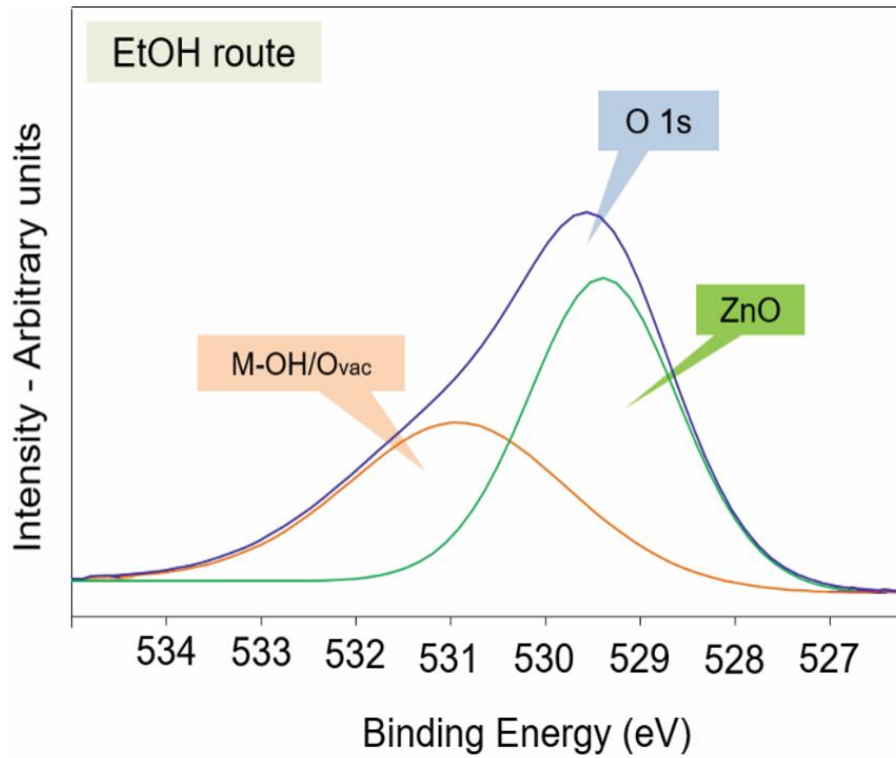


Figure 5-3: XPS spectra of O 1s for ZnO films resulting from the thermal conversion of precursor ZnAc cast from EtOH.

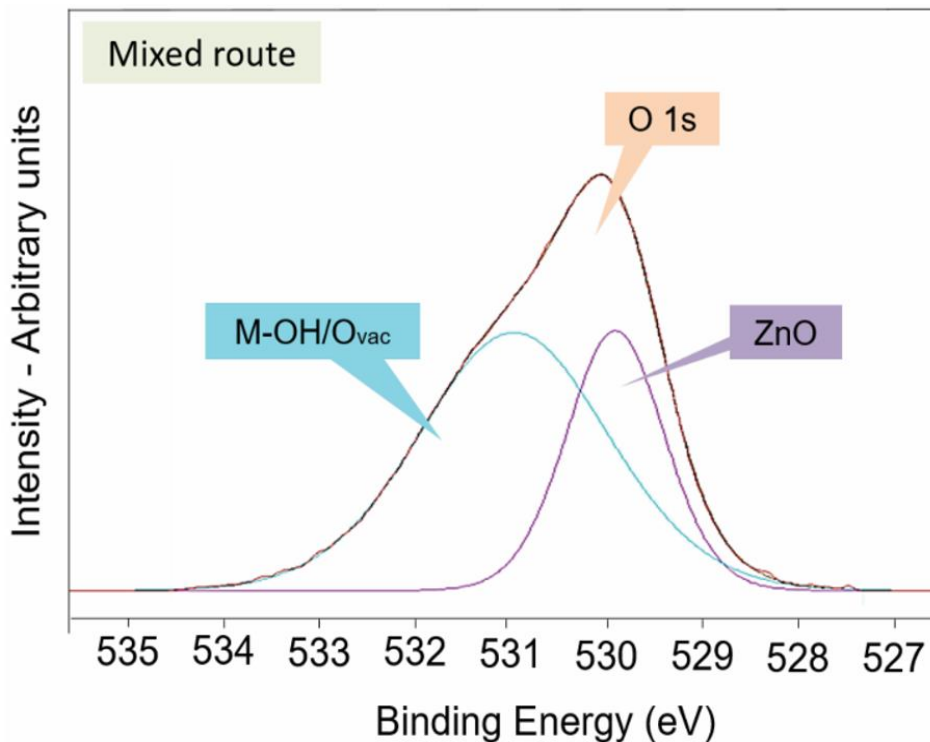


Figure 5-4: XPS spectra of O 1s for ZnO films resulting from the thermal conversion of precursor ZnAc cast from mixed solvent, EtOH: Acetone 1:1.

Generally, XPS analysis displays the chemical identity of these films as a regular ZnO, with Zn-OH surface groups therefore endorsing successful conversion of the precursor for both casting solvents, but exposes no differences at the level of atomic binding between the different casting solvents.

Table 5-1 shows all XPS peak positions, and their widths (FWHM).

Table 5-1

	EtOH route		Mixed route	
	Position (eV)	FWHM (eV)	Position (eV)	FWHM (eV)
Zn_{1/2}	1021±0.17	1.75±0.03	1023±0.23	2.5±0.042
Zn_{3/2}	1045±0.12	2.0±0.019	1047±0.20	2.5±0.025
O 1s	529.6±0.44	2.8±0.051	530±0.39	2.2±0.047
Zn-O	529.4±0.31	1.9±0.02	529.9±0.50	1.07±0.02
M-OH	531.2±0.22	2.8±0.04	531±0.42	2.2±0.018

Table 3: Summary of the observed XPS peak positions, and their FWHM, for ZnO films via ZnAc precursor route from different solvents: EtOH route and Mixed route.

5.1.2.2 Scanning Electron Microscopy (SEM)

SEM has been used to evaluate the surface morphology of precursor-route ZnO films cast from ZnAc in EtOH and mixed solvent. The energy of the incident electrons was set at 15 keV, providing magnifications from (50,000 to 85,000) and resolution less than 10 nm. Fig. 5-5 shows the morphology of a ZnO thin film surface resulting from the conversion of EtOH cast precursor, and Fig. 5-6 the mixed solvent cast precursor. On the 10nm size scale, the thin film resulting from EtOH cast precursor exhibits a granular morphology and has densely packed structure. The recognisable small grains have sizes in the order of 7 to 15 nm. However, the thin film resulting from mixed solvent cast precursor displays little contrast, grains are hardly recognisable and they have a bigger size in the order of 17-20nm. The absence of clearly visible morphological features of the ZnO surface resulting from the conversion of mixed solvent shows a very homogeneous film. Large grain size and a very homogeneous film leads to increased electron mobility. We believe, using poor solvent, e.g. pure EtOH, small aggregates of precursor molecules form in the casting solvent rather than

fully dissolve as in a mixed solvent. Such aggregates will transfer to the contact substrate after casting. After this, thermal conversion defined boundaries can be formed in ZnO grains, which in turn limits the mobility, as will be shown in the next section.

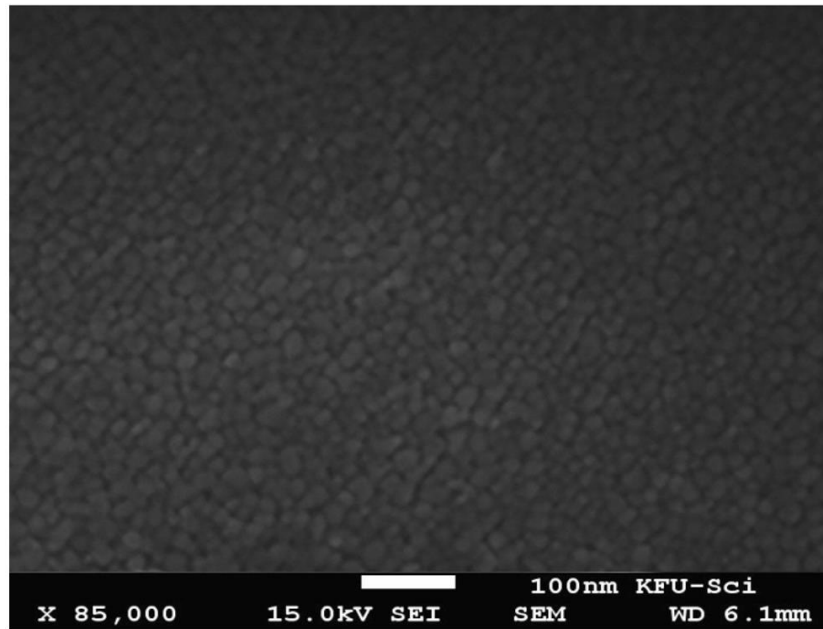


Figure 5-5: SEM images of ZnO films resulting from the thermal conversion of precursor ZnAc cast from EtOH.

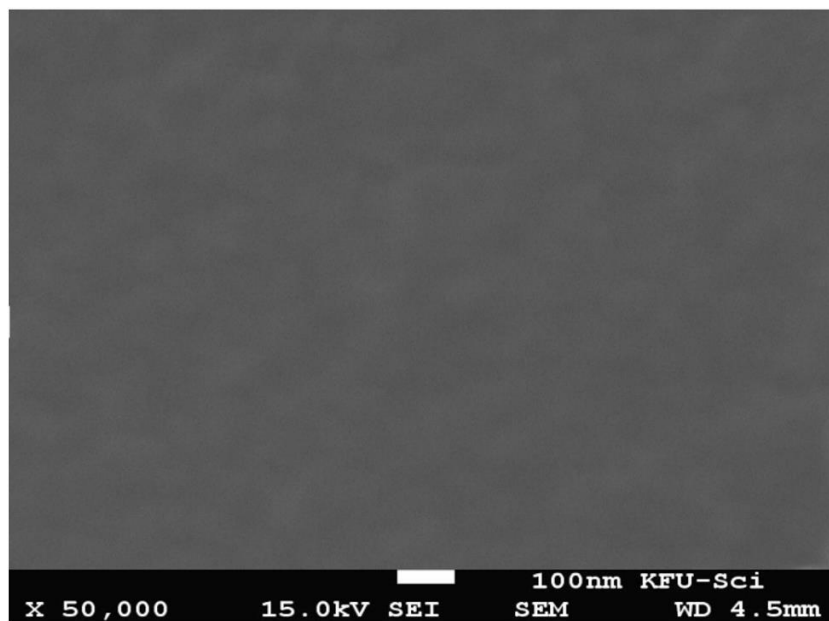


Figure 5-6: SEM images of ZnO films resulting from the thermal conversion of precursor ZnAc cast from mixed solvent, EtOH: Acetone 1:1.

5.1.2.3 Electrolyte-gated ZnO TFT Electrical Characteristics

The charge carrier mobility can be limited by grain boundaries. However, the absence of morphological features and the homogeneity of mixed solvent cast ZnO (Fig. 5-6) suggests improvement in the performance of ZnO TFT. In order to prove that the ZnO film resulting from the conversion of mixed solvent cast precursor leads to better performance than that from the EtOH route, both types should be tested as ZnO films in TFTs. ZnO-TFTs were gated by phosphate-buffered saline (PBS) as an aqueous gate medium. 0.01 Molar PBS has been prepared by dissolving one PBS tablet (Aldrich catalogue No. P4417) in 200 mL of DI water (pH for 0.01M PBS solution is 7.4). PBS (described in Chapter 1, Section 1.6.2.2) is considered to be a realistic medium for biosensor applications due to the fact that ion concentrations of PBS are close to those in living organisms, and it is non-toxic to cells. Therefore, it is often employed in the life sciences and in the development of biosensors to simulate bodily fluids.^[58, 59, 77] A droplet of PBS (around 2 μ L) was applied on the top of the active area of TFTs and electrically addressed by an L-shaped Gold (Au) gate needle. An L-shaped gate needle was orientated along the width of the transistor channel, to overlap the channel completely. Because the surface of ZnO is hydrophilic, PBS forms a flat 'puddle' with a small contact angle. The L-shaped gate needle was lowered carefully to very close proximity (200 μ m adjusted by a glass cover slip used as a spacer) using a probe head. To contact source and drain contact pads, a sharp tungsten (W) needles was used to pierce through the ZnO film that formed on the pads, as seen in Fig 5-7.

We used Keithley source/measure units to record TFT output and transfer characteristics. All measurements were carried out under ambient atmosphere. The resulting transistor output and characteristics are shown in Fig. 5-8 (for EtOH-route) and Fig. 5-9 (for mixed-route) and the transfer characteristics are in Fig. 5-10 and Fig. 5-11, for the EtOH-route and mixed-route, respectively. By applying positive gate voltages, TFTs turn 'on' which is expected for electron-transporting transistors, as seen in output characteristics, Fig. 5-8 and Fig. 5-9. As we mentioned in Chapter 1, Section 1.4.1, ZnO exhibits electron rather than hole transport.^[31, 34-36, 167] Output characteristics show little hysteresis, a truly linear 'linear' regime and, at high drain voltages, the drain current is saturated. Low gate voltage output characteristics were

magnified (insets to Fig. 5-8 and Fig. 5-9), and show that TFTs are ‘off’ at $V_G = 0$ V, but ‘on’ at $V_G = +0.2$ V. This implies that the threshold voltage for ZnO TFTs is between 0V and 0.2V, which is in the range of what was found in previous reports on PBS-gated ZnO. [36] Such low threshold voltages (V_{th}) are observed with all electrolyte-gated TFTs, due to high specific capacitance of the electric double layer (EDL) formed at the gate/electrolyte and semiconductor/electrolyte interfaces. In parallel, gate leakage currents were measured: the gate current leakage for the EtOH route was $< 5 \mu\text{A}$ at $V_D = V_G = 1\text{V}$, while it was $0.2 \mu\text{A}$ for the mixed solvent route. The gate current leakage for both routes was always small compared to the drain current.

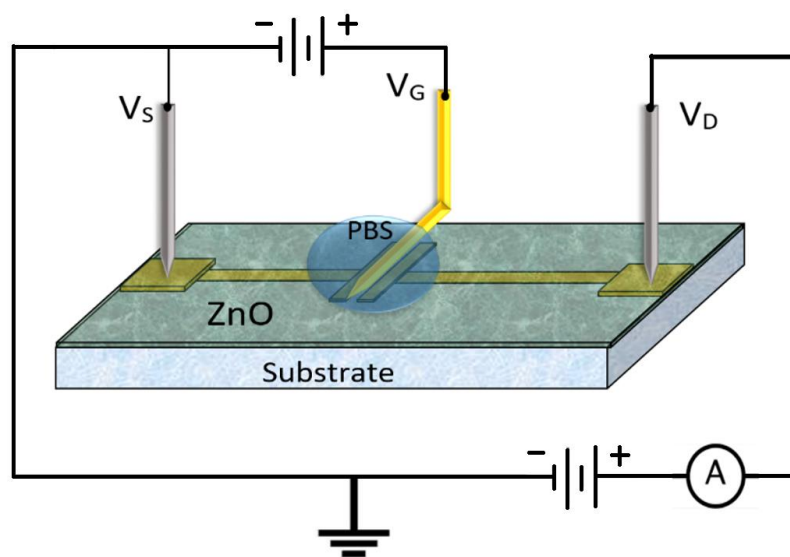


Figure 5-7: Scheme of water- gated ZnO TFT architecture.

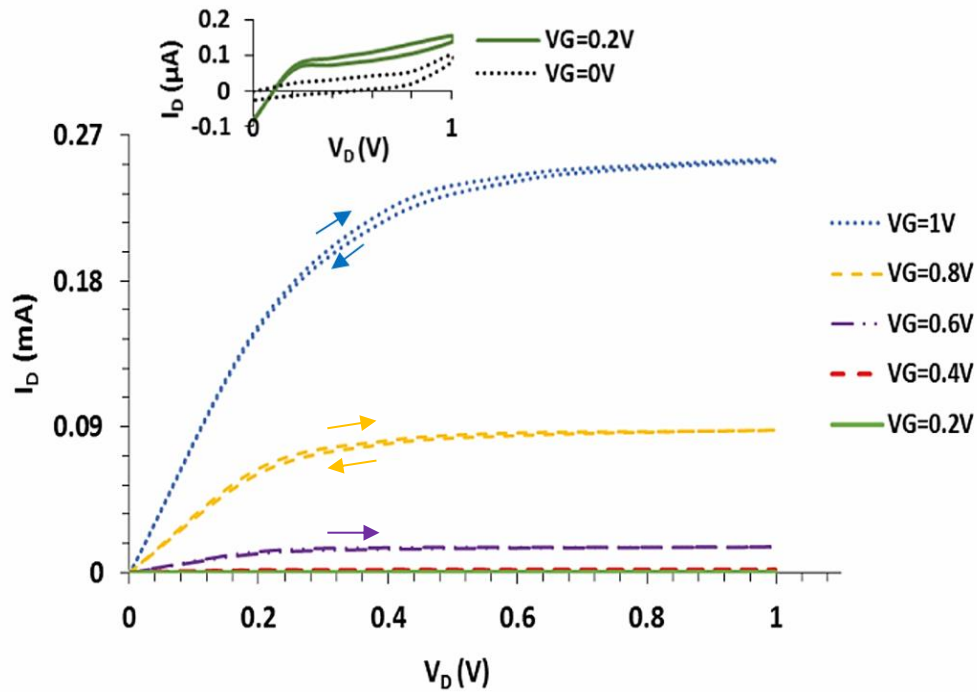


Figure 5-8: Output characteristics for ZnO TFTs gated by PBS. ZnO film resulting from precursor cast from pure EtOH. Insets to output characteristics display magnified output characteristics at low V_G .

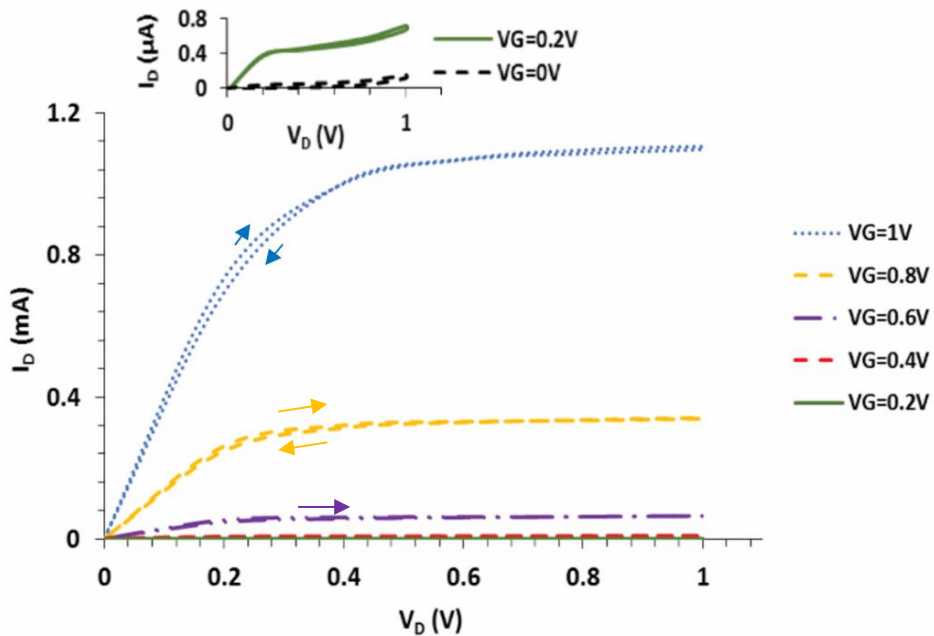


Figure 5-9: Output characteristics for ZnO TFTs gated by PBS. ZnO film resulting from precursor cast from mixed EtOH/acetone (1:1). Insets to output characteristics display magnified output characteristics at low V_G .

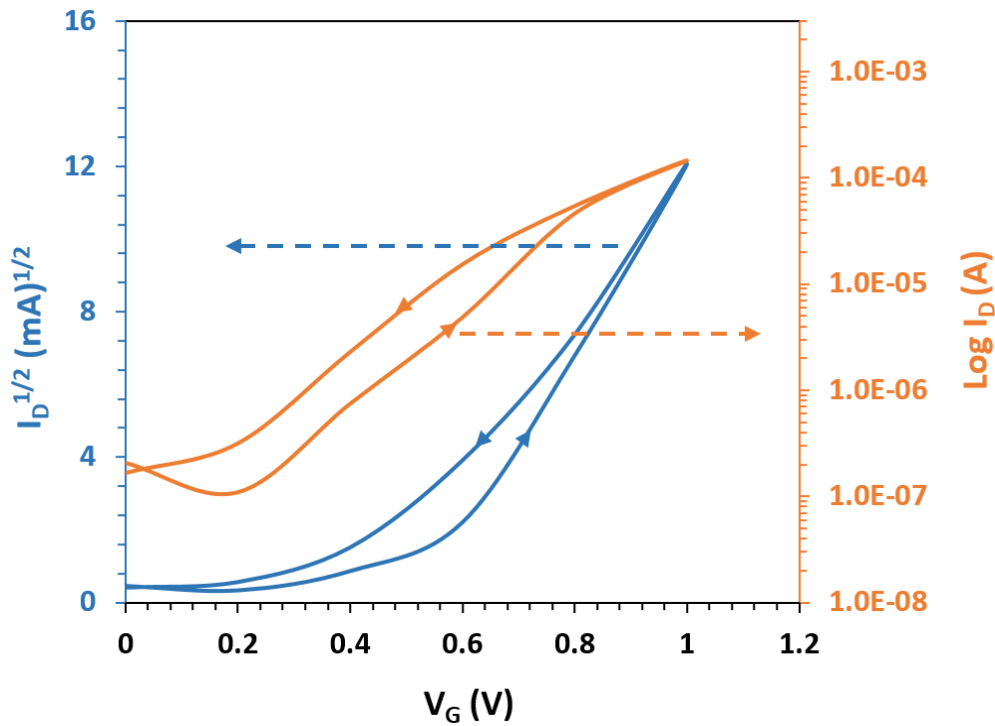


Figure 5-10: Saturated transfer characteristics for ZnAc precursor route ZnO TFTs gated by PBS electrolyte. Precursor cast from pure EtOH. Blue scale: represents transfer characteristics on $I_D^{1/2}$. Orange scale represents transfer characteristics on $\log I_D$.

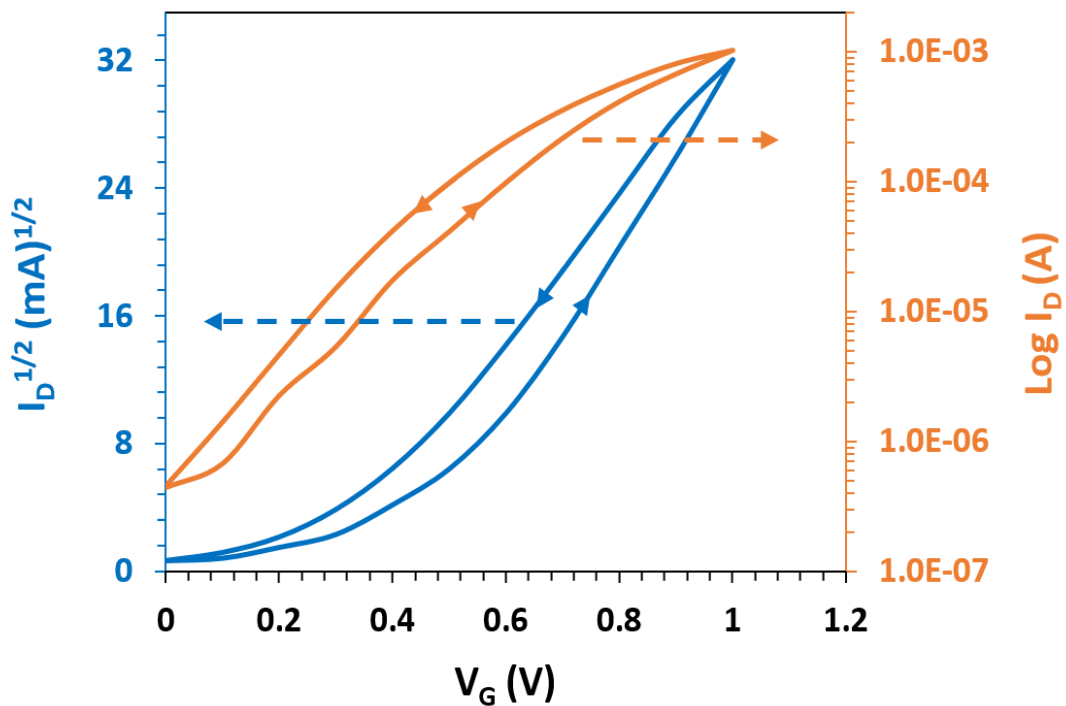


Figure 5-11: Saturated transfer characteristics for ZnAc precursor route ZnO TFTs gated by PBS electrolyte. Precursor cast from mixed EtOH: acetone (1:1). Transfer characteristics are shown in two different representations (on $I_D^{1/2}$ (Blue) and $\log I_D$ (Orange) scale).

Saturated transfer characteristics for ZnO TFTs, Fig. 5-10 and Fig. 5-11, display some hysteresis. Such a phenomenon is sometimes observed for ZnO TFTs under DI water and ionic liquid (IL) gate media.^[35, 87] At high gate voltages (above 0.8V), saturated transfer characteristics for ZnO TFTs resulting from the EtOH route (Fig. 5-10) display a rather curved $I_{D,sat}^{1/2}$ vs. V_G plots approach linearity which is in agreement with what is predicted by generic TFT theory only at high voltage. This could indicate that the capacitance of PBS was increased or carrier mobility was increased, at high gate voltages/carrier densities in the channel. Thus, it was better to extract the threshold voltage (V_{th}) from low V_G in output characteristics. However, field effect transistor activity can be obviously shown from transfer characteristics, e.g., off \rightarrow on switching of I_D with V_G ; for the EtOH route on/off ratio [$I_D(V_G = 1V) / I_D(V_G = 0V)$] is 710, whereas for mixed route it is 2340. These values are in the range ($10^2 \dots 10^4$) which agrees with previously published data for ZnO TFTs under different electrolyte gate media.^[36, 87]

Although characteristics are qualitatively similar between the different casting solvents, a significant quantitative difference can be observed in sheet resistance and mobility. First we can easily identify the saturated drain current from Fig. 5-8 and Fig. 5-9. For EtOH-cast ZnO TFT (Fig. 5-8), $I_{D,sat}$ at $V_G = V_D = 1V$ is 0.26 mA; therefore the sheet resistance (*cf.* Equation 4-2) can be calculated as $R_{\square} (1V) = W/L [V_D = 1 V / I_{D,sat} = 0.26 \text{ mA}] = 128 \text{ k}\Omega/\square$, whereas the saturated drain current for mixed solvent – cast ZnO TFT (Fig. 5-9) – is significantly higher, $I_{D,sat}$ at $V_G = V_D = 1V$ is 1.1 mA, corresponding to a sheet resistance of $R_{\square} (1V) = 30 \text{ k}\Omega/\square$.

In the case of electrolyte-gated TFTs, the calculation of carrier mobility from standard transistor equations is problematic because of uncertainty about the accuracy of the figure for specific capacitance C_i .^[35, 57] Therefore, the figure-of-merit μC_i was used, which can be easily and directly extracted from measured characteristics without assumptions about C_i .^[9] Once evaluating saturated transfer characteristics at high gate voltage ($V_G = 0.8V \dots 1V$), the slope of $\sqrt{I_D}$ vs. V_G plot, for EtOH route $\sim 0.02342 \pm 0.00005 \text{ A}^{1/2}/V$ and for mixed route $0.04415 \pm 0.00008 \text{ A}^{1/2}/V$, since $2L/W = 0.06$, the value of μC_i (as described in Chapter 3, Section 3.2.1.3, Equation 3-8) for EtOH-cast films is $33 \pm 0.1 \mu\text{AV}^{-2}$, and $117 \pm 0.05 \mu\text{AV}^{-2}$ for films cast from mixed

solvent, almost 5 times larger. If a specific capacitance (C_i) is considered as $3 \mu\text{F}/\text{cm}^2$, as reported by Kergoat *et al.*,^[57] the electron mobility for EtOH-cast ZnAc-precursor ZnO and mixed-solvent cast ZnAc-precursor ZnO are $10.9 \pm 0.077 \text{ cm}^2\text{V}^{-1}\text{s}^{-1}$ and $39 \pm 0.007 \text{ cm}^2\text{V}^{-1}\text{s}^{-1}$, respectively. It should be noted that such evaluation of mobilities from electrolyte-gated transistors should be treated with caution. However, the near fivefold improvement remains true regardless, as C_i will be equal in both cases.

For comparison, Table 5-2 places our results in context with other results from literature on directly comparable devices, *i.e.* solution-processed ZnO as a semiconductor gated with electrolyte.

Table 5-2

Reference	Preparation	Gate medium	R_o [$\text{k}\Omega/\square$]	μC_i [μAV^{-2}]
Park <i>et al.</i> ^[24]	Li-doped ZnO cast from ammonia solution	Ionic liquid	110 @ 1V	8.3
Singh <i>et al.</i> ^[36]	ZnAc precursor cast from EtOH	PBS	5000 @ 0.5V	1.4
Singh <i>et al.</i> ^[36]	ZnAc precursor cast from EtOH	DI water	77000 @ 0.5V	0.23
Al Naim <i>et al.</i> ^[35]	ZnAc precursor cast from EtOH	DI water	180 @ 0.8V	26
Thiemann <i>et al.</i> ^[37]	ZnAc precursor sprayed from MeOH	Ionic liquid	50 @ 1V	48
This work	ZnAc precursor cast from EtOH	PBS	128 @ 1V	33 ± 0.1
This work	ZnAc precursor cast from EtOH : Acetone	PBS	30 @ 1V	117 ± 0.05

Table 4: Performance characteristics of electrolyte-gated TFTs with solution-processed ZnO.

From Table 5-2 we can conclude that ZnO films from a mixed-solvent route processed ZnAc precursor clearly indicate improved performance compared to any other ZnO films processed from solution. ZnO from a mixed-solvent route displays low sheet resistance and high figure-of-merit (μC_i) even compared to work employing a higher

capacitance gate medium, such as ionic liquid,^[87] or casting dissolved (rather than precursor route) ZnO.^[24]

Mixed-solvent route ZnO also compares favourably with electrolyte-gated organic TFTs, even those using the state-of-the-art hole transporting polymer, Poly(2,5-bis(3-hexadecylthiophen-2-yl)thieno[3,2-b]thiophene) (PBTTT). In Chapter 4, we reported lower sheet resistance R_{\square} (1V) = 640 k Ω / \square for water-gated and 102 k Ω / \square for IL-gated PBTTT. For further comparison we refer to Table 4-1 in Chapter 4, which gives an overview of top performance organic TFTs covering a range of concepts and materials (evaporated and solution processed semiconductors, electrolyte- and 'dry'-gated TFTs, hole and electron transporters). We find the sheet resistance reported here for the ZnO TFT prepared from the ZnAc precursor processed via mixed solvent is significantly lower than the lowest sheet resistances for any organic TFT reported to date.

The estimated carrier mobility of 39 cm²/Vs and low sheet resistance of 30 k Ω / \square in our solution-processed ZnO films is only matched by ZnO films processed by conventional 'dry' methods. Fortunato *et al.*^[31] and Zhang *et al.*^[32] reported electron carrier mobility of 70 cm²/Vs and 60 cm²/Vs from sputtered ZnO and gated by silicon oxynitride (SiO_xN_y) and Ta₂O₅ gate dielectrics, respectively. The electron mobilities are calculated at rather high voltages though (Fortunato *et al.*: 10 V; Zhang *et al.*: 5V). Brox-Nilsen *et al.*^[33] reported electron mobility of 50 cm²/Vs again gated with Ta₂O₅ at a slightly lower voltage (4 V). The highest electron mobility of 110 cm²/Vs for ZnO TFTs was reported by Bayraktaroglu *et al.*^[28] who used pulsed laser deposition to grow ZnO onto a substrate held at 350 °C. However, these direct deposition techniques do not capitalize on the ease of processing accorded by soluble precursor routes, and sheet resistance even in the TFT of Bayraktaroglu *et al.* was R_{\square} (15V) = 25 k Ω / \square . None of Fortunato *et al.*, Zhang *et al.*, Brox-Nilsen *et al.*, and Bayraktaroglu *et al.* report gating with an aqueous electrolyte, which could be fundamental for biosensor applications.

5.1.3 Conclusion

It is well established that the choice of processing solvent plays a critical role in the performance of organic semiconductor devices.^[168] This report shows a similar observation on inorganic semiconductor devices prepared via a solution-processed precursor. We find ZnAc dissolves more readily in a 1:1 mix of ethanol and acetone than in either pure ethanol, acetone, or isopropanol. From SEM results, we find that ZnAc cast from a better solvent gives homogeneous ZnO films without granular morphology. This reflects the absence of solute aggregation in the good solvent used for casting the precursor. The performance of ZnO from a ZnAc precursor in mixed (i.e., good) solvent in TFTs was superior to ZnO cast from poor solvent (pure EtOH), and compares well to previously reported electrolyte-gated TFTs using solution-processed ZnO.

5.2 Zinc Chloride (ZnCl₂) as a Precursor for Solution-Processed ZnO

Given the current interest in the II-VI semiconductor ZnO, a number of routes to prepare ZnO via solution-based processes have been reported in the literature. These include e.g. Zinc nitrate hexahydrate in water and NaOH,^[17] intrinsic Zn(OH)₂, precipitated Zn(OH)₂ and pristine ZnO powder in ammonium hydroxide.^[24, 169] So far, probably the ‘mildest’ (using benign and environmentally acceptable precursors and solvents) route to solution-processed ZnO is via the precursor Zinc acetate (ZnAc) dihydrate in methoxyethanol^[34] or in ethanol.^[35, 36] Semiconducting films of the II-VI semiconductor Zinc oxide (ZnO) then result from pyrolysis (thermally driven chemical conversion) of the solution-deposited ZnAc film into ZnO. Our work on water-gated ZnO TFTs prepared via the ZnAc pyrolysis was reported in Section 5.1 of this thesis. Now, ZnAc is often converted to ZnO by spray pyrolysis directly onto a hot substrate.^[87, 164]

I here report a new precursor route to ZnO via pyrolysis of the Zinc salt, Zinc chloride (ZnCl₂), dissolved in the most environmentally friendly solvent, water.

5.2.1 Preparation and Processing of ZnCl₂ Solution

ZnCl₂ solution was prepared by dissolving 1.36 g of ZnCl₂ in 100 mL of DI water to form 0.1M ZnCl₂ solution. For control experiments we similarly prepared 0.1M Zinc sulphate (ZnSO₄) in DI water; we then sprayed aqueous ZnCl₂ solutions onto heated (450 °C) TFT contact substrates which are described in Chapter 2, Section 2.2.1.1, or ‘fused silica’ spectroscopic substrates for optical study. We used a commercial GaGa Milano 134K airbrush with a 0.2 mm nozzle at 1.5 bar pressure, Fig. 5-12. Spraying was by 3 ‘puffs’ from a 15 cm distance above the contact substrate lasting 1 ... 2 seconds in 20 s intervals. Contact substrates were then kept on the hot plate at 450 °C for 30 more minutes, as was described in Section 2.3.2.2.



Figure 5-12: Picture of sprayed aqueous ZnCl_2 solutions onto heated (450 °C) TFT contact substrates.

5.2.2 Result and Discussion

5.2.2.1 UV-visible Absorption Spectrum

UV-vis absorption spectroscopy is used routinely to examine the optical properties of ZnO nanoparticles and film.^[141] For optical and absorption spectra from sprayed ZnCl_2 , we used spectroscopic substrates, known as ‘quartz’ or ‘fused silica’ substrates. This type of substrate is transparent in the UV region. The film was formed on these substrates as we described in Section 5.2.1. The optical transmission spectrum of the film on quartz substrates resulting from aqueous ZnCl_2 sprayed onto substrates heated to 450 °C is shown in Fig. 5-13 (blue dashes).

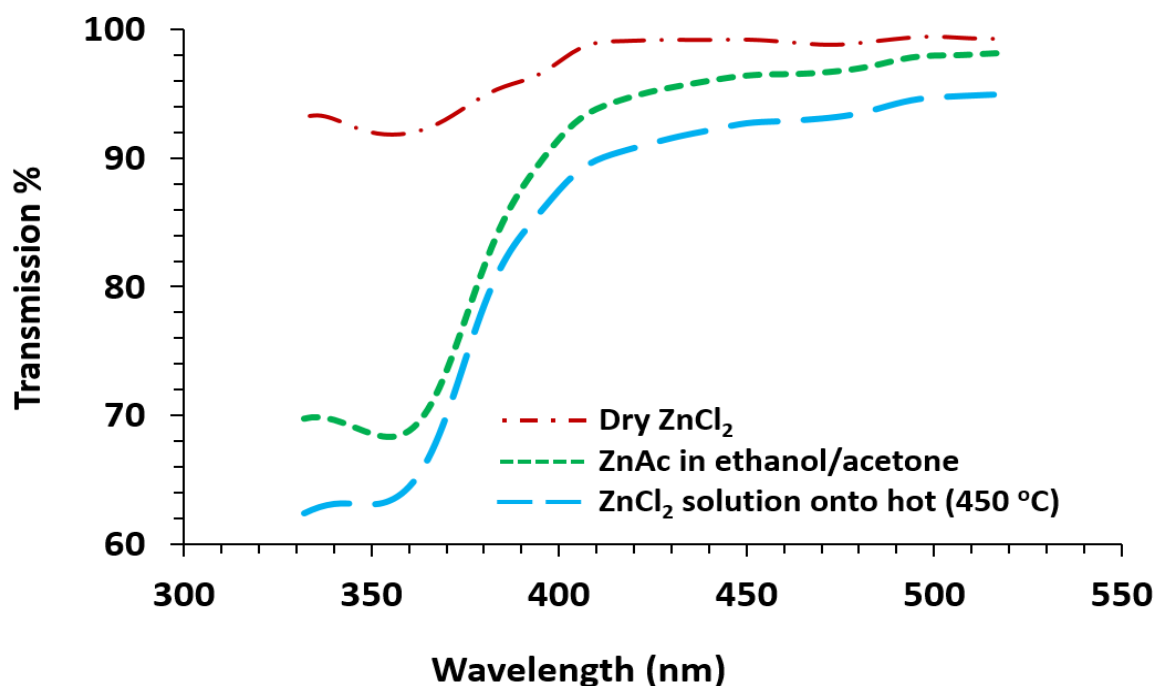


Figure 5-13: Optical transmission spectra for 3 sprayed films: Aqueous ZnCl₂ solution onto hot (450°C) substrate (blue, dashed), ZnAc in ethanol/acetone 1:1 onto hot substrate (green, dotted), aqueous ZnCl₂ solution onto ambient temperature substrate, dried under vacuum, heated afterwards (red, dot dash).

At short wavelengths, optical transmission is limited to ~ 62 %, but the average value of transmittance in the visible range is found to be ~ 95%. The film shows an absorption edge λ_{edge} of ~ 365 nm corresponding to an optical band gap of 3.3 ± 0.02 eV. We compare this transmission spectrum with that of a ZnO film prepared via ZnAc precursor dissolved in mixed ethanol/acetone solvent, as described in Section 5.1 (green dots). It is clear that both films show very similar spectra and absorption edges. This comparison leads to the preliminary conclusion that the pyrolysis of sprayed ZnCl₂ solution has led to the same product, namely Zinc oxide (ZnO). The remainder of Section 5.2 is dedicated to confirming this surprising conclusion beyond doubt, and to developing an understanding of the underlying chemical process.

As a first step to understanding how sprayed ZnCl₂ pyrolyses into ZnO we undertook two control experiments. Firstly, we sprayed ZnCl₂ solution in the same way but onto substrates held at ambient temperature. Then we dried such films under a dynamic vacuum for around 1 h, and only then heated them to 450 °C after drying. The

transmission spectrum for the resulting films (red dot-dash in Fig. 5-13) showed no pronounced ‘absorption edge’ at 365 nm characteristic of semiconducting ZnO. Also these films remained soluble in water, which is in contrast to films resulting from sprayed ZnCl₂ solution on hot substrate, which turned insoluble in water, just like ZnO films resulting from spray pyrolysis of ZnAc. Secondly, we sprayed an aqueous solution of another zinc salt, zinc sulphate (ZnSO₄), onto a hot substrate. Again, the resulting film remained soluble in water and did not show an absorption edge. We therefore conclude that the formation of ZnO from an aqueous ZnCl₂ requires the simultaneous presence of zinc ions, chloride ions, and water, at the time of pyrolysis.

5.2.2.2 X-Ray Photoelectron Spectroscopy Surface (XPS)

For further analysis of spray pyrolyzed ZnCl₂ → ZnO films, we have performed an XPS characterization, using a Kratos Axis Ultra DLD instrument with a monochromated aluminium source. A wide-range XPS survey scan (0 .. 1200 eV) of a spray pyrolyzed ZnCl₂ film now shows a number of peaks that can be assigned and quantified for elemental composition from their peak area, as shown in Fig 5-14 and Table 5-3:

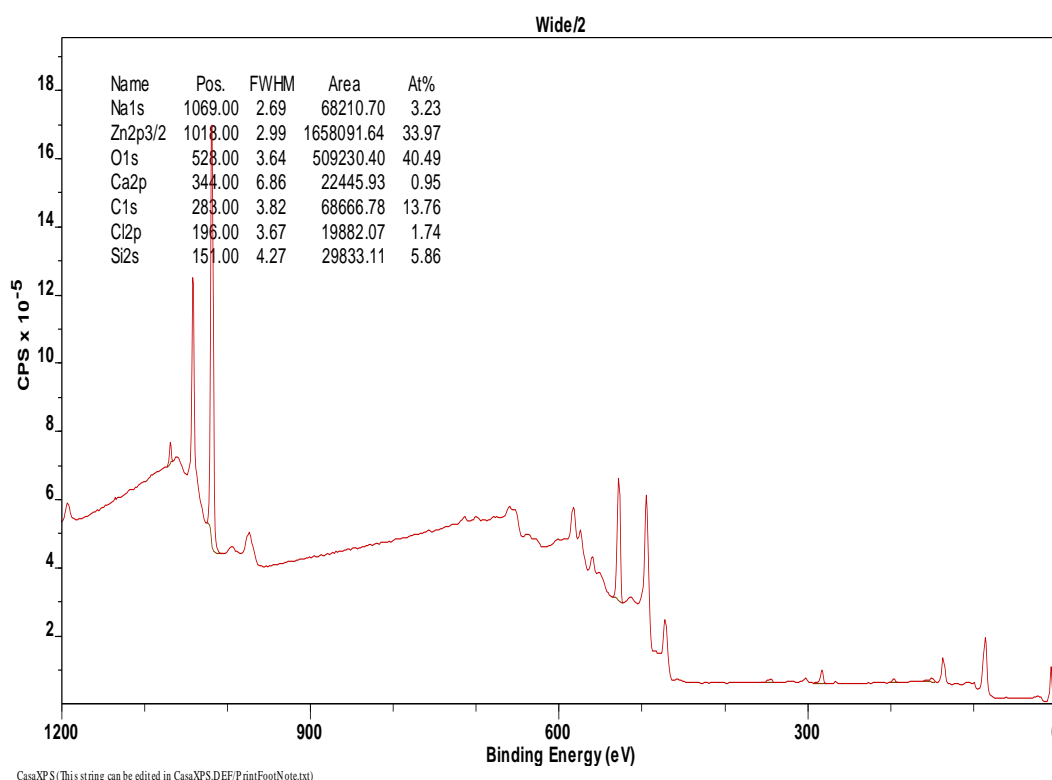


Figure 5-14: Quantified survey scan of of a spray pyrolyzed ZnCl₂ film.

Table 5-3

Approx. Position [eV]	1069	1018	528	344	283	198	151
Assignment	Na 1s	Zn 2p	O 1s	Ca 2p	C 1s	Cl 2p	Si 2s
Atom %	3.2	34.97	40.49	0.95	13.76	1.74	5.86

Table 5: Elemental composition for ZnO film resulting from precursor ZnCl₂.

The surface composition shown in Table 5-3 is dominated by zinc and oxygen, leading to a Zn:O ratio not far from 1:1 consistent with the surface layer being zinc oxide. The slight excess of O over Zn, and the presence of small amounts of Si, Na, and Ca are explained by the use of soda lime glass substrates, which contain Si, Na, Ca, and O. Chloride is likely to be a residue from the ZnCl₂ precursor, but has only a small presence of 1.7%, which is much lower than that in the original ZnCl₂. The organic surface contamination always contains graphitic carbon adsorbed on the surface during exposure of the sample to the ambient atmosphere. For that reason graphitic carbon is used as a reference for ZnO XPS calibration as was mentioned in Chapter 3, Section 3.1.5 and Chapter 5, Section 5.1.2.1.

Zinc peroxide (ZnO₂) consists of the same chemical elements as ZnO; therefore it should be considered that the chemical identity of spray pyrolyzed ZnCl₂ is ZnO₂ instead of ZnO. However, this should lead to a larger (2:1) excess of O over Zn. Also, ZnO₂ is unstable at temperatures above 230 °C and decomposes into ZnO,^[170] and shows a larger and indirect band gap than ZnO^[170] when spectroscopic studies (Fig. 5.13) showed the same direct band gap for spray pyrolyzed ZnCl₂ films as for ZnO. We can therefore exclude ZnO₂.

For more detailed analysis, we again studied highly resolved spectra of O 1s and Zn p XPS peaks, 5-15 and 5-16, similar, as before, to ZnO films derived from pyrolyzed ZnAc (Fig. 5-2 and Fig. 5.4) In Fig. 5-15, the O 1s peak is deconvoluted into 3 overlapping Gaussian peaks centred at 530.2 eV, 531.5 eV, and 532.7 eV labelled A, B, and C. The strongest is located at (A) 530.2 eV, with two weaker peaks at slightly higher binding energies (531.5 eV, 532.7 eV). Peak (A) was attributed to oxygen in the ZnO lattice, peak (B) was assigned to oxygen deficient regions in the ZnO matrix,^[36]

peak (C) was associated to hydroxide (-OH surface groups), or to oxygen defects, i.e. oxygen outside the lattice structure.^[36] In Fig. 5-16, we find the Zn 2p peak is split into the Zn 2p_{3/2} and Zn 2p_{1/2} doublet at 1021 eV/1045 eV. The positions and values of both O 1s and Zn 2p peaks are in the range of what was found in previous reports.^[144, 145, 147, 148] However, since the Zn 2p XPS doublet is rather insensitive between metallic zinc and ZnO, we also studied the Zn LMM Auger peak, as seen in the inset Fig. 5-16. The LMM Auger peak is located at 988 eV which agrees with Zn bonded to oxygen, rather than metallic zinc or any other common zinc compound.^[143]

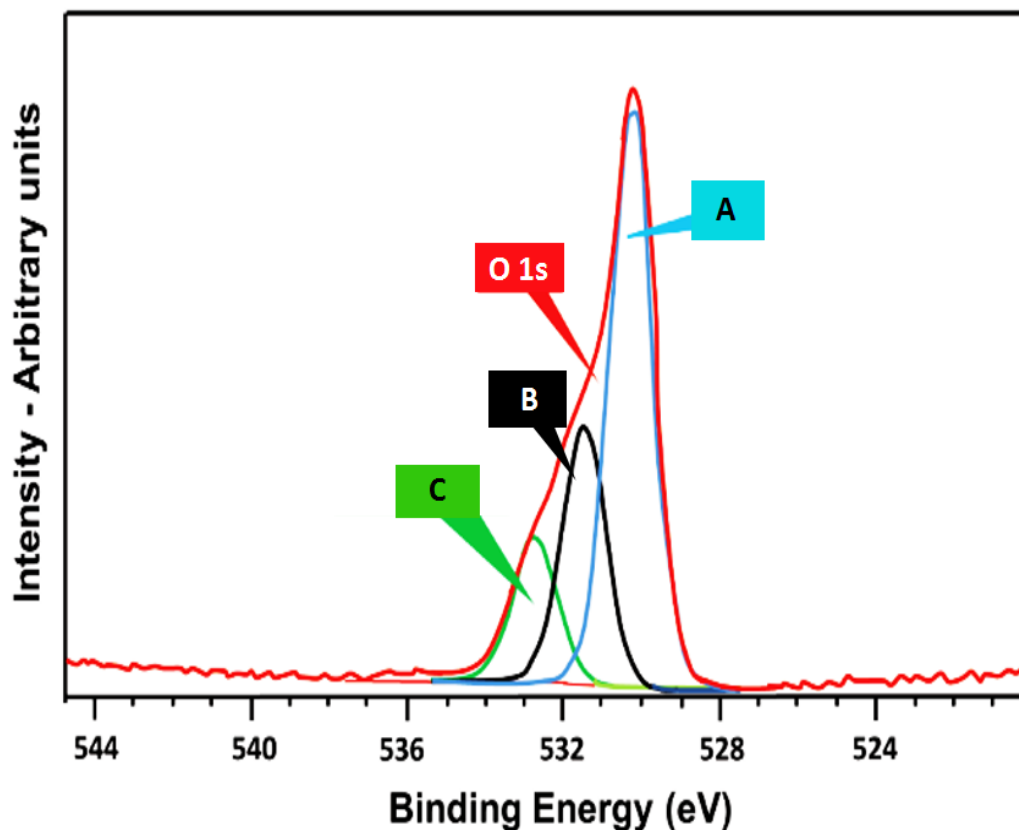


Figure 5-15: Highly resolved XPS spectra of spray pyrolyzed films in the O 1s peaks, A: represents ZnO, B: denotes oxygen deficient region in ZnO matrix, and C assigns hydroxide (-OH surface groups), or to oxygen defects.

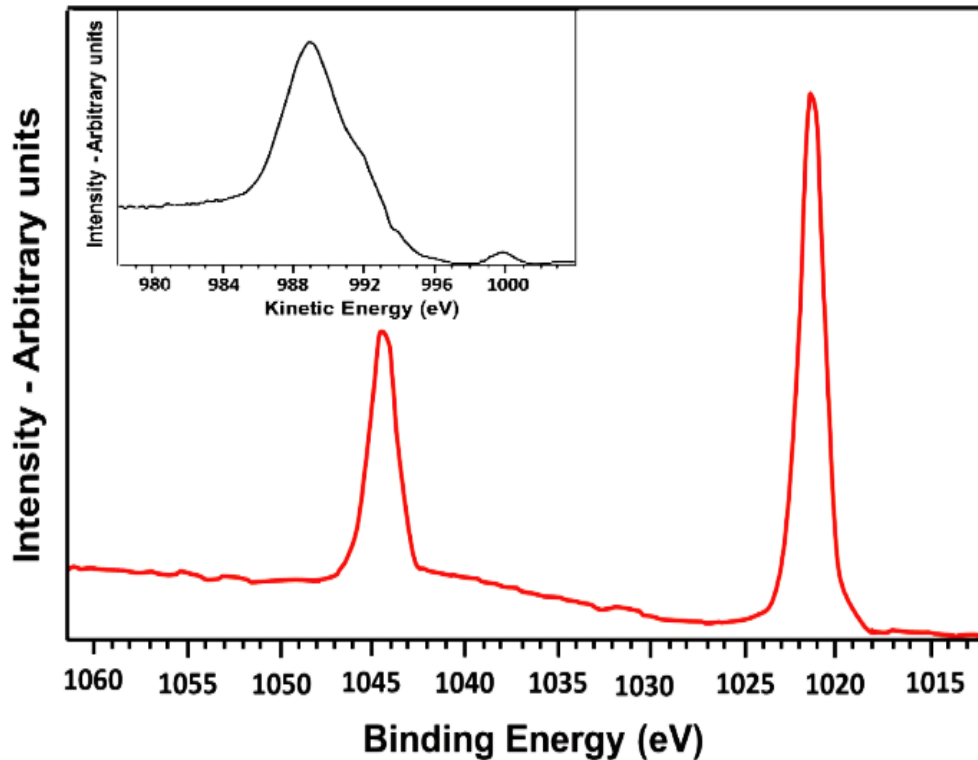


Figure 5-16: Highly resolved XPS spectra of spray pyrolyzed films in the Zn 2p peaks at 1021 eV / 1045 eV. Note the splitting of Zn 2p into Zn 2p_{3/2} and Zn 2p_{1/2}. Inset: Zn LMM Auger peak at ~ 988 eV.

XPS studies on spray pyrolyzed ZnCl₂ are therefore fully consistent with the identification of resulting films as ZnO. However, XPS does not allow a determination of the crystal structure of ZnO, which may be either wurtzite or zincblende, but the thermodynamically stable wurtzite structure is most likely.^[23]

5.2.2.3 Electrolyte-gated ZnO TFT Electrical Characteristics

Semiconducting properties of spray pyrolyzed ZnCl₂ films were tested electrically using Keithley 2400 source/measure units to record TFT output and transfer characteristics. We used TFT contact substrates (described in Chapter 2, Section 2.2.1.1) and covered the pad contacts with glass before spraying, so only the active area is exposed to sprayed solution. Then we sprayed ZnCl₂ onto substrates held at 450°C. After spraying, the substrates were kept on the hot plate for 30 more minutes. After that, substrates were left at room temperature to cool down.

A droplet of DI water was then applied on the top of the active area of TFT and electrically addressed by an L-shaped tungsten (W) gate needle. Because the surface of ZnO is hydrophilic, the gate needle was lowered to a very close proximity (200 μm adjusted by a glass cover slip used as a spacer) using a probe head. The L-shaped gate needle was orientated along the width of the transistor channel, in a similar way to previous work described in Section 5.1. Source and drain contacts were electrically addressed by tungsten (W) needles, as seen in Fig. 5-17. All measurements were carried out under ambient atmosphere.

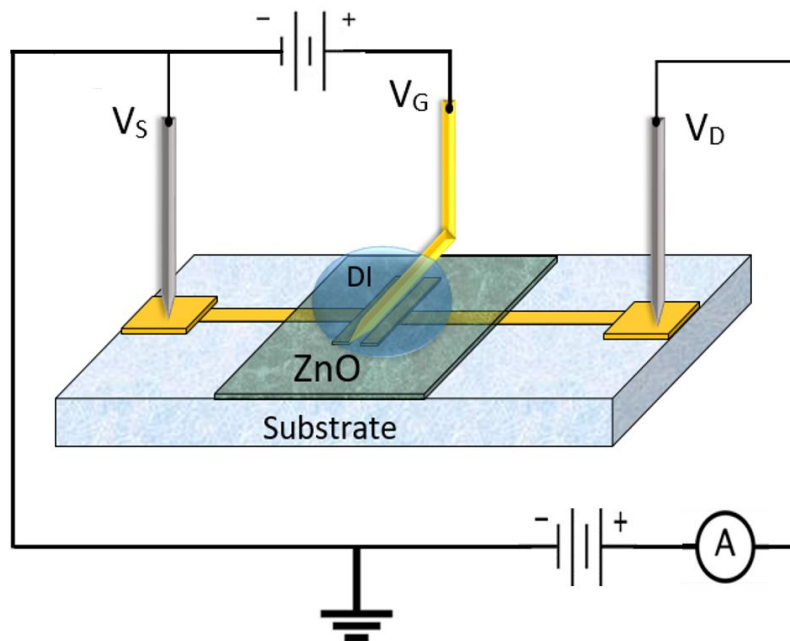


Figure 5-17: Scheme of water- gated TFTs using films of spray pyrolysed aqueous ZnCl_2 solutions.

First we tested a blank substrate and a non-gated spray pyrolyzed ZnCl_2 film; we found the sheet resistance was at least $330 \text{ G}\Omega/\square$ and $10 \text{ G}\Omega/\square$, respectively, meaning low doping levels.

Fig. 5-18 shows the resulting output characteristics and Fig. 5-19, and Fig. 5-20 display the transfer characteristics for water-gated TFTs using spray pyrolyzed ZnCl_2 films in their channel. Characteristics clearly show field effect transistor action for positive drain-and gate voltage, as expected for a TFT with an electron-transporting semiconducting channel, like ZnO. The saturation for $V_D > V_G$ can be seen in the

output characteristics (Fig. 5-18), and a threshold voltage from the (linear) transfer characteristic for the tungsten (W) gate can be estimated as $V_{th} \sim 0.2$ V (Fig. 5-19), which is similar to the threshold voltage of ZnO resulting from ZnAc pyrolysis via mixed solvent (described in the previous Section 5-1) and also it is similar to previous reports.^[35, 36] As we described before, such a low threshold voltage results from the high capacitance of EDL in electrolyte gate media.^[57] The saturated drain current $I_{D,sat}$ at $V_G = V_D = 0.6$ V is ~ 72 μ A, corresponding to a sheet current (*cf.* Equation 4-1) $I_{\square}(0.6$ V) = $L/W * I_{D,sat}(0.6V) = 2.16$ μ A/ \square , and a sheet resistance (*cf.* Equation 4-2) of $R_{\square}(0.6$ V) = $W/L [V_D = 0.6V / I_{D,sat} = 72 \mu A] = 278$ k Ω / \square .

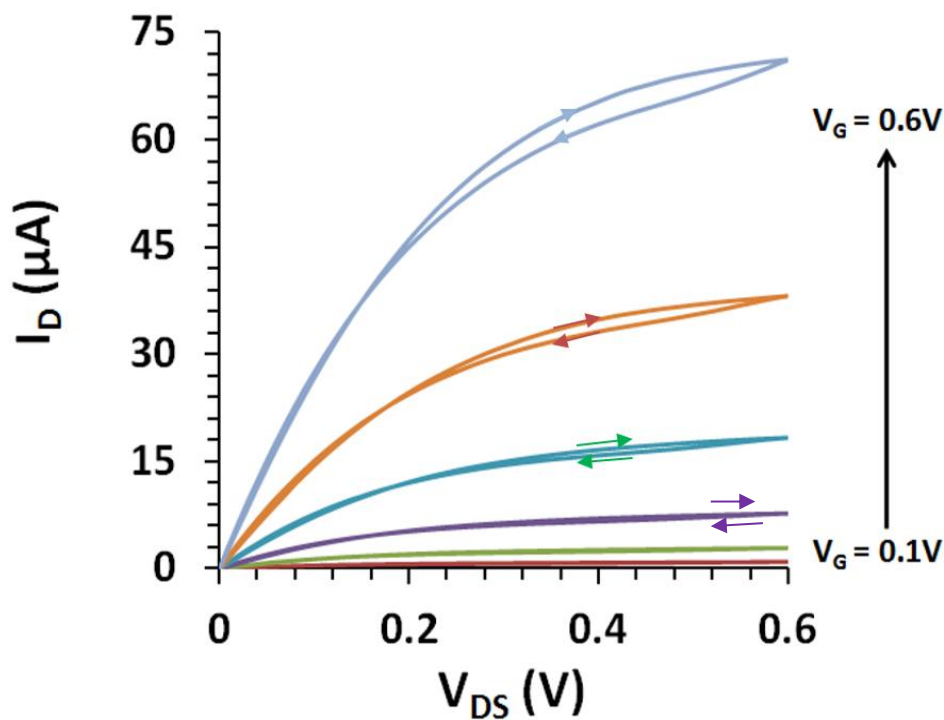


Figure 5-18: Output characteristics of water- gated TFTs using films of spray pyrolysed aqueous ZnCl₂ solutions in the transistor channel.

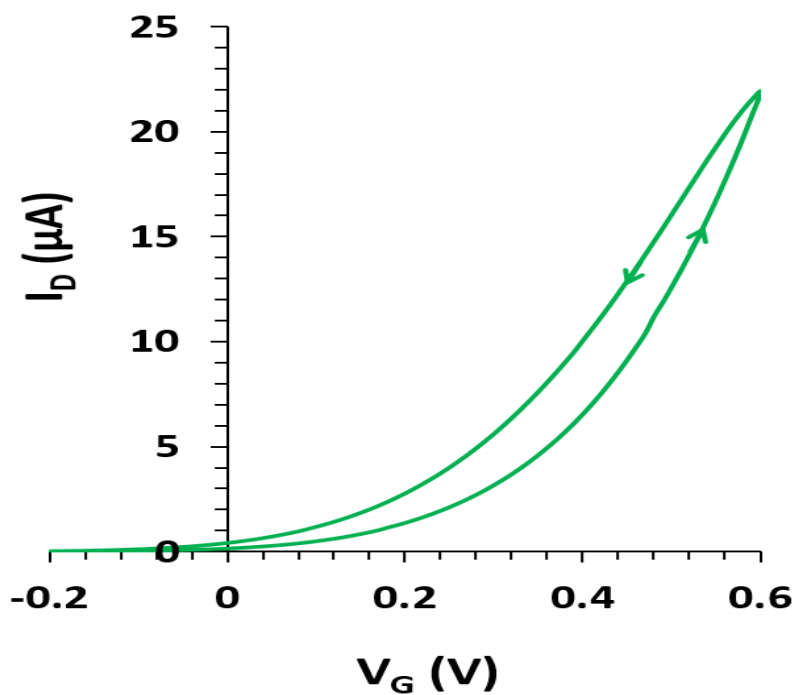


Figure 5-19: Linear transfer characteristics ($V_D = 0.1$ V) of water-gated TFTs using films of spray pyrolysed aqueous $ZnCl_2$ solutions in the transistor channel.

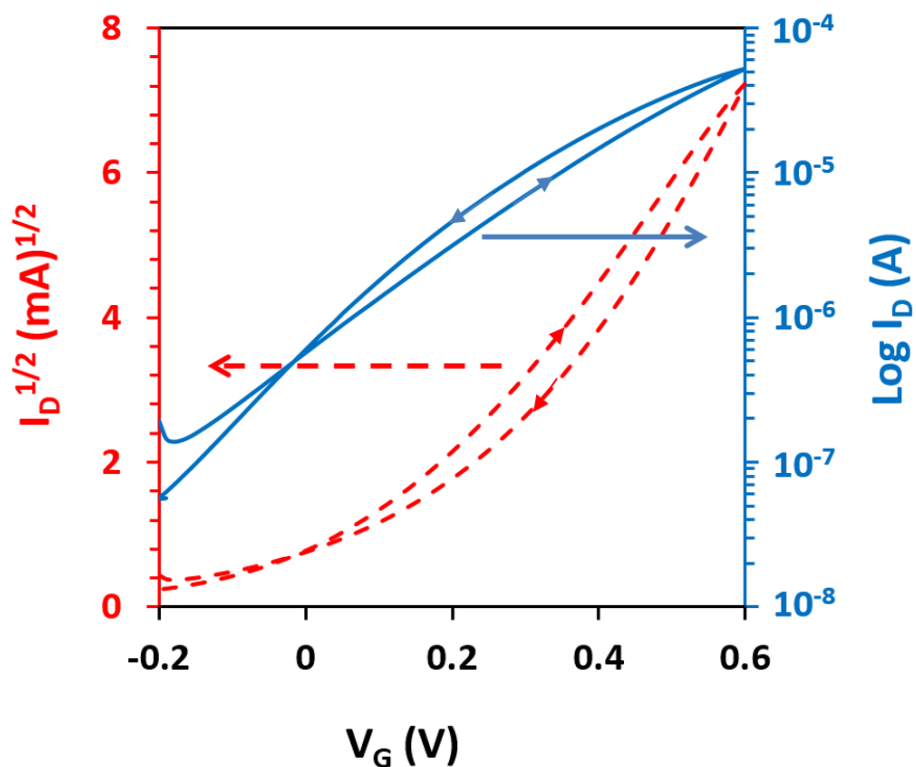


Figure 5-20: Saturated transfer characteristics of water-gated TFTs using films of spray pyrolysed aqueous $ZnCl_2$ solutions in the transistor channel. Root (red dashed) and log (blue) drain current scales.

By comparing these performance characteristics with water-gated TFTs using ZnO prepared via the ZnAc EtOH-route (Section 5-1), these characteristics are shown to be similar, e.g. $I_{\square} (1 \text{ V}) = 7.9 \mu\text{A}/\square$ and $R_{\square} (1 \text{ V}) = 128 \text{ k}\Omega/\square$. Also, our performance characteristics of ZnO TFT resulting from spray pyrolysis of the ZnCl₂ solution are similar to those in previous water-gated TFTs using ZnO prepared via the ZnAc precursor route by Al Naim *et al.*,^[35] which reported $I_{\square} (0.8 \text{ V}) = 4.4 \mu\text{A}/\square$ and $R_{\square} (0.8 \text{ V}) = 180 \text{ k}\Omega/\square$. We can take the on/off ratio from Fig. 5-20 as ~ 300 , and the inverse subthreshold slope (S^{-1}) as $215 \pm 0.1 \text{ mV/decade}$. Our ZnCl₂ derived films perform similarly to the water-gated ZnAc precursor route ZnO TFTs reported in the literature^[35, 36] and to that in the previous Section 5-1. This again supports our conclusion that spray pyrolysis of water-borne ZnCl₂ does indeed lead to semiconducting ZnO.

For a better understanding of the process leading from ZnCl₂ to ZnO, we performed electrical control experiments, as we did for optical characterization. In this case we sprayed aqueous ZnCl₂ solutions onto TFT substrate at an ambient temperature, dried under vacuum for 1 h, and heated after drying to 450 °C. On the other hand, we sprayed aqueous ZnSO₄ onto the TFT substrate held at 450 °C. We found that the films resulting from both control experiments are soluble in water which make them difficult to gating and TFT characterization did not lead to drain current, or recognisable transistor characteristics.

Furthermore, we also studied the minimum required substrate temperature for successful spray pyrolysis of ZnCl₂ to convert to ZnO. We sprayed ZnCl₂ solutions onto TFT substrates held at temperatures ranging from 150 to 400 °C. From experiments we found that substrates held at 250 °C gave TFTs with similar properties to those reported in Fig. 5-18 and Fig. 5-20, but not for substrates held at 200 °C or below. In addition, spraying fewer than 3 ‘puffs’ did not lead to working devices. We used a Veeco Dektak XT surface contact profilometer (described in Section 3.1.2) to measure the film thickness for 3 puffs; the result showed a film thickness of $\sim 85 \text{ nm}$, but significant surface roughness up to $\sim 40 \text{ nm}$.

5.2.3 Conclusion

Films resulting from spray pyrolysis of aqueous ZnCl_2 exhibit the same insolubility in water, optical absorption edge, XPS and Auger spectra, and semiconducting properties in TFTs as ZnO. We therefore conclude that they are ZnO. Although zinc peroxide (ZnO_2) consists of the same chemical elements as ZnO, we can exclude the possibility that our films consist of zinc peroxide. ZnO_2 is unstable above 230 °C,^[170] hence would decay at the pyrolysis temperature we used. Also ZnO_2 has a larger (and indirect) band gap (3.8 eV \longleftrightarrow 327 nm), which is incompatible with what we observed in Fig. 5-13. Our spectra match the 100% ZnO spectra reported in a comparison of ZnO_2 vs. ZnO by Audrey.^[171] XPS elemental proportions also support that our film is ZnO over ZnO_2 . For all the results above we therefore identify it as ZnO.

From control experiments, we find that, the simultaneous presence of zinc ions, chloride ions, and water, is required at the time of pyrolysis for the formation of ZnO from an aqueous ZnCl_2 . Both control experiments where either water or chloride are absent at the time of (attempted) pyrolysis, did not lead to ZnO semiconducting films. Therefore, we believe that the actual ZnO precursor is the $\text{ZnCl}_x\text{H}_2\text{O}_{(4-x)}$ species that forms when ZnCl_2 salt dissolves in water.^[172, 173] This species obviously depends on the simultaneous presence of zinc ions, chloride ions, and water. We cannot precisely define the reaction mechanism leading from $\text{ZnCl}_x\text{H}_2\text{O}_{(4-x)}$ to ZnO, but it is interesting to mention that the synthesis of zinc peroxide (ZnO_2) nanoparticles from aqueous ZnCl_2 solution has been reported by Chen *et al.*^[170] ZnO_2 thermally converts into ZnO at 230 °C.^[170] Similarly, we find a minimum required substrate temperature of 250 °C for formation of semiconducting films from sprayed ZnCl_2 solution. While we can exclude ZnO_2 in the resulting film, it may transiently appear as an intermediate on the route from $\text{ZnCl}_x\text{H}_2\text{O}_{(4-x)}$ to ZnO.

Regardless of the precise nature of the precursor and its conversion mechanism, I can report a new solution-based precursor route to a high performance inorganic semiconductor, ZnO, using only easily available and environmentally benign chemicals, namely ZnCl_2 and water. Also, the substrate temperature required for

pyrolysis is only 250 °C, considerably lower than for ZnO from the ZnAc precursor route in the previous Section 5-1 and in the literature.^[34-36]

I have here shown one potential application for ZnO prepared from spray pyrolysis of aqueous ZnCl₂, namely in water-gated TFTs. However, given the many potential applications of ZnO in the initial overview in this chapter, this is only one of many possibilities. For example, ZnO can be used as a transparent film for thermal management in large windows and glass curtain walls. Currently, this is by a later application of ZnO-containing thermal management films.^[174] However, a ZnO coating could instead be deposited by spraying water-borne ZnCl₂ onto hot window panes immediately, during manufacture. Unlike ZnAc precursor spraying, this process would release only water vapour rather than solvent fumes.

6 Water-gated Thin Film Transistors as Sensors for Water-borne Analyte

In 2010, Horowitz *et al.*^[57] demonstrated that OTFTs can be gated via a field effect by using DI water as an electrolytic gate medium. This discovery marks the beginning of a new family of ‘electrophysical’ rather than electrochemical transducers for water-borne analytes, wherein the sample under test is an active part of the transducer, namely, a water-gated thin film transistor (WGTFT). This offers an alternative e.g. to the traditional ISFET, which employs ‘dry’ (dielectric) gate insulators without direct contact between the water-borne analyte and semiconductor.^[175]

Water-borne cations may represent either valuable micronutrients (Na^+ , K^+ , Ca^{2+} ,...) or deadly poisons (Hg^{2+} , Cd^{2+} , Pb^{2+} ,...).^[176, 177] The detection of dissolved cations in natural water is therefore considered one of the most important subjects in sensor technology, being of extensive interest in biology and medical fields.

The selective response of WGTFTs to water-borne ions has since been demonstrated by introducing suitable sensitizer layers into the transistor architecture.^[56, 108] Transduction is via the WGTFT which is sensitive to interfacial potentials that build up across such sensitizer layers when in contact with solutions of water-borne cations. A detailed description of such devices, suitable sensitizers, and a quantitative description of threshold shift are given in Chapter 1, Section 1.7.3 of this thesis.

In this chapter, I present my work on cation-sensitive WGTFTs. Section 6-1 presents the discovery that the organic semiconductor PBTTT acts innately in response to some water-borne cations. In Section 6-2, I demonstrate a simplified water-gated OTFT architecture for selective detection of water-borne cations. In both cases, WGTFTs respond to water-borne cations without the need for separate sensitizer layers.

6.1 Innate sensitivity of PBTTT to divalent water-borne cations

In this section, I show that water-gated OTFTs employing the organic semiconductor PBTTT (described in Chapter 1, Section 1.5.4.2), display sensitivity to water-borne divalent cations, and selectivity between mono and divalent cations, without introducing sensitizers. Sensitivity and selectivity are innate to PBTTT itself.

6.1.1 Experimental Section

6.1.1.1 Device Fabrication

TFT contact substrates were fabricated as described in Chapter 2, Section 2.2.1.1. Briefly, 5 source/drain gold contact pairs per substrate with a geometry width/length (W/L) = 1 mm/30 μm = 33 were fabricated through a shadow mask using a high vacuum evaporator to deposit first a 5 nm Cr adhesion layer, and then 120 nm Au. A casting solution of an organic semiconductor (PBTTT) and poly(3-hexylthiophene) (rrP3HT) were prepared as described in Chapter 2, Section 2.3.1.1. Briefly, 7 mg/ml of PBTTT and 10 mg/ml of rrP3HT were dissolved in 1,2 dichlorobenzene (DCB) at 100 °C and filtered with a 0.45 μm PTFE syringe filter. Thin films of semiconducting rrP3HT and PBTTT were formed on TFT contact substrates, as described in Chapter 2, Section Section 2.3.1.1, by spin casting. Films were then dried using a dynamic vacuum at 180 °C for 30 min. Inorganic semiconducting ZnO resulting from the ZnAc precursor cast from mixed solvent (described in Chapter 5, Section 5.1) was used for control experiments. Also, a rrP3HT cast solution was deliberately doped with 4% wt/wt of the Pd(0) complex tris(dibenzylideneacetone)dipalladium(0) [Pd₂(dba)₃], sourced from Aldrich, and used in another control experiment.

For cation sensing tests, different stock solutions (concentration of 0.1M) of different chloride salts were prepared, including monovalent alkali metals such as sodium (Na) and potassium (K), divalent alkaline earth metals such as calcium (Ca), magnesium (Mg), barium (Ba), and the divalent transition metal Zn. These stock solutions were prepared as follows: 14.7 g of CaCl₂·2H₂O, 58.44g of NaCl, 74.55g of KCl, 20.82g of BaCl₂, 20.33 g of MgCl₂, and 13.63g of ZnCl₂ were dissolved in 1L of DI water. CaCl₂

solutions were subsequently diluted 10-fold repeatedly from 0.1M stock solutions down to 1 μM .

6.1.1.2 Electrical Characteristics

Keithley source/measure units (as described in Chapter 3, Section 3.2.1) controlled by a LabVIEW routine were used to record output and linear transfer characteristics. For electrolyte gating, around 1 μL droplets of DI water and sample solutions as gate media were placed via a microliter syringe over the channel area of the PBTTT OTFT substrates. TFTs were electrically addressed using an L-shaped gold gate needle (for organic semiconductor) or tungsten gate needle (for ZnO) (gate needles sourced from American Probe and Technologies). L-shaped gate needles were held at a fixed distance ($\sim 100\mu\text{m}$) from the surface of the semiconductor by means of a probehead. TFT substrates were discarded after a single test cycle (DI water/test solution/DI water) in order to exclude biasing due to irreversible effects of prior exposure. After a single use, gate needles were rinsed with DI water.

OTFTs linear transfer characteristics were recorded by sweeping V_G from 0 to -0.6 V and back to 0 V in steps of 0.02 V at fixed $V_D = -0.1$ V; voltage signs were reversed for ZnO. All measurement were taken under an ambient atmosphere. Threshold voltages V_{th} were extracted from linear transfer characteristics, (as described in Chapter 3, Section 3.2.1.3), by linear extrapolation of drain current $I_D(V_G)$ curves to $I_D = 0$. The change of threshold voltage due to cation concentration c , $\Delta V_{th}(c)$, was calculated as the difference between V_{th} under cation vs. V_{th} under DI water measured on the same substrate immediately before. The product of (linear) carrier mobility and specific gate capacitance, μC_i , were evaluated, as described in Chapter 3 Section 3.2.1.3, *c.f.* Equation 3-7. Results are reported as figure-of-merit μC_i rather than μ itself because the specific capacitance of electrolyte solutions is not accurately identified, and will differ with concentration of cations.

6.1.2 Results and Discussion

Fig. 6-1 displays the output characteristic of PBTTT OTFT gated with DI water.

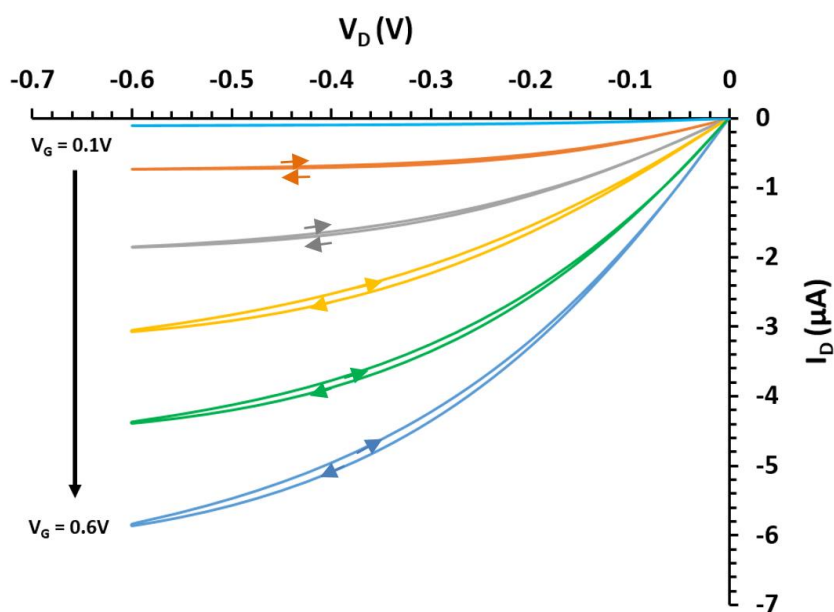


Figure 6-1: Output characteristics of water-gated PBTTT OTFTs.

The output characteristic (Fig. 6-1) for a water-gated PBTTT film is close to ideal, with very little hysteresis and a low threshold between 0V and 0.1V. The estimated carrier mobility, by assuming a specific gate capacitance of $3 \mu\text{F}/\text{cm}^2$,^[57] is about $0.7 \pm 0.001 \text{ cm}^2/\text{Vs}$.

The responses of PBTTT TFTs gated with 0.1M solutions of various cations display a significant difference between mono and divalent cations. The response (i.e., threshold shift) was too weak to be quantified when PBTTT TFTs were gated with monovalent cation solutions (Na^+ , K^+) (see Fig. 6-5a below), as compared to gating with DI water. However, when PBTTT TFTs were gated with 0.1M solutions of divalent cations (Ca^{2+} , Mg^{2+} , Ba^{2+} , Zn^{2+}), the threshold displays a strong response, without introducing any sensitizers (Fig. 6.2 and Fig. 6.5b). For that reason, divalent cation (Ca^{2+}) solutions spanning five orders of magnitude in concentration (1 μM to 100 mM) were used to study the quantitative extent of that response.

Fig. 6-2 shows linear transfer characteristics of water-gated PBTTT OTFTs gated with CaCl_2 solutions with concentrations from 1 μM to 100 mM. Characteristics at each concentration are referenced to a linear transfer characteristic of the same device under DI water. The 1 μM Ca^{2+} linear transfer characteristic is similar to the DI water transfer characteristic. However, with concentrations higher than 1 μM , it is

immediately evident that increasing Ca^{2+} concentration causes an increasing threshold, and decreasing carrier mobility. This is a remarkable observation because no cation-sensitive component was deliberately introduced to the OTFT, like the sensitized PVC membranes in the work of Schmoltnner *et al.* [56] and Melzer *et al.* [108] or in a similar manner to the Section 6-2. In this case it is obvious that the threshold shift is an innate property of the PBTTT OTFT itself. Nevertheless, Ca^{2+} can be sensed with a similar limit-of-detection (LoD) of $\sim 1\mu\text{M}$, as Schmoltnner *et al.* [56] found for Na^+ . The 'off' currents (I_D at reverse bias gate voltages) remain low even under a high Ca^{2+} concentration.

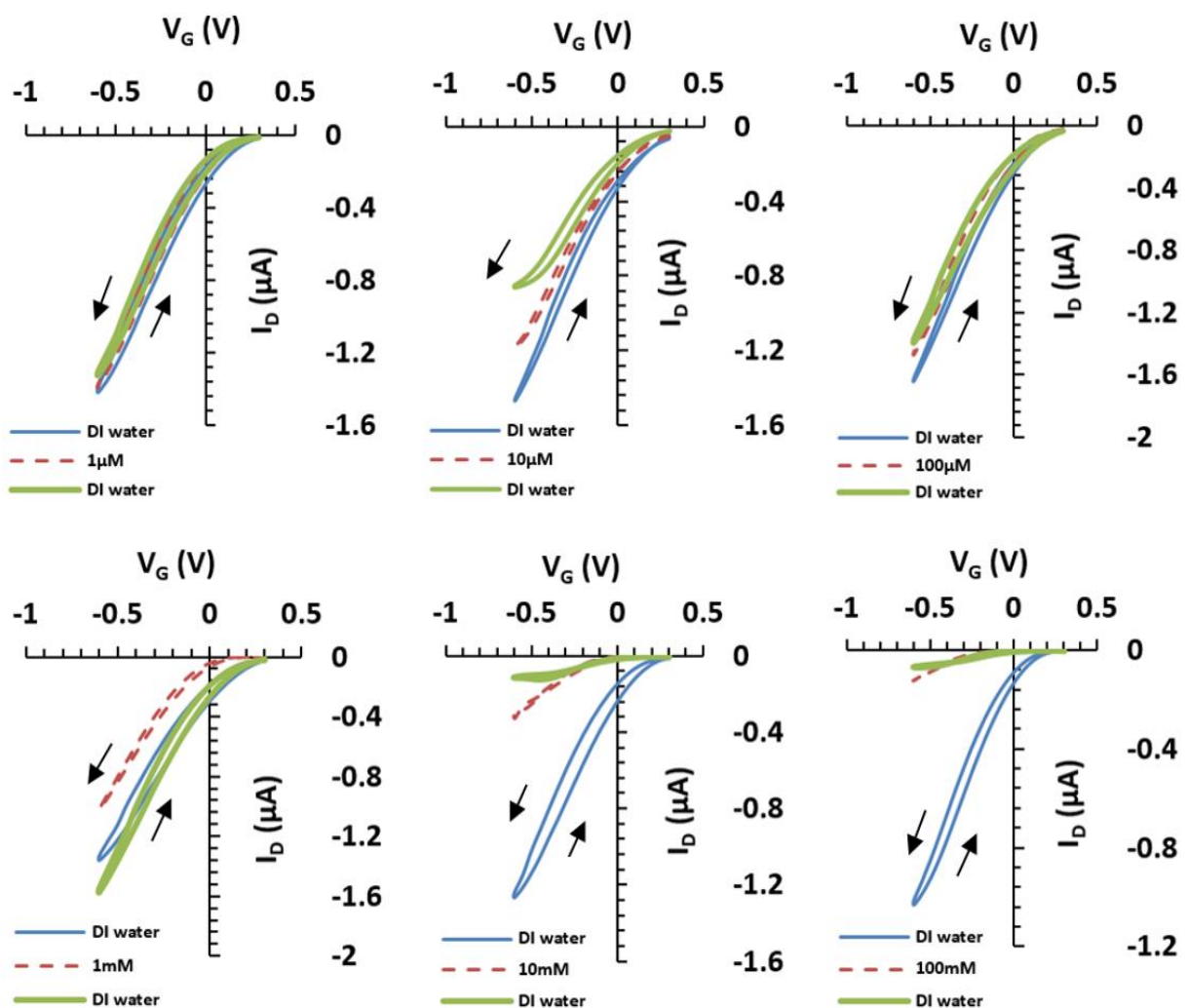


Figure 6-2: Linear transfer characteristics of water-gated PBTTT OTFTs with different CaCl_2 concentrations (red), each referenced to same characteristic taken under DI water (blue) immediately before and (green) DI water immediately after. Substrates were discarded after single use. Hysteresis arrows are the same for DI and CaCl_2 .

As mentioned in Chapter 3, the value of the threshold voltage (V_{th}) can be extracted from linear transfer characteristics plotted on a linear I_D scale by linear extrapolation of the linear transfer characteristics from high gate voltages to the intercept with the gate voltage axis ($I_D = 0$). Such extrapolation requires some judgement down to what gate voltage the linear characteristics is considered truly linear. The following figure shows 3 possible fits to the same characteristics, including a perceived 'best' fit (in red), and a perceived upper/lower limit (blue dashes / solid green line), leading to three alternative (but similar) readings of threshold.

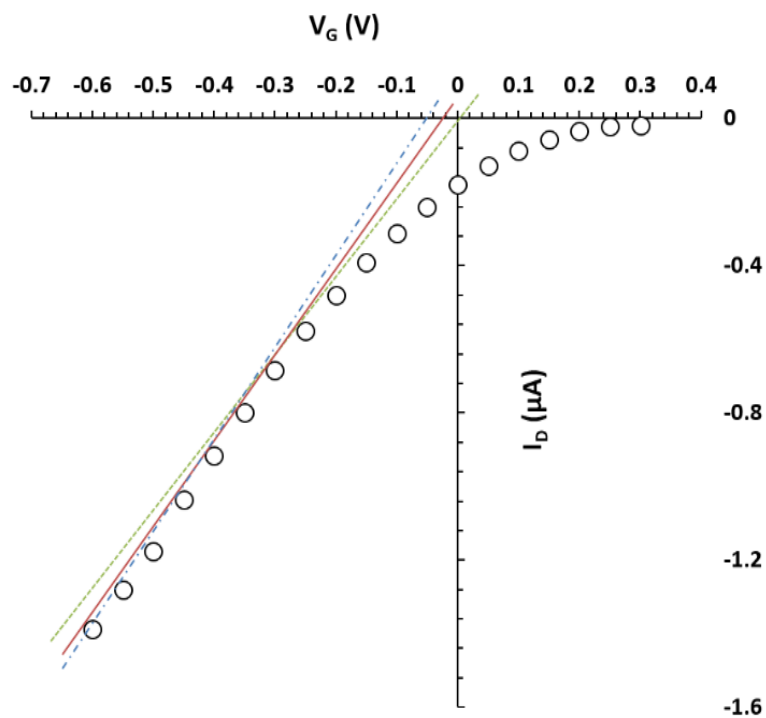


Figure 6-3: The alternative values of threshold shift ΔV_{th} that can be extracted from the same linear transfer characteristics plotted on a linear I_D scale by linear extrapolation to $I_D = 0$.

Table 6-1 shows all three readings, their mean, and standard deviation, when the set of characteristics shown in Fig. 6-2 are evaluated in the way illustrated in Fig 1; $1 \mu\text{M}$ CaCl_2 corresponds to Fig. 6-3.

Concentration	$V_{th(1)}$	$V_{th(2)}$	$V_{th(3)}$	Mean [mV]	Standard deviation [mV]
1μM	3.1	5.0	2.1	3.40	1.5
10μM	22.5	30	33	28.5	5.4
100μM	80.2	55.4	60.0	65.20	13.2
1mM	130	137.6	121.7	129.76	7.0
10mM	184.5	180.3	175.6	180.13	4.7
100mM	240	250.9	255.1	248.66	7.8

Table 6-1: shows all three readings, their mean, and standard deviation, when the set of characteristics shown in Fig. 6-2.

This method was applied always when extracting threshold from linear transfer characteristics presented in this thesis. The error bars shown in all plots of threshold voltage are given by the corresponding standard deviations.

As was described in Chapter 1, Section 1.7.3, the quantitative analysis of cation complexation can be explained approximately by the Nernst equation (1-21), or better by its refinement, the Nikolsky-Eisenman equation (1-25). Briefly, the Nernst and Nikolsky-Eisenman equations can be written as:^[56, 107]

$$\Delta V_{th} = s \Delta \log(a) \quad (6 - 1a)$$

$$\Delta V_{th} = s \Delta \log(a + a_{st}) \quad (6 - 1b)$$

where s is the Nernst slope or slope of calibration curve given by $58.16/z$ mV/decade at $T = 20$ °C with z as the valency of the detected ions; here $z = 2$ and then $s = 29.08$ mV/decade; a is the ion's activity, and a_{st} is a constant characteristic of the respective cation-sensitive system and it is related to the limit of detection (LoD). Ion activity (a) is related to analyte concentration c ; in the limit of low concentration a is proportional to c , hence $\Delta \log a = \Delta \log c$. At high concentration ($c \gg c_{st}$), Equations 6-1a and 6-2b are virtually identical. However, at low concentrations in the order c_{st} and below, a limit-of-detection (LoD) can be predicted by the Nikolsky-Eisenman equation (6-1b), since $c_{LoD} \sim c_{st}$. LoD is practically detected but is not reflected by the Nernst equation which unrealistically tends to $-\infty$ for $c \rightarrow 0$.

The value of c_{st} can be estimated by using the following method: plot the observed ΔV_{th} data against $\log c$ and fit a straight line at high concentrations in order to estimate the slope s . Then, extrapolate the fit line to low concentration and find the concentration where measured data stand above the extrapolated high c straight line by $s \log 2 = 17 \pm 0.15$ mV. According to Equation 6-1b, the value of this concentration equals c_{st} .

In Fig. 6-4, we show the threshold shifts under different concentrations of Ca^{2+} , extracted from Fig. 6-2, plotted vs. $\log c(Ca^{2+})$. At high c , we find Nernstian behaviour with a good straight line fit. At low c , we observe a limit of detection, where the response characteristic flattens. The above described method gives $c_{st} = 4.5 \pm 0.02 \mu M$ ~ limit-of-detection (c_{LOD}). Finally ΔV_{th} vs. $\log (c + 4.5 \pm 0.02 \mu M)$ was plotted, as seen in the inset of Fig. 6-4. This gives a good straight line fit with a slope $s = 55 \pm 2.7$ mV/decade. Remarkably, this value is close to the slope 59.16 mV/dec predicted for a single valency ion ($z = 1$) (e.g. Na^+), rather than for a double valency ion ($z = 2$) like Ca^{2+} . This point will be addressed in the conclusions.

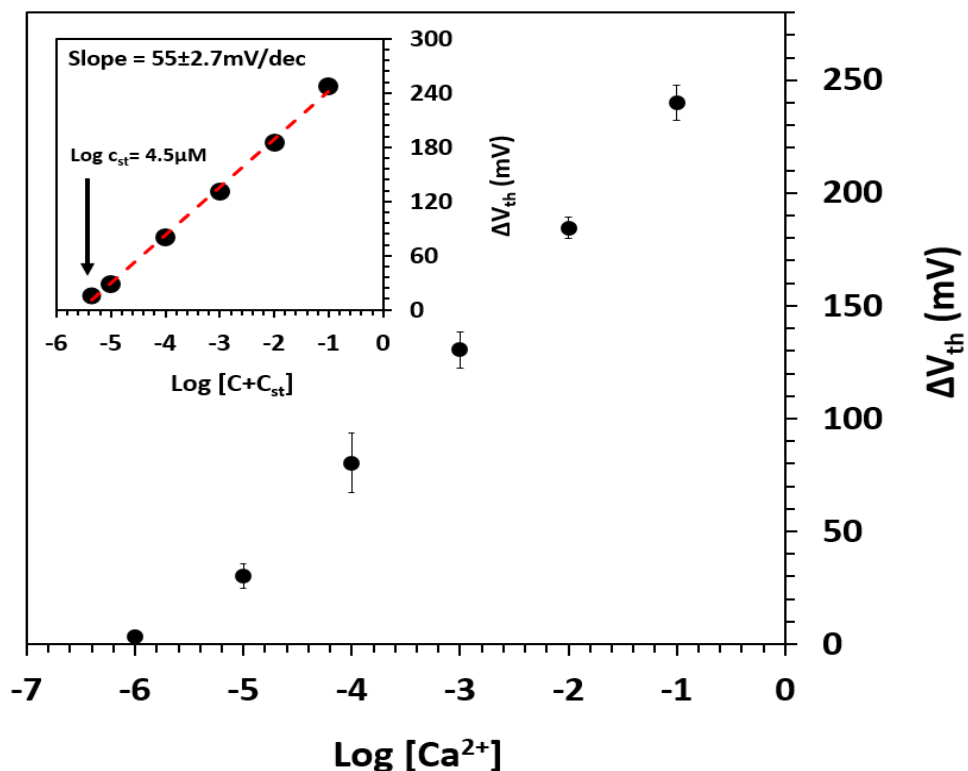


Figure 6-4: Threshold shift ΔV_{th} vs. $\log (c)$ scale and vs. $\log (c - c_{st})$ scale (inset, $c_{st} = 4.5 \mu M$). Slope s in the inset is 55 ± 2.7 mV/decade.

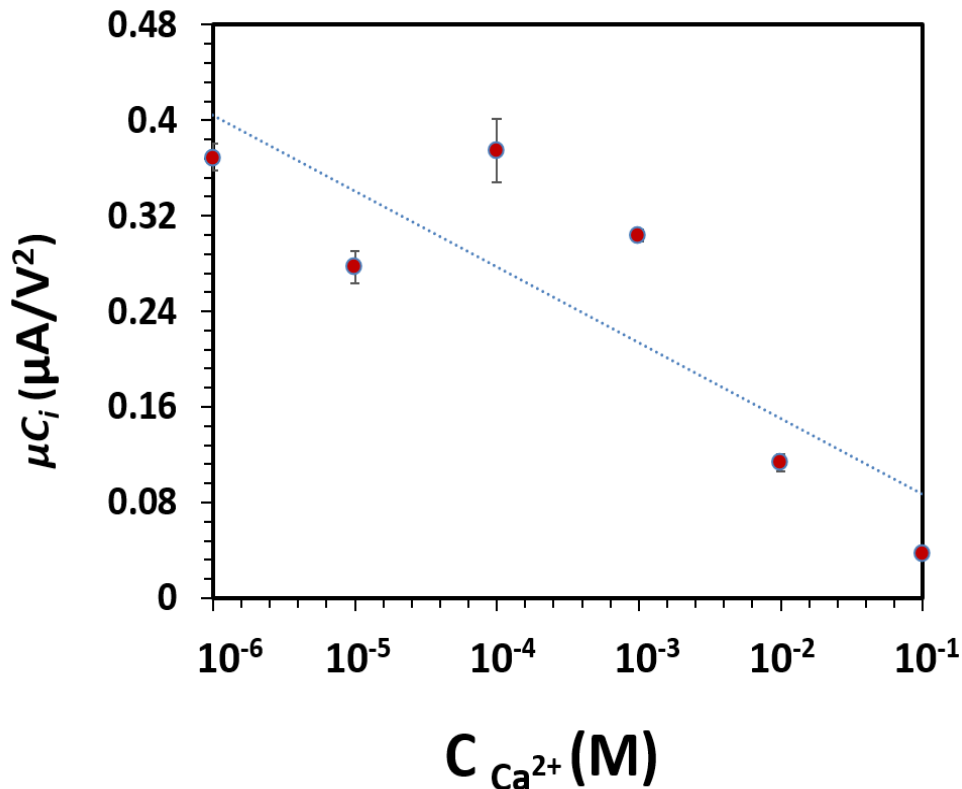


Figure-6-5: Product of carrier mobility and specific capacitance for all water- gated PBTTT OTFTs gated with CaCl₂ solutions of different concentrations.

Fig. 6-5 also displays a systematic decrease of the product of carrier mobility and specific capacitance with increasing Ca²⁺ concentration; however, there is no theoretical model for this shift. Ion-sensitive water gated transistors by Schmoltner *et al.*^[56] show only a threshold shift in response to cation exposure, but mobility remains without change. In the more sophisticated design of Schmoltner *et al.* ^[56] there is no direct contact between the test solution and the semiconductor: only a reference solution of fixed ion concentration remains in contact with the semiconductor, whereas the analyte solution of varying concentration is in contact with the PVC membrane. In our simpler transistor design, the sample solutions of different concentration are in direct contact with the semiconductor. Therefore, cation concentration may have an influence on mobility as well as threshold. Mobility and threshold therefore have to be detached for analysis, as was done here. Another observation is that after exposure to high Ca²⁺ concentrations, PBTTT-TFTs did not recover their initial behaviour when they gated with DI water, even after washing of the semiconductor film.

6.1.3 Control Experiments

Following the remarkable observation of sensitivity to divalent cations in a water gated transistor without any deliberate sensitizing, a number of control experiments were undertaken to investigate how specific this sensitivity is. Fig. 6-6 displays a comparison of water-gated PBTTT TFTs exposed to a number of different (mono and divalent) cations dissolved in water. Here the comparison was done between DI water and the highest cation concentration (0.1M = 100 mM) of the previous range.

For monovalent cations (Na^+ , K^+), *cf.* Fig. 6-6a, it is obvious that PBTTT TFTs show no shift in a threshold voltage and only a little change of slope (*i.e.* μC_i) in the linear transfer characteristic. However, a significant threshold shift and mobility decline is clearly observed with 100mM vs. DI water for all divalent cation samples (Ba^{2+} , Mg^{2+} , Zn^{2+}) (Fig. 6-6b), which is quantitatively analogous to the response to Ca^{2+} . This demonstrates that the response of unsensitised PBTTT OTFTs is tied to the bivalent character of the cations, and does not depend on the precise chemical character of bivalent cations (alkaline earth vs. transition metal). The comparison between Na^+ and Ca^{2+} is particularly interesting, e.g. Na^+ and Ca^{2+} both have similar ionic radii (114 pm for Na^+ vs. 116 pm for Ca^{2+} [178]). However, the response of the threshold is exhibited for the bivalent ion only. Furthermore, Mg^{2+} has an ionic radius of 86 pm, which is considerably smaller than Ca^{2+} or Na^+ ; however, the threshold response to Mg^{2+} is similar to Ca^{2+} . It is clear from the above discussion that the sensitivity is controlled by cation valency, not its size.

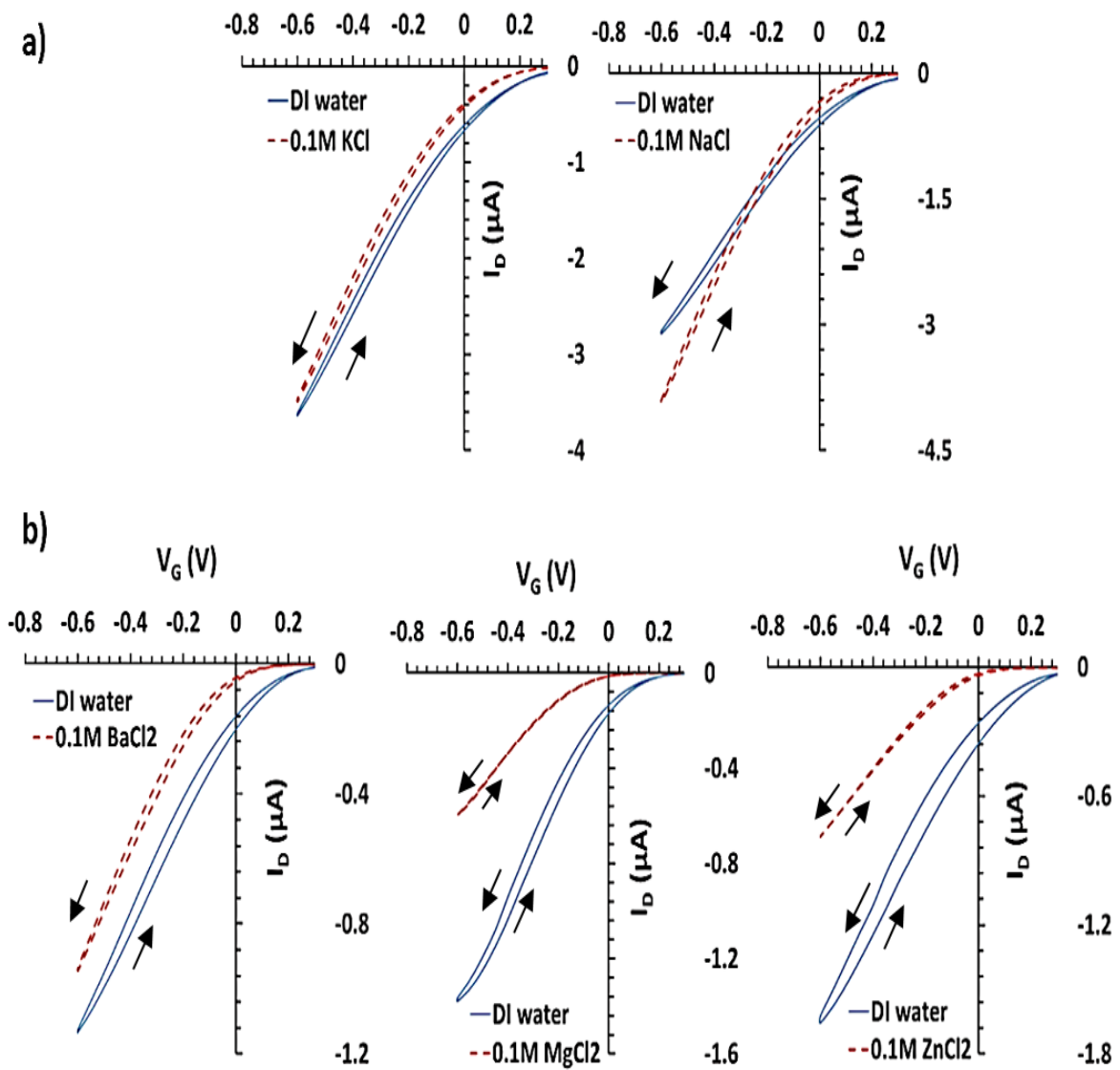


Figure 6-6: PBTFT OTFTs gated with solutions of various cations. **6-6a**: Monovalent cations (Na^+ , K^+). **6-6b**: Divalent cations (Ba^{2+} , Mg^{2+} , Zn^{2+}). All PBTFT-OTFT were electrically addressed with a gold (Au) gate needle.

Figure 6-7 illustrates a summary plot of threshold shift for PBTFT OTFTs gated with solutions of various cations that presented in Fig. 6-6.

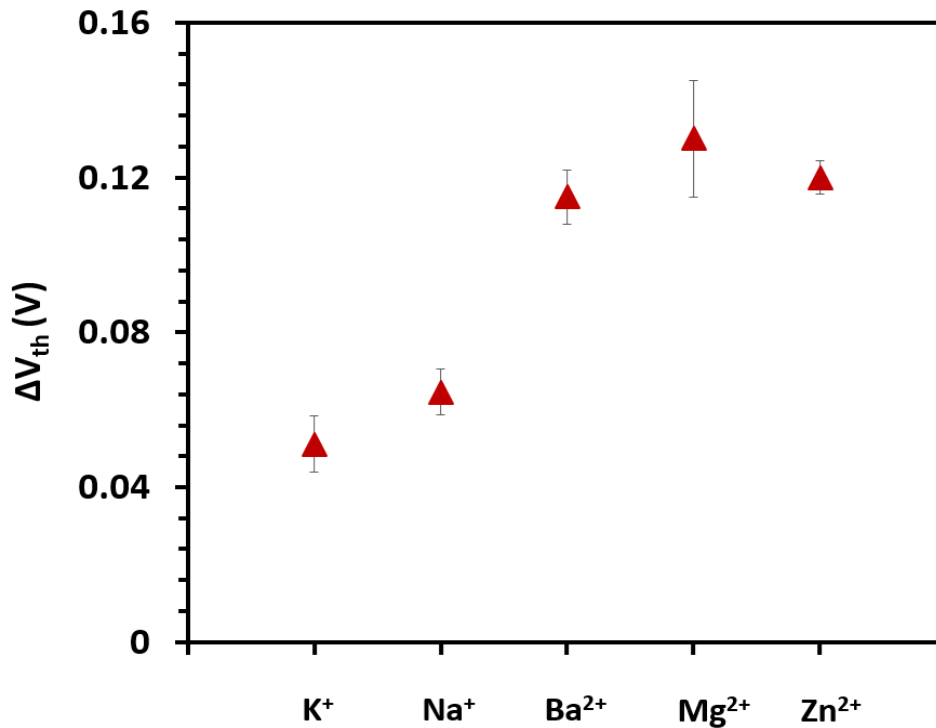


Figure 6-7: A summary plot showing threshold voltage shift for PBTtT OTFTs gated with solutions of various cations. Extracted from Fig. 6-6.

In a further control experiment, a different type of semiconductor was used in the TFT channel to test the response of water-gated TFTs under exposure to Ca^{2+} cations. Here, an inorganic, non-polymeric semiconductor, precursor-route ZnO was used as an electron transporter, since there is no water-gated electron transporting organic semiconductor known to date. A solution-processed ZnO is known to work well under water-gating,^[35, 36] as described in Chapter 5, Section 5.1.

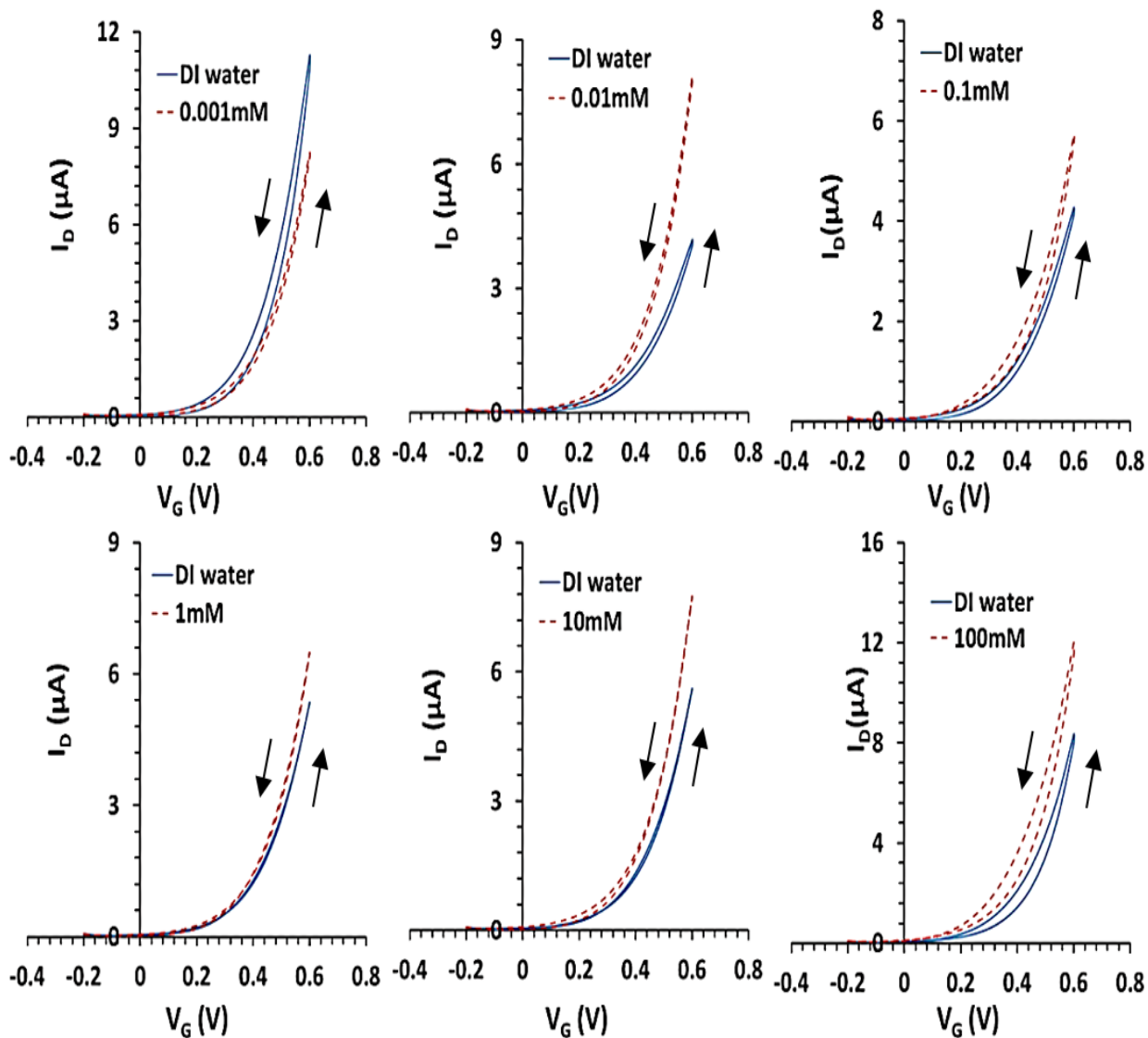


Figure 6-8: Linear transfer characteristics of water-gated ZnO OTFTs with different CaCl₂ concentrations (red), each referenced to same characteristic taken under DI water (blue) immediately before.

Fig. 6-8 illustrates the linear transfer characteristics of water-gated ZnO TFTs gated with CaCl₂ solutions with concentrations from 1 μM to 100 mM. Note, the sign of voltages and current for ZnO is reversed (now positive) due to the electron-transporting character of ZnO- rather than the hole-transporting character of PBTFT. As expected, ZnO TFT under water-gating displays good performance (described in Chapter 5). However, water-gated ZnO TFTs do not show a systematic threshold shift with Ca²⁺ concentration, which is in contrast to PBTFT, as seen in Fig. 6-8. For ZnO TFTs, threshold voltage response does not depend on a Ca²⁺ concentration of up to 10mM; only at very high concentration (100mM), a small threshold shift is observed

(as seen in Fig. 6-8 where the scale is expanded 25-fold compared to Fig. 6-4). This small threshold shift at high Ca^{2+} concentration may be related to the higher capacitance of concentrated salt solutions rather than a Nernstian threshold shift due to the interactions of semiconductor cation.

Similarly, μCi (Fig. 6-9) shows only weak and irregular variation with Ca^{2+} concentration, not the systematic drop as for PBTTT OTFTs, Fig. 6-5.

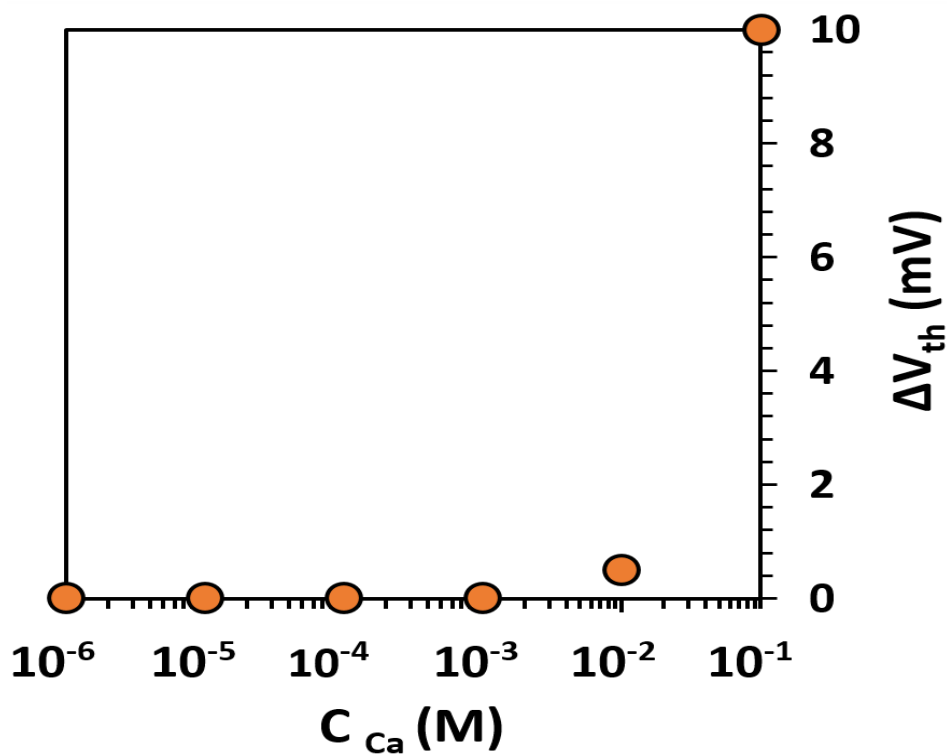


Figure 6-9: Threshold shift for water-gated ZnO OTFTs gated with CaCl_2 solutions of different concentrations against logarithmic concentration scales. All ZnO-TFTs were electrically addressed with a Tungsten (W) gate needle. Fig. 6-8 is similar to Fig. 6-4 but with a different semiconductor, ZnO vs. PBTTT.

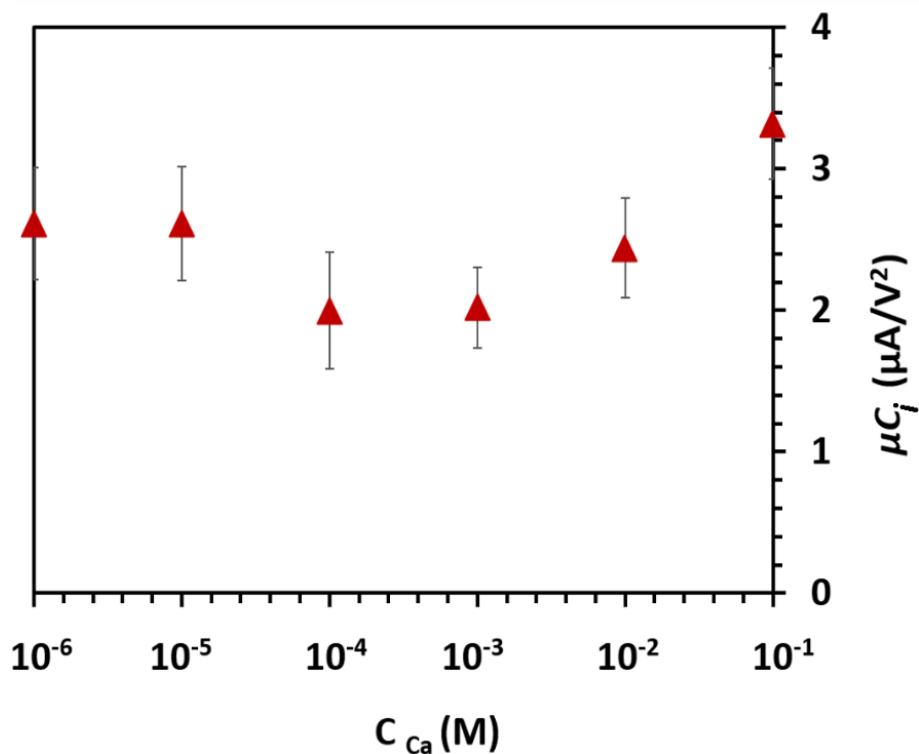


Figure 6-10: The product of carrier mobility and specific capacitance (μC_i) for water-gated ZnO OTFTs gated with $CaCl_2$ solutions of different concentrations against logarithmic concentration scales. Fig. 6-9 is analogous to Fig. 6-5 but with a different semiconductor, ZnO vs. PBTTT.

In similar experiments, ZnO TFTs were gated with 0.1M of Na^+ , K^+ , Ba^{2+} , and Mg^{2+} cation solutions (Fig. 6-10). Again no significant threshold shift for water-gated ZnO TFTs were observed. There is only a small shift of threshold voltage in the opposite direction than for PBTTT TFTs gated with divalent cations. The sensitivity to divalent cations observed in water-gated PBTTT OTFTs is absent with inorganic semiconductor ZnO TFTs.

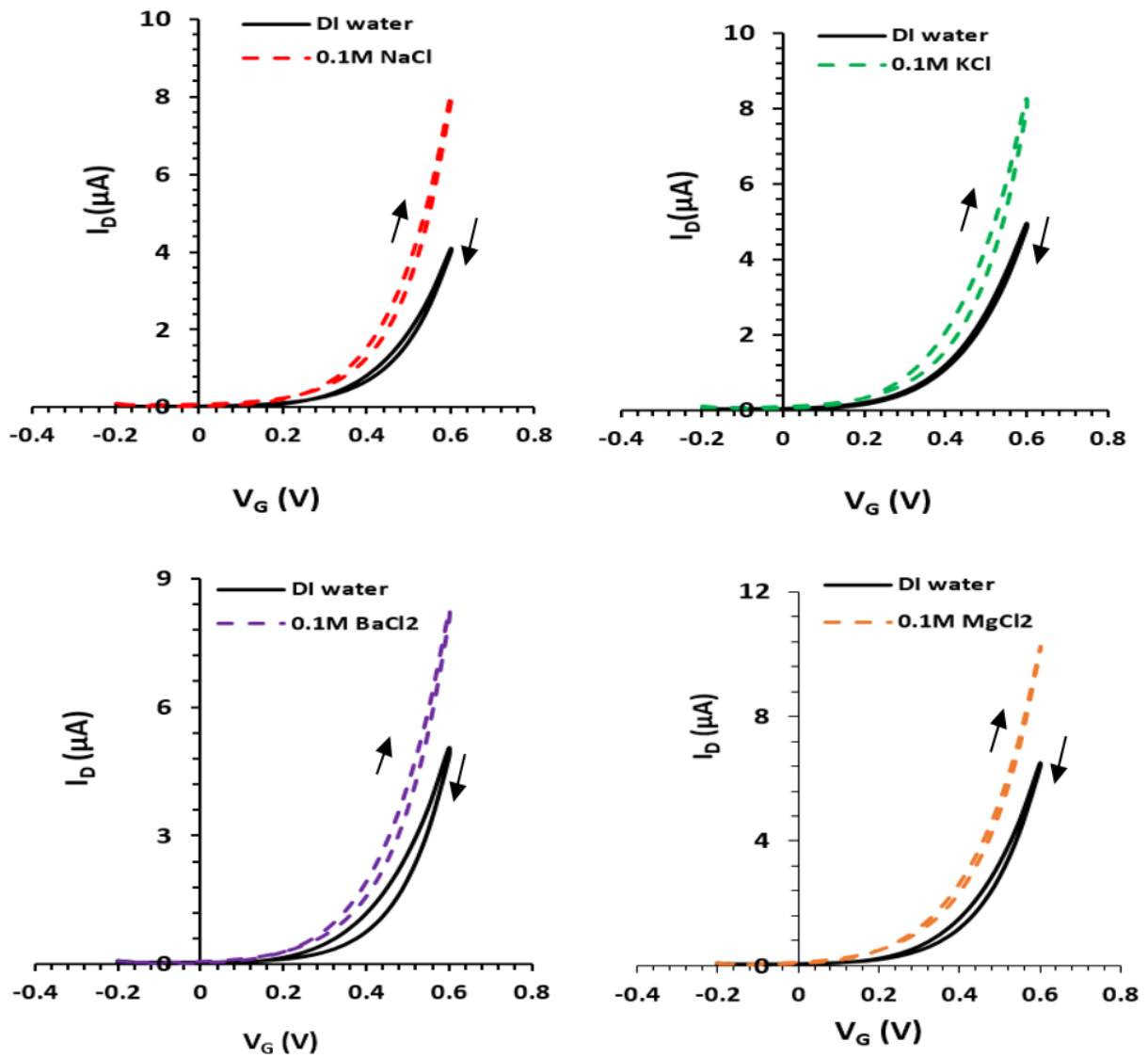


Figure 6-11: Linear transfer characteristics of water-gated ZnO-TFTs of various cations. Monovalent cations (Na^+ , K^+) and divalent cations (Ba^{2+} , Mg^{2+}). All ZnO-TFTs were electrically addressed with a Tungsten (W) gate needle.

Figure 6-12 illustrates a summary plot of threshold shift for ZnO TFTs gated with solutions of various cations that presented in Fig. 6-11.

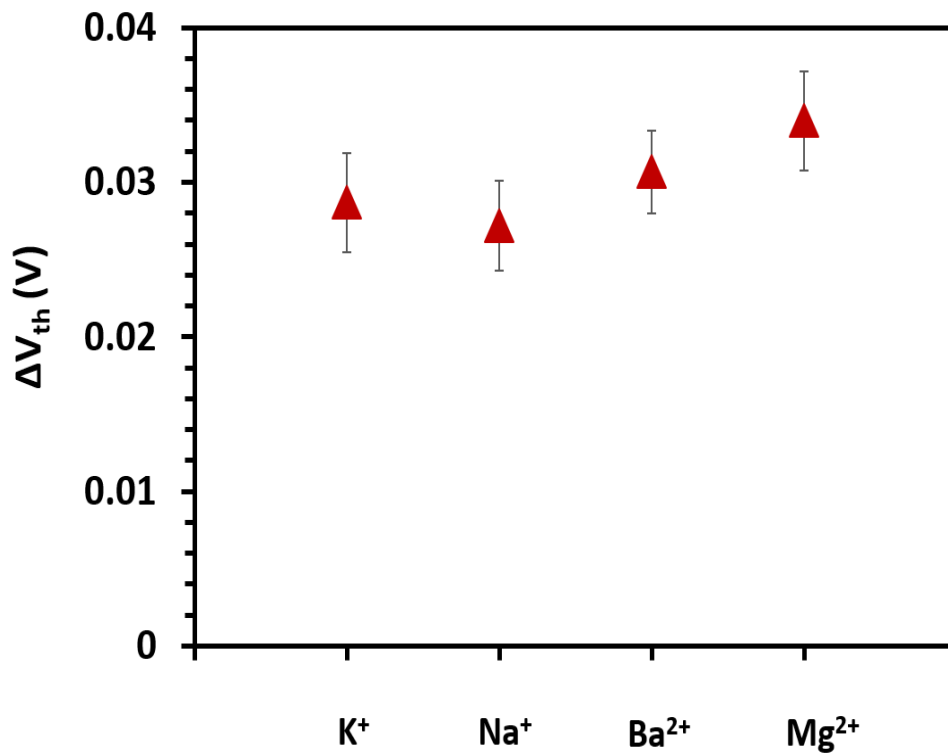


Figure 6-12: A summary plot showing threshold voltage shift for ZnO TFTs gated with solutions of various cations. According to Fig. 6-11.

As a final control experiment, the widely studied hole-transporting semiconducting polymer rrP3HT was used to test the response of divalent cations, Fig. 6-13. There is only a small threshold shift even under 100 mM Ca ion vs. DI water, while there is no shift under 100mM Ba, Zn, K, and Na ions vs. DI water. Although both rrP3HT and PBTTT are based on thiophene, the innate sensitivity to divalent ions observed in water-gated PBTTT TFTs is absent in rrP3HT OTFTs.

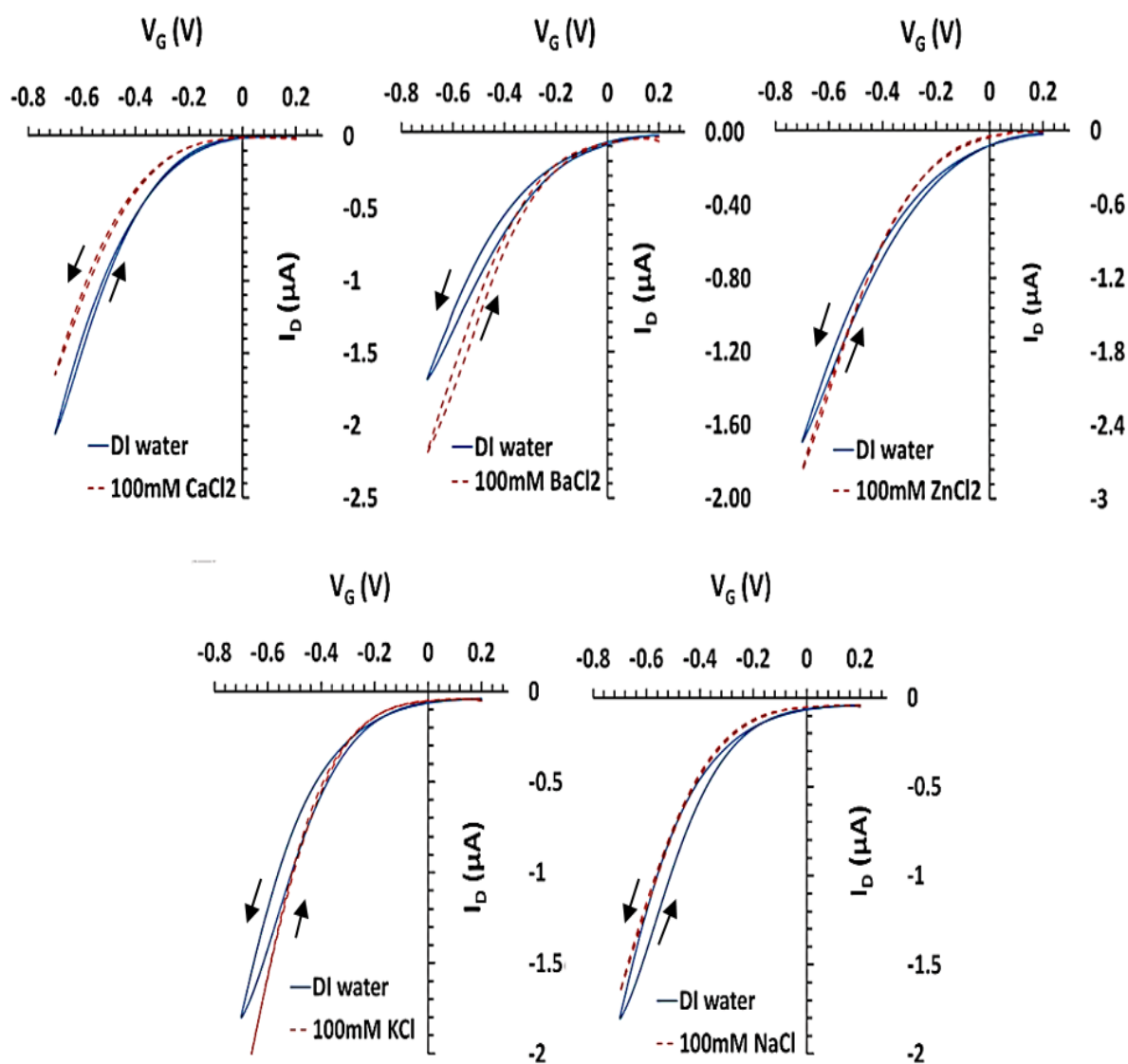


Figure 6-13: Linear transfer characteristics of rrP3HT OTFTs gated with various cations of (Ca^{2+} , Ba^{2+} , Zn^{2+} , K^+ , and Na^+) (red), referenced to same characteristic taken under DI water (blue) immediately before. OTFTs were electrically addressed with an Au gate needle.

Figure 6-14 illustrates a summary plot of threshold shift for P3HT OTFTs gated with solutions of various cations that presented in Fig. 6-13.

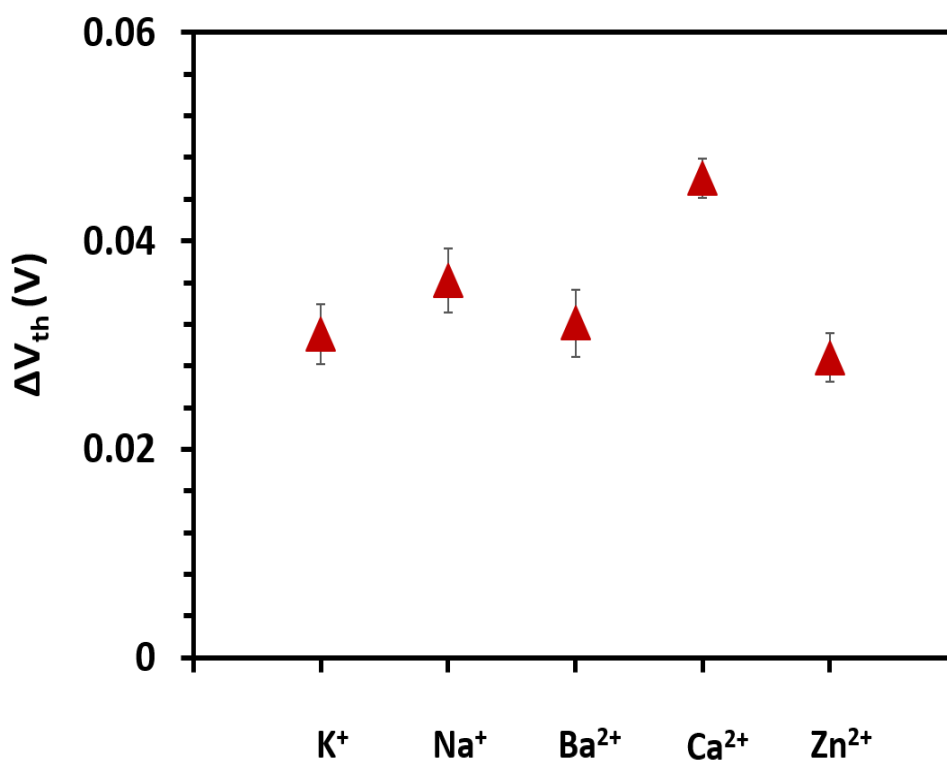


Figure 6-14: A summary plot showing threshold voltage shift for P3HT OTFTs gated with solutions of various cations. According to Fig. 6-13.

6.1.4 Conclusions

Using the hole-transporting semiconducting polymer PBTTT in the channel of a water-gated TFT leads to a sensitivity in their threshold voltage in response to divalent metal cations in the gating water. As there was no cation-sensitive component introduced deliberately, this sensitivity is an innate property of the PBTTT semiconductor. Also, there is no similar response of water-gated PBTTT transistors to monovalent cations. When a different semiconductor was used, such as ZnO as an inorganic electron transporter or rrP3HT as another hole-transporting organic semiconductor, sensitivity to divalent cations is also absent. From a number of control experiments, the observed sensitivity in water-gated PBTTT TFTs clearly results from the interaction between semiconductor PBTTT and divalent cations.

We assign the observed innate sensitivity to catalyst residues remaining from the Stille coupling used in the synthesis of PBTTT. As was described in Chapter 1, Section 1.5.4.2, Stille coupling is catalyzed by the organometallic Pd(0) complex

tris(dibenzylideneacetone)dipalladium(0), $\text{Pd}_2(\text{dba})_3$.^[64] This is somewhat similar to the sensitizers utilized as the active part of cation-selective PVC membranes; these are also organic metal-complexing agents at low concentrations.^[104, 105] This includes the PVC membrane utilized by Schmoltner *et al.* ^[56] which is described in ^[179]. Since alkaline earth metals have the ability to form organometallic complexes,^[180] we believe they may compete with Pd for complexation with tris(dibenzylideneacetone). In contrast, an inorganic semiconductor such as ZnO is impermeable and does not comprise catalyst residue. In addition, our interpretation is confirmed by the lack of strong divalent cation sensitivity in rrP3HT. Although rrP3HT is chemically similar to PBTTT, rrP3HT polymerization is catalyzed by Rieke Zinc^[61] rather than $\text{Pd}_2(\text{dba})_3$. This introduces no organometallic residue into P3HT.

The concentration of Pd- based organometallic catalyst $\text{Pd}_2(\text{dba})_3$ remaining in PBTTT even after deliberate clean- up with a 'scavenger'^[64] is not known, albeit it is probably very low. However, we note that neither Nernstian nor Nikolsky- Eisenman theory specify a minimum concentration of ionophore required to give a voltage shift in response to primary cation concentration, *cf.* Equations (6-1a/b). Logic dictates there must be such a minimum, because there cannot be a response in the limit of zero ionophore concentration, *i.e.* the absence of ionophore altogether- but this minimum is not given by the established theories, which describe voltage shift in terms of primary ion concentration only, independent of ionophore concentration. c_{st} in the Nikolsky- Eisenman equation 6-1b gives a limit- of- detection (*i.e.*, minimum concentration required for a voltage response) for the *primary ion* in water, but not for the ionophore concentration in the sensitised membrane.

For a control experiment to support the above interpretation further, we therefore, deliberately doped a rrP3HT solution with a rather high concentration (4% wt/wt) of $\text{Pd}_2(\text{dba})_3$, to make sure we are above the unknown minimum concentration of ionophore. The resulting $\text{Pd}_2(\text{dba})_3$ - doped rrP3HT OTFT shows a strong shift of threshold voltage to 100 mM Ca^{2+} (Fig. 6-15), similar to PBTTT OTFTs in Fig. 6-2 for 100 mM Ca^{2+} , which is in contrast with undoped rrP3HT OTFTs (Fig. 6-13). This confirms that $\text{Pd}_2(\text{dba})_3$ introduces sensitivity to divalent cations when present in rrP3HT semiconducting polymer.

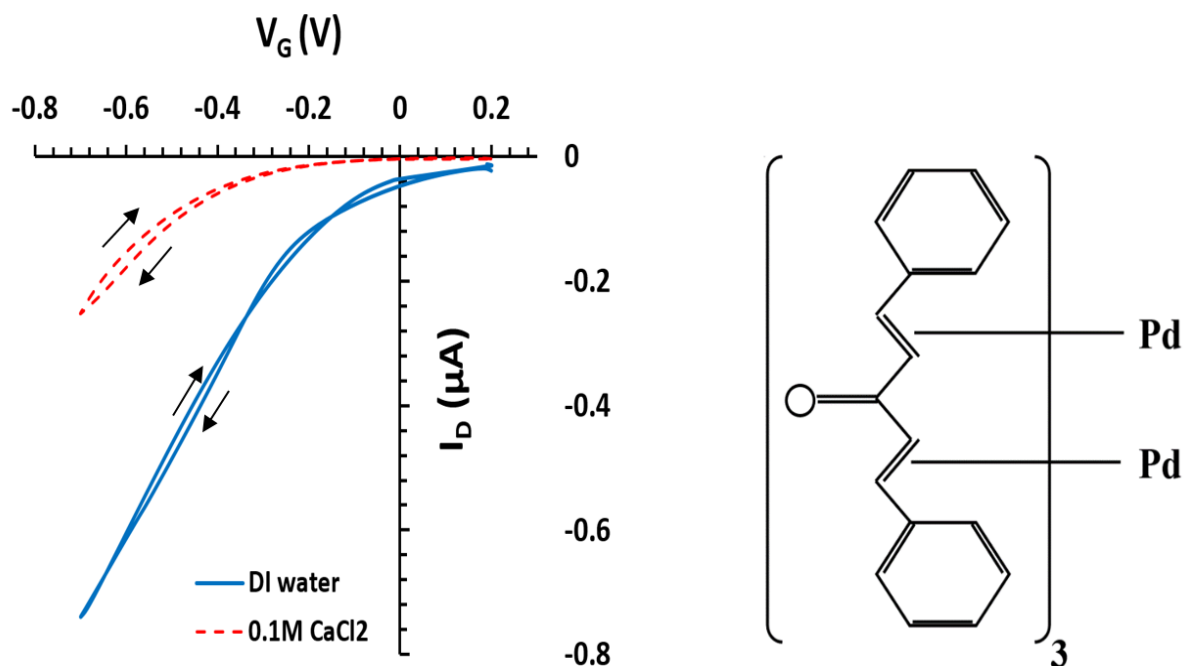
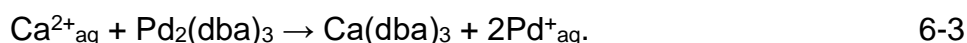


Figure 6-15: (left) Linear transfer characteristics of rrP3HT OTFTs gated with DI water (blue, solid line), and 100 mM CaCl₂ solution (red dashes). rrP3HT casting solution was deliberately doped with Pd(0) catalyst, Pd₂(dba)₃. rrP3HT : Pd(0) catalyst OTFTs were electrically addressed with a gold gate needle. Right the chemical structure of Pd₂(dba)₃.

Curiously, the shift of threshold voltage of PBTTT OTFT due to the response to divalent cations gives a slope of 55±2.7 mV/decade, close to the value for monovalent cations (a single valency ion ($z = 1$, slope = 58.16 mV/dec at 20 °C), albeit PBTTT sensitivity is for divalent ions only. Speculatively, this could be because a single divalent cation replaces both Pd(0) in Pd₂(dba)₃, which goes into solution as 2 Pd⁺:



The release of two Pd⁺ for every complexed Ca²⁺ could cancel the division by $z = 2$ of the slope in Equation 6-1b, and Pd(I) is a likely Pd oxidation state. Nevertheless, we have no confirmation for this mechanism.

Practically, this interpretation could be utilized to detect the existence or arrival of divalent ions against a background of monovalent ions, even though the former are less concentrated than the latter, with a generic OTFT design. Remarkably, the perform of PBTTT-based bivalent cation sensitive OTFTs does not require

electrochemical reference electrode or ion-specific PVC membrane. On the other hand, the innate sensitivity of PBTTT to divalent cations must be taken into account in future water-gated OTFT--based sensor designs. Divalent cations will act as interferants that must be accounted for. To avoid such interference, a simple way is the use rrP3HT rather than PBTTT. However, the most practically relevant conclusion from the work presented in this section, 6.1, is that the addition of a cation-selective sensitizer to films of a semiconducting polymer can lead to WGTFTs that are sensitive to ions in the gating water, without the need for a separate cation-selective membrane. In Section 6.2, I will use this insight to demonstrate highly selective, membrane-free ion selective WGTFTs.

6.2 Detecting Water-borne Cations with Sensitised Polythiophene

As was mentioned in Chapter 1, Section 1.7.3, the interaction between water-borne cations and a cation-selective sensitizer is usually mediated by introducing sensitizers in plasticized PVC membranes.^[104-106] Recently, ion-sensitive membranes (sensitized PVC membranes) containing ionophores selective towards specific cations have been incorporated into WGTFT in order to detect dissolved cations in water.^[56, 108] In this section, a simplified OTFT architecture for selective detection of water-borne cations, without using a PVC membrane or even an electrochemical reference electrode as in previous reports^[56, 108] has been demonstrated. It is achieved by deliberately adding a small amount of a calcium-selective calix[4]arene, 'calcium ionophore VI' ^[113] as a sensitizer to a rrP3HT spin casting solution. WGOTFT cast from sensitized rrP3HT solutions shows a selective response to calcium cations dissolved in the gating water in a very similar way to PVC membrane-sensitized devices, but with significantly simplified device architecture.

6.2.1 Experimental Section

6.2.1.1 Device Fabrication

TFT contact substrates were fabricated as described in Chapter 2, Section 2.2.1.1. Briefly, 5 source/drain gold contact pairs per substrate with a geometry width/length (W/L) = 1 mm/30 μm = 33 were fabricated using a high vacuum evaporator to deposit first a 20 nm Cr adhesion layer, and then 120 nm Au. A casting solution of an organic semiconductor (rrP3HT) was prepared as described in Chapter 2, Section 2.3.1.1. Briefly, 10 mg of rrP3HT was dissolved in 1ml of 1,2 dichlorobenzene (DCB) at 65 °C and filtered with a 0.45 μm polytetrafluoroethylene syringe filter. For sensitized transistors, 0.1 mg/mL (1% wt./wt. of rrP3HT) 'Calcium ionophore VI' sourced from Sigma Aldrich (Cat. No. 72385) was added to the same casting solution. Calcium ionophore VI, described by McKittrick *et al.* ^[113], is a calix[4]arene macrocycle (*cf.* Fig. 6-12) that selectively complexes Ca^{2+} in its central cavity. McKittrick *et al.* ^[113] used this ionophore with a PVC membrane-based electrochemical transducer to sense water-borne Ca^{2+} .

For control experiments, we prepared rrP3HT solution without adding the calcium ionophore VI. TFT device substrates were completed by spin casting onto contact substrates for 60s at 2000 rpm. After casting, films were dried under a dynamic vacuum at 110 °C for 40 min. Different salts' stock solutions (including CaCl₂, KCl, NaCl, ZnCl₂ and BaCl₂) were prepared by dissolving 0.1 M concentration in DI water, as described in a previous section 6-1. A stock solution of CaCl₂ was subsequently repeatedly diluted 10-fold down to 1 μM.

A PTFE film with small 'windows' cut into it was used to cover transistor substrates. These small windows expose individual source/drain contact pairs with the intermediate the channel of the transistor. A small plastic pool with capacity of 50 μL was placed over the window. The pool was filled with DI water for a reference measurement and then repeatedly emptied and filled again with CaCl₂ solutions ranging from 1 μM → 100 mM in ascending order. We used fresh OTFT substrates for similar tests on KCl, ZnCl₂, NaCl, and BaCl₂, but with DI water and a concentration of 0.1M only.

6.2.1.2 Electrical Characteristics

Keithley source/measure units, as described in Chapter 3, Section 3.2.1, were used to record TFT characteristics. TFTs were electrically addressed by an Au gate needle (sourced from American Probe and Technologies) bent into an L shape and inserted into the pool at a distance close to the active area of the transistor and touching the surface of the aqueous gate medium. No electrochemical reference electrode or PVC membrane was employed in these experiments. Our setup is illustrated in Fig. 6-16. OTFT transfer characteristics were recorded by sweeping the gate voltage V_G from 0.2 to -0.7 V and back to 0.2 V in steps of 0.02 V at a fixed drain voltage $V_D = -0.3$ V. After each gate voltage step, a delay time was set at 2s for equilibration before recording drain current $I_D(V_G)$. Negligible hysteresis between V_G ramping directions was observed. After each measurement, the gate needles were washed and cleaned with DI water to remove any remaining salts.

The transfer characteristics of DI water and sample solution-gated OTFTs were recorded and plotted in the same graph (Fig. 6-18 (top)). In order to extract the threshold voltage shift ΔV_{th} between DI water, as a reference measurement, and analyte solution-gated OTFTs, the sample-gated transfer characteristics were shifted horizontally along the V_G axis to find the best possible overlap to the DI-gated characteristic. ΔV_{th} is the shift required for best overlap, the procedure is illustrated in Fig. 6-18 (bottom). This method had been used by Casalini *et al.* [59] for a water-gated dopamine-sensing OTFT. However, the described method does not assume a specific mathematical form for the $I_D(V_G)$ characteristic. This technique is most appropriate for the current situation because our transfer characteristics are neither strictly linear nor saturated.

6.2.2 Results and Discussion

Fig. 6-16 displays the sensitized water-gated OTFT setup we are using for the detection of water-borne Ca^{2+} .

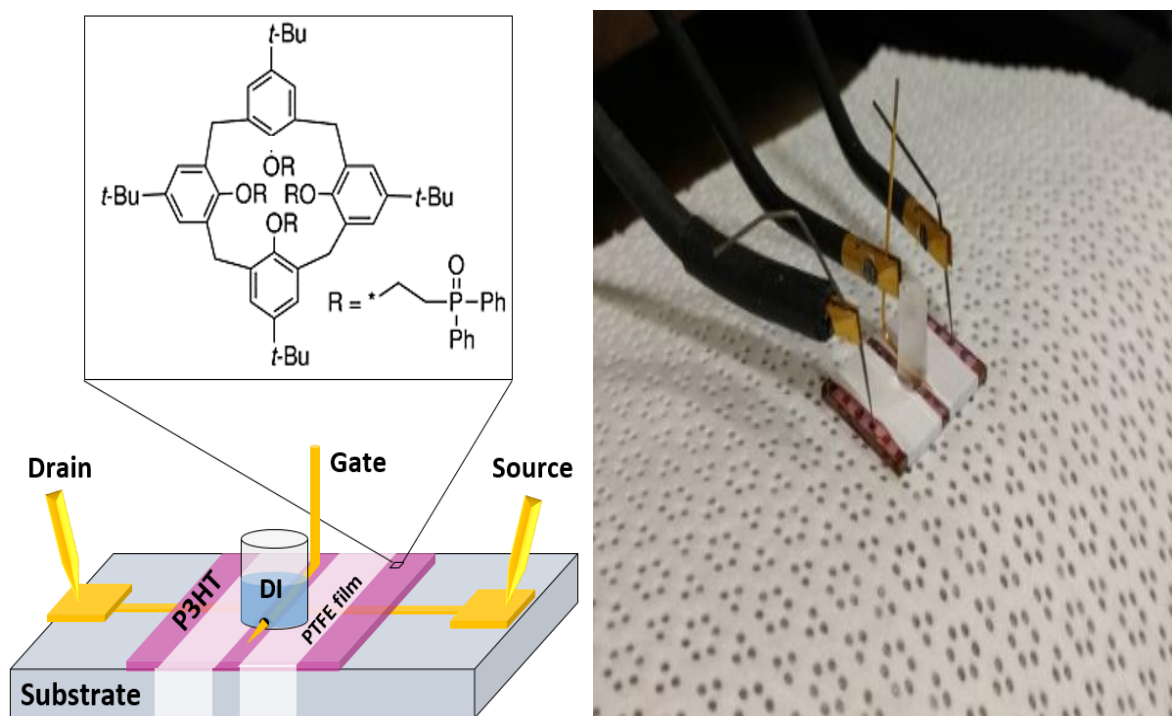


Figure 6-16: Design of our Ca^{2+} sensitive water-gated OTFT. The semiconducting rrP3HT film is doped with 1% wt./wt of 'calcium ionophore VI', the ionophore's molecular structure is shown in the inset.

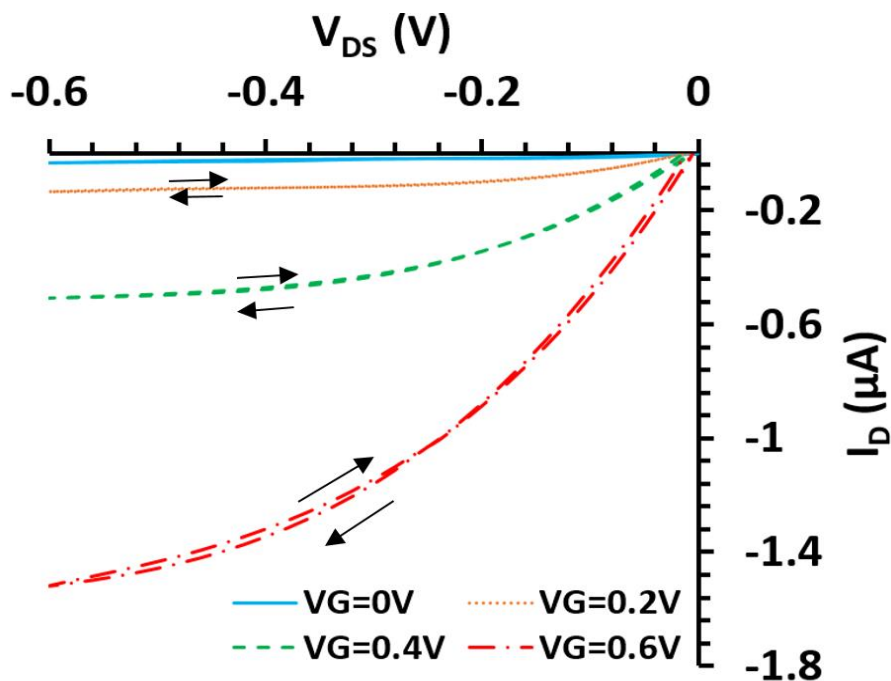


Figure 6-17: Output characteristics of DI water gated rrP3HT: 1% Calcium ionophore OTFTs.

The output characteristic, Fig. 6-17 for a water-gated P3HT: 1% ionophore film is close to ideal, with very little hysteresis and a low threshold (≈ 0.2 V). The estimated carrier mobility, by supposing a specific gate capacitance of $3 \mu\text{F}/\text{cm}^2$ [57], is $\sim 0.25 \pm 0.001 \text{ cm}^2/\text{Vs}$ for this film. Therefore, the use of P3HT films in water-gated OTFTs is not compromised by the doping of a 1% ionophore. However, doping P3HT with a 1% ionophore acts as a sensitizer for the detection of Ca^{2+} ions added to the gating water, as it will be described in the following sections.

The transfer characteristics for ionophore sensitized P3HT TFTs under DI water, and under different concentrations of CaCl_2 solutions ranging from $1 \mu\text{M}$ to 100 mM are shown in Fig. 6-18. All transfer characteristics were taken on the same OTFT substrate. Fig. 6-18 (top), clearly displays an increase of the threshold ΔV_{th} with increasing Ca^{2+} concentration. This is quantified by the ‘master curve’ (Fig. 6-18 (bottom)), in which all transfer characteristics at different CaCl_2 concentrations were shifted along the V_G axis for best overlap with the DI water transfer characteristic. Note the excellent overlap of all curves means that only the threshold is affected by Ca^{2+} ; carrier mobility is not. Threshold shift, ΔV_{th} for each shifted curve was recorded and identified with respect to the DI water curve as a reference measurement. The value

of this threshold shift, ΔV_{th} was then plotted in Fig. 6-19 against a logarithmic concentration scale.

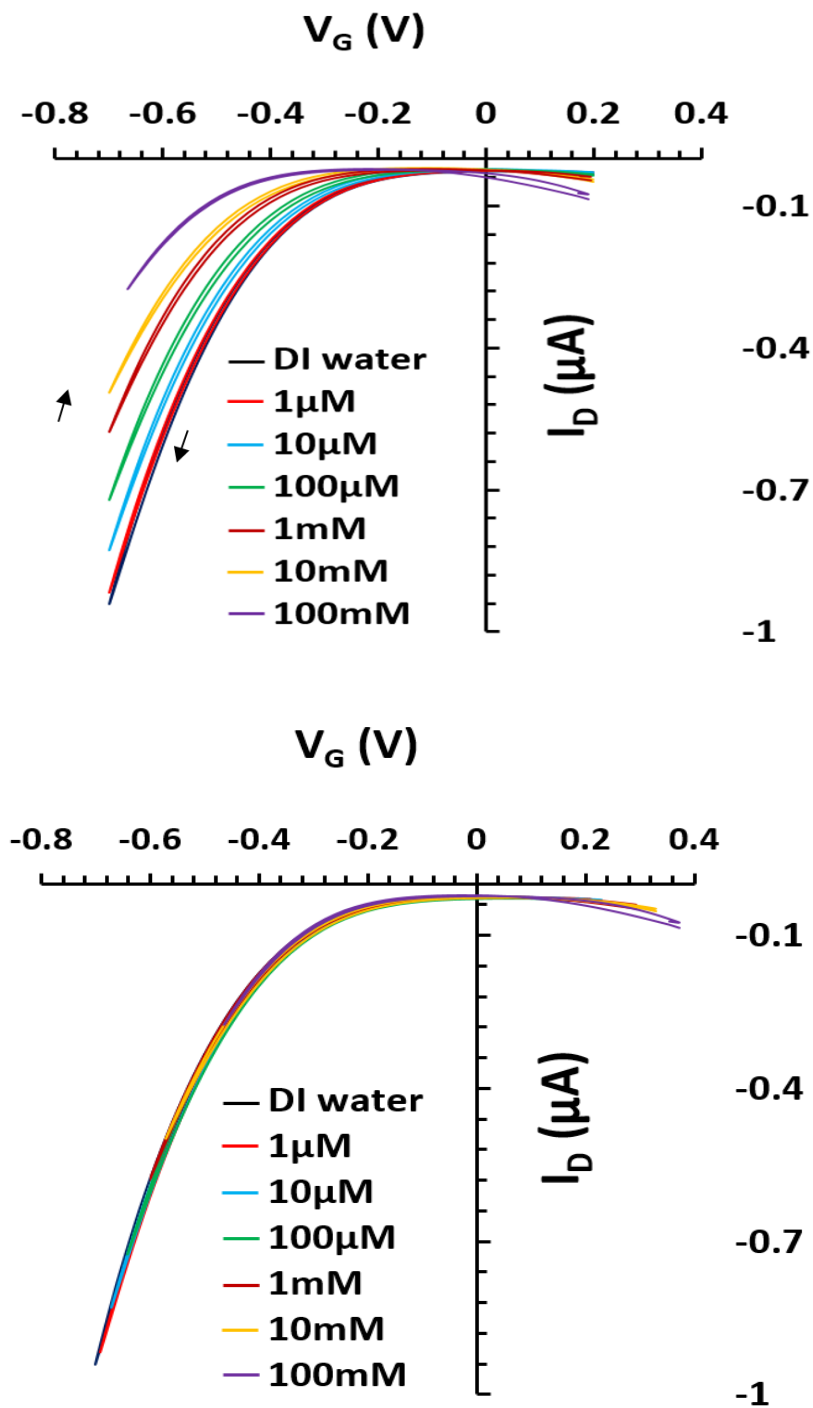


Figure 6-18: (Top) Transfer characteristics of water and different concentrations of CaCl_2 solutions gated rrP3HT: 1% Calcium ionophore VI OTFTs. Dark blue: DI water, coloured graphs for increasing concentration from $1 \mu\text{M} \rightarrow 100 \text{ mM}$. (Bottom) The same transfer characteristics of gated Ca concentrations shifted along the V_G axis for best overlap with DI water gated transfer characteristic. ΔV_{th} was taken as the V_G shift required for best overlap.

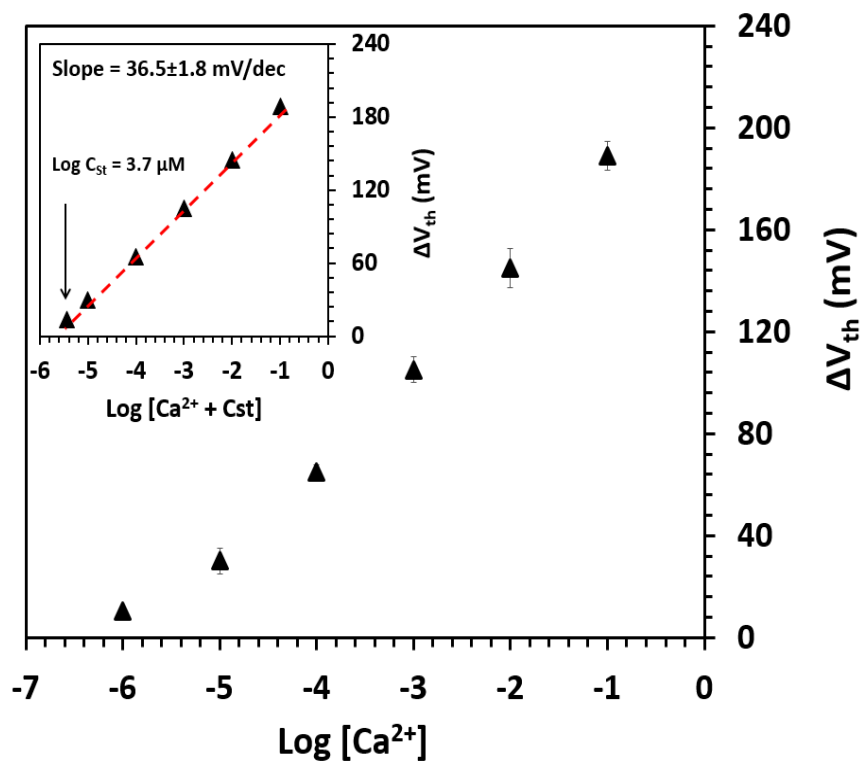


Figure 6-19: Threshold shift ΔV_{th} plotted against $\log (Ca)$, and the insert against $\log (c Ca + 3.7 \mu M)$ according to eq. 6-1b.

The quantitative analysis of cation complexation with ionophore can be explained by the Nikolsky-Eisenman equation, as described in the previous section (6-1). According to the equations (6-1a/b), threshold shift is independent of ionophore concentration; therefore, no effort was made to optimize it here, or elsewhere.^[56, 104, 108, 113]

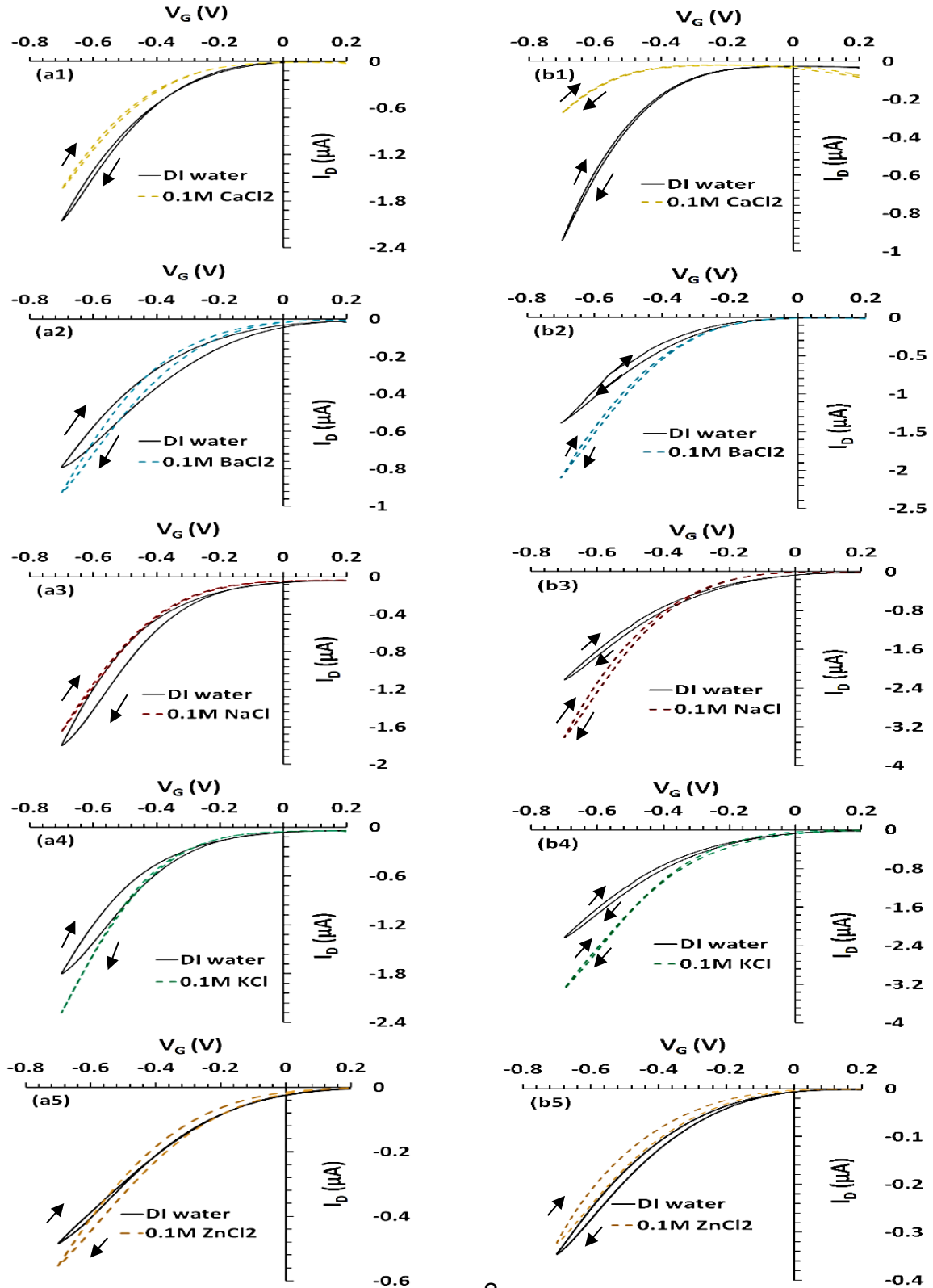
The value of c_{st} is determined (as described in the previous section) by plotting observed ΔV_{th} data against $\log c$, fitting a straight line at high c , estimating slope s , and finding c_{st} as the point where results stand above the extrapolated high c straight line by $s \log 2$. This is implied by *c.f.* Equation 6-1b as the point where $\log c = \log c_{st}$. We here estimated $c_{st} = 3.7 \pm 0.012 \mu M \sim c_{LoD}$. The same ΔV_{th} data against a $\log (c + c_{st})$ scale was then plotted, using $c_{st} = 3.7 \pm 0.012 \mu M$. This provides a near-perfect straight line with a slope 36.5 ± 1.8 mV/dec, inset to Fig. 6-15.

The value of LoD is in the range found in water-gated transistors using a PVC membrane sensitized with ionophore, *i.e.* in the order (1...10 μM).^[56, 108] However, it may be somewhat lower for some electrochemical transducers (e.g. 0.04 μM in ^[104]).

This LoD value was also compared to that of the original publication by McKittrick *et al.*^[113] McKittrick *et al.* transduced the same ionophore by traditional membrane potentiometry. Although they did not explicitly quote a limit-of-detection, Fig. 1 in their report suggests a similar LoD value as that found here.

6.2.3 Control Experiments

In order to prove if that result in Fig. 6-18 and Fig. 6-19 is certainly caused by sensitizing P3HT with ionophore and that our device is selective to the ‘target’ analyte Ca^{2+} over other water-borne cations, a series of control experiments were performed. These control experiments display only the comparison of rrP3HT TFTs gated with concentrated (0.1M) cation solutions vs. DI water-gating. Fig. 6-20 shows two columns for unsensitized and sensitized rrP3HT TFT gated with DI water as a reference measurement vs. different salt solutions, where the left column is for unsensitized rrP3HT TFTs, while the right column is for sensitized rrP3HT TFTs. Fig. 6-20 (a1 and b1) are both gated with 0.1M CaCl_2 in comparison to DI water as a gate medium. A sensitized rrP3HT TFT (b1) showed a strong response to 0.1M CaCl_2 , as we expected, like in Fig. 6-18 (top). The unsensitized OTFT’s transfer characteristic (a1) is very similar under DI water and 0.1M CaCl_2 . This is evidence that unsensitized rrP3HT transistors display no innate sensitivity to calcium ions. The sensitivity to calcium ions occurs as a result of the addition of ‘calcium ionophore VI’ to the rrP3HT casting solution. The response of unsensitized and sensitized rrP3HT devices to another bivalent earth alkali cation, 0.1M BaCl_2 , is shown in Figs 6-20 (a2 and b2). Transfer characteristics for both (unsensitized and sensitized) are similar to each other, and to the DI water-gated characteristic. This is evidence that the ionophore used is selective to calcium ions, and imparts no barium sensitivity. Similarly, Figs 6-20 (a 3 and 4) and (b 3 and 4) compare the response of unsensitized and sensitized rrP3HT TFTs to 0.1M sodium (NaCl) and potassium (KCl), respectively. The response also shows a very small threshold shift even for the sensitised device, Figs 6-20 (b 3 and 4), which is in the opposite direction than for Ca^{2+} .



2

Figure 6-20: Response of P3HT transistors (a) without and (b) with 1% 'Calcium ionophore VI' sensitizer to 0.1M NaCl, 0.1M KCl, 0.1M BaCl₂ and 0.1M CaCl₂. The selective sensitizer imparts sensitivity to Ca²⁺ (b1) but not to Ba²⁺ (b2). Response of P3HT TFT with and without 1% 'Calcium Ionophore VI' to 0.1M NaCl (a3, b3), KCl (a4, b4), and ZnCl₂ (a5, b5). P3HT: 1% 'Calcium ionophore TFT displays little threshold response to 0.1M Na⁺, K⁺, and Zn²⁺ solutions.

McKittrick *et al.*^[113] have recognized the Ca^{2+} selectivity of the same ionophore over Li^+ , NH_4^+ and Mg^{2+} using traditional membrane-based potentiometry and there is very little response for unsensitized OTFTs, Figs 6-16 6-20 (a 3 and 4). Also, the response of unsensitized and sensitized rrP3HT devices to 0.1M transition metal, Zn^{2+} , is shown in Figs 6-20 (a5 and b5). Again, a sensitized transistor shows little response to Zn^{2+} .

Figure 6-21 illustrates a summary plot of P3HT transistors with 1% 'Calcium ionophore VI' sensitizer gated with solutions of various cations compared to threshold voltage of P3HT transistors without sensitizers for the same solutions, presented in Fig. 6-20.

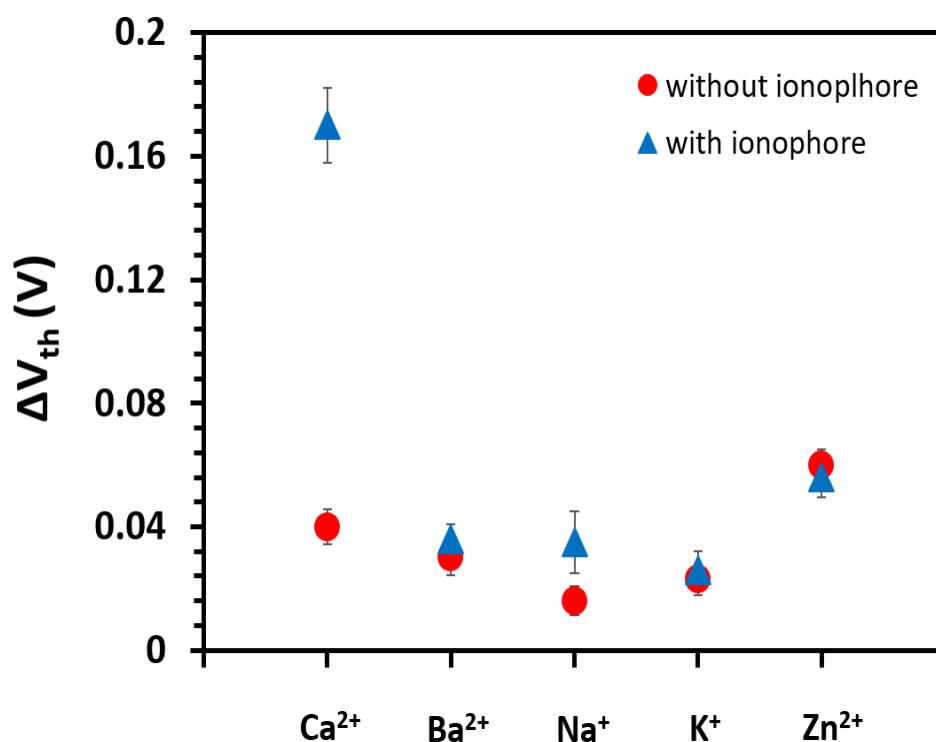


Figure 6-21: Shows threshold voltage shift of P3HT transistors with 1% 'Calcium ionophore VI' sensitizer to 0.1M CaCl_2 , 0.1M BaCl_2 , 0.1M NaCl , 0.1M KCl , and 0.1M ZnCl_2 compared to threshold voltage of P3HT transistors without sensitizers for the same solutions, as shown in Fig. 6-20.

In summary, control experiments show that unsensitized rrP3HT transistors display little response to any cations dissolved in the gating water, whereas, rrP3HT transistors sensitised with 1% 'calcium ionophore VI' selectively respond to Ca^{2+} ions in the gating DI water only with a threshold shift.

6.2.4 Effect of Voltage Sweep Rate

The speed of response is a significant feature for an ion-selective device. As was mentioned in the electrical characteristics section, a delay time of 2s was set after each gate voltage step for equilibration before recording drain current $I_D(V_G)$. In this section, different delay times (i.e., different voltage sweep rates when recording transfer characteristics) were studied to explore if we can obtain a limit-of-detection lower than that obtained with 2s (for 2s: voltage sweep rate for each 0.02V step = 10 mV/s) . In this study we used new 'calcium ionophore VI' sensitized rrP3HT TFTs. Also, we used the same procedures as in Section 6.2.1.

Figs 6-22 and 6-23 show the recorded transfer characteristics at 1s and 3s delay time (voltage sweep rate 20 mV/s for 1s delay and 6.7 mV/s for 3s), respectively, for rrP3HT transistors sensitized with 1% 'calcium ionophore VI', under DI water and under CaCl_2 solutions of increasing concentrations from 1 μM to 100 mM. Here, we only plotted DI water-gated and sample-gated transfer characteristics in the same graph but without shifting the sample-gated characteristics horizontally along the V_G axis as we did in Fig. 6-18 (bottom). Threshold voltage shifts ΔV_{th} were measured by linear extrapolation of drain current $I_D(V_G)$ curves to $I_D = 0$, between DI water (as a reference measurement) and analyte solution-gated OTFTs.

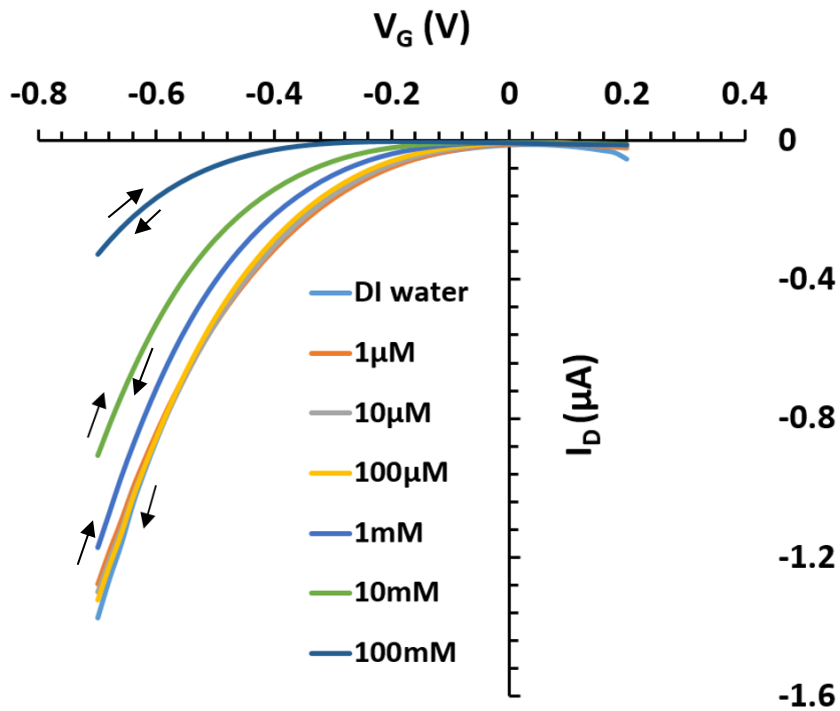


Figure 6-22: Transfer characteristics of water (black color) and different concentrations of CaCl_2 solutions gated rrP3HT: 1% Calcium ionophore VI OTFTs. Delay time was set at 1s for equilibration before recording drain current $I_D(V_G)$.

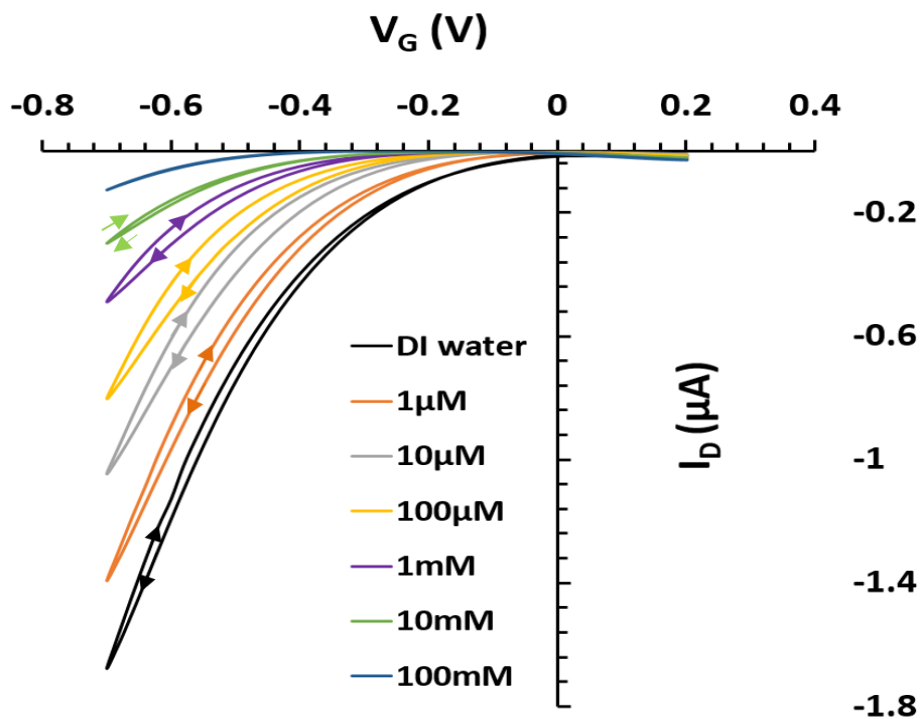


Figure 6-23: Transfer characteristics of water (black color) and different concentrations of CaCl_2 solutions (coloured graphs for increasing concentration from $1 \mu\text{M} \rightarrow 100 \text{mM}$) gated rrP3HT: 1% Calcium ionophore VI OTFTs. Delay time was set at 3s for equilibration before recording drain current $I_D(V_G)$.

Fig. 6-22 for a 20 mV/s voltage sweep rate, shows clearly a little response at low concentrations (1 μ M.....100 μ M). This is probably because the voltage sweep rate on recording transfer characteristics was faster than the equilibration process time of Ca²⁺ complexation by the ionophore in a P3HT film, whereas, sensitized rrP3HT devices show a strong response to a high concentration (1mM to 100mM) even at a fast measurement of transfer characteristics. While the transfer characteristic (Fig. 6-23) for a water-gated P3HT: 1% ionophore film with 6.7 mV/s sweep rate clearly displays a response even to 1 μ M Ca²⁺ concentrations, meaning Ca²⁺ complexation in a P3HT:1% ionophore film gets sufficient time for the equilibration process.

The same procedure to extract the value of LoD was used here. For a 1s delay, LoD is about 80 μ M with a good straight line fit with a slope $s = 39.5 \pm 2.06$ mV/decade, as seen in the inset to Fig. 6-24. The LoD for 3s delay time is approximately 2.6 μ M with a straight line and slope s of 33.9 ± 3.5 mV/decade, as in the inset to Fig.6-25.

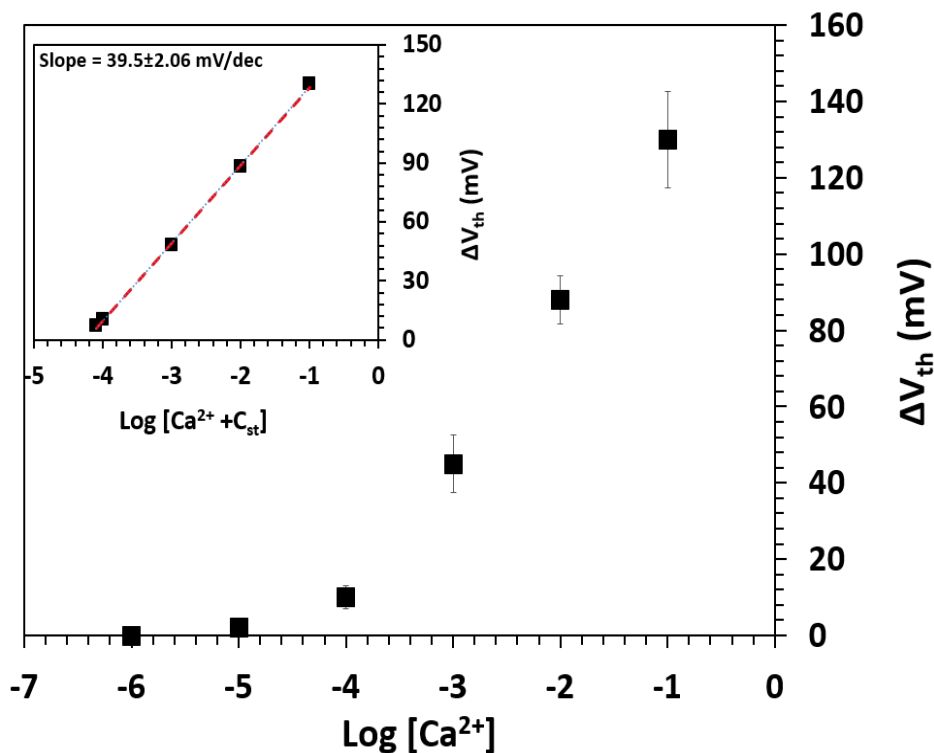


Figure 6-24: Threshold shift ΔV_{th} plotted against $\log (Ca)$, and the insert against $\log (c Ca + 80 \mu M)$ according to eq. 6-1b. Delay time was set at 1s for equilibration before recording drain current $I_D(V_G)$.

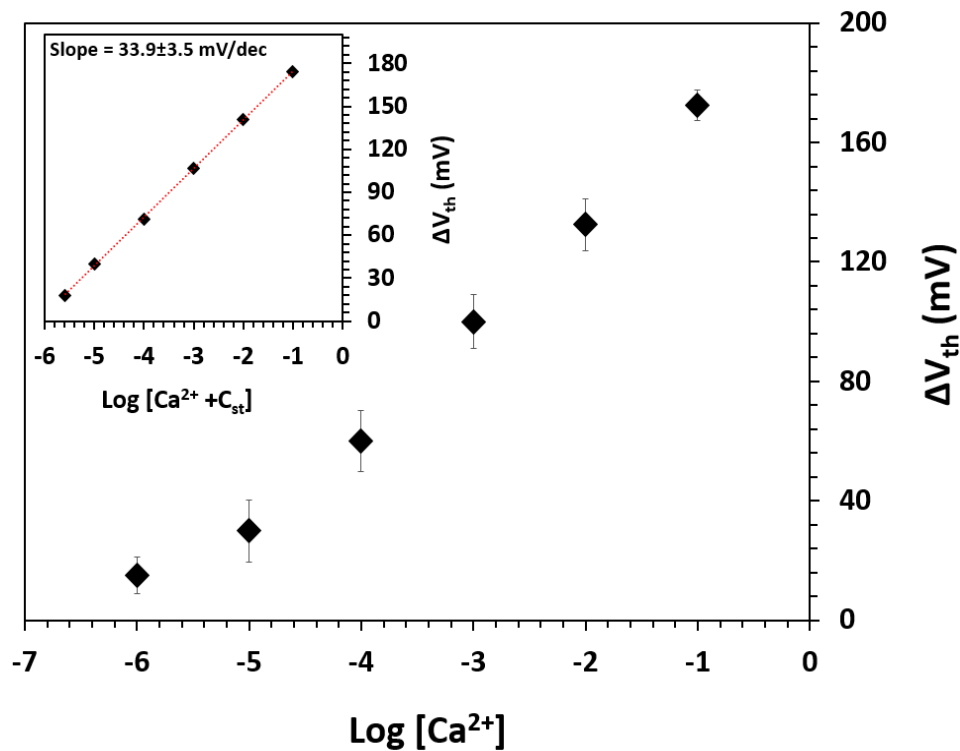


Figure 6-25: Threshold shift ΔV_{th} plotted against $\log (Ca)$, and the insert against $\log (c Ca + 2.6 \mu M)$ according to eq. 6-1b. Delay time was set at 3s for equilibration before recording drain current $I_D(V_G)$.

The above study, comparing an ion-selective WGTFT response under different voltage sweep rates, shows that care must be taken with the interpretation of experimentally determined limits of detection (LoDs). The Nikolsky-Eisenman equation, Equation 1-22, explains LoD as the result of interference from ions other than the target ion, *i.e.* in terms of the selectivity of the employed ionophore for its respective target ion over interfering co-cations, and the concentration of such interferants in the sample solution. Note that even in DI water, there is always H_3O^+ present as an interferant, at concentration $0.1 \mu M$ ($pH 7 \leftrightarrow [H_3O^+] = 0.1 \mu M$). However, the Nikolsky-Eisenman LoD is given by equilibrium constants (namely, the equilibrium constants for target cation vs. co-cation binding to the ionophore), and co-cation concentrations. But as the study in the above paragraph 6.2.4 shows, practically observed LoD depends on a dynamic parameter, namely gate voltage sweep rate when recording transfer characteristics. The Nikolsky-Eisenman ‘equilibrium’ LoD thus represents a lower limit for practically observed LoDs that is approached only in the limit of sufficiently slow gate voltage sweep. As the above data show, ‘sufficiently slow’ is below 10 mV/s. Section 6.2.4 therefore suggests the design of a non-sweeping (static or DC)

determination of threshold voltage to reach the minimum possible LoD, which is what we practically desire. For more detail see the future work section.

6.2.5 Conclusions

Two processes are behind the electrical detection of water-borne cations with ionophores: cation-ionophore complexation, and the transduction of this complexation into an electrical signal that can be observed by the shift of interfacial potential. In traditional sensors, these processes are usually split into two separate functional components: classically, by introducing ionophore in plasticized PVC membranes for the complexation with cation, and an electrochemical transducer (e.g. [104] or a TFT[56, 108]) to detect the shift of interfacial potential. Here, we unite these processes in a single layer that is deposited in a single step. This was done by deliberately adding a small amount of water-insoluble (it is insoluble in water, but soluble in the P3HT solvent) cation-selective ionophore to the casting solution of a semiconducting rrP3HT before processing into a water-gated TFT. The resulting TFT detects and transduces water-borne cations without loss of selectivity, sensitivity, or limit of detection, but with much simplified device preparation. In this simple device, no PVC membrane or electrochemical reference electrode was used. The study of water-borne cation detection under different gate voltage sweep rates suggests that practical limit-of-detection should be minimized by a static method; see future work.

7 Overall Conclusion and Proposed Future Work

The work presented in the thesis shows a collections of experimental work that focussed on two major objectives with regard to electrolyte- gated thin films transistors (EGTFTs):

- I. The study and development of solution- processed semiconductors and electric contacts for use in electrolyte- gated TFTs
- II. Using water- gated TFTs (WGTFTs) as sensors for the sensing of waterborne analytes.

The First objective was achieved as in section **4.1**, **5.1** and **5.2**. In section **4.1**, organic semiconducting polymer PBTTT, known for its extremely high carrier mobility, was combined with a high capacitance electrolytic gate medium, an ionic liquid. This combination leads to produce high sheet current and low sheet resistance, which compares favourably to other high- performance OTFTs from the recent literature. In section **5.1**, the performance of a water gated TFT using acetate precursor- route ZnO can be improved by choosing a better processing solvent. Zinc acetate dissolves more readily in mixed solvent (1:1 EtOH/Acetone) than either EtOH, 2-propanol, or acetone, alone, which improves the film morphology of ZnO films, and improved performance of TFT-ZnO when gated with water- based electrolyte, PBS. This is reminiscent of the situation for solution- processed organic semiconductors, where it is well established that the processing solvent plays a critical role on resulting film morphology and performance . Section **5.2** shows the discovery of a new precursor route to ZnO via pyrolysis of the Zinc salt, Zinc chloride ($ZnCl_2$), dissolved in the most environmentally friendly solvent, water. Absorption spectroscopy and XPS of ZnO resulting from spray pyrolysis of $ZnCl_2$ solution in water are similar to ZnO resulting from Zinc acetate pyrolysis from ethanol, or mixed solvent. Also, the electrical properties of water gated ZnO-TFTs show no significant difference between ZnO from spray pyrolysis of $ZnCl_2$ solution in water, and ZnO via Zinc acetate precursor cast from mixed solvent. In addition, the minimum pyrolysis temperature for converting aqueous $ZnCl_2$ to ZnO is 250 °C, significantly lower than for Zinc acetate pyrolysis. Lower conversion temperature and the use of water rather than organic solvent as

spray medium make the ZnCl_2 precursor route to ZnO an attractive alternative to the established Zinc acetate precursor route.

Chapter 6 reports on a WGTFT used as sensor for waterborne analytes. Section 6.1 shows that using PBTTT in the channel of a water-gated TFT leads to Nernstian sensitivity of their threshold voltage in response to divalent metal cations in the gating water. This observation could be utilized to detect the presence or arrival of divalent ions against a background of monovalent ions, even when the monovalent ions are much more concentrated than the divalent ions, with a generic OTFT design. No electrochemical reference electrode, and no ion-specific PVC membrane are required in PBTTT-based bivalent cation sensitive OTFTs. As there was no cation-sensitive component introduced deliberately, sensitivity is an innate property of the PBTTT semiconductor. It is shown that cation sensitivity is caused by catalyst residue from PBTTT synthesis, with the catalyst acting as an ionophore. Section 6.2 builds on the observation that an ionophore dispersed within an organic semiconductor leads to a membrane-free Nernstian WGTFT ion sensor. We now used rrP3HT as semiconductor, which contains no ionophoric catalyst residue, but deliberately added a Calcium-selective ionophore as sensitizer to the casting solution. A rrP3HT WGTFT cast from sensitized rrP3HT solutions shows selective response to calcium cations dissolved in the gating water in a very similar way to PVC membrane sensitized devices, but with significantly simplified device architecture and without electrochemical reference electrode.

From the above conclusions I can summarize some proposed future work:

- 1- For PBTTT OTFT gated with ILs (section 4.1): the Limited durability warrants further improvement, e.g. via finding an IL that is a non-solvent for PBTTT. While the theory for solubility of polymers in conventional organic solvents, is well established ^[181], this is not yet the case for solubility (or, non-solubility) of polymers in IL, so there are no selection criteria yet available. This is a challenge to the IL community, the limited state-of-the-art has been reviewed by Neil Winterton ^[182].

- 2- For spray pyrolysed $\text{ZnCl}_2 \rightarrow \text{ZnO}$ films (section **5.2**): It is well established that Li-doped ZnO leads to high and more stable performance TFTs of ZnO even when gated with solution-processed gate media [24]. Therefore, Lithium chloride (LiCl) can be added to ZnCl_2 and then we can study and compare the resulting film with that in section **5.2**.

- 3- Section **6.2** paves the way to a new, simple route to use the enormous back catalogue of cation selective, water insoluble macrocycles (e.g. [101, 102, 104-106, 111, 183-188]) for practical cation sensors. For future work, we propose two lines. First line, our simple sensor, in addition to devices incorporating PVC membranes (e.g. [56, 104, 108]), show near-Nernstian response only down to a limiting concentration, which sets a limit of detection (LoD) which is estimated as c_{st} by the Nikolsky-Eisenman equation (1-24). As Nikolsky theory links c_{st} to the sensitizer rather than the transducer, we suggest to dope rrP3HT with macrocycles that are known to give very low LoD in potentiometric transducers, e.g. [104]. Second line, the read-out of our sensor is currently not in real time as ΔV_{th} is estimated manually from measured and plotted transfer characteristics. We propose combining (hole transporting) WGTFTs with a commercial n-type MOSFET (e.g. the 2N7000) into a CMOS inverter, and feeding back inverter output to its input. In this way the inverter voltage is forced to stabilize at the inverter's 'trip point', given by the intersection of the inverter characteristic with the $V_{out} = V_{in}$ line. The trip point (output = input), which depends linearly on the threshold of both transistors in the inverter; assuming 2N7000 threshold is constant, the trip point therefore reflects WGTFT threshold only. However, as long as WGTFT threshold does not change, trip point is static and does not require the sweep of a 'probe' voltage. In this characterization scheme, experimentally found LoD should agree with the theoretical minimum, *i.e.* the equilibrium LoD as given by c_{st} in the Nikolsky-Eisenman equation.

Published papers and attended conferences

- 1- Saud A. Algarni, **Talal M. Althagafi**, Patrick J. Smith, Martin Grell, "An ionic liquid-gated polymer thin film transistor with exceptionally low "on" resistance," *Applied Physics Letters*, 2014. 104(18): p. 182107.
- 2- **Talal M. Althagafi**, Saud A. Algarni, Abdullah Al Naim, Javed Mazher , Martin Grell, "Precursor-route ZnO films from a mixed casting solvent for high performance aqueous electrolyte-gated transistors," *Physical Chemistry Chemical Physics*, 2015. 17(46): p. 31247-31252.
- 3- **Talal M. Althagafi**, Abbad F. Al Baroot, and Martin Grell, " A new precursor route to semiconducting Zinc Oxide," *IEEE Electron Device Letters*, vol. 37, pp. 1299-1302, 2016.
- 4- **Talal M. Althagafi**, Saud A. Algarni, Martin Grell, "Innate cation sensitivity in a semiconducting polymer," *Talanta*, 2016. 158: p. 70-76.
- 5- **Talal M. Althagafi**, Abbad F. Al Baroot, Saud A. Algarni, Martin Grell, "A membrane- free cation selective water- gated transistor," *Analyst*, 2016.
- 6- Saud A. Algarni, **Talal M. Althagafi**, Abdullah Al Naim, Martin Grell, "A water-gated organic thin film transistor as a sensor for water-borne amines," *Talanta*, 2016. 153: p. 107-110.
- 7- Jonathan Stringer, **Talal M. Althagafi**, Christopher C.W. Tse, Van Duong Ta, Jonathan D. Shephard, Emre Esenturk, Colm Connaughton, Thomas J. Wasley, Ji Li, Robert W. Kay, and Patrick J. Smith, "Integration of additive manufacturing and inkjet printed electronics: a potential route to parts with embedded multifunctionality," *Manufacturing Rev.* 3, 12 (2016).
- 8- **Talal M. Althagafi**, Saud A. Algarni, Patrick J. Smith, Martin Grell, "An ionic liquid-gated polymer thin film transistor with exceptionally low "on" resistance," (poster presentation), *UK Semiconductors '14 Conferences*, Sheffield, United Kingdom, Jul, 2014.

References

- [1] L. J. Edgar, "Method and apparatus for controlling electric currents," ed: U.S. Patent 1745175, 1930.
- [2] K. Dawon, "Electric field controlled semiconductor device," ed: U.S. Patent 3102230, 1963.
- [3] J. S. Kilby, "Miniaturized electronic circuits," ed: U.S. Patent 3138743, 1964.
- [4] P. K. Weimer, "The TFT A New Thin-Film Transistor," *Proceedings of the IRE*, vol. 50, pp. 1462-1469, 1962.
- [5] E. Fortunato, *et al.*, "Oxide Semiconductor Thin-Film Transistors: A Review of Recent Advances," *Advanced Materials*, vol. 24, pp. 2945-2986, 2012.
- [6] C. Tanase, *et al.*, "Local charge carrier mobility in disordered organic field-effect transistors," *Organic Electronics*, vol. 4, pp. 33-37, 2003.
- [7] C. Tanase, *et al.*, "Unification of the Hole Transport in Polymeric Field-Effect Transistors and Light-Emitting Diodes," *Physical Review Letters*, vol. 91, p. 216601, 2003.
- [8] Z. Bao and D. J. Gundlach, *Organic Field-Effect Transistors VI*, 2007.
- [9] L. A. Majewski, *et al.*, "One Volt Organic Transistor," *Advanced Materials*, vol. 17, pp. 192-196, 2005.
- [10] S. H. Kim, *et al.*, "Electrolyte-Gated Transistors for Organic and Printed Electronics," *Advanced Materials*, vol. 25, pp. 1822-1846, 2013.
- [11] N. Kamoun Allouche, *et al.*, "Synthesis and properties of chemical bath deposited ZnS multilayer films," *Materials Chemistry and Physics*, vol. 123, pp. 620-624, 2010.
- [12] P. D. Byrne, *et al.*, "High-Performance Thin-Film Transistors from Solution-Processed Cadmium Selenide and a Self-Assembled Multilayer Gate Dielectric," *Advanced Materials*, vol. 20, pp. 2319-2324, 2008.
- [13] K. R. Chauhan, *et al.*, "Preparation of CdTe thin film by electrodeposition in butyl methyl imidazolium bath at 80 °C," *Journal of Electroanalytical Chemistry*, vol. 713, pp. 70-76, 2014.
- [14] G. Sasikala, *et al.*, "Electrodeposition and optical characterisation of CdS thin films on ITO-coated glass," *Thin Solid Films*, vol. 302, pp. 71-76, 1997/06/20 1997.
- [15] S. D. Gunjal, *et al.*, "Structural, Optical and Electrical Properties of Spray Pyrolysis Deposited CdS Films," *Macromolecular Symposia*, vol. 347, pp. 9-15, 2015.
- [16] A. D. Stiff-Roberts, *et al.*, "Spin-Cast Deposition of CdSe-CdS Core-Shell Colloidal Quantum Dots on Doped GaAs Substrates: Structural and Optical Characterization," *IEEE Transactions on Nanotechnology*, vol. 6, pp. 413-420, 2007.
- [17] S. T. Meyers, *et al.*, "Aqueous Inorganic Inks for Low-Temperature Fabrication of ZnO TFTs," *Journal of the American Chemical Society*, vol. 130, pp. 17603-17609, 2008/12/24 2008.
- [18] E. c. SunChemical company, "<http://www.sunchemical.com/>, <http://www.erconinc.com/home.htm>."
- [19] R. L. Hoffman, *et al.*, "ZnO-based transparent thin-film transistors," *Applied Physics Letters*, vol. 82, pp. 733-735, 2003.

- [20] P. F. Carcia, *et al.*, "Transparent ZnO thin-film transistor fabricated by rf magnetron sputtering," *Applied Physics Letters*, vol. 82, pp. 1117-1119, 2003.
- [21] S. Masuda, *et al.*, "Transparent thin film transistors using ZnO as an active channel layer and their electrical properties," *Journal of Applied Physics*, vol. 93, pp. 1624-1630, 2003.
- [22] K. Nomura, *et al.*, "Thin-Film Transistor Fabricated in Single-Crystalline Transparent Oxide Semiconductor," *Science*, vol. 300, pp. 1269-1272, 2003.
- [23] Ü. Özgür, *et al.*, "A comprehensive review of ZnO materials and devices," *Journal of Applied Physics*, vol. 98, p. 041301, 2005.
- [24] S. Y. Park, *et al.*, "Low-Temperature, Solution-Processed and Alkali Metal Doped ZnO for High-Performance Thin-Film Transistors," *Advanced Materials*, vol. 24, pp. 834-838, 2012.
- [25] M. Tadatsugu, *et al.*, "Transparent and Conductive ZnO Thin Films Prepared by Atmospheric-Pressure Chemical Vapor Deposition Using Zinc Acetylacetonate," *Japanese Journal of Applied Physics*, vol. 33, p. L743, 1994.
- [26] M. Niskanen, *et al.*, "Porphyrin adsorbed on the (10[1 with combining macron]0) surface of the wurtzite structure of ZnO - conformation induced effects on the electron transfer characteristics," *Physical Chemistry Chemical Physics*, vol. 15, pp. 17408-17418, 2013.
- [27] Z. Zhang, *et al.*, "P-type single-crystalline ZnO films obtained by (N,O) dual implantation through dynamic annealing process," *Superlattices and Microstructures*.
- [28] B. Bayraktaroglu, *et al.*, "Microwave ZnO Thin-Film Transistors," *IEEE Electron Device Letters*, vol. 29, pp. 1024-1026, 2008.
- [29] L. Ching-Ting and L. Yung-Hao, "P-type ZnO thin-film transistors and passivation using photoelectrochemical oxidation method," *Applied Physics Express*, vol. 7, p. 076502, 2014.
- [30] M. H. Huang, *et al.*, "Room-Temperature Ultraviolet Nanowire Nanolasers," *Science*, vol. 292, pp. 1897-1899, 2001.
- [31] E. Fortunato, *et al.*, "High field-effect mobility zinc oxide thin film transistors produced at room temperature," *Journal of Non-Crystalline Solids*, vol. 338–340, pp. 806-809, 2004.
- [32] L. Zhang, *et al.*, "High performance ZnO-thin-film transistor with Ta₂O₅ dielectrics fabricated at room temperature," *Applied Physics Letters*, vol. 95, p. 072112, 2009.
- [33] C. Brox-Nilsen, *et al.*, "Sputtered ZnO Thin-Film Transistors With Carrier Mobility Over 50 $\frac{\text{cm}^2}{\text{Vs}}$," *IEEE Transactions on Electron Devices*, vol. 60, pp. 3424-3429, 2013.
- [34] B. S. Ong, *et al.*, "Stable, Solution-Processed, High-Mobility ZnO Thin-Film Transistors," *Journal of the American Chemical Society*, vol. 129, pp. 2750-2751, 2007/03/01 2007.
- [35] A. Al Naim and M. Grell, "Electron transporting water-gated thin film transistors," *Applied Physics Letters*, vol. 101, p. 141603, 2012.
- [36] M. Singh, *et al.*, "Bio-sorbable, liquid electrolyte gated thin-film transistor based on a solution-processed zinc oxide layer," *Faraday Discussions*, vol. 174, pp. 383-398, 2014.
- [37] A. Vithal Ghule, *et al.*, "Simultaneous thermogravimetric analysis and in situ thermo-Raman spectroscopic investigation of thermal decomposition of zinc

- acetate dihydrate forming zinc oxide nanoparticles," *Chemical Physics Letters*, vol. 381, pp. 262-270, 2003.
- [38] G. Adamopoulos, *et al.*, "High-Mobility Low-Voltage ZnO and Li-Doped ZnO Transistors Based on ZrO₂ High-k Dielectric Grown by Spray Pyrolysis in Ambient Air," *Advanced Materials*, vol. 23, pp. 1894-1898, 2011.
- [39] Y.-Y. Noh, *et al.*, "Downscaling of self-aligned, all-printed polymer thin-film transistors," *Nat Nano*, vol. 2, pp. 784-789, 2007.
- [40] A. Tsumura, *et al.*, "Macromolecular electronic device: Field-effect transistor with a polythiophene thin film," *Applied Physics Letters*, vol. 49, pp. 1210-1212, 1986.
- [41] C. Clarisse, *et al.*, "Field-effect transistor with diphthalocyanine thin film," *Electronics Letters*, vol. 24, pp. 674-675, 1988.
- [42] P. M. T. John C. Kotz, John R. Townsend, "Chemistry & Chemical Reactivity," *Brooks/Cole*, vol. Eighth Edition, p. 405, 2012.
- [43] G. Tzamalīs, *et al.*, "Fluorescence light emission at 1 eV from a conjugated polymer," *Chemical Physics Letters*, vol. 489, pp. 92-95, 2010.
- [44] M. L. Tiago, *et al.*, "Ab initio calculation of the electronic and optical properties of solid pentacene," *Physical Review B*, vol. 67, p. 115212, 2003.
- [45] M. Ahles, *et al.*, "n-type organic field-effect transistor based on interface-doped pentacene," *Applied Physics Letters*, vol. 85, pp. 4499-4501, 2004.
- [46] N. Beaumont, *et al.*, "Increased efficiency in small molecule organic photovoltaic cells through electrode modification with self-assembled monolayers," *Energy & Environmental Science*, vol. 4, pp. 1708-1711, 2011.
- [47] F.-C. Chen, *et al.*, "Efficient Hole-Injection in Highly Transparent Organic Thin-Film Transistors," *Electrochemical and Solid-State Letters*, vol. 10, pp. H186-H188, June 1, 2007 2007.
- [48] R. Schroeder, *et al.*, "Improving organic transistor performance with Schottky contacts," *Applied Physics Letters*, vol. 84, pp. 1004-1006, 2004.
- [49] H. Bässler and A. Köhler, "Charge Transport in Organic Semiconductors," in *Unimolecular and Supramolecular Electronics I: Chemistry and Physics Meet at Metal-Molecule Interfaces*, R. M. Metzger, Ed., ed Berlin, Heidelberg: Springer Berlin Heidelberg, 2012, pp. 1-65.
- [50] X. Gao and Z. Zhao, "High mobility organic semiconductors for field-effect transistors," *Science China Chemistry*, vol. 58, pp. 947-968, 2015.
- [51] J. Becker, *et al.*, "Measurements of charge carrier mobilities and drift velocity saturation in bulk silicon of $\langle 111 \rangle$ and $\langle 100 \rangle$ crystal orientation at high electric fields," *Solid-State Electronics*, vol. 56, pp. 104-110, 2011.
- [52] H. T. Nicolai, *et al.*, "Unification of trap-limited electron transport in semiconducting polymers," *Nat Mater*, vol. 11, pp. 882-887, 2012.
- [53] A. Rasul, *et al.*, "Flexible high capacitance nanocomposite gate insulator for printed organic field-effect transistors," *Thin Solid Films*, vol. 518, pp. 7024-7028, 2010.
- [54] L. A. Majewski and M. Grell, "Organic field-effect transistors with ultrathin modified gate insulator," *Synthetic Metals*, vol. 151, pp. 175-179, 2005.
- [55] K.-J. Baeg, *et al.*, "High mobility top-gated poly(3-hexylthiophene) field-effect transistors with high work-function Pt electrodes," *Thin Solid Films*, vol. 518, pp. 4024-4029, 2010.

- [56] K. Schmoltner, *et al.*, "Electrolyte-Gated Organic Field-Effect Transistor for Selective Reversible Ion Detection," *Advanced Materials*, vol. 25, pp. 6895-6899, 2013.
- [57] L. Kergoat, *et al.*, "A Water-Gate Organic Field-Effect Transistor," *Advanced Materials*, vol. 22, pp. 2565-2569, 2010.
- [58] L. Kergoat, *et al.*, "DNA detection with a water-gated organic field-effect transistor," *Organic Electronics*, vol. 13, pp. 1-6, 2012.
- [59] S. Casalini, *et al.*, "Organic field-effect transistor for label-free dopamine sensing," *Organic Electronics*, vol. 14, pp. 156-163, 2013.
- [60] R. D. McCullough, *et al.*, "Design, synthesis, and control of conducting polymer architectures: structurally homogeneous poly(3-alkylthiophenes)," *The Journal of Organic Chemistry*, vol. 58, pp. 904-912, 1993/02/01 1993.
- [61] T.-A. Chen, *et al.*, "Regiocontrolled Synthesis of Poly(3-alkylthiophenes) Mediated by Rieke Zinc: Their Characterization and Solid-State Properties," *Journal of the American Chemical Society*, vol. 117, pp. 233-244, 1995/01/01 1995.
- [62] H. Sirringhaus, "Device Physics of Solution-Processed Organic Field-Effect Transistors," *Advanced Materials*, vol. 17, pp. 2411-2425, 2005.
- [63] M. S. A. Abdou, *et al.*, "Interaction of Oxygen with Conjugated Polymers: Charge Transfer Complex Formation with Poly(3-alkylthiophenes)," *Journal of the American Chemical Society*, vol. 119, pp. 4518-4524, 1997/05/01 1997.
- [64] M. Heeney, *et al.*, "Stable Polythiophene Semiconductors Incorporating Thieno[2,3-b]thiophene," *Journal of the American Chemical Society*, vol. 127, pp. 1078-1079, 2005/02/01 2005.
- [65] L. M. Dumitru, *et al.*, "Plain Poly(acrylic acid) Gated Organic Field-Effect Transistors on a Flexible Substrate," *ACS Applied Materials & Interfaces*, vol. 5, pp. 10819-10823, 2013/11/13 2013.
- [66] B. H. Hamadani, *et al.*, "Undoped polythiophene field-effect transistors with mobility of $1\text{cm}^2\text{V}^{-1}\text{s}^{-1}$," *Applied Physics Letters*, vol. 91, p. 243512, 2007.
- [67] R. P. Ortiz, *et al.*, "High-k Organic, Inorganic, and Hybrid Dielectrics for Low-Voltage Organic Field-Effect Transistors," *Chemical Reviews*, vol. 110, pp. 205-239, 2010/01/13 2010.
- [68] L.-L. Chua, *et al.*, "General observation of n-type field-effect behaviour in organic semiconductors," *Nature*, vol. 434, pp. 194-199, 2005.
- [69] Y.-Y. Noh and H. Sirringhaus, "Ultra-thin polymer gate dielectrics for top-gate polymer field-effect transistors," *Organic Electronics*, vol. 10, pp. 174-180, 2009.
- [70] M. E. Roberts, *et al.*, "Cross-Linked Polymer Gate Dielectric Films for Low-Voltage Organic Transistors," *Chemistry of Materials*, vol. 21, pp. 2292-2299, 2009/06/09 2009.
- [71] H. Du, *et al.*, "Electric double-layer transistors: a review of recent progress," *Journal of Materials Science*, vol. 50, pp. 5641-5673, 2015.
- [72] H. Wang and L. Pilon, "Intrinsic limitations of impedance measurements in determining electric double layer capacitances," *Electrochimica Acta*, vol. 63, pp. 55-63, 2012.
- [73] N. E. McTigue and J. M. Symons, "Water Dictionary - A Comprehensive Reference of Water Terminology (2nd Edition)," ed: American Water Works Association (AWWA).
- [74] <http://www.myronl.com/applications/diapp.htm>.
- [75] S. H. Yalkowsky, *Handbook of Aqueous Solubility Data*: CRC Press, 2003.

- [76] Y. Fujii, *et al.*, "Analysis of electric double layer in aqueous solutions of sodium chloride," in *Electrical Insulation and Dielectric Phenomena (CEIDP), 2010 Annual Report Conference on*, 2010, pp. 1-4.
- [77] F. Buth, *et al.*, "Biofunctional Electrolyte-Gated Organic Field-Effect Transistors," *Advanced Materials*, vol. 24, pp. 4511-4517, 2012.
- [78] G. Wang, *et al.*, "A review of electrode materials for electrochemical supercapacitors," *Chemical Society Reviews*, vol. 41, pp. 797-828, 2012.
- [79] R. Hagiwara and Y. Ito, "Room temperature ionic liquids of alkylimidazolium cations and fluoroanions," *Journal of Fluorine Chemistry*, vol. 105, pp. 221-227, 2000.
- [80] U. Löffelmann, *et al.*, "Solvent-free inkjet printing process for the fabrication of conductive, transparent, and flexible ionic liquid-polymer gel structures," *Journal of Polymer Science Part B: Polymer Physics*, vol. 50, pp. 38-46, 2012.
- [81] S. Ono, *et al.*, "High-mobility, low-power, and fast-switching organic field-effect transistors with ionic liquids," *Applied Physics Letters*, vol. 92, p. 103313, 2008.
- [82] S. W. Lee, *et al.*, "Periodic Array of Polyelectrolyte-Gated Organic Transistors from Electrospun Poly(3-hexylthiophene) Nanofibers," *Nano Letters*, vol. 10, pp. 347-351, 2010/01/13 2010.
- [83] M. J. Panzer and C. D. Frisbie, "High Carrier Density and Metallic Conductivity in Poly(3-hexylthiophene) Achieved by Electrostatic Charge Injection," *Advanced Functional Materials*, vol. 16, pp. 1051-1056, 2006.
- [84] E. Said, *et al.*, "Polymer field-effect transistor gated via a poly(styrenesulfonic acid) thin film," *Applied Physics Letters*, vol. 89, p. 143507, 2006.
- [85] J. Lee, *et al.*, "Ion Gel-Gated Polymer Thin-Film Transistors: Operating Mechanism and Characterization of Gate Dielectric Capacitance, Switching Speed, and Stability," *The Journal of Physical Chemistry C*, vol. 113, pp. 8972-8981, 2009/05/21 2009.
- [86] T. Uemura, *et al.*, "Low-voltage operation of n-type organic field-effect transistors with ionic liquid," *Applied Physics Letters*, vol. 95, p. 103301, 2009.
- [87] S. Thiemann, *et al.*, "Ionic Liquids for Electrolyte-Gating of ZnO Field-Effect Transistors," *The Journal of Physical Chemistry C*, vol. 116, pp. 13536-13544, 2012/06/28 2012.
- [88] W. Xie and C. D. Frisbie, "Organic Electrical Double Layer Transistors Based on Rubrene Single Crystals: Examining Transport at High Surface Charge Densities above 10^{13} cm^{-2} ," *The Journal of Physical Chemistry C*, vol. 115, pp. 14360-14368, 2011/07/28 2011.
- [89] A. Al Naim, *et al.*, "Water-gated organic nanowire transistors," *Organic Electronics*, vol. 14, pp. 1057-1063, 2013.
- [90] O. Inganäs, "Hybrid electronics and electrochemistry with conjugated polymers," *Chemical Society Reviews*, vol. 39, pp. 2633-2642, 2010.
- [91] O. Larsson, *et al.*, "Controlling the Dimensionality of Charge Transport in an Organic Electrochemical Transistor by Capacitive Coupling," *Advanced Materials*, vol. 23, pp. 4764-4769, 2011.
- [92] T. Someya, *et al.*, "Integration and Response of Organic Electronics with Aqueous Microfluidics," *Langmuir*, vol. 18, pp. 5299-5302, 2002/06/01 2002.
- [93] M. E. Roberts, *et al.*, "Water-Stable Organic Transistors and Their Application in Chemical and Biological Sensors," *Proceedings of the National Academy of Sciences of the United States of America*, vol. 105, pp. 12134-12139, 2008.

- [94] M. Magliulo, *et al.*, "Electrolyte-Gated Organic Field-Effect Transistor Sensors Based on Supported Biotinylated Phospholipid Bilayer," *Advanced Materials*, vol. 25, pp. 2090-2094, 2013.
- [95] C. Suspene, *et al.*, "Copolythiophene-based water-gated organic field-effect transistors for biosensing," *Journal of Materials Chemistry B*, vol. 1, pp. 2090-2097, 2013.
- [96] C.-H. Chiu, *et al.*, "Simultaneous determination of manganese, iron and cobalt in copper with a multi-element graphite furnace atomic absorption spectrometer," *Spectrochimica Acta Part B: Atomic Spectroscopy*, vol. 58, pp. 575-580, 2003.
- [97] E. A. Takara, *et al.*, "On-line preconcentration/determination of copper in parenteral solutions using activated carbon by inductively coupled plasma optical emission spectrometry," *Journal of Pharmaceutical and Biomedical Analysis*, vol. 39, pp. 735-739, 2005.
- [98] C. Xiong, *et al.*, "Speciation of dissolved Fe(II) and Fe(III) in environmental water samples by micro-column packed with N-benzoyl-N-phenylhydroxylamine loaded on microcrystalline naphthalene and determination by electrothermal vaporization inductively coupled plasma-optical emission spectrometry," *Analytica Chimica Acta*, vol. 559, pp. 113-119, 2006.
- [99] J. Wang, *et al.*, "Flow injection on-line dilution for multi-element determination in human urine with detection by inductively coupled plasma mass spectrometry," *Talanta*, vol. 55, pp. 117-126, 2001.
- [100] T. Liu, *et al.*, "An inorganic-organic hybrid optical sensor for heavy metal ion detection based on immobilizing 4-(2-pyridylazo)-resorcinol on functionalized HMS," *Journal of Hazardous Materials*, vol. 201-202, pp. 155-161, 2012.
- [101] L. d. Coo, *et al.*, "Spectrophotometric study of the solubility and the protolytic properties of 1-(2-pyridylazo)-2-naphthol in different ethanol-water solutions," *Analytica Chimica Acta*, vol. 360, pp. 153-159, 1998.
- [102] Z. Biyiklioğlu and H. Kantekin, "The synthesis, using microwave irradiation and characterization of novel, organosoluble metal-free and metallophthalocyanines substituted with flexible crown ether moieties," *Dyes and Pigments*, vol. 80, pp. 17-21, 2009.
- [103] P. Bergveld, "Development of an Ion-Sensitive Solid-State Device for Neurophysiological Measurements," *IEEE Transactions on Biomedical Engineering*, vol. BME-17, pp. 70-71, 1970.
- [104] S. K. Menon, *et al.*, "Azo calix[4]arene based neodymium(III)-selective PVC membrane sensor," *Talanta*, vol. 83, pp. 1329-1334, 2011.
- [105] N. Alizadeh, *et al.*, "Poly(vinyl chloride)-membrane ion-selective bulk optode based on 1,10-dibenzyl-1,10-diaza-18-crown-6 and 1-(2-pyridylazo)-2-naphthol for Cu²⁺ and Pb²⁺ ions," *Analytica Chimica Acta*, vol. 464, pp. 187-196, 2002.
- [106] A. A. Abdel Aziz, "A novel highly sensitive and selective optical sensor based on a symmetric tetradentate Schiff-base embedded in PVC polymeric film for determination of Zn²⁺ ion in real samples," *Journal of Luminescence*, vol. 143, pp. 663-669, 2013.
- [107] B. P. Nikolsky, "Theory of the glass electrode. I. Theoretical. //," *J. Phys. Chem. (U.S.S.R.)*, vol. 10, pp. 495-503., 1937.

- [108] K. Melzer, *et al.*, "Selective ion-sensing with membrane-functionalized electrolyte-gated carbon nanotube field-effect transistors," *Analyst*, vol. 139, pp. 4947-4954, 2014.
- [109] K. Melzer, *et al.*, "Polymeric ion-selective membrane functionalized gate-electrodes: Ion-selective response of electrolyte-gated poly (3-hexylthiophene) field-effect transistors," *Organic Electronics*, vol. 15, pp. 595-601, 2014.
- [110] F. Perret and A. W. Coleman, "Biochemistry of anionic calix[n]arenes," *Chemical Communications*, vol. 47, pp. 7303-7319, 2011.
- [111] V. Arora, *et al.*, "Calixarenes as sensor materials for recognition and separation of metal ions," *Arkivoc*, vol. 2, pp. 172-200, 2007.
- [112] K. Sharma and P. J. Cragg, "Calixarene based chemical sensors," *Chem Sensors*, vol. 1, pp. 1-18, 2011.
- [113] T. McKittrick, *et al.*, "Calcium-selective electrode based on a calix[4]arene tetraphosphine oxide," *Talanta*, vol. 43, pp. 1145-1148, 1996/07/01 1996.
- [114] H. H. Gatzen, *et al.*, "Vacuum Technology," in *Micro and Nano Fabrication: Tools and Processes*, ed Berlin, Heidelberg: Springer Berlin Heidelberg, 2015, pp. 7-63.
- [115] M. T. Thomas, "16. Vacuum Deposition Techniques*," in *Methods in Experimental Physics*. vol. Volume 14, G. L. Weissler and R. W. Carlson, Eds., ed: Academic Press, 1980, pp. 521-575.
- [116] D. Johannsmann, "Introduction," in *The Quartz Crystal Microbalance in Soft Matter Research: Fundamentals and Modeling*, ed Cham: Springer International Publishing, 2015, pp. 1-22.
- [117] M. Medina-Sánchez, *et al.*, "An Inkjet-Printed Field-Effect Transistor for Label-Free Biosensing," *Advanced Functional Materials*, vol. 24, pp. 6291-6302, 2014.
- [118] Y. Zhang, *et al.*, "Fabrication of patterned thermoplastic microphases between composite plies by inkjet printing," *Journal of Composite Materials*, vol. 49, pp. 1907-1913, 2015.
- [119] S. H. Eom, *et al.*, "Polymer solar cells based on inkjet-printed PEDOT:PSS layer," *Organic Electronics*, vol. 10, pp. 536-542, 2009.
- [120] J. Perelaer, *et al.*, "Printed electronics: the challenges involved in printing devices, interconnects, and contacts based on inorganic materials," *Journal of Materials Chemistry*, vol. 20, p. 8446, 2010.
- [121] E. Tekin, *et al.*, "Inkjet printing as a deposition and patterning tool for polymers and inorganic particles," *Soft Matter*, vol. 4, p. 703, 2008.
- [122] H. Meier, *et al.*, "Inkjet printed, conductive, 25 μm wide silver tracks on unstructured polyimide," *physica status solidi (a)*, vol. 206, pp. 1626-1630, 2009.
- [123] F. Xue, *et al.*, "Inkjet printed silver source/drain electrodes for low-cost polymer thin film transistors," *Microelectronic Engineering*, vol. 83, pp. 298-302, 2006.
- [124] Y. Noguchi, *et al.*, "Direct inkjet printing of silver electrodes on organic semiconductors for thin-film transistors with top contact geometry," *Applied Physics Letters*, vol. 93, p. 043303, 2008.
- [125] P. J. Smith, *et al.*, "Direct ink-jet printing and low temperature conversion of conductive silver patterns," *Journal of Materials Science*, vol. 41, pp. 4153-4158, 2006.
- [126] T. H. J. van Osch, *et al.*, "Inkjet Printing of Narrow Conductive Tracks on Untreated Polymeric Substrates," *Advanced Materials*, vol. 20, pp. 343-345, 2008.

- [127] C. E. Hendriks, *et al.*, "'Invisible' Silver Tracks Produced by Combining Hot-Embossing and Inkjet Printing," *Advanced Functional Materials*, vol. 18, pp. 1031-1038, 2008.
- [128] H. P. Le, "Progress and Trends in Ink-jet Printing Technology," pp. 49-62(14), 1998.
- [129] A. U. Chen and O. A. Basaran, "A new method for significantly reducing drop radius without reducing nozzle radius in drop-on-demand drop production," *Physics of Fluids (1994-present)*, vol. 14, pp. L1-L4, 2002.
- [130] J. Perelaer, *et al.*, "Ink-jet Printing and Microwave Sintering of Conductive Silver Tracks," *Advanced Materials*, vol. 18, pp. 2101-2104, 2006.
- [131] M. C. Petty, "Electrical Conductivity," in *Molecular Electronics*, ed: John Wiley & Sons, Ltd, 2007, pp. 65-128.
- [132] L. A. Majewski, *et al.*, "Influence of processing conditions on the stability of poly(3-hexylthiophene)-based field-effect transistors," *Applied Physics Letters*, vol. 88, p. 222108, 2006.
- [133] D. Perednis and L. J. Gauckler, "Thin Film Deposition Using Spray Pyrolysis," *Journal of Electroceramics*, vol. 14, pp. 103-111, 2005.
- [134] L. Filipovic, *et al.*, "Modeling spray pyrolysis deposition," in *Proceedings of the world congress on engineering*, 2013, pp. 987-992.
- [135] D. Perednis and L. J. Gauckler, "Solid oxide fuel cells with electrolytes prepared via spray pyrolysis," *Solid State Ionics*, vol. 166, pp. 229-239, 2004.
- [136] L. M. Bertus, *et al.*, "Influence of spray pyrolysis deposition parameters on the optoelectronic properties of WO₃ thin films," *Thin Solid Films*, vol. 520, pp. 4282-4290, 2012.
- [137] J. C. Vigié and J. Spitz, "Chemical Vapor Deposition at Low Temperatures," *Journal of The Electrochemical Society*, vol. 122, pp. 585-588, April 1, 1975.
- [138] N. Stelzer and J. Schoonman, "Synthesis of terbia-doped yttria-stabilized zirconia thin films by electrostatic spray deposition (ESD)," *Journal of Materials Synthesis and Processing* 4 (6), 429-438.(1996), 1996.
- [139] H. H. Afify, *et al.*, "Influence of substrate temperature on the structural, optical and electrical properties of ZnO thin films prepared by spray pyrolysis," *Journal of Materials Science: Materials in Electronics*, vol. 2, pp. 152-156, 1991.
- [140] S. E. Microscopy, "<https://www.purdue.edu/ehps/rem/rs/sem.htm>."
- [141] J. F. d. Lima, *et al.*, "Transparent UV-absorbers thin films of zinc oxide: Ceria system synthesized via sol-gel process," *Optical Materials*, vol. 35, pp. 56-60, 2012.
- [142] J. C. Vickerman and I. Gilmore, *Surface Analysis: The Principal Techniques*: Wiley, 2011.
- [143] XPS, "<http://xpssimplified.com/elements/zinc.php>," 2016.
- [144] R. Al-Gaashani, *et al.*, "XPS and optical studies of different morphologies of ZnO nanostructures prepared by microwave methods," *Ceramics International*, vol. 39, pp. 2283-2292, 2013.
- [145] J. H. Zheng, *et al.*, "Synthesis and optical properties of flower-like ZnO nanorods by thermal evaporation method," *Applied Surface Science*, vol. 257, pp. 5083-5087, 2011.
- [146] J. Das, *et al.*, "Micro-Raman and XPS studies of pure ZnO ceramics," *Physica B: Condensed Matter*, vol. 405, pp. 2492-2497, 2010.

- [147] L. G. Mar, *et al.*, "An XPS study of zinc oxide thin film growth on copper using zinc acetate as a precursor," *Thin Solid Films*, vol. 223, pp. 341-347, 1993/02/15 1993.
- [148] S. Oertel, *et al.*, "High-mobility metal-oxide thin-film transistors by spray deposition of environmentally friendly precursors," *Thin Solid Films*, vol. 553, pp. 114-117, 2014.
- [149] C. D. Wagner, *et al.*, "Two-dimensional chemical state plots: a standardized data set for use in identifying chemical states by x-ray photoelectron spectroscopy," *Analytical Chemistry*, vol. 51, pp. 466-482, 1979/04/01 1979.
- [150] D. Briggs, "Handbook of X-ray Photoelectron Spectroscopy C. D. Wanger, W. M. Riggs, L. E. Davis, J. F. Moulder and G. E. Muilenberg Perkin-Elmer Corp., Physical Electronics Division, Eden Prairie, Minnesota, USA, 1979. 190 pp. \$195," *Surface and Interface Analysis*, vol. 3, pp. v-v, 1981.
- [151] C. Ucurum, *et al.*, "Impact of electrical measurement parameters on the hysteresis behavior of pentacene-based organic thin-film transistors," *Organic Electronics*, vol. 11, pp. 1523-1528, 2010.
- [152] S. Y. Park, *et al.*, "Cooperative polymer gate dielectrics in organic thin-film transistors," *Applied Physics Letters*, vol. 85, pp. 2283-2285, 2004.
- [153] IEEE, "IEEE Standard," *IEEE* vol. 0_1 . pp. 1620-2004, 2004.
- [154] L. Hague, *et al.*, "Simplified Real-Time Organic Transistor Characterisation Schemes for Sensing Applications," *Science of Advanced Materials*, vol. 3, pp. 907-911, 2011.
- [155] A. Dragoneas, *et al.*, "An electrical characterisation system for the real-time acquisition of multiple independent sensing parameters from organic thin film transistors," *J. Sens. Sens. Syst.*, vol. 4, pp. 169-177, 2015.
- [156] J. Veres, *et al.*, "Low-k Insulators as the Choice of Dielectrics in Organic Field-Effect Transistors," *Advanced Functional Materials*, vol. 13, pp. 199-204, 2003.
- [157] L. Hague, *et al.*, "Discovery of a New Odour Sensing Mechanism Using an n-Type Organic Transistor," *Sensor Letters*, vol. 9, pp. 1692-1696, 2011.
- [158] W. F. Pasveer, *et al.*, "Unified Description of Charge-Carrier Mobilities in Disordered Semiconducting Polymers," *Physical Review Letters*, vol. 94, p. 206601, 2005.
- [159] M. Spijkman, *et al.*, "Beyond the Nernst-limit with dual-gate ZnO ion-sensitive field-effect transistors," *Applied Physics Letters*, vol. 98, p. 043502, 2011.
- [160] H. Minemawari, *et al.*, "Inkjet printing of single-crystal films," *Nature*, vol. 475, pp. 364-7, Jul 21 2011.
- [161] H. Klauk, "Organic thin-film transistors," *Chemical Society Reviews*, vol. 39, pp. 2643-2666, 2010.
- [162] M. E. Burnett and S. Q. Wang, "Current sunscreen controversies: a critical review," *Photodermatology, Photoimmunology & Photomedicine*, vol. 27, pp. 58-67, 2011.
- [163] C. Klingshirn, "ZnO: Material, Physics and Applications," *ChemPhysChem*, vol. 8, pp. 782-803, 2007.
- [164] A. Ashour, *et al.*, "Physical properties of ZnO thin films deposited by spray pyrolysis technique," *Applied Surface Science*, vol. 252, pp. 7844-7848, 2006.
- [165] M. Belmares, *et al.*, "Hildebrand and Hansen solubility parameters from Molecular Dynamics with applications to electronic nose polymer sensors," *Journal of Computational Chemistry*, vol. 25, pp. 1814-1826, 2004.

- [166] H. AlQahtani, *et al.*, "Highly sensitive alkane odour sensors based on functionalised gold nanoparticles," *Sensors and Actuators B: Chemical*, vol. 160, pp. 399-404, 2011.
- [167] P. F. Carcia, *et al.*, "High-performance ZnO thin-film transistors on gate dielectrics grown by atomic layer deposition," *Applied Physics Letters*, vol. 88, p. 123509, 2006.
- [168] J. H. Cho, *et al.*, "High-Capacitance Ion Gel Gate Dielectrics with Faster Polarization Response Times for Organic Thin Film Transistors," *Advanced Materials*, vol. 20, pp. 686-690, 2008.
- [169] J. H. Kim, *et al.*, "Origins of Highly Stable Al-evaporated Solution-processed ZnO Thin Film Transistors: Insights from Low Frequency and Random Telegraph Signal Noise," *Scientific Reports*, vol. 5, p. 16123, 2015.
- [170] W. Chen, *et al.*, "Synthesis, Thermal Stability and Properties of ZnO₂ Nanoparticles," *The Journal of Physical Chemistry C*, vol. 113, pp. 1320-1324, 2009/01/29 2009.
- [171] A. L. Companion, "The diffuse reflectance spectra of zinc oxide and zinc peroxide," *Journal of Physics and Chemistry of Solids*, vol. 23, pp. 1685-1688, 1962/12/01 1962.
- [172] T. Yamaguchi, *et al.*, "X-ray diffraction and Raman studies of zinc(II) chloride hydrate melts, ZnCl₂.rH₂O (r = 1.8, 2.5, 3.0, 4.0, and 6.2)," *The Journal of Physical Chemistry*, vol. 93, pp. 2620-2625, 1989/03/01 1989.
- [173] D. E. Irish, *et al.*, "Raman Study of Zinc Chloride Solutions," *The Journal of Chemical Physics*, vol. 39, pp. 3436-3444, 1963.
- [174] S.-g. Mei, *et al.*, "Preparation and Characterization of Gallium Doped ZnO/Epoxy Composite as Thermal-Insulating Coating," *Asian Journal of Chemistry*, vol. 24, p. 2210, 2012.
- [175] P. Bergveld, "The development and application of FET-based biosensors," *Biosensors*, vol. 2, pp. 15-33, 1986/01/01 1986.
- [176] Y. Zhou, *et al.*, "Selective and sensitive colorimetric sensor of mercury (II) based on gold nanoparticles and 4-mercaptophenylboronic acid," *Sensors and Actuators B: Chemical*, vol. 196, pp. 106-111, 2014.
- [177] T. Gunnlaugsson, *et al.*, "Highly selective fluorescent chemosensors for cadmium in water," *Tetrahedron*, vol. 60, pp. 11239-11249, 2004.
- [178] R. Shannon, "Revised effective ionic radii and systematic studies of interatomic distances in halides and chalcogenides," *Acta Crystallographica Section A*, vol. 32, pp. 751-767, 1976.
- [179] A. Cadogan, *et al.*, "All-solid-state sodium-selective electrode based on a calixarene ionophore in a poly(vinyl chloride) membrane with a polypyrrole solid contact," *Analytical Chemistry*, vol. 64, pp. 2496-2501, 1992/11/01 1992.
- [180] H. Schumann, *et al.*, "Butenyl-Substituted Alkaline-Earth Metallocenes: A First Step towards Olefin Complexes of the Alkaline-Earth Metals," *Angewandte Chemie International Edition*, vol. 43, pp. 6208-6211, 2004.
- [181] C. M. Hansen, "Hansen Solubility Parameters— A User's Handbook," *CRC Press Inc.*, vol. Boca Raton.
- [182] N. Winterton, "Solubilization of polymers by ionic liquids," *Journal of Materials Chemistry*, vol. 16, pp. 4281-4293, 2006.
- [183] M. A. Qazi, *et al.*, "An excellent copper selective chemosensor based on calix[4]arene framework," *Analytica Chimica Acta*, vol. 761, pp. 157-168, 2013.

- [184] L. Lvova, *et al.*, "Porphyrin-based chemical sensors and multisensor arrays operating in the liquid phase," *Sensors and Actuators B: Chemical*, vol. 179, pp. 21-31, 2013.
- [185] M. Kandaz, *et al.*, "Selective metal sensor phthalocyanines bearing non-peripheral functionalities: Synthesis, spectroscopy, electrochemistry and spectroelectrochemistry," *Polyhedron*, vol. 28, pp. 257-262, 2009.
- [186] L. K. Kumawat, *et al.*, "A novel optical sensor for copper ions based on phthalocyanine tetrasulfonic acid," *Sensors and Actuators B: Chemical*, vol. 212, pp. 389-394, 2015.
- [187] H. N. Kim, *et al.*, "Fluorescent and colorimetric sensors for detection of lead, cadmium, and mercury ions," *Chemical Society Reviews*, vol. 41, pp. 3210-3244, 2012.
- [188] R. Ludwig and N. Dzung, "Calixarene-Based Molecules for Cation Recognition," *Sensors*, vol. 2, p. 397, 2002.